Automated calibration of ceilometer data and its applicability for quantitative aerosol monitoring

Alexander Maximilian Geiß

München 2016

Automated calibration of ceilometer data and its applicability for quantitative aerosol monitoring

Alexander Maximilian Geiß

Dissertation
an der Fakultät für Physik
der Ludwig–Maximilians–Universität
München

vorgelegt von
Alexander Maximilian Geiß
aus München

München, den 6. Mai 2016

Erstgutachter: Prof. Dr. Bernhard Mayer

Zweitgutachter: Dr. Martin Weissmann

Tag der mündlichen Prüfung: 2. Juni 2016

Contents

Zusammenfassung

Aerosolpartikel sind ein wichtiger Bestandteil der Erdatmosphäre. Sie haben Einfluss auf das globale Klima, aber auch auf die Luftqualität und somit letztlich auch auf die menschliche Gesundheit. Schadstoffe breiten sich insbesondere in der Mischungsschicht (ML) aus, dem untersten Teil der Erdatmosphäre. Die ML-Höhe wird direkt von der Erdoberfläche aus beeinflusst. Die Physik der ML ist von großem Interesse für die Meteorologie, da dynamische und thermodynamische Prozesse sowie die Zusammensetzung der Atmosphäre eine große Rolle spielen. In letzter Zeit haben vor allem Wetterdienste Netzwerke mit automatisierten Rückstreulidargeräten mit einer Wellenlänge (Ceilometer) aufgebaut. Folglich muss untersucht werden, welches Potential Ceilometer bei der quantitativen Bestimmung der räumlichen sowie zeitlichen Aerosolverteilung in der Atmosphäre haben. Im Hinblick auf Ceilometernetzwerke ist die Entwicklung einer automatischen Bestimmung der ML-Höhe für Untersuchungen der Luftqualität und eine automatisierte Kalibrierung der Ceilometer nötig. Erst mit einer automatisierten Kalibrierung kann man optische Eigenschaften anhand von Ceilometernetzwerken ableiten.

Es ist gelungen die hier entwickelte absolute Kalibrierung, welche auf der Bestimmung der Lidarkonstante C_L basiert, vollständig zu automatisieren. Sie kann in einem dreistufigen Verfahren auf verschiedenste Ceilometer angewendet werden. Dadurch kann man den Partikelrückstreukoeffizienten β_p unabhängig vom Signal-Rausch-Verhältnis, dem größten Problem der Ceilometer, bei fast allen Wetterbedingungen sowohl bei Tag als auch bei Nacht bestimmen. Mit der Anwendung auf eine fünfjährige Messreihe von einem Jenoptik CHM15kx lässt sich eine Lidarkonstante an 391 von 1900 verfügbaren Tagen ermitteln. Unter Nutzung von C_L können β_p-Profile mit einer Genauigkeit von 17% abgeleitet werden. Um Untersuchungen der ML vorzunehmen, wird der automatische Algorithmus COBOLT (Continuous Boundary Layer Tracing) zur Bestimmung der ML-Höhe entwickelt. Im Gegensatz zu ML-Tagesgängen von häufig benutzten Algorithmen, die große Sprünge oder gar Lücken in der von ihnen bestimmten ML-Höhe aufweisen, basiert COBOLT auf einer Zeit-Höhen-Verfolgung. Auf

Grundlage eines “best-of-all”-Ansatzes und unter der Verwendung aktueller Methoden zur Schichtbestimmung wird ein Parameter definiert. Dieser Parameter erlaubt unter Verwendung eines “multi-member”-Ansatzes ein Verfolgen der ML-Höhe zur Auswertung von vollständigen ML-Tagesgängen ohne Zwischenschritte. Der Vergleich und die Validierung von ML-Höhen aus Daten von Radiosonden und zwei anderen Algorithmen zur ML-Höhenbestimmung zeigen die Zuverlässigkeit von COBOLT.

Die Kalibrierung von Ceilometern und der Algorithmus zur Mischungsschichthöhenbestimmung eröffnen eine Vielzahl von Anwendungsmöglichkeiten. Zu den gezeigten Beispielen gehört eine Statistik des β_p-Profils und eine Statistik der ML-Höhen über München. Dabei werden sowohl die ML-Höhen von ländlichen Gebieten mit urbanen Zentren verglichen, als auch eine Validierung von Chemietransportmodellen und eine Untersuchung des Einflusses der ML-Höhen auf die Luftqualität vorgenommen.

Abstract

Aerosols are important constituents of the Earth's atmosphere. Their impact on global climate, but also on air quality and hence human health is huge. A region were pollutants can disperse is the Mixing Layer (ML), the lowermost part of the Earth's atmosphere. It's thickness is directly influenced from the Earth's surface. The physics of the ML is of great interest for the meteorological community as effects on the dynamics, thermodynamics and air quality of the atmosphere are crucial. Recently, networks of automated single-wavelength backscatter lidars ("ceilometers") have been implemented, primarily by weather services. As a consequence, the potential of ceilometers to quantitatively determine the spatio-temporal distribution of atmospheric aerosols must be investigated. With regard to ceilometer networks, automatic mixing layer height retrievals for air quality studies and a fully automated calibration of ceilometers to derive aerosol optical properties is required.

The absolute calibration approach, which is based on the determination of the lidar constant C_L was fully automated and is applicable in a three-step procedure to several ceilometer types. As a result, the particle backscatter coefficient β_p can be determined at virtually any weather condition during day and night, independent of the main ceilometer issue—the limited signal-to-noise ratio. Applied to 5 years of measurement of a Jenoptik CHM15kx, a lidar constant could be determined on 391 days out of 1900 available days. With knowing C_L, β_p-profiles within an accuracy of typically 17% can be derived. To allow investigations of the ML, the automatic ML-height retrieval algorithm COBOLT (Continuous Boundary Layer Tracing) was developed. In contrast to ML-cycles with large jumps or even temporal gaps, determined by already available and frequently used algorithms, COBOLT uses a time-height tracking procedure. On basis of a best-of-all-approach utilizing state-of-the-art layer detection techniques, a traceable parameter is defined and allows to detect complete diurnal ML-cycles without steps by including a multi-member approach. Validation and crosschecks with ML-heights from radiosonde data and two other ML-height retrieval algorithms demonstrated the reliability of COBOLT.

A wide range of applications is possible with a calibrated ceilometer and a reliable ML-height retrieval algorithm. Following examples are shown: a β_p-profile statistic and ML-height statistic above Munich; ML-height comparisons between rural and an urban site, as well as a validation of a chemistry transport model and an investigation of ML-height influences on air quality.

1 Introduction

Aerosols are important constituents of the Earth's atmosphere. They are liquid or solid particles suspended in a gas, usually in air. Aerosol particles are omnipresent in the ambient air, but due to their size, ranging between 0.005 µm and larger than 10 µm, they are only visible to the unaided eye if the particles are sufficiently large or the concentration is high (e. g. sandstorm). The source can be natural, e. g. volcanic ash, as well as anthropogenic, e. g. biomass burning. Aerosols can be classified by their properties, size, shape, formation and effects. Although the particles are comparatively small in size, their impact on global climate, but also on air quality and hence human health (Aneja et al., 2008; Davidson et al., 2005) is huge. The effect of aerosols can be divided into direct and indirect effects, as illustrated in Fig. 1.1. Depending on their microphysical properties, particles can absorb and scatter shortwave radiation from the sun or terrestrial longwave radiation. This reduces the amount of radiation reaching the Earth surface (Hansen et al., 1980; Coakley and Cess, 1985; Satheesh and Moorthy, 2005) and thus influences the radiation budget in a direct way. Indirect effects are caused by the hygroscopicity of aerosols. Acting as a condensation nuclei, aerosols can increase the amount of droplets in a cloud and therefore, support cloud formation processes and influence the cloud albedo (Twomey, 1974). In addition, the life cycle of clouds is changed and the precipitation can be decreased. In case of strongly absorbing aerosol, an effect on the tropospheric stability and consequently reduced cloud formation can be observed (Hansen et al., 1997; IPCC, 2013). By today, aerosols continue to contribute the largest uncertainty to the total radiative forcing estimate (IPCC, 2013). For a full understanding of global climate changes and in order to improve climate and weather prediction models, the aerosol properties, their impact, the source regions and the global distribution, horizontally and vertically, must be quantified. This also includes the investigation of optical and microphysical properties of aerosols under different meteorological conditions.

Over the last decades several measurement campaigns and field experiments provided the basis for the characterization of physical, chemical, optical and radiation

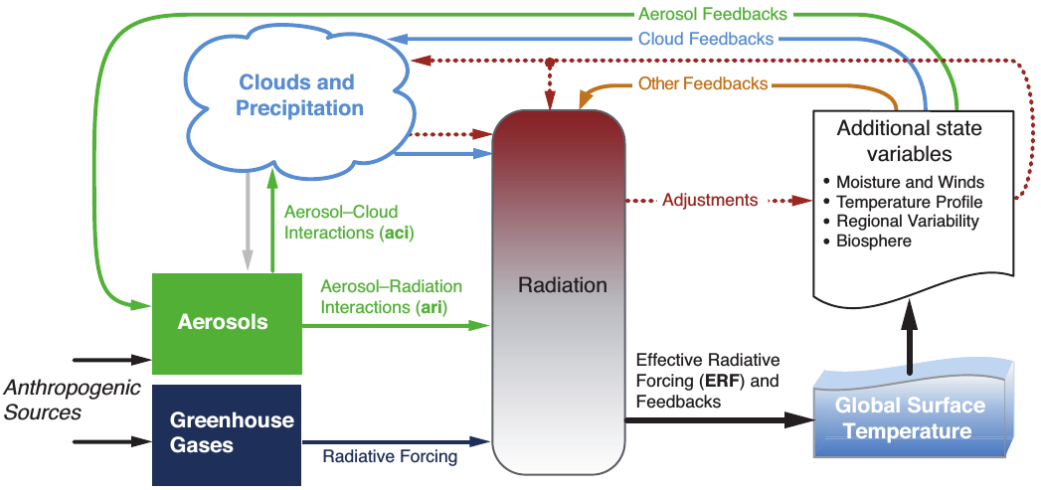

Figure 1.1: Schematic representation of the role of aerosols (IPCC, 2013).

properties of aerosol from different source regions. These include, for example, INDOEX in the Indian Ocean (Müller et al., 2000; Ramanathan et al., 2001), SAFARI-2000 in the South Atlantic and South Africa (King et al., 2003), ACE-2 in the North Atlantic (Flamant et al., 2000; Ansmann et al., 2001; Raes et al., 2000), ACE-Asia in East Asia and in the Northwest Pacific (Shimizu et al., 2004; Huebert et al., 2003), MINOS in the Mediterranean region (Lelieveld et al., 2002), NEAQS in the North Atlantic (Quinn and Bates, 2005), AMMA in West Africa (Heese and Wiegner, 2008), as well as SAMUM-1 and SAMUM-2 in Africa and on the Cape Verde islands (Groß et al., 2011; Tesche et al., 2011; Ansmann et al., 2011). A recent example is SALTRACE, a campaign in the Atlantic Ocean where Saharan mineral dust was characterized during and after its long range transport into the Caribbean (Chouza et al., 2015; Groß et al., 2015; Wex et al., 2016; Groß et al., 2016). Knowledge about the global aerosol distribution, however, still remains insufficient but is essential: Since aerosols show a large spatial and temporal variability, the regional impact can be quite different.

To get information about the spatio-temporal distribution of aerosol, lidar (Light Detection and Ranging) has proven to be a valuable instrument during the measurement campaigns. First used with flash lamps as radiation source for distance measurements (Middleton and Spilhaus, 1953), the invention of the Q-switched laser (Maiman, 1960; McClung and Hellwarth, 1962) allowed first measurements for atmospheric purposes (Fiocco and Smullin, 1963). Further improvements of the lasers and the receiver optics allow the retrieval of atmospheric parameters. Depending on its configuration

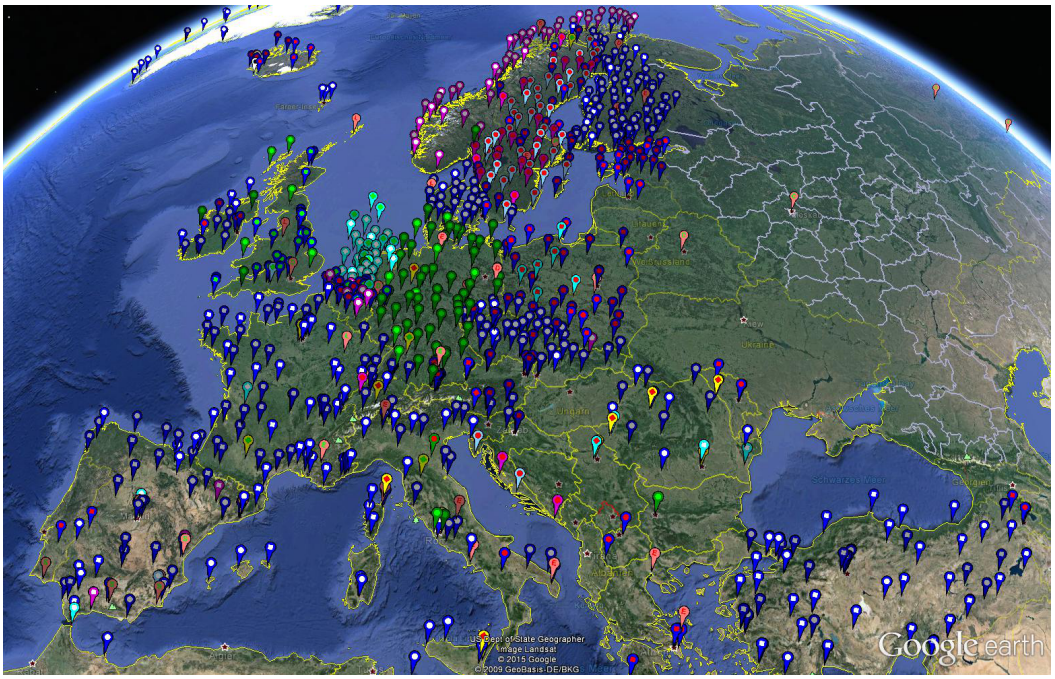

Figure 1.2: Ceilomap of the DWD lists all currently operated ceilometers (www.dwd.de/ceilomap).

with a different number of wavelengths as well as the use of polarization channels, different properties can be obtained for the characterization of aerosols. By operating backscatter lidars, it is possible for example to use aerosol in elevated layers as indicator for tracing air streams in the free troposphere to validate computer models. Backscatter lidars are also useful for air quality forecasts in the mixing layer or for detecting and locating volcanic ash plumes, as it was done in case of the Eyjafjallajökull eruption on Iceland during April 2010 (Gasteiger et al., 2011; Weinzierl et al., 2012; Groß et al., 2012; Wiegner et al., 2012). For this event, lidar was an important tool for aerosol soundings in order to reduce time of airspace closure and minimize the economic impact caused by interrupted flight operations. For the quantitative retrieval of optical and microphysical properties, high spectral resolution lidars (HSRL) or Raman lidars can be used. To account for the regional variability of the aerosol distribution, lidar networks of different states of complexity have been set up in the last years. Most of them are research oriented and provide a limited temporal sampling only. Examples are the Asian Dust Network (http://www-lidar.nies.go.jp/AD-Net/), MPLNET (Micro Pulse Lidar Network, Welton et al. (2001)) and the European aerosol research lidar network (EARLINET, Pappalardo et al. (2014)). The operation of such state-of-

the-art lidar systems is beneficial for characterizing aerosols, however, an unattended continuous operation is still an exception. In order to obtain aerosol measurements in high spatio-temporal resolution and to provide a better horizontal coverage, the ceilometer has come into focus.

1.1 Ceilometer

Ceilometers are simple single-wavelength backscatter lidars, operating with low pulse energy and high pulse repetition frequencies. This characteristic makes them eye-safe and allows unattended and continuous operation. Originally designed to determine cloud base heights, improvements of the hardware now enable the utilization for aerosol remote sensing. Low-cost and low-maintenance are great advantages for setting up whole ceilometer networks. Fig. 1.2 gives an overview of ceilometer networks currently operated mainly by national weather services. Currently, approximately 2200 instruments from different manufacturers are in operation and it is expected that in future, the amount of ceilometers will further increase. The German weather service (DWD), for example, recently ordered 100 instruments from the manufacturer Lufft (www.lufft.com) and also the Dutch weather service announced to replace 39 old instruments by new Lufft ceilometers.

This large number of operating ceilometers can provide a huge data basis for aerosol studies and near real time information for weather prediction and air quality issues. However, the diversity of instruments makes an evaluation difficult. First attempts in comparing and testing the performance and behavior of various ceilometers (e. g. Vaisala, Lufft, Campbell) were done in course of the Ceilometer Performance Experiment (Ceilinex, www.ceilinex2015.de) in Lindenberg 2015. Large differences between instruments of different manufacturers and even between instruments of the same type could be observed. For example, the measurement range or the signal to noise ratio was found to be quite different. These large differences must be taken into account if aerosol parameters shall be determined.

By means of ceilometers, the determination of qualitative parameters, i. e. planetary boundary layer and cloud base heights, as well as quantitative parameters, i. e. particle backscatter coefficients, are possible. To asses the benefit of ceilometers and to determine which parameters can be obtained under specific conditions with which accuracy, is a current research topic.

1.2 Planetary boundary layer

The planetary boundary layer (PBL) is the lowermost part of the Earth's atmosphere and directly influenced from the Earth's surface by different processes, that are: frictional drag, evaporation and transpiration, heat transfer, pollution emission and terrain induced flow modification. Its thickness varies in space and time depending on weather- as well as on surface conditions and in particular on the zenith angle of the sun. Typical values for the mid-latitudes are 50 m up to 2500 m what corresponds to the lower 1% to 20% of the troposphere. But a falling below or exceeding of these values is also possible. The solar radiation acts as a motor for the PBL evolution resulting in a warming or cooling of the ground which in turn forces changes in the PBL via transport processes.

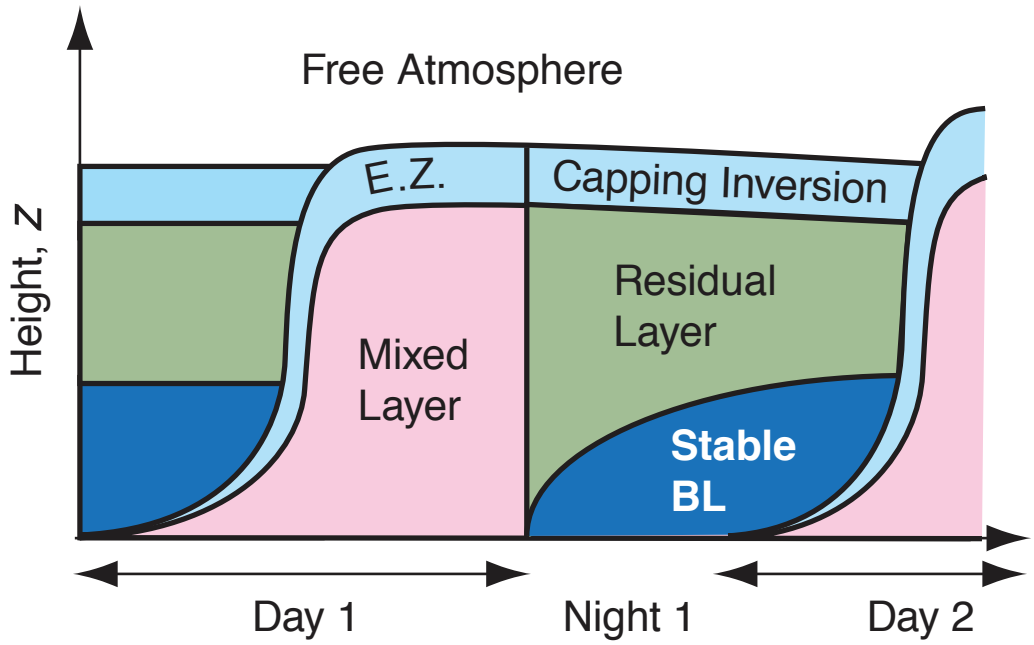

Figure 1.3: Diurnal planetary boundary layer evolution over land under cloud-free conditions. Its structure can be divided in three major characteristic parts - (1) turbulent mixing layer, (2) less turbulent residual layer and (3) nocturnal stable boundary layer (Wallace and Hobbs, 2006).

In Fig. 1.3 this diurnal variation in the structure of the PBL is depicted and can be roughly divided in three major parts (Stull, 1988 // 1997): The mixing layer (ML), the residual layer (RL) and the stable nocturnal boundary layer (SBL).

The ML starts to grow after sunrise when, with increasing radiation, positive buoyancy flux is apparent and the atmospheric stratification becomes unstable. Convection-driven turbulence creates thermals of warm air rising from the ground which leads to vertical mixing of particles, heat and moisture. The result is a homogenized potential temperature and a well-mixed aerosol distribution within the ML. Though, limited by a capping inversion on top, overshooting thermals with enough potential energy are capable to penetrate the stable inversion forcing less turbulent air from the free troposphere to be mixed into the deepening ML. This process is called entrainment and takes place in the entrainment zone (EZ), which can be seen as the interface between the ML and the decoupled free troposphere. If by continuous growing a height is reached where air is saturated with water vapour, the so-called lifting condensation level (LCL), fair weather cumulus clouds can form on top of the ML. Since most of the pollutants are emitted near the surface, the ML is the region where dispersion and transport of atmospheric trace elements is possible. As a consequence of the aerosol trapping below the stable inversion layer of the EZ, a strong negative gradient of the aerosol concentration is obvious at the top of the ML.

About half an hour before sunset the solar heating of the ground is reduced and the generation of raising thermals stops, allowing turbulence to decay in the formerly well mixed layer. This resulting air layer is called residual layer (RL) because its initial mean state variables are the same as those of the recently decayed mixed layer. In the absence of advection, constituents dispersed in the ML during daytime will remain aloft in the RL during nighttime. This neutrally stratified layer allows turbulent flows nearly of equal intensity in all directions. However, the RL is not influenced any longer by turbulent transport from the ground due to the developing nocturnal stable boundary layer (SBL) near the surface. In general, as incoming shortwave radiation drops below the long-wave outgoing radiation, cooling of the ground occurs and thus statically stable stratification establishes near the surface which supresses turbulence. Opposed to the daytime ML, which has a clearly defined top, the stable BL has a poorly defined top with no distinct gradient, e. g. in aerosol concentration. Turbulence or mixing can only occur when wind shear is induced by strong surface winds. The SBL is deepening till the sun rises and repeats the diurnal PBL cycle again.

The physics of the PBL is of great interest for the meteorological community as effects on the dynamics and thermodynamics of the atmosphere are crucial. However, there is still lack of information and knowledge about the planetary boundary

layer processes, although many different methods to determine PBL-heights have been conducted on theoretical (numerical weather models) and experimental (profiling instruments) basis. When utilizing numerical models for PBL-height prediction, different parameterization schemes are available and have to be considered (Bright and Mullen, 2002; Cohen et al., 2015). For validating and cross checking model-derived PBL-heights, reliably measured and continuously derived values of PBL-heights are necessary. Therefore different experimental methods, both, in-situ and remote sensing based on different atmospheric parameters are used.

In Holzworth (1964) and Holzworth (1967) thermodynamic vertical profiles from radiosonde measurements provided the basis for applying the parcel method: the mixing layer height is the intersection of the actual potential temperature profile with the dry-adiabatic ascent starting at the near-surface temperature. Data obtained from radiosonde measurements are also part of the so-called Bulk-Richardson method (Hansen, 1966). The atmosphere is assumed to be a fluid whose Bulk-Richardson number has to surpass a critical value beyond which the atmosphere is considered decoupled. Microwave radiometer derived temperature profiles allow the application of the parcel method as well (Granados-Muñoz et al., 2012). Seibert et al. (2000) gives a profound review of various methods including numerical modeling and radiosonde measurements which are used for a global climatology in Seidel et al. (2010). Further instruments for PBL-height detection are SODAR (Sound Detection and Ranging) and optional RASS (Radio Acoustic Sounding System) which are utilizing backscattering of sound and radio waves, respectively. Because of temperature and humidity gradients in the atmosphere, backscattering of sound- and radio waves is different and gives information about the vertical structure of the lower troposphere (Beyrich, 1995; Emeis et al., 2004).

The strong gradients of aerosol backscatter can be used for detecting mixing layer heights by lidar (Kunkel et al., 1977; Boers et al., 1984; Melfi et al., 1985). The amount of data a lidar measurement yields, makes an automatic evaluation inevitable. Several studies of different automatic PBL-height detection methods applied to lidar backscatter profiles have already been done. For example, first derivative (Endlich et al., 1979; Flamant et al., 1997; Menut et al., 1999), second derivative (Menut et al., 1999), temporal variance (Hooper and Eloranta, 1986; Menut et al., 1999; Hennemuth and Lammert, 2006), wavelet covariance transform (Cohn and Angevine, 2000; Davis et al., 2000; Brooks, 2003; Morille et al., 2007; Baars et al., 2008) and idealized-profile

method (Steyn et al., 1999; Eresmaa et al., 2006; Eresmaa et al., 2012). Numerous comparisons between different measurement techniques (Russell et al., 1974; Coulter, 1979; Kaimal, J. C. et al., 1982; Marsik et al., 1995; Fischer et al., 1998; Wiegner et al., 2006; Emeis et al., 2008; Schween et al., 2014) revealed advantages and disadvantages of these methods.

A general conclusion of investigations during the last few years is that ceilometers can provide a very valuable contribution to aerosol monitoring if continuous, autonomous and unattended measurements from area-covering ceilometer networks are implemented. First attempts were done to develop an all-purpose algorithm applicable to various instruments (Morille et al., 2007; Haeffelin et al., 2012). To this day, however, no uniform algorithm has been found which works reliably at any weather condition during day and night in order to track the whole diurnal ML-cycle.

1.3 Objectives and outline

To be of benefit for aerosol research, it is desired to derive the particle extinction coefficient α_p as a function of height, or at least the particle backscatter coefficient β_p. The feasibility by means of ceilometer was already demonstrated by e. g. Heese et al. (2010). However, as being a backscatter lidar, the derivation of α_p from ceilometer measurements suffers from the inherent problem of an unknown lidar ratio S_p. As a consequence, the determination of α_p is associated with high uncertainties. Furthermore, the low pulse energy leads to low signal to noise ratios, causing problems to find an aerosol-free region in the free troposphere, which is necessary for the so-called Rayleigh calibration in order to derive α_p or β_p. Moreover, a Rayleigh calibration is impossible if low clouds are present. To overcome these limitations a different approach was described by Wiegner and Geiß (2012). By applying a two-step absolute calibration of the ceilometer, the lidar constant C_L can be used to derive particle backscatter coefficients β_p with high temporal and spatial resolution at day and night, and even in case of clouds up to the cloud base. However, the large number and diversity of instruments currently operating, make an individual determination of the lidar constant C_L necessary. Furthermore, due to maintenance, system upgrades or firmware updates, C_L can not really be considered as constant. To track the changes, a fully automated algorithm for the absolute calibration is needed. The development of such an algorithm is one objective of this thesis. The algorithm must be fully automated

and applicable to instruments of different manufacturers with different configurations and hardware properties in order to derive a quantitative aerosol optical property, i. e. β_p.

A second objective is the development of an algorithm for ML-height determination. In order to quantify the attribution of elevated aerosol to the total atmospheric column, information about the ML-height is essential. Reliable ML-heights can be used to validate and improve weather models. Furthermore, the ML-height is an important parameter when considering air quality, especially in urban regions where dispersal of smog and pollutants can be critical. These applications require a reliable and continuous tracking of the ML without unrealistic short time changes of the ML-height. No temporal gaps should appear.

The thesis is structured as follows: In Sect. 2 the basic principles of ceilometer remote sensing are introduced. An overview of the lidar principle is given and the limitations of ceilometers are explained.

Sect. 3 starts with an introduction to the ceilometer used in this thesis and presents auxiliary instruments and datasets. The development of a fully automated procedure for an absolute calibration applicable to ceilometers is described. The main part of this work is the development of an automatic procedure to track complete diurnal cycles of the ML ("COBOLT") and a thorough discussion of its properties.

A few examples presented in Sect. 4 highlight the large set of applications of the new methodology. It includes a climatology of β_p-profiles and aerosol optical depth, statistics and comparisons of the ML-height above Munich and nearby stations, as well as the validation of a chemistry transport model and air quality studies.

This thesis concludes with a synopsis of the results and gives suggestions for future applications.

2 Fundamentals of ceilometer applications

Ceilometers are compact simple one-wavelength backscatter lidars with low pulse energy and high pulse repetition frequencies. They are using the principle of light detection and ranging which is described in the following chapter; relevant scattering processes in the atmosphere, its representation in the lidar equation and its solution including error sources are outlined.

2.1 The lidar principle

If electromagnetic radiation propagates from a light source through the earth atmosphere, it experiences attenuation. Responsible for this mechanism are interactions of the light beam with air molecules and small particles (e. g. dust, ice crystals ...). The incident light can be absorbed or its direction is changed by scattering processes, referred to as radiative transfer. The sum of both processes is denoted by extinction and can be described by the extinction coefficient which represents the loss of energy per unit length from the incident light beam due to both scattering and absorption and is expressed in the "lidar community" as α. The human eye can recognize such processes in the electromagnetic spectral region of the visible light when, e. g. clouds are apparent or a layer of Saharan dust blurs the sky. The attenuation of light can be related to the properties of the atmosphere through which the light is travelling by Bouger-Lambert-Beer's law (Bouguer, 1729; Lambert, 1760; Beer, 1852):

$$I(\lambda) = I_0(\lambda)\, e^{-\tau(\lambda)} \tag{2.1}$$

Here $I_0(\lambda)$ denotes the irradiance of the light source, $I(\lambda)$ the attenuated irradiance after propagation through the scattering and absorbing atmosphere and $\tau(\lambda)$ the optical depth of the atmosphere. The optical depth is the integral over the extinction coefficient α and depends on optical properties of the particles and air molecules:

$$\tau(\lambda) = \int_0^{z_{max}} \alpha(z', \lambda)\, dz' \tag{2.2}$$

The attenuation of the incident radiation is denoted by the transmission T, ranging between 0 and 1 for turbid and clean atmosphere, respectively:

$$T(\lambda) = e^{-\tau(\lambda)} \tag{2.3}$$

The interaction between particles and radiation, especially their scattering efficiency depends on the non-dimensional size parameter x which is the relative size of a spherical particle expressed as the ratio of its area cross-section with particle radius r and wavelength λ.

$$x = \frac{2\pi r}{\lambda} \tag{2.4}$$

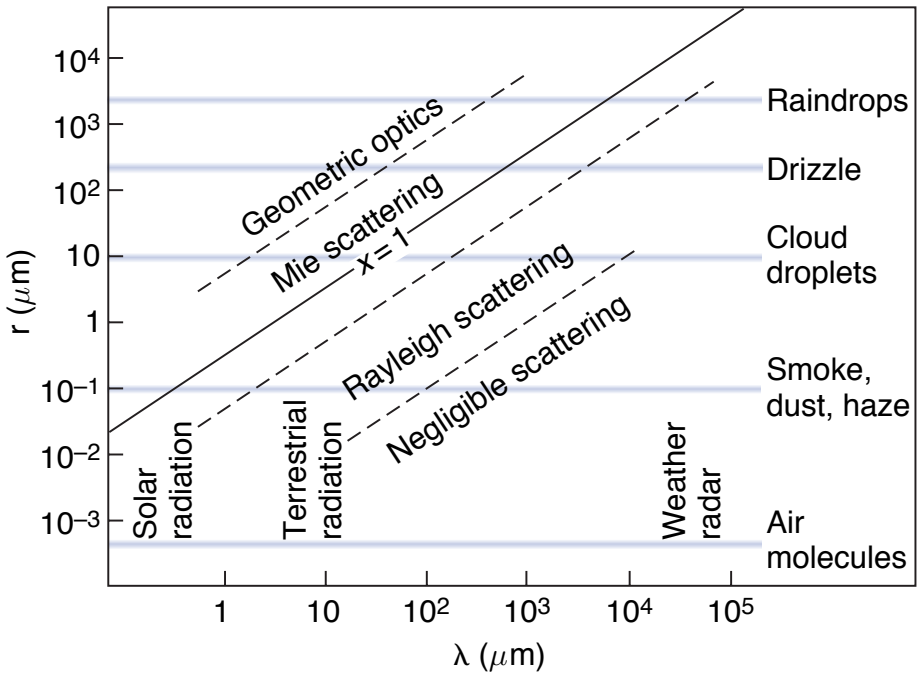

Figure 2.1: Light scattering regimes depending on the particle radius and the incident radiation wavelength (Wallace and Hobbs, 2006).

In Fig. 2.1 different size parameter regions are shown for various kinds of atmospheric constituents and incident radiation wavelength. Considering a wavelength of 1 µm in the near infrared, the size parameter ranges from $x \approx 0.006$ for air molecules to $x \approx 0.6$ for dust and smoke particles up to $x \approx 60$ for cloud droplets. Regarding this parameter, three different light scattering regimes can be identified: First, the so-called Rayleigh scattering regime (Rayleigh, 1899; Young, 1981) which is present

if the scattering particles are small compared to the wavelength of the incident light ($x \ll 1$). The scattered intensity is proportional to λ^{-4} what results in stronger scattering of shorter wavelength and thus leads to a blue sky, when light is dominantly scattered from molecules. Second, the Mie scattering regime (Mie, 1908), when the particles are in the same size range or larger than the wavelength of the incident light ($0.1 \leq x \leq 50$). The particle shape is assumed to be spherical. Mie scattering can, for example, be observed when light propagates through a strong dust layer and the wavelength dependency of the scattered light is low, resulting in a white appearance of the sky around the sun. With the third scattering regime, optical phenomena like rainbows can be explained with laws of geometric optics (e. g. refraction), when light is scattered from large particles ($x \geq 50$).

Atmospheric scattering includes elastic and inelastic processes. This fact can be used for aerosol remote sensing by complex lidar systems (Raman lidar). If the incident radiation is scattered inelastically, the internal energy of the scattering molecule is changed and the wavelength of the scattered radiation is shifted, usually to longer wavelengths. The differences in the wavelength shift can be used to distinguish between different molecules. These signals can serve for calibration. In contrast, when radiation is scattered elastically, the wavelength of the scattered radiation is the same as of the incident radiation.

The fundamentals of the scattering theory are exploited by lidars —and hence ceilometers— to determine range-resolved properties of the atmosphere. Lidar is an active remote sensing instrument which uses a pulsed laser as radiation source by emitting short, high-energy and coherent light beams with a narrow linewidth. While traveling through the atmosphere, the emitted laser beam interacts with aerosols, molecules and cloud particles, depending on the physical properties of these constituents. Photons scattered under an angle of 180° can be collected by a telescope. A detection unit converts light into a current (e. g. photomultiplier, photodiode) and a data processing unit storages the digitized signal (Fig. 2.2). With the knowledge of the velocity of light c and the time between emitting and receiving the photons t, the data can be spatialized. The achieved range resolution is typically affected by sampling time t_s of the detection unit.

$$z = \frac{c\,t_s}{2} \tag{2.5}$$

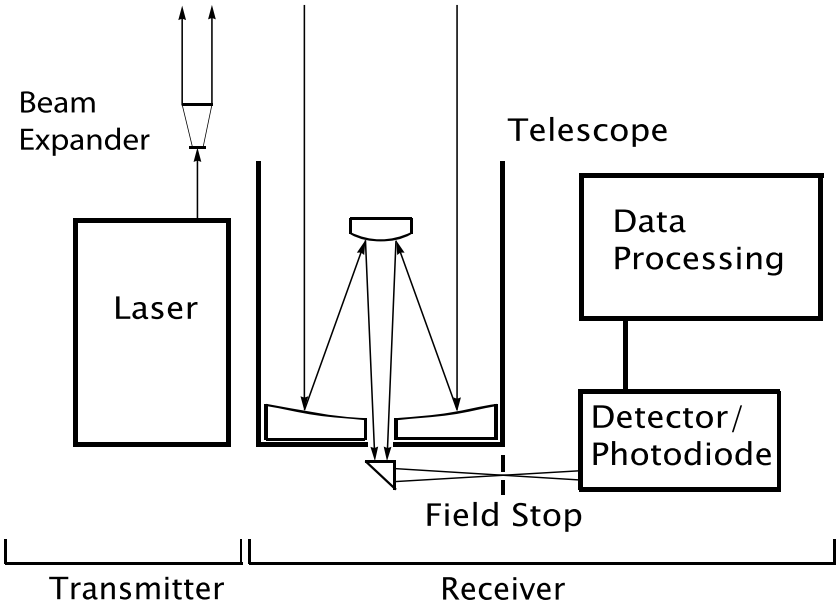

Figure 2.2: Schematic of a bi-axial lidar (adapted from Weitkamp (2005))

The signal $P_{obs}(z, \lambda)$ which is measured by the receiver unit is a superposition of three contributions: On the one hand the backscattered fraction $P(z, \lambda)$ of the photons emitted by the laser, on the other side the background radiation P_{bg} which arises from scattered sunlight during the day or scattered moonlight during the night. Additional contributions arise from electrical interference, here referred to as dark current $P_{dc}(z)$. The relevant signal for aerosol remote sensing is expressed as a difference of the observed signal and the background- and dark current radiation:

$$P(z, \lambda) = P_{obs}(z, \lambda) - P_{bg} - P_{dc}(z) \tag{2.6}$$

The background signal can be determined by measuring the signal right before the emission of laser pulses or at the far end where no contributions from atmospheric backscattering can be expected. To obtain the dark currents, so-called zero measurements are performed in which radiation is blocked from the receiver by obscuring the telescope. Thus, only contributions from the electronics are registered.

After subtracting P_{bg} and $P_{dc}(z)$, the lidar signal can be described as follows:

$$P(z, \lambda) = C_L(\lambda) \, \frac{1}{z^2} \, O(z) \, \beta(z, \lambda) \, \exp\left\{-2 \int_0^z \alpha(z', \lambda) \, dz'\right\} \tag{2.7}$$

The received signal $P(z, \lambda)$ measured in a lidar receiver depends on the inverse of the squared range z between the transmitter and the scattering event, the wavelength dependent backscatter coefficient $\beta(z, \lambda)$ which is the probability that a transmitted photon is backscattered into an unit solid angle at 180° and the transmission on the way back and forth, expressed by the exponential function. System specific parameters are included in the overlap function $O(z)$, also denoted by geometric form factor (Halldórsson and Langerholc, 1978) or crossover function (Sassen and Dodd, 1982) and in the lidar constant $C_L(\lambda)$. The overlap function describes the crossover of the area of laser irraditation and the field of view of the telescope. The experimental determination of this range-dependent function is difficult and defective, but can extinguish measurement artefacts in the near range, which have influence on, for example, layer detection. However, for reliable quantitative results the distance z_{ovl} where $O(z) = 1$ for $z > z_{ovl}$ can be estimated and should be used. Above this height the whole scattering volume is inside the field of view. The lidar constant $C_L(\lambda)$ in contrast is range-independent and describes the efficiencies of the transmitter and the receiver. The number of transmitted laser photons $P_0(\lambda)$ can be expressed as the laser pulse energy E_0 divided by the energy of a single photon at the corresponding wavelength.

$$P_0(\lambda) = \left(\frac{E_0 \, \lambda}{c \, h} \right), \tag{2.8}$$

The length of the scattering volume is given by $ct_s/2$ and is thus controlled by the detection rate of the receiver unit. Note, that the lidar constant is not necessarily a constant. As it depends on properties of the laser, the transmitting optics and the detector settings, it might be adjusted by the user or automatically by the system. For example, the amplification of the receiver can be changed by means of the HV supply. That means, by changing the high voltage supply of the photodetector, the lidar constant C_L of the system is changed—a fact that is discussed in detail in chapter 3.3. Thus C_L must be treated as a function of time, i. e. $C_L = C_L(t)$.

Because scattering of light with molecules and aerosols or hydrometeors occurs in different regimes (see Fig. 2.1), it is convenient to divide the extinction coefficient α, as well as the backscatter coefficient β in a molecular and a particle part.

$$\alpha = \alpha_m + \alpha_p \tag{2.9}$$

$$\beta = \beta_m + \beta_p \tag{2.10}$$

Regarding these two types of contributions and considering only elastic scattering the lidar equation can be written in the following form:

$$P(z) = C_L \frac{1}{z^2} O(z) \left[\beta_p(z) + \beta_m(z)\right] \exp\left\{-2 \int_0^z \left[\alpha_p(z') + \alpha_m(z')\right] dz'\right\} \tag{2.11}$$

The dominating term in this equation is the $1/z^2$-proportionality of the lidar signal $P(z)$ resulting in a strong decrease of $P(z)$ with distance of the scattering volume. This factor is known and independent of system characteristics as well as of physical parameters of the atmosphere. Under typical atmospheric conditions and for typical aerosol lidar wavelengths, the transmission is a smooth function decreasing from 1 at the ground to, say, 0.5 in the free troposphere. Thus, the particle backscatter coefficient $\beta_p(z)$ and its strong variability compared to other terms in the equation provides the spatial information of the presence of aerosol layers and clouds. Consequently, when considering the range corrected lidar signal $P(z)z^2$, henceforth referred to as $X(z)$, one directly gets an impression of the atmospheric layering.

$$X(z) = P(z)\, z^2 = C_L\, O(z) \left[\beta_p(z) + \beta_m(z)\right] \exp\left\{-2 \int_0^z \left[\alpha_p(z') + \alpha_m(z')\right] dz'\right\} \tag{2.12}$$

An example is shown in Fig. 2.3. Near the surface from 0–0.3 km the steep increase of the signal strength illustrates the region of incomplete overlap, limiting a reliable evaluation of the near range. The signal measured up to 2.5 km is indicating the planetary boundary layer. The low signal between 2.5 km and 7 km, however, suggests a range where Rayleigh scattering prevails, i. e. an aerosol free region. The strong signal in a height of 7–9 km originates from scattering ice particles in a cirrus cloud—multiple peaks are indicating a layered structure of the cloud. In a height above 9 km the limit of the visibility range of the instrument, i. e. its far range, is evident: the signal noise beyond the cirrus cloud is hampering a reliable analysis of the lidar signal in this region.

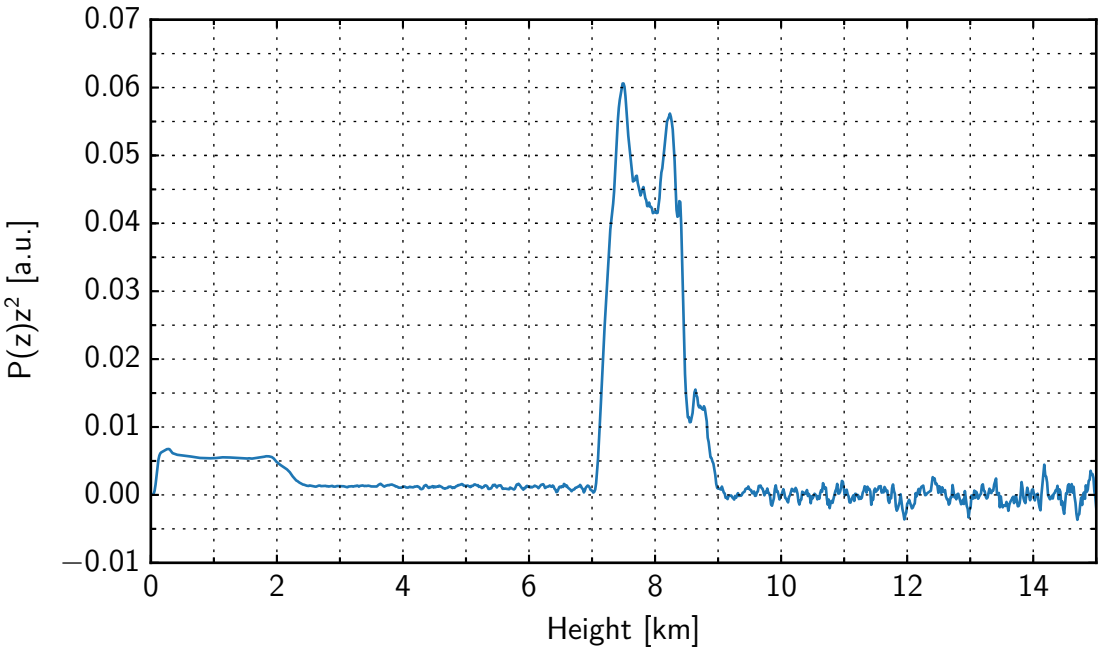

Figure 2.3: Example of a range corrected signal $P(z)\,z^2$ at 1064 nm.

For the quantitative retrieval of optical properties of aerosol particles from measured lidar data, an inversion of the lidar equation Eq. (2.11) is necessary. However, Eq. (2.11) has four unknown variables α_m, β_m, α_p and β_p and is therefore underdetermined. A solution of this problem is presented in the following.

2.2 Solution of the lidar equation

2.2.1 Retrieval of β_p

A method for the retrieval of quantitative aerosol properties from the lidar Eq. (2.11), namely the particle extinction coefficient α_p or the particle backscatter coefficient β_p, is provided in an analytical solution described by Klett and Fernald (Fernald et al., 1972; Fernald, 1984; Klett, 1981; Klett, 1983; Klett, 1985). To solve Eq. (2.11) with 4 unknowns, i. e. α_m, β_m, α_p and β_p, two lidar ratios S_m and S_p are introduced. They are defined as follows:

$$S_m = \frac{\alpha_m(\lambda, z)}{\beta_m(\lambda, z)} = \frac{8\pi}{3}\, sr \tag{2.13}$$

for molecules and

$$S_p(\lambda, z) = \frac{\alpha_p(\lambda, z)}{\beta_p(\lambda, z)} \tag{2.14}$$

for particles.

Now that β_m and α_m can be expressed as a proportional relation with the lidar ratio S_m it is merely necessary to calculate either α_m or β_m. This can be done by considering the Rayleigh atmosphere using following relation, which yields α_m in good approximation.

$$\alpha_m(z, \lambda) = 8.022 \cdot 10^{-4}\, \rho_L(z)\, \lambda^{-4.08} \tag{2.15}$$

The molecular extinction coefficient is derived in [km^{-1}] when $\rho_L(z)$ is given in [$\mathrm{kg/m}^3$] and λ in [µm]. Air density can be calculated from the gas law using temperature and pressure profiles of radiosonde ascents or from meteorological analyses, e. g. NCEP (National Centers for Environmental Prediction) or ECMWF (European Centre for Medium-Range Weather Forecast).

$$\rho_L(z) = \frac{p(z)}{R_f(z)\, T(z)} \tag{2.16}$$

$T(z)$ denotes the temperature in Kelvin and $R_f(z)$ the specific gas constant for humid air. Its value can be determined with the knowledge of the relative humidity ϕ, the saturation vapour pressure $e_w(z)$, the specific gas constant for water vapour R_d and dry air R_L.

$$R_f(z) = \frac{R_L}{1 - \phi(z)\, \dfrac{e_w(z)}{p(z)} \left(1 - \dfrac{R_L}{R_d}\right)} \tag{2.17}$$

The saturation vapour pressure is calculated with Magnus' formula

$$e_w(z) = 611.213\,\mathrm{Pa}\, \exp\left(\frac{17.5042 \cdot \vartheta(z)}{241.2\,^\circ\mathrm{C} + \vartheta(z)}\right) \tag{2.18}$$

by inserting the temperature $\vartheta(z)$ in [°C]. The molecular backscatter coefficient can then be derived from $\alpha_m(z)$ and S_m.

In contrast to the lidar ratio S_m, which is constant with height and wavelength, the particle lidar ratio S_p depends on the shape, size, refractive index, hygroscopy

and other parameters of the aerosol particles—properties which are usually not known in detail, in particular in case of a mixture of particles from different origins. As a consequence, the lidar ratio for particles depends on the wavelength and in case of changing aerosol composition also on height.

Aerosole type	Lidar ratio S_p
Marine particles	20–35 sr
Saharan dust	50–80 sr
Less absorbing urban particles	35–70 sr
Absorbing particles from biomass burning	70–100 sr

Table 2.1: Typical lidar ratios for different aerosol types at 532 nm wavelength (Weitkamp, 2005).

Characteristic values are ranging between $S_p = 20\,\text{sr}$ and $S_p = 100\,\text{sr}$ as shown in Tab. 2.1. It is obvious that the lidar ratio covers a wide range of values, depending on the particle source region. Therefore in case of different aerosol layers the lidar ratio can vary with height and consequently should be considered as a range-dependent parameter (Evans, 1988). If columnar lidar ratios are used, e. g. derived from sun photometer measurements, large differences between true and estimated values are the consequence (Sasano and Nakane, 1984; Sasano et al., 1985). With the knowledge of the source regions of the aerosol from backward trajectories (e. g. HYSPLIT, Draxler and Rolph (2012)), a lidar ratio table can be used to constrain S_p. The software package OPAC (Optical Properties of Aerosol and Clouds, Hess et al. (1998)) provides such a table, by calculating aerosol and cloud optical properties on basis of microphysical properties (size distribution, spectral refractive index) from Mie theory. Recently, Koepke et al. (2015) applied T-Matrix calculations for ellipsoids to account for the non-sphericity of particles.

Significant progress has been achieved with the implementation of Raman lidars. These systems allow to directly measure lidar ratios at 355 nm and 532 nm. This technique is, however, typically linked to night time measurements and requires temporal averages of 1–2 hours. As shown in Fig. 2.4, Groß et al. (2011) measured aerosol particles of different source regions by means of two Raman lidars operating at an wavelength of 355 nm and 532 nm, respectively. It is obvious that the lidar ratio explicitly depends on the observed aerosol type (e. g. dust, marine aerosol, volcanic ash) and the wavelength. However, the Raman method is not used in this work due to the

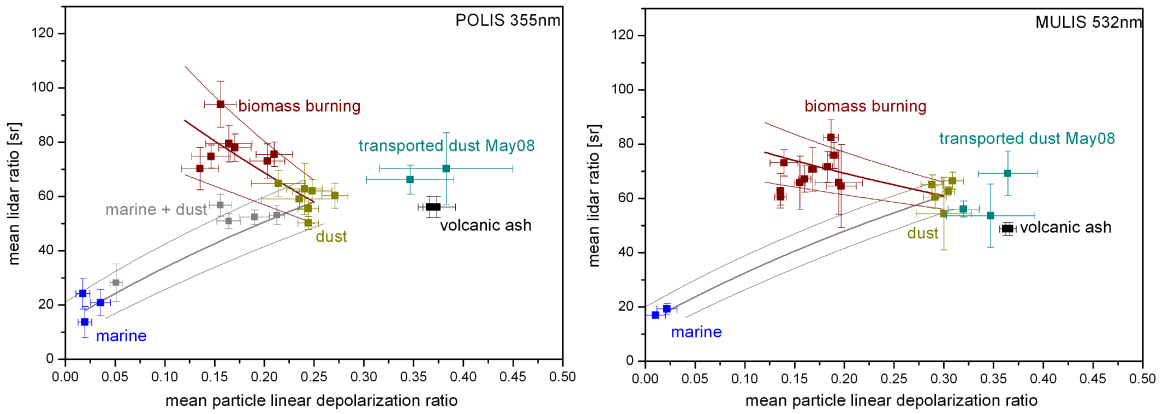

Figure 2.4: Mean lidar ratio over mean particle linear depolarization ratio at 355 nm (left) and at 532 nm (right) (Groß et al., 2011).

fact that ceilometers have no Raman channels. Furthermore, a table of measured lidar ratios for a wavelength of 1064 nm, which is the operating wavelength of the ceilometer used in this study, can not be found in literature to this day. Hence, to cover the diversity of different aerosol types, a lidar ratio estimate is given with an error of ±10 sr to ±20 sr (Ackermann, 1998) resulting in a systematic error in α_p and β_p. This is neither a restriction when considering mixing layer height determinations or aerosol layer detections nor it is when deriving β_p, since the transmission T is almost 1. For the derivation of α_p from any elastic backscatter lidar the inherent problem of an unknown lidar ratio S_p remains which results in α_p-retrievals affected linearly by a defective lidar ratio.

Now, with the knowledge of α_m, β_m and S_p, 4 unknown variables in Eq. (2.11) can be reduced to 1, and then Eq. (2.11) can be solved. A derivation of the particle backscatter coefficient $\beta_p(z)$ from Eq. (2.11) is presented by Fernald et al. (1972) (cf. Appendix A).

$$\beta_p(z) = \frac{Z_\beta(z)}{N_\beta(z)} - \beta_m(z) \tag{2.19}$$

with

$$Z_\beta(z) = z^2\, P(z)\, \exp\left\{-2 \int_{z_{ovl}}^{z} \left[S_p(z')\, \beta_m(z') - \alpha_m(z')\right] dz'\right\} \tag{2.20}$$

and

$$N_\beta(z) = C_L - 2\int_{z_{ovl}}^{z} S_p(z')\, Z_\beta(z')\, dz' \tag{2.21}$$

In principle the aerosol backscatter coefficient can be solved according to Eq. (2.19) using the lidar constant C_L (see Eq. (2.21). However, the determination of the lidar constant from system parameters is not always possible, in particular if commercial ceilometers are used and no detailed hardware information is provided. In addition, the data inversion suffers from the lack of knowledge of regions in the near range where $z < z_{ovl}$ (see Eq. (2.20) and (2.21)), which results in uncertainties concerning the transmission in this incomplete overlap region. By using a lidar capable of measuring with a low full overlap, i. e. $\exp\{-2\int_0^{z_{ovl}}[S_p(z')\beta_m(z') - \alpha_m(z')]\, dz'\} \approx 1$, the resulting uncertainties of an integration from the range of complete overlap z_{ovl}, can be minimized. An improvement of the overlap region can also be achieved when applying a method for an overlap correction. For avoiding the problem of an unknown lidar constant C_L in the retrieval of β_p, established techniques are available and briefly discussed in the following.

2.2.2 Rayleigh calibration

To derive β_p-profiles from Eq. (2.19) if C_L is unknown, an alternative formula using a reference value of β_p at a given height z_0 can be used:

$$N_\beta(z) = \frac{z_0^2\, P(z_0)}{\beta_m(z_0) + \beta_p(z_0)} - 2\int_{z_0}^{z} S_p(z')\, Z_\beta(z')\, dz'. \tag{2.22}$$

In principle, z_0 can be freely selected by the user. Because of the integration limits from z_0 to z, this version is also denoted by "forward-algorithm". This approach, however, is numerically unstable due to the difference in (2.22), where a wrong boundary value of $\beta_p(z_0)$ leads to negative values and hence to growing errors with increasing distance from the lidar (Bissonnette, 1986; Kovalev and Eichinger, 2004). Furthermore, it must be noted that the reference value $\beta_p(z_0)$ has to be in the region of complete overlap when z_0 is small, what makes an application difficult.

For that reason Klett (1981) uses a reference value $\beta_p(z_{max})$ at the far end of the measurement range and changes the integration limits from z to z_{max}. This approach is known as the "backward-algorithm" and has a sum instead of a difference in Eq. (2.22). That makes it numerically more stable and less sensitive to wrong boundary values. For the determination of the reference value $\beta_p(z_{max})$ the so-called Rayleigh-calibration

is used with the assumption of an aerosol-free reference-region in a height z_{max}, that means, $\beta_p(z_{max}) = 0$. A new formulation of Eq. (2.20) and (2.21) yields

$$Z_\beta(z) = z^2\, P(z)\, \exp\left\{2 \int_z^{z_{max}} [S_p(z')\, \beta_m(z') - \alpha_m(z')]\, dz'\right\} \tag{2.23}$$

$$N_\beta(z) = \frac{z_{max}^2\, P(z_{max})}{\beta_m(z_{max}) + \beta_p(z_{max})} + 2 \int_z^{z_{max}} S_p(z')\, Z_\alpha(z')\, dz'. \tag{2.24}$$

However, the assumption that no aerosol is present in the reference region is not valid in any case and can be accounted for by setting $\beta_p(z_{max}) > 0$.

For ceilometer applications, the forward approach with using a reference value close to the ceilometer fails as β_p is unknown in this region. The backward algorithm in combination with a reference value in the far range (Eq. (2.24)), where no aerosol contributions are expected, is in principle suitable and numerical stable if some important conditions are fulfilled: For the detection of an aerosol-free region, typically at an altitude of more than 3 km, a signal to noise ratio (SNR) sufficient to distinguish the signal from noise is mandatory. Because of the low laser pulse energy of a ceilometer this cannot be achieved in any case. Since the SNR depends on background radiation, nighttime measurements without radiation from the sun are preferable. To increase the SNR, temporal averaging can be applied, if the aerosol distribution is stable. Typical averaging times are at around 1–2 hours. Furthermore, no clouds may occur below the aerosol-free region, thus limiting a determination of β_p to particular weather conditions. To avoid these restrictions in retrieving β_p, the use of a previously determined lidar constant C_L in combination with Eqs. (2.19), (2.20) and (2.21) provides results at any weather condition during day and night, independent of a sufficient SNR in the free troposphere. However, regular recalibration is required as system components might change with time (aging, degradation) or unexpected dependencies might occur, e. g. temperature dependence of the sensitivity. The numerical instability arising from the difference in Eq. (2.21) is no obstacle when using a wavelength in the near-infrared where the optical depth is low and hence $C_L \gg 2 \int Z dz$. A method to correct the incomplete overlap region, in particular applicable for ceilometers operating in a network, is described in the next section.

2.2.3 Near range

Usually only measured data beyond the full overlap can be reliably used for processing ceilometer returns. In this region the volume containing the transmitted pulse is completely imaged onto the detector at all ranges. To observe also regions closer to the surface, which is important for boundary layer investigations or visibility estimations, tilting of the instrument or an overlap correction is necessary. Because tilting of the instrument is technically challenging, expensive and leads to horizontal shifted observed scattering volumes with height, an application to networks of ceilometers is hardly feasible and hence an overlap correction is preferred. Especially if only shallow boundary layers are existing in the lowermost part of the atmosphere, layer detection can suffer from artefacts in the measured profiles induced by e. g. internal reflections of the laser light. With regard to climatologies this can lead to a bias in mixing layer height retrievals. However, for some instruments an incomplete overlap in the near range where the signal strength is large is necessary to avoid saturation of the detector in order to retain the capability of resolving signals from larger distances.

When considering the transmitter receiver geometry it has to be kept in mind that usually two different optical ceilometer configurations (Harms, 1979; Kovalev and Eichinger, 2004) are implemented (Fig 2.5). First option is a coaxial setup with the telescope and the laser having the same optical axis. This concept is, for example, used by Vaisala and Campbell Scientific ceilometers. The second option is a biaxial setup with parallel optical axes with a distance d. With tilting both axes and changing the field of view of the telescope, the height of complete overlap can be adjusted but can lead to long-distance cut-off for large inclination angles. JenOptik ceilometers have such a transmitter receiver configuration. In practice, all bi-axial and coaxial ceilometers have a region of incomplete overlap, but being much smaller for the coaxial geometry (Harms, 1979). Different approaches for overlap corrections using numerical calculations are discussed by Halldórsson and Langerholc (1978), Sassen and Dodd (1982), Ancellet et al. (1986), Kuze et al. (1998) and Stelmaszczyk et al. (2005), or by Velotta et al. (1998) who used a ray tracing technique. For all theoretical approaches the system parameters must be known in detail, however, they are difficult to obtain, especially for ceilometers where such information is usually not disclosed by the manufacturer. For this purpose better applicable experimental approaches are available making use of the slope method (Collis, 1966; Kunz and Leeuw, 1993). In principal, constant extinction coefficients are necessary in the line of sight. Sasano

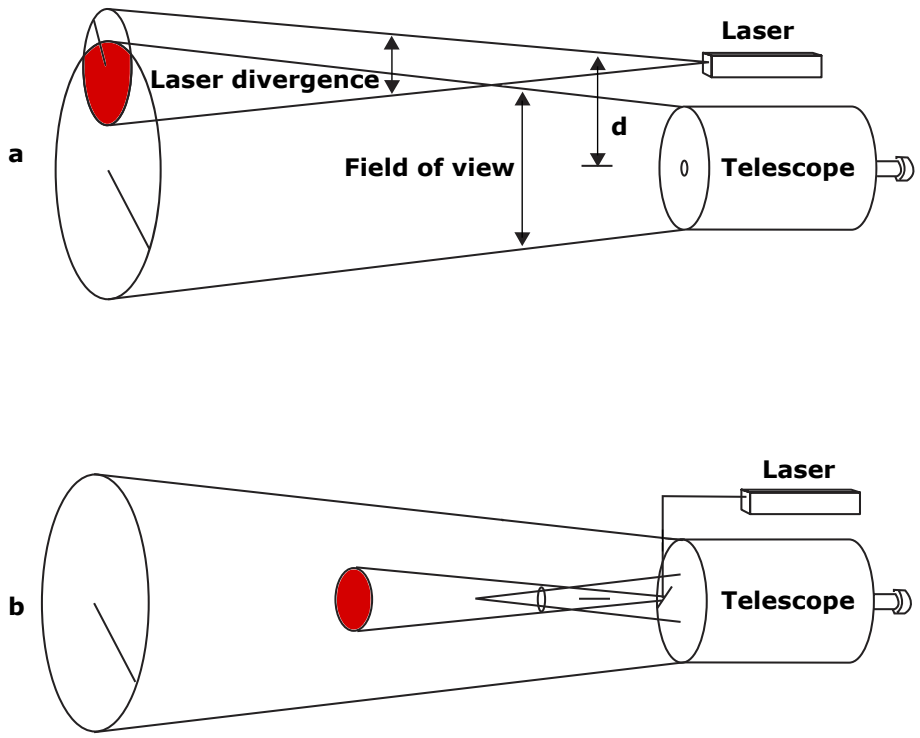

Figure 2.5: Configuration of different ceilometer setups with different overlap geometries. Biaxial configuration (a) and coaxial configuration (b) with overlap in red (adapted from Kovalev and Eichinger (2004)).

et al. (1979) uses a clear atmosphere, Tomine et al. (1989) an atmosphere with fog or mist, Dho et al. (1997a) an atmosphere with well-mixed aerosol and Dho et al. (1997b) an atmosphere with inhomogeneous aerosol distribution. In general, aerosol-free conditions do not occur in the near range close to the surface thus making the attempt proposed by Sasano et al. (1979) difficult. On the other hand, conditions with well mixed aerosols, fog or mist are more frequent and thus better applicable. However, when considering ceilometers with low laser power, a reliable use of the slope method can be done for horizontal pointing ceilometers if certain meteorological conditions are fulfilled: Horizontal homogeneity of the aerosol distribution up to a distance of 1.5–3 km from the ceilometer is necessary. That means, no local sources of aerosol, pollution or humidity along the ceilometer path may be present. In addition, these conditions must persist for time averages up to one hour, sufficient to assure statistical homogeneity.

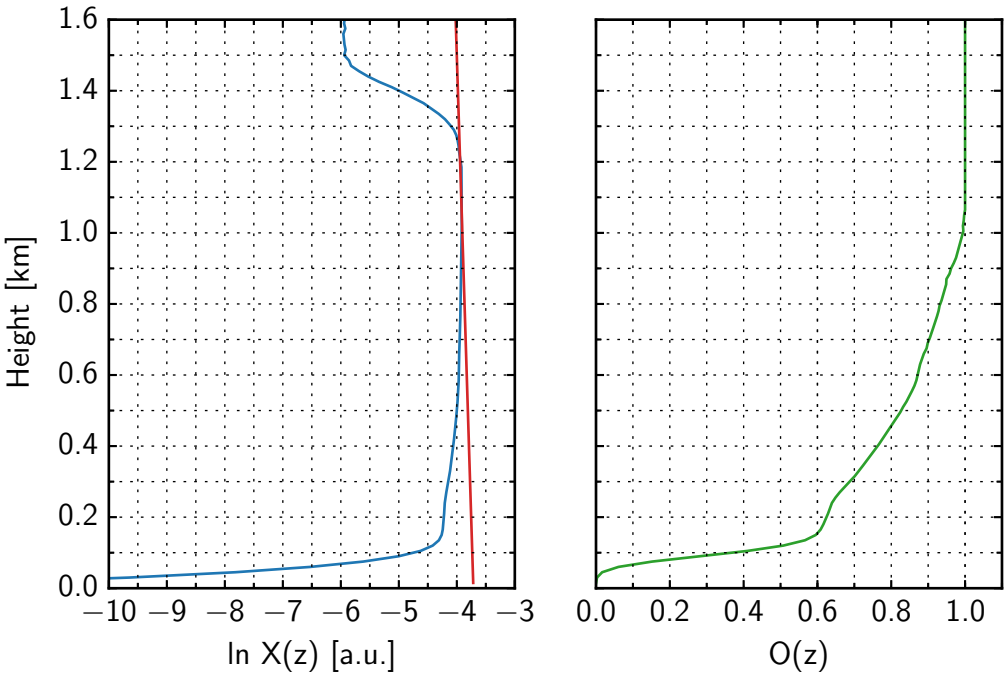

Figure 2.6: Experimental determination of the overlap function in a homogeneous atmosphere: the logarithm of the range corrected signal $X(z)$ (blue), the logarithm of the fitted signal $X_F(z)$ derived from linear regression at an height where $O(z)$ is assumed to be 1 (red), the resulting overlap correction factor $O(z)$ (green).

With all conditions met, the slope method can be applied to the measured ceilometer profiles. If we recall the lidar equation in the range-corrected form

$$X(z) = C_L\, O(z)\, [\beta_p(z) + \beta_m(z)]\, \exp\left\{-2 \int_0^z [\alpha_p(z') + \alpha_m(z')]\, dz'\right\} \tag{2.25}$$

and assume horizontal homogeneity, i. e. $\beta_p(z)$, $\beta_m(z)$, $\alpha_m(z)$ and $\alpha_p(z)$ are constant, the lidar equation can be simplified to,

$$\ln [X(z)] = \ln [C_L\, \beta(z)] + \ln [O(z)] - 2\alpha z. \tag{2.26}$$

If considering distances greater than z_{ovl} where $O(z) = 1$, a linear equation is obtained

$$\ln [X(z)] = \ln [C_L\, \beta(z)] - 2\alpha z \quad \text{for} \quad z \geq z_{ovl} \tag{2.27}$$

where $\ln[C_L\,\beta(z)]$ is the intercept and -2α the slope of the linear regression line. Using these values to calculate a hypothetical "correct" lidar signal $X_F(z)$ for all distances z, $O(z)$ can be determined using following relation:

$$O(z) = \begin{cases} \dfrac{X(z)}{X_F(z)} & \text{if} \quad z < z_{ovl} \\ 1 & \text{if} \quad z \geq z_{ovl} \end{cases} \tag{2.28}$$

The condition of constant extinction is more likely fulfilled in horizontal than in vertical direction. Nevertheless, this proposed method, albeit for horizontal pointing ceilometers, can also be applied to vertical pointing ceilometers. The assumption of range-independency of $\beta_p(z)$ and $\alpha_p(z)$ is fulfilled if a homogeneous well-mixed boundary layer is existing. $\beta_m(z)$ and $\alpha_m(z)$, in contrast, are not vertically constant but small compared to $\beta_p(z)$ and $\alpha_p(z)$, respectively. In particular, when considering aerosol concentrations in the mixing layer where $\beta_m(z) \ll \beta_p(z)$ and $\alpha_m(z) \ll \alpha_p(z)$, the molecular part can be neglected and Eqs. (2.26), (2.27) and (2.28) can be applied. However, the application requires vertical homogeneity of the aerosol distribution up to ranges well above the expected height of the complete overlap region—such extended mixing layers are not often met. In addition, it has to be taken into account that due to convection processes, humidity changes and cloud forming at the mixing layer top can occur, thus violating the homogeneity condition.

An example of an overlap estimation with a vertical pointing ceilometer is shown in Fig. 2.6. The logarithm of the range corrected ceilometer signal, $\ln X(z)$, is shown in blue and decreases linearly from 0.9–1.3 km, as expected from a homogeneous aerosol distribution in this height region. Thus, the height of full overlap z_{ovl}, above where $O(z) = 1$, is assumed to be 0.9 km. After applying a linear regression between 0.9 km and 1.3 km, the hypothetical signal $X_F(z)$ is obtained (red) and can be used to determine the overlap function $O(z)$ from Eq. (2.28).

When applying the overlap correction, the user has to decide for himself down to which height he trusts a reliable correction and which accuracy he needs for evaluations in a meteorological sense. With decreasing height, where values of $O(z)$ are converging towards zero, the influence of $O(z)$ on $P(z)$ is hence increasing. In addition, the SNR is decreasing in very low regions. However, very low values of $O(z)$ can still be useful for a correction in case of qualitative analyzes of the boundary layer, e. g. boundary layer height determination, since artificial layers can still be eliminated. But if quantitative parameters, e. g. β_p-profiles are of interest, a correction with low values

in $O(z)$ would induce large uncertainties in the derived parameter. With regard to the example in Fig. 2.6, an extension of the measurement range to 120 m, where $O(z) > 0.5$ for $z > 120$ m, is still possible when determining boundary layer heights. However, for quantitative retrievals the measurement range should be limited to 300 m, where $O(z) > 0.7$ for $z > 300$ m.

2.2.4 Far range

All ceilometer measurements are influenced by noise. If noise is dominating, the data is normally considered useless in a meteorological sense and excluded. A general accepted threshold for the signal to noise ratio (SNR), discriminating between useful and not useful data, does not exist. Furthermore, no standard technique to calculate the SNR is available. Usually SNR-values of more than 1 are considered as trustworthy but also thresholds of 2, 3, 4 or even larger values can be selected. The choice is primarily driven by the meteorological application, e. g. quantitative or qualitative evaluation, and it is up to the user what he defines as reliable. In this work, an SNR of more than 1 is usually used to define the evaluable range. In general the SNR can be described by following relations:

The photons obey a Poisson distribution and the noise ΔP can thus be denoted by the square root of P. The raw backscattered laser light, which is the evaluable ceilometer signal, is the difference of the observed signal and the background fraction $P_{bg} + P_{dc}(z)$. Hence, the lidar signal P is superimposed by the noise of the lidar signal $\sqrt{P}$ and by the noise of the background $\sqrt{P_{bg} + P_{dc}(z)}$, which can be calculated from the signal of the uppermost range bins where the lidar signal is still assumed to be negligible. For one single pulse follows (McIntyre, 1966; Elbaum and Diament, 1976; Schroeder, 2000):

$$SNR(z) = \frac{P(z)}{\sqrt{P(z) + P_{bg} + P_{dc}}} \tag{2.29}$$

According to Heese et al. (2010) the background fraction $P_{bg} + P_{dc}(z)$ should be doubled in the denominator—demonstrating the fact that different approaches are possible.

If n independent measurements are averaged, the SNR increases by a factor of $\sqrt{n}$. Hence, the accuracy and quality of a lidar signal for a better retrieval of high and thin aerosol layers can be improved, however, at the expense of a reduced time resolution.

For some instruments, in particular for ceilometers, not all parameters which are necessary for the SNR-calculation (e. g. number of laser pulses) are provided. For this reason a different method for the determination of the SNR (Durieux and Fiorani, 1998) is used in this work. Temporal averaging can also be observed by a reduction of noise at the far end of the signal, where no contribution of the ceilometer light is expected. Considering the region at the far end, i. e., the last 90 range bins from z_{max} down to z_{max-90}, the standard deviation σ of the signal is used to calculate the $SNR(z)$ as follows:

$$SNR(z) = \frac{P(z)}{\sigma} \tag{2.30}$$

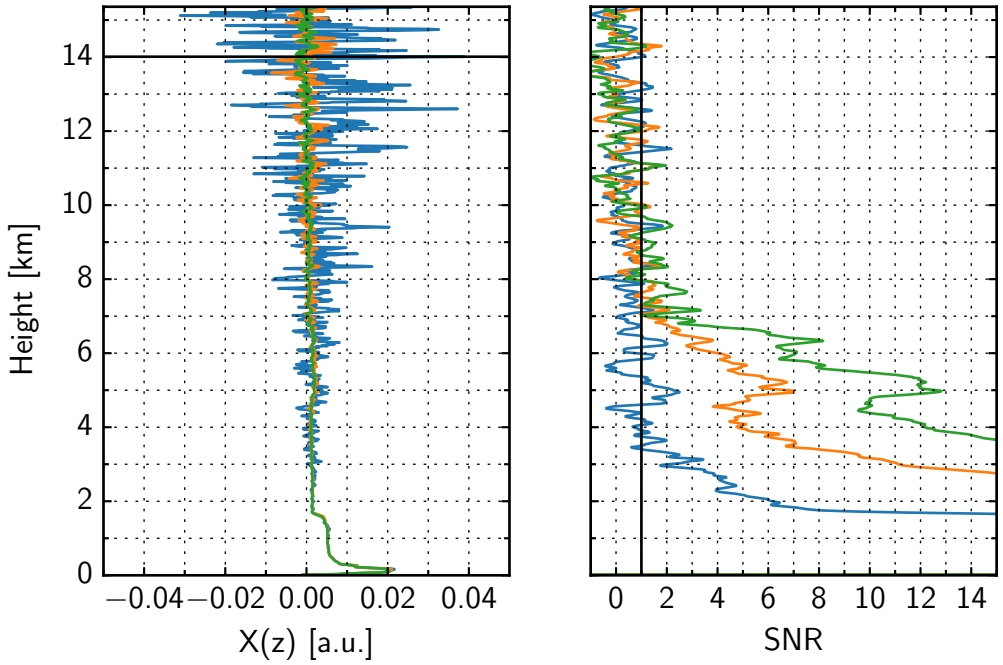

Figure 2.7: Range corrected signal $X(z)$ (left) and SNR (right) of our Jenoptik ceilometer CHM15kx (YALIS) of 29 March 2014 at 02:30 UTC. Shown are time averages of 15 s (blue, ≙100 000 laser pulses), 5 min (orange, ≙2 100 000 laser pulses) and 30 min (green, ≙12 000 000 laser pulses).

An example of this SNR-calculation method is given in Fig. 2.7. Shown is the range-corrected signal $X(z)$ (left panel) and the SNR (right panel) of our Jenoptik ceilometer CHM15kx, named YALIS, from 29 March 2014 at 02:30 UTC—a typical situation with a pronounced residual layer and a small layer at 5 km. Temporal averaging is applied over 15 s corresponding to approximately 100 000 laser pulses (blue),

5 min corresponding to approximately 2.1 million laser pulses (orange) and 30 min corresponding to approximately 12 million laser pulses (green), respectively. The last 90 range bins, which are used for calculating the standard deviation σ, are marked with a black horizontal line in the left panel. Note, not $X(z)$ but $P(z)$ is used for the SNR-calculation. An increase of the SNR (right panel) with longer temporal averages is obvious. If $SNR = 1$ (black line) is selected as threshold, defining the region where signal can be distinguished from noise, the maximum range of the ceilometer is extended from 4 km in the 15 s case to 8 km in the 30 min case. Even the small aerosol layer at 5 km can be resolved. If choosing a threshold of $SNR = 3$ the SNR of the aerosol layer at 5 km is already smaller than the threshold when using a temporal average over 15 s with a maximum range of 3 km. In the 5 min and the 30 min case the SNR of the small layer is still larger than the threshold and the maximum range is 7 km. If considering the improvement of the SNR of all time averages at a height of 4 km, the $\sqrt{n}$-dependent increase is almost fulfilled as the SNR increases from approximately 1.1 by a factor of $\sqrt{21}$ and then again by a factor of $\sqrt{5.7}$. For our ceilometer YALIS, typical maximum ranges for 15 s averages are 1.5 km during day and 4 km during night. They can be extended to 4 km at daytime and 8 km at nighttime in case of 30 min averages. However, a general indication of a maximum range is not possible, since the maximum range depends on the AOD of the penetrated aerosol layers (e. g. mixing layer) and the backscatter intensity from layers above. In addition, varying background radiation caused from, e. g. high cirrus clouds, has additional influence.

3 Methods

The lidar principle outlined in the previous chapter is the basis for any aerosol remote sensing application of a ceilometer described in the following chapter. In practice, a method for an absolute calibration to derive quantitative aerosol properties is presented using a JenOptik ceilometer CHM15kx. Thus, enabling us to retrieve particle backscatter coefficients β_p during virtually any weather conditions and to handle large sets of data, an automated data evaluation has to be developed. The focus is on particle backscatter coefficients and mixing layer heights.

3.1 Jenoptik-Ceilometer CHM15kx

JenOptik (www.jenoptik.de) or since 2014 Lufft (www.lufft.com), respectively, developed a ceilometer in two different configurations. The main difference between the model CHM15k (K-version) and CHM15kx (X-version) is the optical configuration of laser and telescope. The inclination angle of both axes as well as the field of view of the telescope is larger in case of the X-version. This results in a much lower z_{ovl}, however, goes along with a lower SNR in distant regions, especially during the day when high background radiation is existent. To compensate for this problem, an avalanche photodiode (APD) with special characteristics is used in the X-version. In 2011 a major upgrade was introduced by the manufacturer. The new "Nimbus"-version uses an LED test pulse for calibrating the APD in every time step, i. e. the detector settings can be adjusted continuously to achieve best performance. A further modification was the change of the operating system of the main controller from Windows XP to Linux. Because of the advantage of exploring much lower ranges, the Meteorological Institute decided in 2009 to purchase a JenOptik ceilometer CHM15kx.

3.1.1 System

The most relevant specifications of the JenOptik CHM15kx-ceilometer are listed in Tab. 3.1. A solid-state Nd:YAG-laser is used as radiation source in a bi-axial configu-

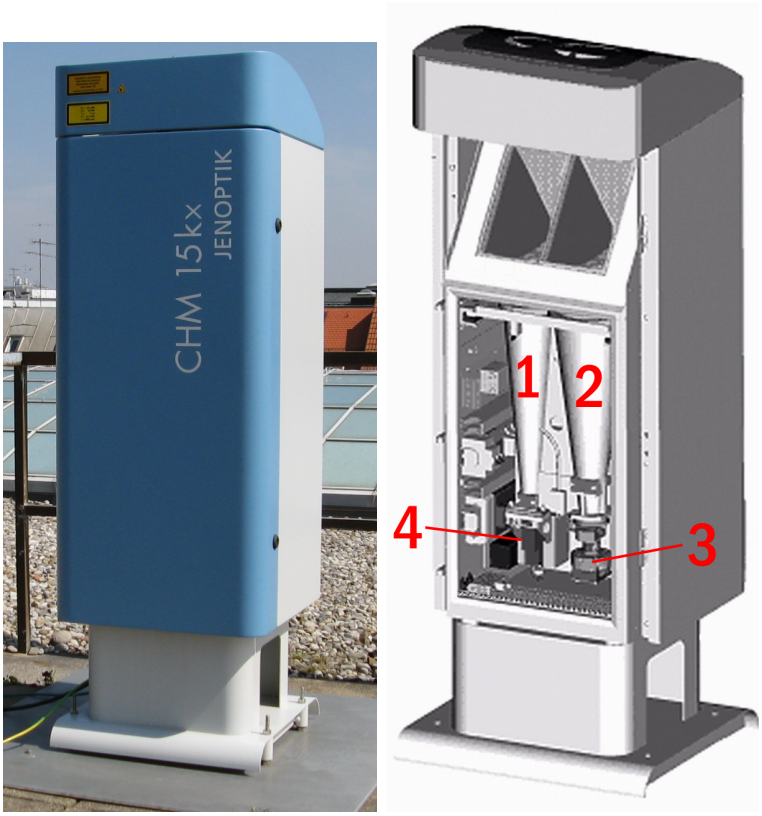

Figure 3.1: JenOptik ceilometer CHM15kx on the roof of the meteorological institute Munich (left). Inside view (right) with transmitter (1), receiver (2), APD-unit (3) and laser (4).

ration. The laser emits pulses of 1 ns length at 1064 nm wavelength with a frequency between 5 and 7 kHz and an energy of approximately 8 µJ per pulse. Due to the low laser power of around 50 mW, eye-safety is guaranteed and the laser is classified as 1M (DIN EN 60825-1) which is mandatory for unattended operation. Because of this low laser energy, only a relative low SNR can be achieved. The laser beam has a divergence of 0.33 mrad and the telescope's field of view is 1.8 mrad. For achieving a low overlap height, the optical axes are tilted by an inclination angle of 0.46 mrad, which results in a z_{ovl} at around 1000 m. However, a reliable correction allows to extend the measurement range to approximately 180 m (see Sect. 3.3.1). An APD is used for signal detection and after digitalization the maximum data range of 15.36 km is divided in 1024 range bins of 15 m each. For the lowest 3 km, data are stored—in addition—with a range resolution of 5 m (600 range bins) in case of the Nimbus-version. Since the amplification of the APD varies strongly with the applied reverse voltage but also with

temperature, a thermal stabilized environment is necessary for the receiver unit. This is realized with an inner and an outer housing, in which an air flow can provide heating or cooling depending on ambient temperature. The APD can therefore operate at a constant temperature of 25 °C. Another advantage of this double-shell housing is the prevention of potential external influences such as solar radiation, wind, rain, snow and dirt.

Data range	15 m–15.36 km
Range resolution	5–15 m
Temporal resolution	5 s–60 min
Laser	Nd:YAG Class 1M
Wavelength	1064 nm
Bandwidth	0.1 nm
Pump system	Diode
Pulse repetition rate	5–7 kHz
Pulse duration	1 ns
Pulse energy	7–9 µJ
Laser power	~50 mW
Beam diameter ($1/e^2$)	90 mm
Laser divergence	0.33 mrad
z_{ovl}	1000 m
Field of view	1.8 mrad
Inclination angle laser–telescope	0.46 mrad

Table 3.1: Specifications of the JenOptik ceilometer CHM15kx

As already mentioned, the gain of the APD is high voltage dependent and the application of the photodiode in a region right below the breakdown voltage can be used to regulate the sensitivity by changing the applied high voltage. So, the high voltage is decreased automatically in case of increasing background radiation, e. g. low bright clouds in the line of sight or when the background radiation is increasing during sunrise. In contrast, if reflecting high cirrus clouds disappear or after sunset, the background radiation decreases and the high voltage is increased. All relevant system parameters, i. e. temperature, window transmissivity, high voltage, laser and APD status are recorded in the data file. In case they are deviating from normal values or in case of a malfunction, an error message is reported. The data of the CHM15kx is stored in Network Common Data Format (NetCDF). An excerpt of important measurement variables is shown in Tab. 3.2.

NetCDF variable	Description
`time`	Measurement time in UTC
`range`	Distance from lidar
`average_time`	Averaging time
`range_gate`	Spatial resolution
`beta_raw`	Quantity proportional to the backscatter profile
`base`	Background radiation (daylight correction factor)
`stddev`	Standard deviation of the raw signal
`laser_pulses`	Number of laser pulses
`temp_int`	Temperature surrounding the optical unit
`temp_ext`	Temperature outside the housing
`temp_det`	Temperature of the APD
`error_ext`	31 Bit service code for reporting errors
`NN1`	Difference between actual and breakdown voltage

Table 3.2: NetCDF-excerpt of important measurement variables of the JenOptik ceilometer CHM15kx

YALIS, the ceilometer of the Meteorological Institute of the Ludwig-Maximilians-Universität (LMU) in Munich, Germany is located at 48.148° N latitude, 11.573° E longitude, and 539 m altitude. Operating continuously since 16 June 2009 the system was subject to several firmware updates and adjustments (see history Tab. 3.3), in which one extended the range of allowed high voltage (HV) supplies, leading to a better SNR during night. The temporal resolution of 30 s was improved to 15 s from June 2012.

3.1.2 Data processing and principle of operation

NetCDF-files saved on the internal computer can be transferred via Ethernet or an RS485 interface as one single file of all measurements since midnight or as small files containing only the latest 5 minutes if bandwidth is small. In case of YALIS, the first option is used until October 2014, the second is applied since the upgrade to the Nimbus status. Furthermore, using the Ethernet or RS485 interface, it is possible to remotely set system properties in order to control the mode of operation. For the derivation of cloud base heights, boundary layer heights and visibility ranges, proprietary algorithms are implemented in the client software. The NetCDF-files include housekeeping data and for documentation of the system's status, a 32-bit service code (Optik Systeme GmbH, 2006) is stored as 8-digit hexadecimal number.

From	To	Comment
12.06.2009	27.10.2014	X 1st generation
		from 21.06.2012: 15 s temporal resolution
		from 10.08.2012: range of possible HV supply extended
	Nov. 2014	upgrade X 1st generation to Nimbus-version
10.11.2014	08.01.2015	K Nimbus
	Jan. 2015	readjustment K Nimbus to X Nimbus
02.02.2015	26.05.2015	X Nimbus
		re-adjustment before CeiLinEx (www.ceilinex2015.de)
27.06.2015	14.09.2015	X Nimbus (at CeiLinEx)
		return to Munich
21.09.2015		X Nimbus

Table 3.3: Phases of different hardware configurations of the JenOptik Ceilometer of the Meteorological Institute (LMU).

The measured backscatter profile is saved in counts in a variable named `beta_raw` (see Tab. 3.2) which is calculated as follows:

$$\text{beta\_raw}(t,z) = \frac{P(t,z) - P_{bg}(t)}{\text{stddev(t)}} \tag{3.1}$$

Based on this quantity the background corrected lidar signal $P(t,z)$ can be obtained by multiplying `beta_raw` by the variable `stddev`. The signal of the background radiation is stored in the variable `base` and denoted by "daylight_correction_factor". To get a first overview of the vertical cloud and aerosol distribution, we plot the range corrected lidar profile $X(z)$ color coded in a time height cross section. In Fig 3.2 the range-corrected signal $X(z)$ (logarithmic scale in arbitrary units) at 1064 nm of 29 March 2011 is shown as an example; vertical axis is height above ground, time is given in UTC. Between sunrise (05:00 UTC) and sunset (17:00 UTC), an increase of the signal noise is obvious especially above 4 km. The colors between light blue and red illustrate the high aerosol backscatter in the boundary layer below 2 km. Deep blue areas indicate low aerosol load and aerosol-free regions. The distinct changes of the color at 01:00 UTC, 09:37 UTC, 09:57 UTC, 10:37 UTC, 17:37 UTC, 17:42 UTC, 17:47 UTC, and 19:07 UTC can be related to the sensitivity settings of the APD described in Sect. 3.1.1. For example, at 09:37 UTC the background radiation is increasing when low bright clouds (white color) are approaching. To prevent the saturation of the APD the high voltage supply is reduced accordingly. This feature of ceilometers of the first

generation makes the data evaluation quite complex as the changes of the amplification must be quantified and the dependence on the high voltage must be assessed. A method is described in detail in Sect. 3.3.2. In principle, these changes of high voltage can be reconstructed with help of the NetCDF-variable `NN1` which stores the difference between the actual and the breakdown voltage in units of 0.1 V, henceforward referred to as Δ. For our ceilometer, Δ ranges between 120 and 155 for the period June 2009–August 2012 and between 95 and 180 for the period August 2012–October 2014. On the basis of a 5 years measurement series, correlations between the background signal `base` and the high voltage changes could be found. In general, as soon as `base` exceeds 0.3, Δ is raised by 5, whereas in some cases more than one of these changes are made within a few minutes, what can be seen in Fig 3.2 at 09:57 UTC. After the adjustment to the new background, the detector-settings may be stable for hours again. A decrease of `base` below 0.001, however, induces a corresponding reduction of Δ by 5 (cf. Fig 3.2 17:42 UTC). In other words, if the background radiation decreases, the sensitivity of the APD is improved by an increase of the applied high voltage. If the limit of $\Delta = 155$ or $\Delta = 180$ is reached, Δ is set to 130 and readjusted until `base` is again below 0.3. If this cannot be achieved and `base` exceeds a threshold of 0.5, the operation mode is changed—henceforth named HB-mode (high background mode). In this case a strong decrease in sensitivity can occur. In addition, a service code is set in the variable `error_ext` for this time step. These cases can be found more frequently in the period June 2009–August 2012 when only a smaller range of possible Δ was available, thus resulting in a limited capability to compensate sudden rises of `base`. When operating in HB-mode, the HV-supply has sort of an offset and the provided values must be treated in a special way (see Sect. 3.3.2).

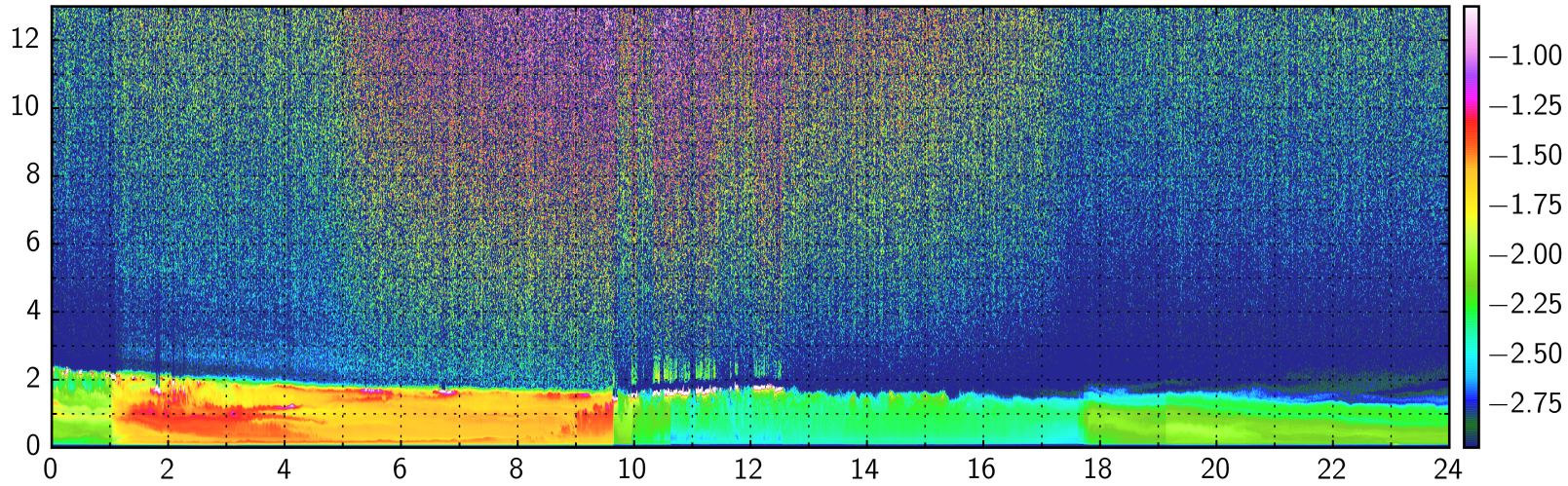

Figure 3.2: Time height cross section of the range-corrected signal (in logarithmic scale, a.u.) at 1064 nm from ceilometer CHM15kx in Munich, 29 March 2011. Changes in signal strength are observable at 01:00 UTC, 09:37 UTC, 09:57 UTC, 10:37 UTC, 17:37 UTC, 17:42 UTC, 17:47 UTC and 19:07 UTC.

3.2 Auxiliary instruments - sun photometer and radiosondes

For the realization of an accurate lidar calibration as well as for verifications and cross checks of obtained results, additional information is needed and can be derived from secondary instruments; this section gives a brief description.

3.2.1 Sun photometer

A sun photometer in contrast to a lidar is a passive remote sensing instrument utilizing the sun as radiation source. It observes the direct irradiance I of the sun using an optical unit with small field of view and different band-pass filters to separate the detected radiation in certain wavelength. The measured irradiance I is attenuated while propagating through the atmosphere according to Bouger-Lambert-Beer's law (equation (2.1)):

$$I(\lambda) = I_0(\lambda)\, e^{-\tau(\lambda)\, m} \tag{3.2}$$

Rearranging for $\tau(\lambda)$ yields:

$$\tau(\lambda) = -\frac{1}{m}\, \ln\left(\frac{I(\lambda)}{I_0(\lambda)}\right) \tag{3.3}$$

In the sun photometer application $I_0(\lambda)$ is the extraterrestrial irradiance, which is the irradiance at the top of the atmosphere, and $\tau(\lambda)$ the optical depth of the atmosphere, which is the quantity of interest when comparing with the ceilometer. Since the sun photometer is pointing to the sun, the transmission path is a function of the sun zenith angle θ and the distance between earth and sun; both factors are represented by m. However, m is equal $1/\cos\theta$ in a good approximation. When solving this equation for $\tau(\lambda)$, information about the extraterrestrial irradiance $I_0(\lambda)$ is necessary which can be obtained with the Langley calibration technique (Schmid and Wehrli, 1995). Thus, aerosol optical depth can be retrieved with an uncertainty of ± 0.01 (Shaw, 1976; Holben et al., 1998; Toledano et al., 2011), however, only if appropriate weather conditions (cloud-free and daylight) prevail. When comparing sun photometer observations with ceilometer measurements it is important to consider that a sun photometer only yields column values—i. e. mean values over all altitudes—whereas a

Figure 3.3: Sonnenphotometer CE 318 des Herstellers Cimel Eleqtronique (CIMEL Electronique, 2000-10-09)

ceilometer provides profiles which are height resolved values of aerosol optical parameters instead.

In this work an automatic sun tracking photometer CE 318 from Cimel Electronique (CIMEL Electronique, 2000-10-09) is used which operates unattended and fully automated at 7 wavelengths (340 nm, 380 nm, 440 nm, 500 nm, 675 nm, 870 nm, 1020 nm). It is the standard instrument of the Aerosol Robotic Network (AERONET), which is a network of ground-based sun photometers which are measuring atmospheric aerosol properties (Holben et al., 1998)). The measured data is available in different quality levels (Level 1.0, 1.5, 2.0), in which Level 1.5 data is cloud screened (Smirnov et al., 2000) and Level 2.0 additionally pre- and post deployment calibrated.

Another parameter provided by sun photometer observations is the Ångström exponent κ, which describes the dependency of aerosol optical depth on wavelength (Ångström, 1964).

$$\kappa = \frac{\ln \tau(\lambda_1) - \ln \tau(\lambda_2)}{\ln \lambda_2 - \ln \lambda_1} \quad \text{with} \quad \lambda_1 < \lambda_2 \tag{3.4}$$

Since the scattering intensity is dependent on particle size and incident wavelength (see section 2.1), the Ångström exponent can give a first assessment of the particle size distribution in the atmosphere. It is inversely related to the average size of the particles in the aerosol: the smaller the particles, the larger the exponent. For ex-

ample, in case of relative large cloud droplets, κ is almost zero and the AOD has no significant wavelength dependence. Once the Ångström exponent is calculated from measurements at two different wavelength λ and λ_0, the AOD at wavelengths of a similar spectral region of λ and λ_0 can be derived.

$$\tau(\lambda_1) = \tau(\lambda_2) \left(\frac{\lambda_1}{\lambda_2}\right)^{-\kappa} \tag{3.5}$$

Now with having independent AOD measurements derived from sun photometer observations a comparison with results obtained from ceilometer data is possible, however, some aspects have to be taken into account.

First, since ceilometers are elastic backscatter lidars, an unknown lidar ratio S_p leads to large errors in the AOD calculated from retrieved aerosol backscatter coefficient profiles $\beta_p(z)$ as follows:

$$\tau_p(\lambda) = \int_0^{z_{max}} \alpha_p(z', \lambda)\, dz' = \int_0^{z_{max}} \beta_p(z', \lambda)\, S_p\, dz' \tag{3.6}$$

Especially in case of elevated aerosol layers with different aerosol optical properties and thus changing lidar ratios, the assumption of a column lidar ratio holds big uncertainties which has to be pointed out (Takamura et al., 1994).

Second, considering the ceilometer's operating wavelength of 1064 nm and the nearest wavelength of the sun photometer at 1020 nm a conversion of τ_{1020} to τ_{1064} is necessary. If AERONET provides a correct Ångström exponent, τ_{1064} is obtained by $\tau_{1064} = \left(\frac{1064\,\mathrm{nm}}{1020\,\mathrm{nm}}\right)^{-\kappa} \tau_{1020}$. Otherwise, if assuming an Ångström exponent of 1, corresponding to a λ^{-1}-dependency of α_p, a linear conversion between both instruments ($\tau_{1064} = \tau_{1020}\, \frac{1064\,\mathrm{nm}}{1020\,\mathrm{nm}}$) is possible. Due to the small difference of both wavelength this simplified approach yields sufficient accuracy.

A third aspect is the region of incomplete overlap of the ceilometer. When calculating the AOD with formula (3.6), no quantitative information from the height below full overlap can be reliably obtained and therefore complicates a comparison with the sun photometer. In the case of the ceilometer CHM15kx, however, the height of full overlap z_{ovl} is very low if corrected accordingly ($z_{ovl} \approx 200\,\mathrm{m}$). Hence, the error of the missing optical depth is negligible when assuming a homogeneous atmosphere in the height $z < z_{ovl}$ and extrapolating α_p down to the ground. A sample calculation illustrates this procedure: Suppose that $\alpha_p(z_{ovl}) = 0.01\,\mathrm{km}^{-1}$, an optical depth of the missing layer of $\tau_{p,ovl} = 0.002$ would be obtained. A relative error of 50% of α_p would

result in an over- or underestimation of the optical depth of less than 0.001. In contrast, when assuming $\alpha_p(z_{ovl}) = 0.1\,\mathrm{km}^{-1}$, a comparative high value, the AOD of the missing layer is $\tau_{p,ovl} = 0.02$. This yields an uncertainty of 0.01 of the AOD, when α_p is within an accuracy of 50%. However, it is required that z_{ovl} is within the boundary layer. For shallow boundary layers, an extrapolation down to the ground would fail.

The last and most limiting aspect in comparing both instruments, however, is the fact that sun photometer measurements are only available during daytime when the ceilometer has the lowest SNR. This necessitates long time averages of the ceilometer signal which is often hampered by bad weather conditions or inhomogeneous aerosol distributions.

3.2.2 Radiosondes

To realize the Rayleigh-calibration presented in section 2.2.2, temperature and pressure profiles are necessary. Furthermore, they are used to calculate the molecular part α_m and β_m according to Eq. (2.15) to divide α and β into its molecular and particle part. Radiosonde measurements are one option to provide such thermodynamic properties, which can also be used to determine boundary layer heights independently by means of the characteristic thermodynamic in this lowermost part of the atmosphere—shown in section 3.4.2. The radiosonde is an in-situ research instrument used for measuring profiles of thermodynamic properties of the atmosphere. It is usually attached to a weather balloon and consists of a transmitter for sending data to the ground and a measurement unit with sensors. The German Weather Service (DWD) launches weather balloons at 12 stations in Germany, 2–4 times a day, depending on the weather situation. The sonde yields direct measurements of pressure, temperature and humidity whereas wind parameters can be derived indirectly from horizontal shifting obtained by position tracking with a GPS-sensor. The maximum measurement height is 20–30 km and is reached when the expanding balloon envelope surpasses its maximum extent. The launch time of the radiosonde ascent is 5 UTC, 11 UTC, 17 UTC and 23 UTC, respectively, chosen so that an altitude of 10 km is reached before 6 UTC, 12 UTC, 18 UTC and 24 UTC, respectively. That means, that the planetary boundary layer top is penetrated at around 5–10 minutes after start, depending on the boundary layer height when assuming an ascent rate of approx. 5 m/s. In case of the ceilometer of the Meteorological Institute Munich, radiosondes ascending at the DWD-site at Oberschleißheim (8 km north) twice a day (00 UTC and 12 UTC) are used. Due to the

small distance between both sites, these radiosonde measurements are assumed to be representative for the Munich site.

3.3 Calibration

As already mentioned in Sect. 2.2.2, quantitative aerosol parameters, i. e. α_p and β_p, can be derived by using a reference value obtained from e. g. Rayleigh calibration, or by using a lidar constant C_L. For the Rayleigh calibration certain meteorological as well as instrumental specific conditions must be fulfilled, hampering an application especially in case of a ceilometer at any time. A method to determine the lidar constant for a ceilometer CHM15kx is described in the following section. The determination of C_L for this instrument is complicated because of its principle of operation outlined in Sect. 3.1.2 and its overlap of $z_{ovl} = 1000\,\mathrm{m}$ (see Sect. 3.3.3).

For this reason, the calibration is carried out in three steps. The first step yields an overlap correction for the instrument, extending the measurement range to approximately 180 m above ground. The second step provides the determination of conversion factors η to quantify the relative changes of C_L, controlled by the key parameter $\Delta(t)$, i. e. $C_L = C_L(\Delta(t))$. This part relies on the ceilometer data alone which must fulfill prescribed meteorological conditions which are explained in the following. The third step concerns the absolute calibration of the instrument which is based on the determination of a C_L^* for a certain Δ^*. The meteorological conditions required for this procedure are more restricted than they are in the first step. After all three steps are applied, the lidar constant C_L can be converted from a specific Δ^* to an arbitrary Δ by

$$C_L(\Delta(t)) = \eta\, C_L^* \tag{3.7}$$

The whole process is automated and in the case of YALIS applied to 5 years of ceilometer observations.

To give a short overview of the different steps and their effects on the signal, three time height cross sections of the range-corrected signal $X(z)$ from YALIS, 30 March 2014, are presented in Fig. 3.4. The first panel shows the uncorrected signal. Notice the large signal-steps with time and the incomplete overlap region near the surface, resulting in decreasing signal strength towards the ground. The signal of the second panel is already overlap corrected, clearly visible in the first kilometer. The last panel

shows the overlap corrected and relative calibrated signal—no changes of the signal can be seen and a homogeneous diurnal cycle is obtained.

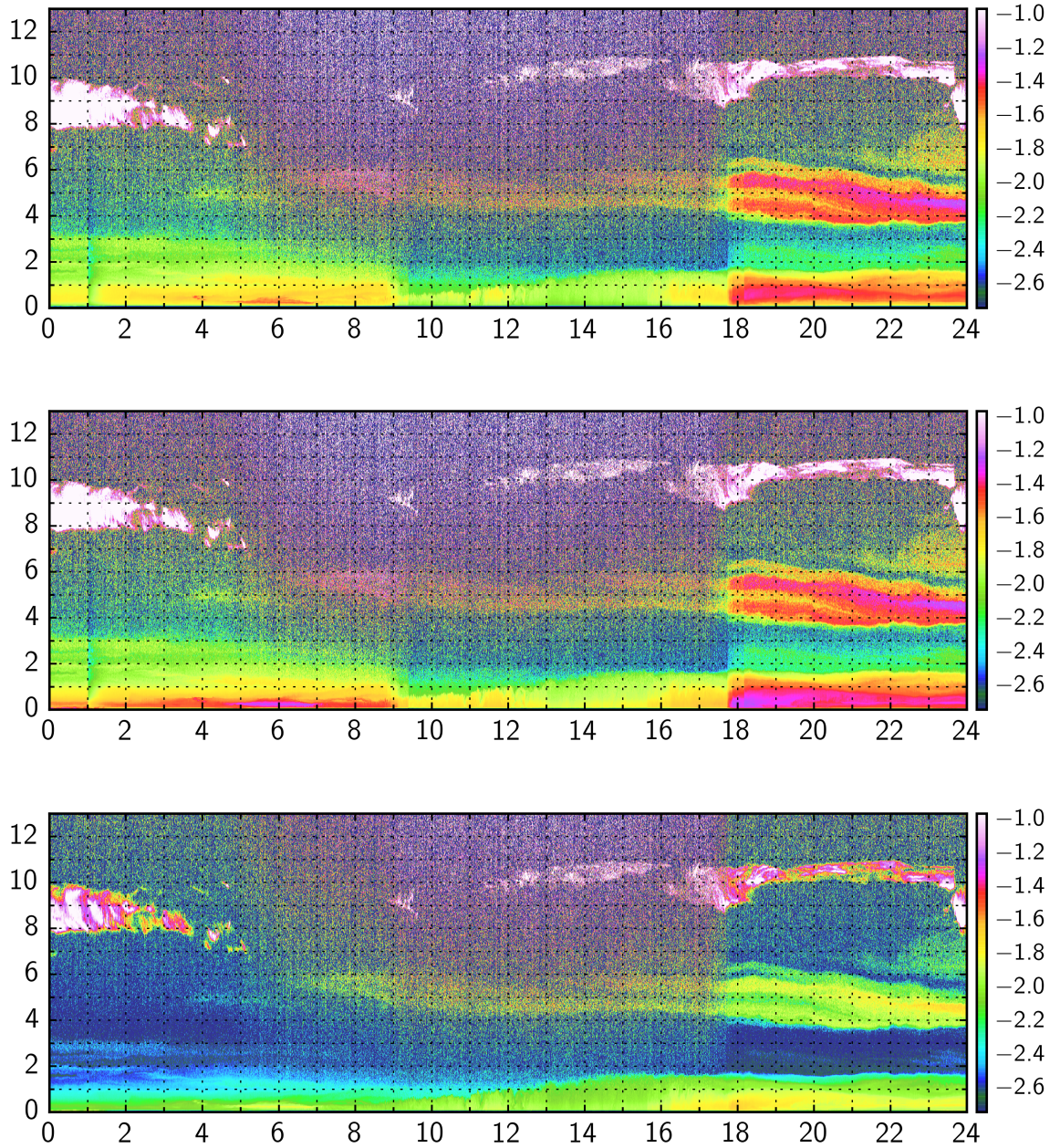

Figure 3.4: Time height cross section of the range-corrected signal (in logarithmic scale, a.u.) at 1064 nm from YALIS, 30 March 2014. First panel: without corrections. Second panel: overlap corrected. Third panel: overlap corrected and relative calibrated.

3.3.1 Overlap correction

The near range of a ceilometer mainly depends on the optical configuration, limiting the measurement range to heights larger than z_{ovl}, i. e. where $O(z) = 1$ as outlined in section 2.2.3. Jenoptik provides overlap functions for their instruments since the launch of the Nimbus version. They are determined at their test site by means of co-located measurements of a reference instrument to ensure that all instruments of a network are comparable. The correction is possible down to approximately 500 m for K-Nimbus instruments. However, the functions are not reliable in any case, showing artificial layers in the corrected region and hence must be treated with caution. With the CHM15kx 1st generation (see Tab. 3.3) an overlap function was not yet supplied. To allow an evaluation of very low aerosol layers, frequently occurring in winter and important to enable us reliably applying an absolute calibration to the CHM15kx, the incomplete overlap for heights $z < 1$ km must be corrected.

An approach for an overlap correction with horizontal homogoneous conditions is not possible at the measurement site in Munich due to many local aerosol sources. Furthermore, the temporal variance is large. However, since the ceilometer CHM15kx is continuously operated in a vertical alignment since June 2009, the approach for an overlap correction by using a vertical homogeneous atmosphere described in section 2.2.3 can be used for this purpose. From 5 years of ceilometer observations, days with a well developed convective ML with a minimum height of 1.4 km are selected. This is due to the fact that the ceilometer has full overlap at $z_{ovl} = 1$ km and a region with homogeneous aerosol distribution is needed above to apply the slope method. Only 8 measurement times fulfilling all meteorological requirements were found within 5 years of continuous observation. However, enough to reliably determine an overlap correction. By calculating the overlap function for observations with different HV settings of the APD, i. e. different Δ, a relation between the overlap function $O(z)$ and Δ could be found.

In Fig. 3.5 overlap functions for Δ between 95 and 170 are shown. In detail, from left to right, $\Delta = 95$ (blue), $\Delta = 120$ (red), $\Delta = 130$ (green), $\Delta = 135$ (black), $\Delta = 155$ (blue dashed), $\Delta = 160$ (red dashed), $\Delta = 170$ (green dashed). The black dashed overlap function is determined for $\Delta = 170$ but in HB-mode. All overlap functions have a similar shape showing a rapid decrease in a height of $z = 180$ m. Considering this region, the strong dependence of $O(z)$ on Δ becomes clearly visible, i. e. the overlap is getting better with increasing Δ. To provide overlap functions for

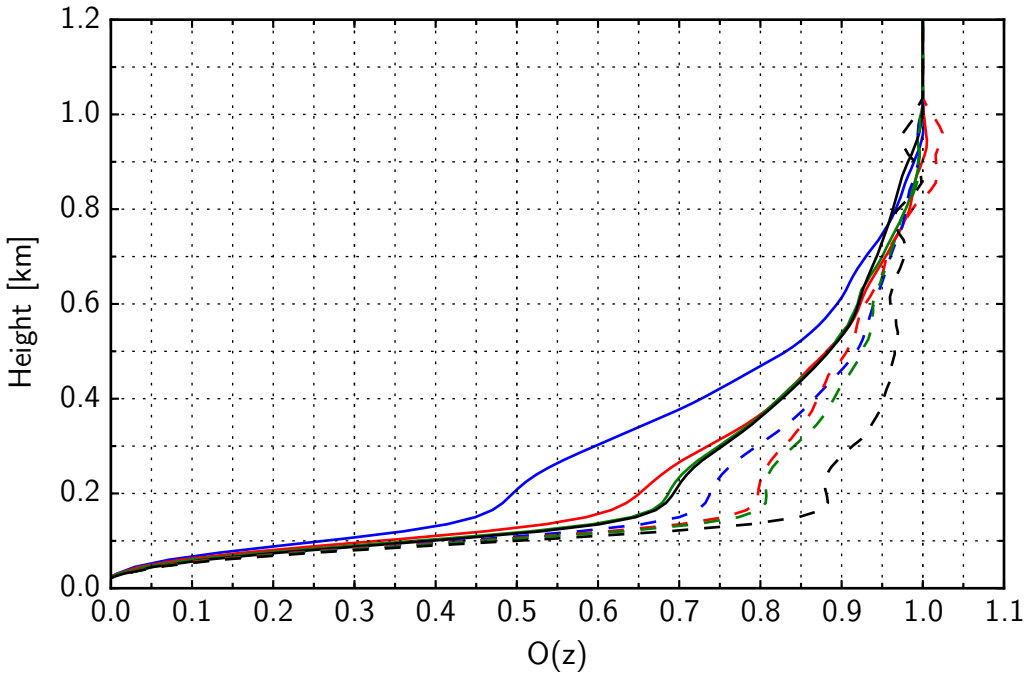

Figure 3.5: Overlap functions of the LMU Ceilometer CHM15kx for different HV supplies; $\Delta = 95$ (blue), $\Delta = 120$ (red), $\Delta = 130$ (green), $\Delta = 135$ (black), $\Delta = 155$ (blue dashed), $\Delta = 160$ (red dashed), $\Delta = 170$ (green dashed) and $\Delta = 170$ in HB-mode (black dashed).

all possible Δ by means of available overlap functions, a linear interpolation between two reference overlap functions is done in every height z. Here, $\Delta = 95$ and $\Delta = 155$ are chosen due to the best meteorological conditions prevailing for their calculation and thus yielding the most reliable results. Hence, the HV-dependent overlap function $O(z, \Delta)$ can be expressed for $95 \leq \Delta \leq 180$.

$$O(z, \Delta) = O(z, 95) + \frac{O(z, 155) - O(z, 95)}{(155 - 95)} (\Delta - 95) \tag{3.8}$$

All derived overlap functions $O(z, \Delta)$ are shown in Fig. 3.6 as light blue lines in Δ-steps of 5. To illustrate the reliability of this procedure, the same overlap functions as shown in Fig. 3.5 are included in the same colors, but with circles instead of lines and triangles instead of dashed lines. Blue circles and blue triangles are representing the reference overlap functions at $\Delta = 95$ and $\Delta = 155$. The calculated overlap functions for other Δ agree very well with the independent derived functions from Eq. (3.8). The HB-mode case with $\Delta = 170$ (black triangle) has the lowest APD-sensitivity of

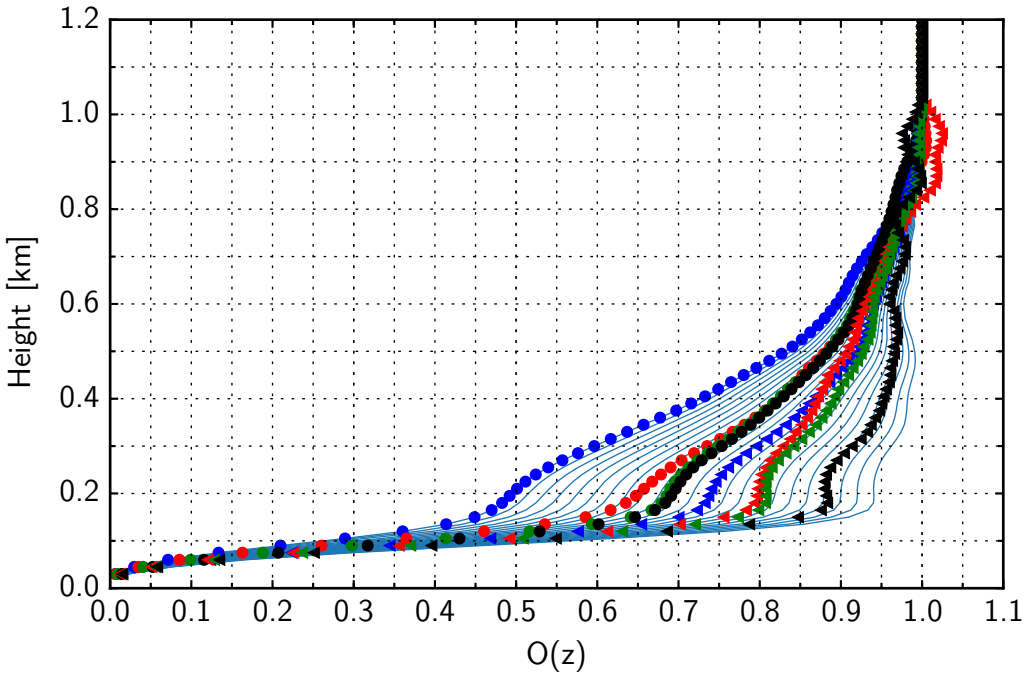

Figure 3.6: Overlap functions of the LMU ceilometer CHM15kx for $95 \leq \Delta \leq 185$ in steps of 5 (light blue). Overlap functions as in Fig. 3.5: $\Delta = 95$ (blue circle), $\Delta = 120$ (red circle), $\Delta = 130$ (green circle), $\Delta = 135$ (black circle), $\Delta = 155$ (blue triangle), $\Delta = 160$ (red triangle), $\Delta = 170$ (green triangle) and $\Delta = 170$ in HB-mode (black triangle).

all calculated overlap functions and hence is closer to 1. In principle, a HB-mode measurement can be regarded as a normal measurement but with hypothetical higher value in Δ, i. e. $\Delta + \delta\Delta$ where $\delta\Delta$ can not be determined with high accuracy but could be limited in section 3.3.2 to $25 \leq \delta\Delta \leq 35$.

When applying the overlap function to the measurements, an extension of the measurement range to the ground is not possible (see Sect. 2.2.3) and the dependency of $O(z)$ on Δ causes additional uncertainty. A possible explanation for this issue is a wrong dead time correction in case of very high counting rates, typical for bright clouds, and was proposed by Jenoptik during personal communication (Frey, 2012). A further reason is an inhomogeneity of the APD, leading to different sensitivities dependent on which part of the surface of the APD is focused by the optics—especially important in the near range. This explanation is also given by a recent study from Hervo et al. (2016), however, here a temperature dependency of the overlap function could be found. It must be noted, that the instrument used in this study is a CHM15k-Nimbus.

Due to the differences between a Nimbus-version and the CHM15kx, a temperature dependence can not be verified. Consequently, this issue remains subject to further investigations of the manufacturers. Since a quantification of this Δ-dependence is not possible, two new heights are introduced: The height $z_{ovl,c}$ is the height above which a quantitative evaluation of ceilometer signals after correction are still reliable in a meteorological sense. A second height $z_{ovl,min}$ is the minimum height where an overlap correction still eliminates artificial aerosol layers, thus enabling us to analyze shallow boundary layers for e. g. boundary layer height determination. When considering the overlap functions of YALIS in Fig. 3.6, an extension of the measurement range to a minimum height of $z_{ovl,min} = 135\,\mathrm{m}$ appears to be reasonable, since $O(135\,\mathrm{m}) > 0.5$ for almost every Δ. When deriving quantitative parameters with YALIS, a height $z_{ovl,c} = 210\,\mathrm{m}$ is used as minimum height of the measurement range, which is the height above the steepest increase of $O(z)$.

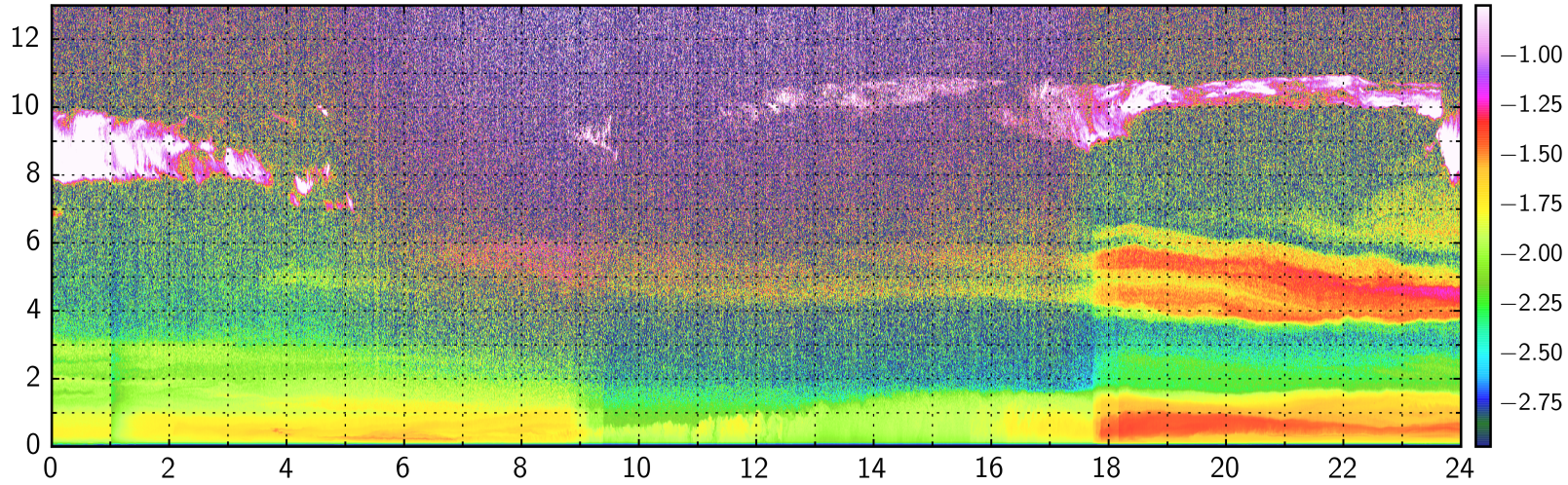

Figure 3.7: Time height cross section of the range-corrected signal (in logarithmic scale, a.u.) at 1064 nm from YALIS, 30 March 2014. Changes in the sensitivity are obvious at 08:50 UTC, 08:56 UTC, 09:06 UTC, 09:09 UTC, 09:24 UTC, 12:26 UTC, 17:43 UTC, 17:44 UTC, 17:46 UTC, 17:51 UTC and 18:10 UTC.

3.3.2 Relative calibration

Normal operation

A typical example of one day of measurements with several changes of the sensitivity of the system can be seen in Fig. 3.7. Shown is the time-height cross section of the range-corrected signal $X(z)$ (logarithmic scale, color coded in arbitrary units) of 30 March 2014; the vertical axis is the height above ground in kilometer, the horizontal axis is time in UTC. The colors between green and red illustrate the high aerosol abundance in the boundary layer up to a height of 1.6 km throughout the day. Above 1.6 km several elevated and stratified aerosol layers are visible, represented by light blue to red colors between 1.6 km and 7 km. High clouds are present during the whole day as can be seen from the many white areas. Changes of the sensitivity are clearly visible from the distinct changes of the colors at 08:50 UTC when Δ changes from 95 to 100, at 08:56 UTC (from 100 to 105), at 09:06 UTC (from 105 to 110), at 09:09 UTC (from 110 to 115), at 09:24 UTC (from 115 to 125) and at 12:26 UTC (from 125 to 130). In all cases Δ is increased, thus leading to a decrease in sensitivity of the APD. In contrast, the changes of color between 17:43 UTC and 18:11 UTC refer to a decrease of Δ and hence to an increase in sensitivity of the APD; in detail, at 17:43 UTC Δ changes from 130 to 125, at 17:44 UTC (from 125 to 120), at 17:46 UTC (from 120 to 115), at 17:51 UTC (from 115 to 110) and at 18:10 UTC (from 110 to 105).

Since these changes can be referred to changes of the HV-supply of the APD the lidar constant C_L can be expressed as a function of Δ. The decrease or increase of C_L during the change from Δ_i to Δ_j (corresponding to times t_i and t_j, respectively) can directly be determined from the ratio of the corresponding signals.

When considering the range-corrected signal $X(z)$ in a fixed height z, Eq. (2.12) can be expressed as a function of time. The ratio of $X(z)$ at time t_i and t_j is

$$\frac{X(t_j,z) = C_L(t_j)\left[\beta_p(t_j,z)+\beta_m(t_j,z)\right]\,\exp\left\{-2\int_{z_0}^{z}[\alpha_p(t_j,z')+\alpha_m(t_j,z')]\,dz'\right\}}{X(t_i,z) = C_L(t_i)\left[\beta_p(t_i,z)+\beta_m(t_i,z)\right]\,\exp\left\{-2\int_{z_0}^{z}[\alpha_p(t_i,z')+\alpha_m(t_i,z')]\,dz'\right\}} \tag{3.9}$$

If the aerosol distribution is constant between times t_i and t_j, all atmospheric terms ($\beta_p(t,z)$, $\beta_m(t,z)$, $\alpha_p(t,z)$ and $\alpha_m(t,z)$) cancel out and following simple relation is obtained:

$$\frac{X(t_j, z)}{X(t_i, z)} = \frac{C_L(t_j)}{C_L(t_i)} \tag{3.10}$$

A factor $\eta(\Delta_i, \Delta_j)$ can be defined and denotes the relation between the lidar constants before and after a change of Δ, i. e. at time t_i and t_j, respectively:

$$\eta(\Delta_i, \Delta_j) = \frac{C_L(\Delta_j)}{C_L(\Delta_i)} = \frac{X(t_j, z)}{X(t_i, z)} \tag{3.11}$$

The conversion factor $\eta(120, 125)$, for example, stands for an increase of Δ by 5. A decrease from $\Delta = 125$ to $\Delta = 120$, in contrast, is denoted by $\eta(125, 120)$.

The factors $\eta(\Delta_i, \Delta_j)$ are determined when the aerosol distribution is stable during 5 minutes. To guarantee a reliable calculation of the conversion factors, heights z in Eq. (3.11) are typically chosen in the mixing layer, where the SNR is large. Furthermore, averages $\overline{X(t_i, z)}$ and $\overline{X(t_j, z)}$ are calculated for heights z between $z_{ovl,c}$ and 825 m (corresponding to range bin 55). The time t_i and t_j is chosen three time steps before and after the change of Δ, respectively. The time interval between both time averages is needed to account for the adaption of the APD to the new HV-setting. A general formulation for $\overline{X(t_i, z)}$ is

$$\overline{X(t_i, z_l)} = \frac{1}{9} \sum_{m=-1}^{1} \sum_{n=-1}^{1} X(t_{i-m}, z_{c-n}) \quad \text{with } z_{ovl,c} < z_l < 825\,\text{m} \tag{3.12}$$

Longer temporal averages are not necessary and might be influenced by a changing aerosol distribution. In addition, several changes of Δ can occur within a few minutes (cf. Fig. 3.7), so that longer averaging times are not available for the determination of η.

The corresponding standard deviation $s(t_i, z)$ for time t_i is derived by

$$s(t_i, z_l) = \sqrt{\frac{1}{9} \sum_{m=-1}^{1} \sum_{n=-1}^{1} \left(X(t_{i-m}, z_{c-n}) - \overline{X(t_i, z_l)} \right)^2}. \tag{3.13}$$

The relative error of the mean signal $\overline{X(t_i, z)}$ is used to decide in which height the conversion factor is determined to achieve high accuracy with small errors and is given by:

$$\delta\overline{X(t_i, z)} = \frac{s(t_i, z)}{\overline{X(t_i, z)}} \tag{3.14}$$

The relative error $\delta\overline{X(t_j, z)}$ for time t_j is calculated accordingly. The relative error of the conversion factor $\delta\eta(\Delta_i, \Delta_j, z)$ can then be determined by

$$\delta\eta(\Delta_i, \Delta_j, z) = \sqrt{\delta\overline{X(t_i, z)}^2 + \delta\overline{X(t_j, z)}^2}, \tag{3.15}$$

calculated for each height z, where t_i is before and t_j after the change of Δ. The height of the minimum value of $\delta\eta(\Delta_i, \Delta_j, z)$ with $z_{ovl,c} < z < 825\,\mathrm{m}$, is finally selected to determine the conversion factor. If in all heights z, $\delta\eta(\Delta_i, \Delta_j, z) > 0.05$, no conversion factor is determined.

One example of this procedure is shown in Fig. 3.8. The range-corrected signals at $z = 780\,\mathrm{m}$, $z = 795\,\mathrm{m}$ and $z = 810\,\mathrm{m}$ are displayed from 08:36 UTC until 09:03 UTC (30 March 2014); the temporal resolution is 15 s. At 08:50 UTC, Δ changes from $\Delta_i = 95$ to $\Delta_j = 100$ (cf. Fig. 3.7). The relative error $\delta\eta(\Delta_i, \Delta_j, z)$ is minimum for $z = 795\,\mathrm{m}$. To calculate $\eta(95, 100)$, Eqs. (3.12), (3.13) and (3.14) are applied. The red bars represent the mean values $\overline{X(t_i, z)}$ and $\overline{X(t_j, z)}$ for $z = 795\,\mathrm{m}$, respectively; the thin red lines are marking the corresponding standard deviation. By using Eq. (3.11), $\eta(95, 100)$ can be calculated to:

$$\eta(95, 100) = \frac{C_L(100)}{C_L(95)} = \frac{\overline{X(t_j, 795\,\mathrm{m})}}{\overline{X(t_i, 795\,\mathrm{m})}} = 0.89 \tag{3.16}$$

The relative error in this case is $\delta\eta(95, 100) = 0.033$.

Following this procedure, conversion factors $\eta(\Delta_i, \Delta_j)$ are determined for Δ-differences of 5 ($\Delta_j - \Delta_i = 5$) ranging from $95 \leq \Delta_i \leq 170$.

When comparing η for different Δ_i in Tab. 3.4 it can be seen that a change of Δ by 5 requires different conversion factors η. That means a change of Δ from 95 to 100 and a change of Δ from 140 to 145 have different effects on the signal strength.

When considering cases with decreasing background radiation and consequently decreasing Δ, conversion factors could be determined in an analogous way. It was found for all values of Δ that an increase of Δ and a subsequent decrease of the same magnitude results in an unchanged sensitivity of the detection unit within an uncertainty of 2%. Hence,

$$\eta(\Delta_i, \Delta_j) = \frac{1}{\eta(\Delta_j, \Delta_i)} \tag{3.17}$$

is valid.

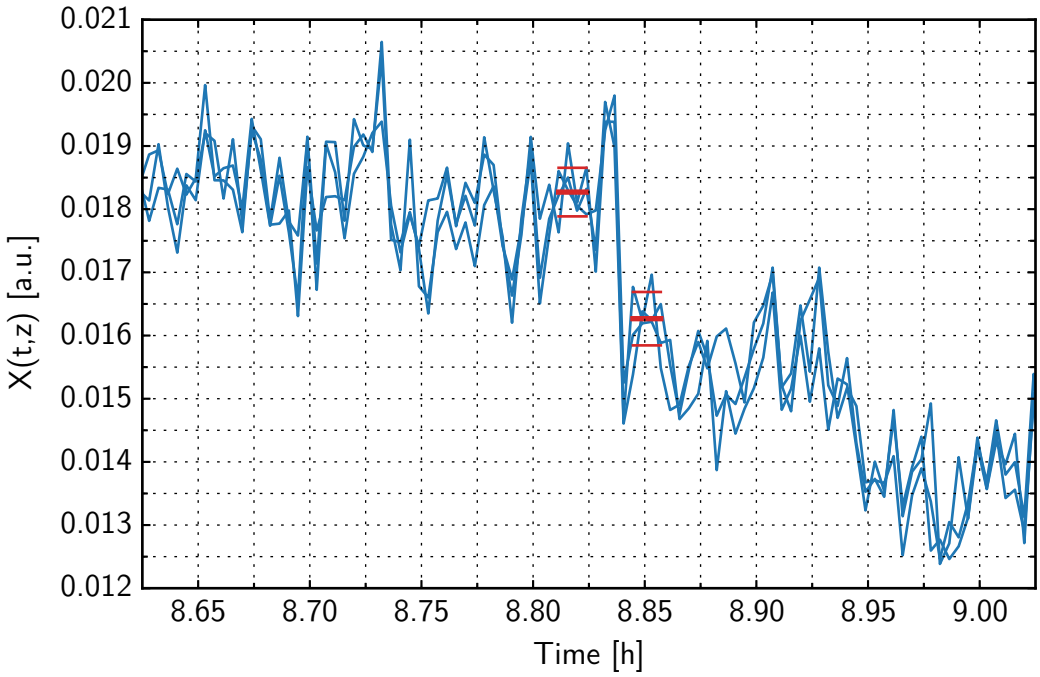

Figure 3.8: Range-corrected signals at $z = 780\,\mathrm{m}$, $z = 795\,\mathrm{m}$ and $z = 810\,\mathrm{m}$ from 08:36 UTC to 09:03 UTC (30 March 2014) in intervals of 15 s. At 08:50 UTC, Δ changes from 95 to 100.

A total number of 2963 cases was used to determine η. Mean values $\overline{\eta(\Delta_i, \Delta_j)}$ are calculated for $\Delta_j - \Delta_i = 5$ and $\Delta_j - \Delta_i = -5$, respectively, as follows:

$$\overline{\eta(\Delta_i, \Delta_j)} = \frac{1}{N+M}\left(\sum_{n=1}^{N} \eta_n(\Delta_i, \Delta_j) + \sum_{m=1}^{M} \frac{1}{\eta_m(\Delta_j, \Delta_i)}\right) \tag{3.18}$$

The corresponding relative standard error $\delta\overline{\eta(\Delta_i, \Delta_j)}$ is derived by calculating the standard deviation $s(\Delta_i, \Delta_j)$ by means of all single $\eta(\Delta_i, \Delta_j)$ and a subsequent substitution into following equation:

$$\delta\overline{\eta(\Delta_i, \Delta_j)} = \frac{s(\Delta_i, \Delta_j)}{\sqrt{N+M}} \frac{1}{\overline{\eta(\Delta_i, \Delta_j)}} \tag{3.19}$$

In Tab. 3.4 mean values of all conversion factors $\eta(\Delta_i, \Delta_j)$ are summarized for possible increases of Δ by 5. With Eq. (3.17) the conversion factors for decreasing Δ can be obtained accordingly.

The set of conversion factors can now be used to account for any change of the sensitivity of the ceilometer: if $C_L(\Delta_i)$ is known, we get $C_L(\Delta_j)$ according to Eq. (3.11).

Δ_i	Δ_j	$\overline{\eta(\Delta_i, \Delta_j)}$	$\delta\overline{\eta(\Delta_i, \Delta_j)}$	# cases
95	100	0.881	0.0043	167
100	105	0.876	0.0041	128
105	110	0.870	0.0028	249
110	115	0.870	0.0027	250
115	120	0.863	0.0028	215
120	125	0.867	0.0037	199
125	130	0.865	0.0040	167
130	135	0.857	0.0036	157
135	140	0.856	0.0037	176
140	145	0.851	0.0040	207
145	150	0.847	0.0037	240
150	155	0.833	0.0035	352
155	160	0.843	0.0051	152
160	165	0.834	0.0046	143
165	170	0.832	0.0050	146
170	175	0.821	0.0039	214

Table 3.4: Mean conversion factors $\overline{\eta(\Delta_i, \Delta_j)}$ for $\Delta_j - \Delta_i = 5$.

In case of rapid multiple changes, i. e. Δ is effectively changing by a multiple of 5, following relation is used to calculate the corresponding conversion factor:

$$\eta(\Delta_i, \Delta_j) = \prod_{k=\Delta_i}^{\Delta_j - 5} \overline{\eta(k, k+5)} \tag{3.20}$$

with corresponding relative error

$$\delta\eta(\Delta_i, \Delta_j) = \sqrt{\sum_{k=\Delta_i}^{\Delta_j - 5} \delta\overline{\eta(k, k+5)}^2}. \tag{3.21}$$

In general, $C_L(\Delta_j) < C_L(\Delta_i)$, if $\Delta_j > \Delta_i$.

High background mode

As already mentioned in section 3.1.2, the operation mode changes from normal operation mode to HB-mode if `base` = 0.5 is exceeded and a service code is set in `error_ext`. This can only happen during daytime when bright clouds are in the line of sight of the ceilometer but is possible at any Δ. The frequency of this change of

operation mode decreased from around every second day for the period June 2009–August 2012 to around every fifth day for the subsequent period. When operating in HB-mode, the APD is less sensitive although the range of values in Δ stay the same. The strong change in sensitivity in the HB-mode can be treated as an offset in Δ and consequently influences the conversion factors η which are dependent on Δ. The new operating range of the APD does not change until the settings are reset the following day at 01:00 UTC. Accompanied with a change to HB-mode, two things have to be considered: Previously determined η are not valid anymore and the change in sensitivity resulting from the change to HB-mode itself must be quantified.

According to the determination of η, an analogous procedure is applied but now only for times after a change to HB-mode has occurred. Following this procedure, conversion factors $\eta_s(\Delta_i, \Delta_j)$ can be determined in the same manner as done during normal operation. The determined conversion factors $\eta_s(\Delta_i, \Delta_j)$ are listed in Tab. 3.5. In 3357 cases the determination of $\eta_s(\Delta_i, \Delta_j)$ was possible.

Δ_i	Δ_j	$\overline{\eta_s(\Delta_i, \Delta_j)}$	$\delta\overline{\eta_s(\Delta_i, \Delta_j)}$	# cases
95	100	0.860	0.0025	175
100	105	0.855	0.0030	146
105	110	0.852	0.0028	147
110	115	0.850	0.0032	156
115	120	0.851	0.0032	150
120	125	0.841	0.0032	140
125	130	0.838	0.0036	148
130	135	0.831	0.0037	185
135	140	0.824	0.0033	248
140	145	0.817	0.0025	367
145	150	0.813	0.0023	448
150	155	0.808	0.0022	547
155	160	0.804	0.0043	192
160	165	0.798	0.0045	150
165	170	0.796	0.0058	112
170	175	0.784	0.0071	46

Table 3.5: Mean conversion factors $\overline{\eta_s(\Delta_i, \Delta_j)}$ in HB-mode for $\Delta_j - \Delta_i = 5$.

In Fig. 3.9 both sets of conversion factors are shown. The red dots represent the values of $\eta(\Delta_i, \Delta_j)$ and the green dots the values of $\eta_s(\Delta_i, \Delta_j)$. The corresponding bars illustrate the 95%-confidence interval, i. e. twice the relative error $\delta\overline{\eta(\Delta_i, \Delta_j)}$.

The lines are obtained by linear regression. It is obvious that η in HB-mode is smaller for the same change of Δ. If comparing values of η and η_s of the same size, an offset $\delta\Delta$ can be limited to $25 \leq \delta\Delta \leq 35$. However, to obtain a higher accuracy when converting a $C_L(\Delta)$ from HB-mode to a $C_L(\Delta)$ in normal operation mode, a further conversion factor must be determined individually for each day where a change of operation mode occurred, henceforward referred to as η_d.

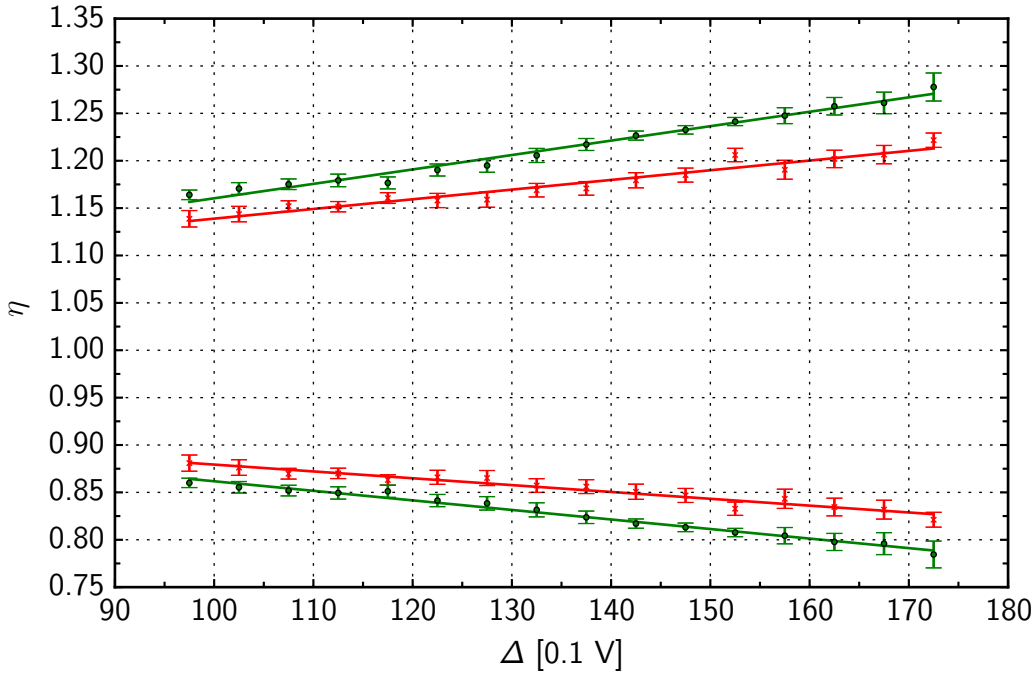

Figure 3.9: Conversion factors $\overline{\eta}$ and $\overline{\eta_s}$ as a function of Δ. Values larger than 1 denote a decrease of Δ by 5 and values less than 1 denote an increase of Δ by 5.

After applying Eqs. (3.11), (3.20) and (3.17) with a predefined fixed Δ_j to every time step of one day of measurement, i. e. to every profile of $X(t, z)$, a homogenised data set is obtained as if it was measured with the fixed Δ_j. If no change to HB-mode has occurred at this day, i. e. a measurement only under normal operation, all previousl steps in the signal disappear. However, if a switch to HB-mode could be detected at a time t_d, a change in the signal strength will remain. A correction of this change in sensitivity at time t_d in the same way as it is done for η and η_s is hindered since the signal is increasing in strength for 10 min after switching to HB-mode—time the APD needs to adapt to the large decrease in HV. Due to signal noise and changing aerosol distribution a single calculated conversion factor would lead to

large errors in the remaining measurement. This problem can be avoided by using the background signal P_{bg} at times where it can be assumed to be reasonably stable, i. e. before sunrise and after sunset. In the case of the measurement site in Munich, times before 03:00 UTC and after 20:00 UTC are appropriate. The background signal P_{bg} is saved in the variable `base` and η_d is obtained by using following relation:

$$\eta_d = \frac{\overline{P_{bg}(t_{NO})}}{P_{bg}(t_{HB})} \tag{3.22}$$

Here, $\overline{P_{bg}(t_{NO})}$ is averaged from 02:00 UTC until 1 h before sunrise and $\overline{P_{bg}(t_{HB})}$ averaged from 1 h after sunset until 23:50 UTC. The relative error $\delta\eta_d$ can be derived by

$$\delta\eta_d = \sqrt{\delta\overline{P_{bg}(t_{NO})}^2 + \delta\overline{P_{bg}(t_{HB})}^2}, \tag{3.23}$$

where $\delta\overline{P_{bg}(t_{NO})}$ and $\delta\overline{P_{bg}(t_{HB})}$ are the relative errors of the mean value of P_{bg}. The lidar constant $C_L(t_{HB})$ for the remaining measurement after switching to HB-mode at time t_d can now be converted to a $C_L(t_{NO})$ before the change by applying the factor η_d after t_d.

An example of this procedure is shown in Fig. 3.10. The background signal of the 22 April 2010 is displayed after conversion with factors η and η_s to $\Delta_j = 140$ (blue). It is already increasing before the sun rises at 04:12 UTC and decreasing when the sun goes down at 18:12 UTC. The steep increase before 02:00 UTC is discussed in the next paragraph. The remaining step between times before and after sunrise is due to the sensitivity change caused by switching to HB-mode. To calculate η_d, a 1 h-average of P_{bg} is used starting at 02:00 UTC and a 4 h average starting at 19:50 UTC, respectively (red). The conversion factor η_d is calculated to 0.452 with a relative error $\delta\eta_d$ of 0.018 which is in good agreement with the previously estimated range of $25 \leq \delta\Delta \leq 35$ when using values of Tab. 3.4 and Eq. (3.20).

01:00 UTC reset

The changing sensitivity of the APD after a change to HB-mode took place is reset the following day at 01:00 UTC. However, a reset is performed every day regardless of whether operating in normal or HB-mode. During the reset, internal checks are performed in order to choose an appropriate Δ and the APD is operating again in normal mode where conversion factors η can be used again instead of η_s. The reset

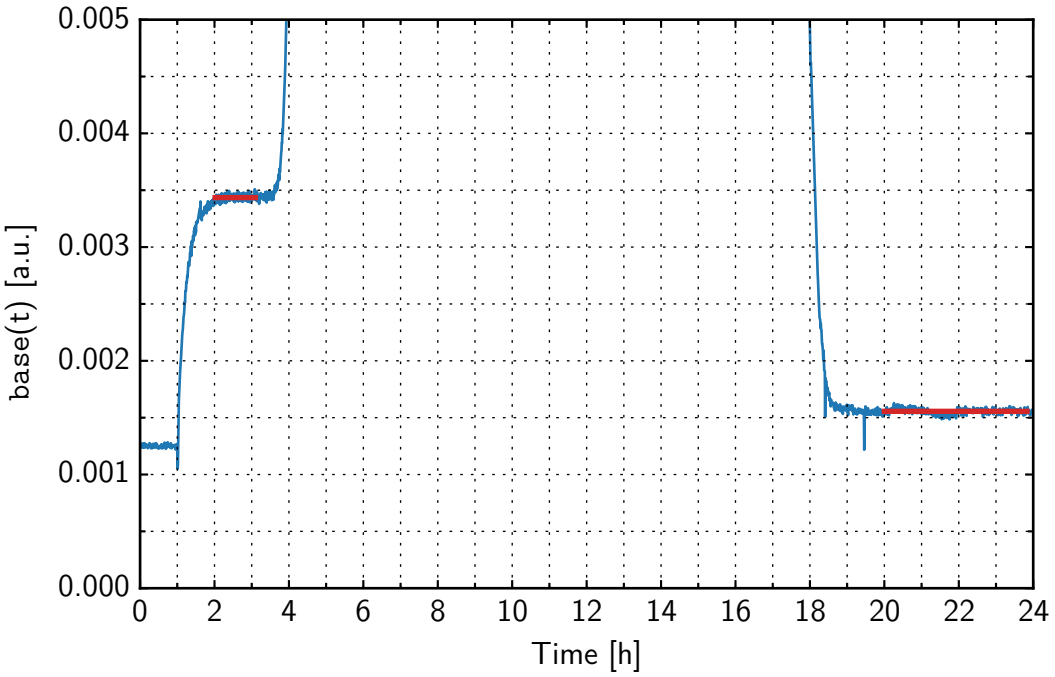

Figure 3.10: Background signal P_{bg} on 22 April 2010 (blue). Time averages before sunrise (04:12 UTC) and after sunset (18:12 UTC) (red).

is accompanied by a strong decrease in signal short after 01:00 UTC and a following increase until 02:00 UTC, when the full signal strength is reached again (cf. Figs. 3.7 and 3.10). This long-lasting increase can be considered as a kind of relaxation time of the APD inducing a continuous change of the lidar constant C_L during this time. To correct for this change another factor η_r is calculated by means of the background radiation in the variable `base` (cf. Fig. 3.10). Between 01:00 UTC and 02:00 UTC no influence of varying background radiation is expected and a reliable correction is derived by

$$\eta_r(t_i) = \frac{P_{bg}(02\,\mathrm{UTC})}{P_{bg}(t_i)} \quad \text{with } 01\,\mathrm{UTC} < t_i < 02\,\mathrm{UTC} \tag{3.24}$$

with t_j is 02:00 UTC and t_i is ranging from 01:00 UTC to 02:00 UTC. A multiplication of $\eta_r(t_i)$ with $X(t_i, z)$ for t_i between 01:00 UTC and 02:00 UTC yields a homogenised signal and the conversion for C_L in this time span, respectively:

$$C_L(t_i) = \eta_r(t_i)\, C_L(02\,\mathrm{UTC}) \quad \text{with } 01\,\mathrm{UTC} < t_i < 02\,\mathrm{UTC} \tag{3.25}$$

If using only one day of measurements, the last remaining change in signal strength between 00:00 UTC and 01:00 UTC, resulting from the changes of the APD sensitivity the day before, can be corrected in the same way as for η_d. Therefore, mean values of P_{bg} are used in Eq. (3.22) before and after 01:00 UTC, respectively.

In Fig. 3.11 the time height cross section from Fig. 3.7 is shown, but after application of the factors η and η_r. The factors η_s and η_d are not needed since no change to HB-mode occurs on this day.

As can be seen, the complicated procedure of the relative calibration is successful and leads to a homogeneous diurnal signal. All steps in the signal disappear. By applying the conversion factors, C_L can be calculated for every Δ:

$$C_L(\Delta(t)) = \eta\,\eta_s\,\eta_d\,\eta_r\,C_L^* \tag{3.26}$$

The relative calibration shown in this section is not necessary for ceilometers of the new "Nimbus"-generation since the invented LED test pulse procedure allows the tracking and quantifying of the relative changes of the sensitivity of the APD and is already applied before data is saved. However, for the large data set of 5 years of YALIS measurements, a correction is mandatory. The conversion factors found here are in good agreement with the single conversion factor $\eta = 1.238 \pm 0.037$ found in Wiegner and Geiß (2012) where only Δ-values of $120 \leq \Delta \leq 155$ were possible. The assumption of a single conversion factor in this case is not a contradiction. After applying all conversion factors, an absolute calibration can be performed to determine C_L^* at a predefined Δ. This is done in the following section.

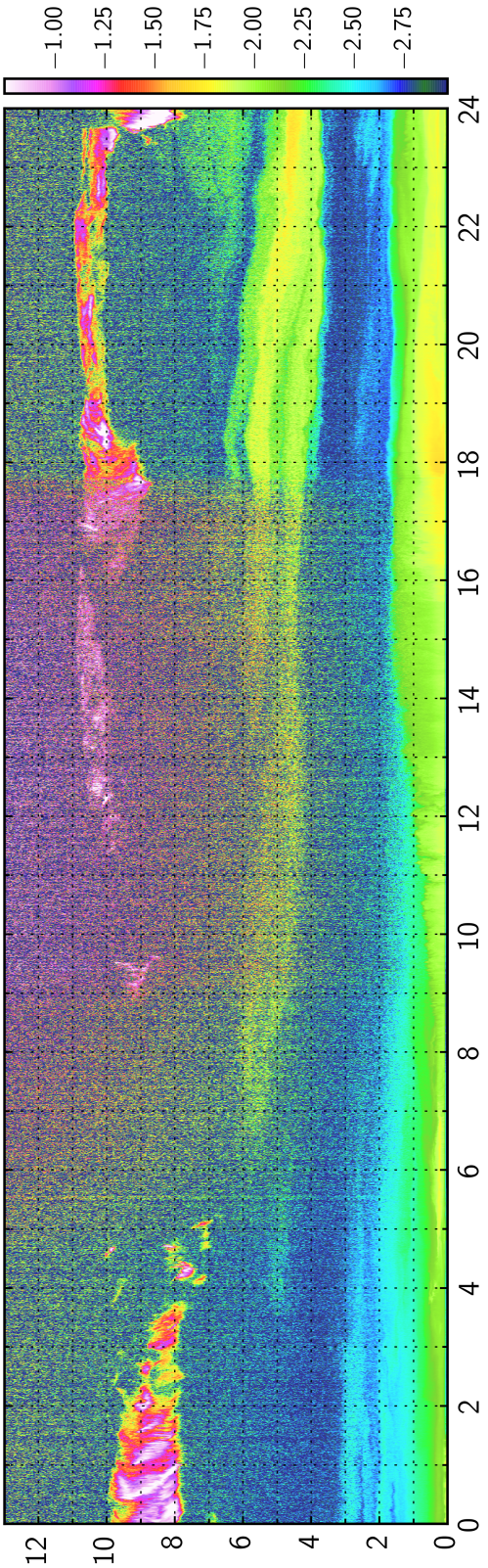

Figure 3.11: Same as Fig. 3.7, but after application of the conversion factors η as described in the text.

3.3.3 Absolute calibration

By knowing when and quantifying how the lidar constant C_L is changing as a function of Δ and thus time t, an absolute value of C_L is needed to retrieve particle backscatter coefficients β_p with Eqs. (2.19),(2.20) and (2.21). In principle, a determination of C_L can be done by rearranging Eq. (2.12) to obtain a solution for C_L as follows:

$$C_L = \frac{X(z)}{\beta_p(z) + \beta_m(z)} O(z) \exp\left\{2 \int_0^z [S_p \beta_p(z') + \alpha_m(z')]\, dz'\right\} \tag{3.27}$$

Here, the particle backscatter coefficient α_p is substituted by $\beta_p S_p$. If the aerosol optical property β_p and the lidar ratio S_p are known, C_L can be calculated.

In practice, the lower integration limit must be set to z_{ovl}, the height of complete overlap after correction. Thus, Eq. (3.27) becomes

$$C_L = \frac{X(z)}{\beta_p(z) + \beta_m(z)} \frac{1}{T_{ovl}^2} \exp\left\{2 \int_{z_{ovl}}^z [S_p \beta_p(z') + \alpha_m(z')]\, dz'\right\} \tag{3.28}$$

with

$$T_{ovl} = \exp\left\{- \int_0^{z_{ovl}} [S_p \beta_p(z') + \alpha_m(z')]\, dz'\right\} \tag{3.29}$$

The parameter T_{ovl} denotes the transmission of the incomplete overlap region. If z_{ovl} is low or the extinction in this region is sufficiently small, T_{ovl} becomes approximately 1, hence leading to a negligible error in C_L. A common procedure is to extrapolate values of α_p and β_p from z_{ovl} down to the ground. The sample calculation of the missing aerosol optical depth below z_{ovl} from section 3.2.1 is used again to demonstrate the negligibility of the resulting error in this case: The height of full overlap $z_{ovl,c}$ of YALIS is at $z_{ovl,c} = 200\,\mathrm{m}$, after applying the overlap correction from section 3.3.1. At a wavelength of 1064 nm, the molecular extinction coefficient is typically small ($\alpha_m \approx 7.2 \times 10^{-4}\mathrm{km}^{-1}\mathrm{sr}^{-1}$ for T=15°C and p=956 hPa) and can be neglected in this example calculation. Assuming that $\alpha_p(z_{ovl,c}) = 0.01\,\mathrm{km}^{-1}$ and an extrapolation down to the ground leads to an underestimation of α_p by 50%, a relative error of T_{ovl} of 0,1% is obtained. In contrast, when assuming $\alpha_p(z_{ovl,c}) = 0.1\,\mathrm{km}^{-1}$, a large value, an underestimation of α_p of 50% in the missing layer yields an uncertainty of 1% in T_{ovl}. In both cases, when α_p is low or high, a $z_{ovl,c}$ reached only at even $z_{ovl,c} = 500\,\mathrm{m}$ would lead to a relative error in T_{ovl} not larger than 0.25% or 2.5%, respectively. The uncertainty is still low when even higher regions of complete overlap

are used, provided that the layer top is still above $z_{ovl,c}$ and hence, not overseen. Consequently, the resulting error in Eq. (3.28) can be regarded as an uncritical factor for the determination of C_L.

For the derivation of β_p, which is needed in Eq. (3.28), the Klett/Fernald-algorithm including Rayleigh calibration (cf. section 2.2.2) is applied to measurements of the CHM15kx. As already mentioned, the backward approach with a reference value at the far end might strongly be affected by noise, in particular when using a wavelength in the near infrared which is less sensitive to Rayleigh scattering. For this reason, an SNR in the free troposphere is necessary, sufficiently large to identify a region free of aerosol. Since the CHM15kx has a low pulse energy, time averaging is mandatory during nighttime when background radiation is low. Daytime measurements cannot be used. To achieve high accuracy in an automated derivation of β_p, a two step procedure is used. First, measurement periods of 150 min are searched which are fulfilling prescribed requirements. These periods are then used to find an aerosol free region allowing a Rayleigh calibration.

Temporal selection process

First of all, it is checked whether a radiosonde ascent is available for the selected day in order to calculate realistic profiles of α_m and β_m by using temperature and pressure profiles in Eq. (2.15). An ascent at 00:00 UTC or at 12:00 UTC is necessary for ceilometer measurements between 00:00 UTC and sunrise. For measurements after sunset, a radiosonde can be used from 12:00 UTC or 00:00 UTC of the following day. In all cases the closest ascent time is used. If no radiosonde observations are available at that times the day is rejected.

With radiosonde data available, time periods of 150 min are examined for clouds, i. e. clouds may not occur up to a height of at least 6000 m. This is done by using a previously estimated threshold of $X(z)$ for clouds.

In the next step it is checked if the aerosol concentration between $z_{ovl,c}$ and 3 km is large enough to assure that possible shallow boundary layers within the region of incomplete overlap are not overseen. For this purpose, the integrated range-corrected signal X_{int} must exceed a threshold value, representative for a low aerosol load. X_{int} is calculated for each time step within the 150 min time period and is defined as

$$X_{int}(t) = \int_{z_{ovl}}^{3\,\mathrm{km}} X(t, z')dz'. \tag{3.30}$$

To guarantee a stable aerosol distribution for a reliable time average, a coefficient of variation c_v is calculated for each 150 min average as follows:

$$c_v = \frac{s(t)}{\overline{X_{int}(t)}} \tag{3.31}$$

where $s(t)$ is the corresponding standard deviation. Only signal averages where $c_v < 0.15$ are used.

This time period selection procedure is repeated and shifted by 5 minutes as long as the whole time average is still before sunrise or after sunset, respectively. That means, more than 1 time period per night can be found. In the next step the time averages fulfilling all conditions are searched for a reference height enabling us to apply a Rayleigh fit.

Reference height selection

Different approaches and criteria for finding an aerosol-free reference height z_{max} are available. In principle, the slope of a hypothetical Rayleigh signal $X_m(z)$ calculated from temperature and pressure profiles is compared with the slope of the measured signal $X(z)$ in a specific range between z_0 and z_1. If both slopes are the same within their uncertainties, it can be concluded that only molecular backscatter is measured and z_{max} can be selected between z_0 and z_1. This reference height can then be used to apply the Rayleigh fit. Instead of using the range-corrected signal $X(z)$, alternatively the logarithm of $X(z)$, the residual signal obtained by $((X(z)-X_m(z))$ or the logarithm of the residual signal can also be used.

In case of the measurement site in Munich, the minimum height for z_0 is set to 3 km, since a region potentially free of aerosol is expected to be above this height. Beginning at this minimum height a search range of 1.5 km length is investigated where certain criteria must be met.

At first, to assure an evaluable signal, the SNR is calculated according to Eq. (2.30) and must be larger than 2 up to height z_1. If this is valid, the relative standard error δX of $X(z)$ between z_0 and z_1 is calculated. The measured Rayleigh signal in this region is expected to be approximately normal distributed. Thus, the relative standard error is a good indication for an aerosol free region and may not be larger than 3%, i. e. $\delta X < 0.03$ must be valid.

In the next step, the slopes of the calculated Rayleigh signal (m_m) and the measured signal (m_s) are compared. The Rayleigh signal can be calculated by

$$X_m(z) = \beta_m(z)\, \exp\left\{-2 \int_0^z \alpha_m(z')\, dz'\right\}, \tag{3.32}$$

where α_m is obtained from Eq. (2.15) with temperature and pressure profiles from radiosondes launched at the DWD site at Oberschleißheim.

The slopes of the Rayleigh signal (m_m) and the measured signal (m_s) are obtained by applying a least square fit to $\log X_m(z)$ and $\log X(z)$ in the range between z_0 and z_1. The corresponding standard error of m_s is denoted by s_s. An uncertainty in m_m is not considered as it is directly calculated from Eq. (3.32). In addition, to account for small scale signal fluctuations within the reference range, the slopes of the first ($m_{s,1}$) and second ($m_{s,2}$) half of the reference range are calculated. This yields the slope $m_{s,1}$ with standard error $s_{s,1}$ between z_0 and z_{max} and the slope $m_{s,2}$ with standard error $s_{s,2}$ between z_{max} and z_1. Following relations must be valid in order to apply a Rayleigh fit:

$$\begin{aligned} |m_s - m_m| &< 1.96 s_s \\ |m_{s,1} - m_m| &< 1.96 s_{s,1} \\ |m_{s,2} - m_m| &< 1.96 s_{s,2} \end{aligned} \tag{3.33}$$

That means, the difference of the slopes must be within the uncertainty of the respective signal slope represented by a 95%-confidence interval.

Subsequently, the lidar signal $X(z)$ is normalized to $X_m(z)$ in the reference range as follows:

$$X_{norm}(z) = X(z)\, \frac{\int_{z_0}^{z_1} X(z')\, dz'}{\int_{z_0}^{z_1} X_m(z')\, dz'} \tag{3.34}$$

The value of $X_{norm}(z_{max})$ is replaced by $\beta_m(z_{max})$ and is the reference value used in the backward approach of the Klett/Fernald-algorithm.

As last criterion, the Rayleigh signal $X_m(z)$ may not be larger than the fitted lidar signal $X_{norm}(z)$ at ranges below the fitting range in consideration of the uncertainty of the lidar signal.

$$\int_{z_i-12}^{z_i+12} X_m(z')\,dz' - \int_{z_i-12}^{z_i+12} X_{norm}(z')\,dz' < 1.96\,(s_{X_{norm}}(z_i) + s_X) \tag{3.35}$$

With $z_i < z_{max}$, $s_{X_{norm}}(z_i)$ as standard error of $\overline{X_{norm}(z_i)}$ and s_X as standard error of $X(z)$ in the reference range. To account for noise, the signals are integrated over 29 range bins ($\equiv 435\,\mathrm{m}$) at every height z_i.

Now, with Eqs. (2.23) and (2.24) the β_p-profile can be retrieved and used to calculate the lidar constant C_L with Eq. (3.27), valid for the given time period.

Uncertainties

Main error sources in determining C_L by this procedure are the uncertainties in $\beta_p(z_{max})$ and S_p. Hence, to account for potential atmospheric conditions and different types of aerosol, i. e. varying S_p, a minimum and maximum lidar constant $C_{L,min}$ and $C_{L,max}$, respectively, are determined for the selected 150 min. When applying the Rayleigh fit it is still possible that particles contribute to the signal in the reference range. To account for this "overseen" aerosol, the difference between the slopes m_m and m_s is assumed to be originating from aerosol. Hence, $\beta_p(z_{max})$ in Eq. (2.24) is larger than 0. To reduce errors in the determination of C_L^*, the particle to molecular backscattering ratio R, defined as

$$R(z) = 1 + \frac{\beta_p(z)}{\beta_m(z)} \tag{3.36}$$

is used as selection criterion, i. e. only cases with $R < 2.0$ are considered.

The reference value $\beta_p(z_{max}) > 0$, henceforward referred to as β_{resi}, can be calculated from the signal slopes as follows:

$$\beta_p(z_{max}) = \frac{\alpha_p(z_{max})}{S_p} = \frac{(m_s - 1.96 s_s) - m_m}{-2S_p} = \beta_{resi} \tag{3.37}$$

Here, the minimum slope of $\ln X(z)$ in the reference range is used within the uncertainty of the 95% - confidence interval.

The second error source is the lidar ratio $S_p(z)$. As already mentioned in Sect. 2.2.1, the lidar ratio strongly depends on the origin and mixture of the aerosol. For this reason, the lidar ratio is estimated with a column value of $50 \pm 10\,\mathrm{sr}$. When using different values for S_p and setting $\beta_p(z_{max})$ to 0 or β_{resi}, it can be seen from error propagation calculations that a maximum value for $C_{L,max}$ is obtained when $S_p = 60\,\mathrm{sr}$

and $\beta_p(z_{max}) = 0$. In contrast, when $S_p = 40\,\mathrm{sr}$ and β_{resi} is used as calculated by Eq. (3.37), a minimum value $C_{L,min}$ is derived. The contribution of the uncertainty in the reference value $\beta_p(z_{max})$ to C_L is larger than the influence of the uncertainty in S_p.

The range of possible solutions of C_L can be described by $C_L \pm \Delta C_L$, where C_L is the mean of the minimum and maximum lidar constant, i. e. $C_L = (C_{L,max} + C_{L,min})/2$ and ΔC_L as systematic error is defined as $\Delta C_L = (C_{L,max} - C_{L,min})/2$. The relative error of the conversion factors η, η_s and η_d, obtained in the relative calibration in Sect. 3.3.2, must be additionally taken into account. This is done by using Gaussian error propagation including ΔC_L, $\delta\eta$, $\delta\eta_s$ and $\delta\eta_d$.

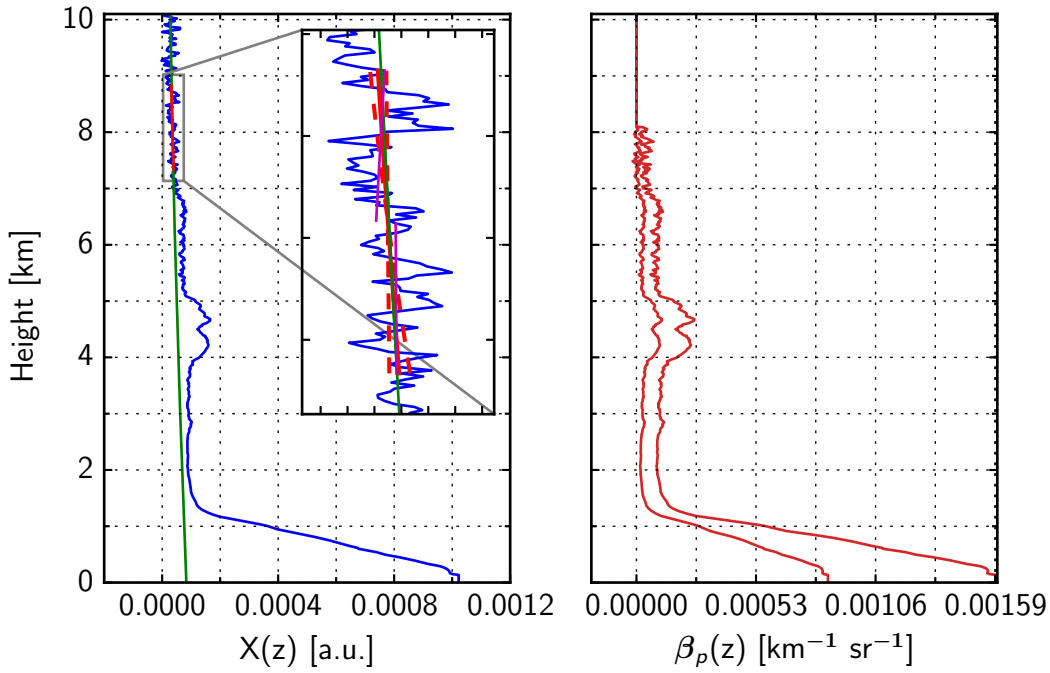

Figure 3.12: Left panel: range-corrected signal of the ceilometer (blue line) of 29 March 2012 averaged from 00:40 until 03:10 UTC and the calculated hypothetical Rayleigh signal (green line). The Rayleigh fit is applied between 7.32 km and 8.82 km (red line). The enlarged extract shows the slope of the signal (red line) and its uncertainty within a 95%-confidence interval (dashed red line). The slopes of the signal in the first and second half of the reference range are marked in magenta. Right panel: particle backscatter coefficient β_p as retrieved from ceilometer measurements: small values with a lidar ratio $S_p = 60\,\mathrm{sr}$ and reference value $\beta_p(z_{max}) = 0$; larger values with $S_p = 40\,\mathrm{sr}$ and reference value β_{resi}.

An example of this reference height selection process is given in Fig. 3.12. Shown is the range-corrected signal of YALIS (left panel) from 29 March 2012, averaged from 00:40 till 03:10 UTC. The signal is measured at $\Delta = 135$ and relative calibrated and normalized to $\Delta = 140$, resulting in an conversion error of $\delta\eta = 0.0037$. The hypothetical Rayleigh signal is plotted in green. The reference range is marked in red and ranges from $z_0 = 7.32\,\mathrm{km}$ to $z_1 = 8.82\,\mathrm{km}$ with z_{max} at 8.07 km. To illustrate the different slopes of the signals derived by least square fits, a zoom of the reference range is shown in an extra panel. The red and dashed red lines represent the fitted lines with slopes m_s and $m_s \pm 1.96 s_s$, respectively. In magenta the fitted lines for the first (slope: $m_{s,1}$) and the second (slope: $m_{s,2}$) half of the reference range are shown. It is obvious that the requirements from Eq. (3.33) are fulfilled. In the right panel the retrieved β_p-profiles are shown. By using a lidar ratio of $S_p = 60\,\mathrm{sr}$ and $\beta_p(z_{max}) = 0$ smaller values for β_p are obtained. The profile with larger values is derived by using a lidar ratio of $S_p = 60\,\mathrm{sr}$ and a reference value of $\beta_{resi} = 3.2 \cdot 10^{-5}\,\mathrm{km^{-1}sr^{-1}}$ which yields a backscatter ratio of $R = 1.9$. The corresponding lidar constants are $C_{L,min} = 12.65\,\mathrm{km^3\,sr}$ and $C_{L,max} = 22.75\,\mathrm{km^3\,sr}$ which gives a mean lidar constant with systematic error of $C_L = 17.70 \pm 5.05\,\mathrm{km^3\,sr}$. To illustrate the error contributions of the lidar ratio S_p and the value of $\beta_p(z_{max})$ to C_L, the relevant parameter combinations are shown in Tab. 3.6. The systematic error of C_L thus mainly originates from the uncertainty of $\beta_p(z_{max})$. Especially in case of the ceilometer with low pulse energy and a wavelength at 1064 nm which is less sensitive to Rayleigh scattering, the uncertainty in the reference value must be taken into account, resulting in a relative error of the determined lidar constant C_L of around 28% in this selected case.

	$S_p = 40\,\mathrm{sr}$	$S_p = 60\,\mathrm{sr}$
$\beta_p(z_{max}) = 0$	$22.01\,\mathrm{km^3\,sr}$	$22.75\,\mathrm{km^3\,sr}$
$\beta_p(z_{max}) > 0$	$12.65\,\mathrm{km^3\,sr}$	$15.48\,\mathrm{km^3\,sr}$

Table 3.6: Lidar constants C_L derived with different possible values of the lidar ratio S_p and the reference value $\beta_p(z_{max})$.

The absolute calibration was applied to 5 years of measurement data of the CHM15kx. In total, 391 days from 1900 available days fulfilled the requirements and in 3888 cases, i. e. at different times during each day, a Rayleigh calibration provided an individual lidar constant $C_L(t_i)$. In every case the range-corrected lidar signal $X(z)$ is relative

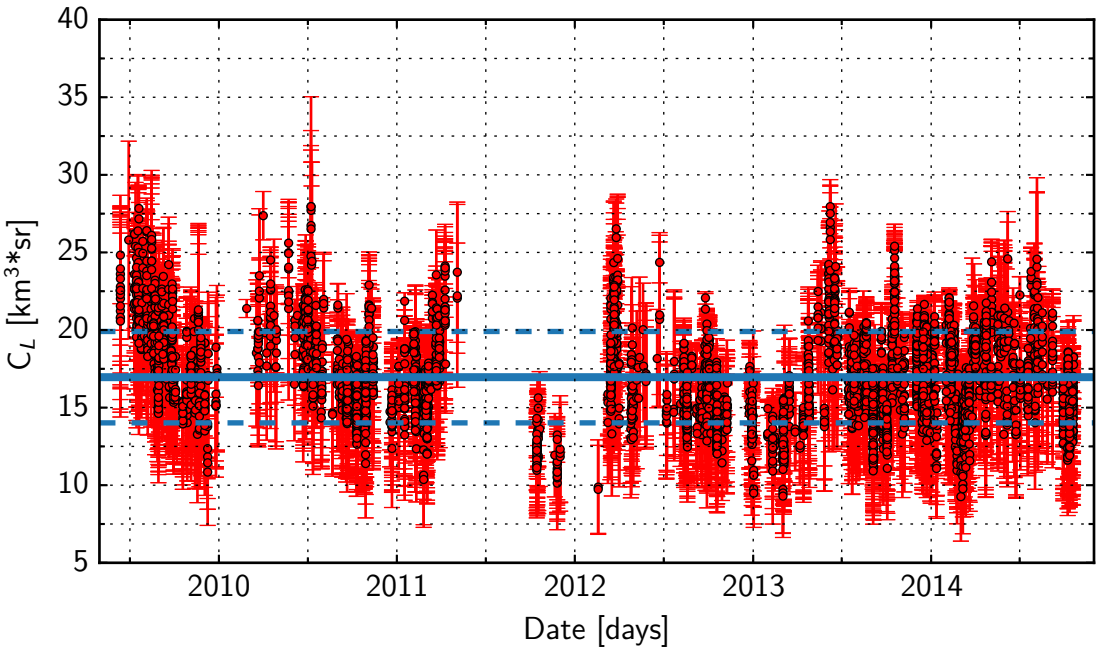

Figure 3.13: Single lidar constants C_L^* of the ceilometer CHM15kx as derived from the absolute calibration at $\Delta^* = 140$—in total 3888 cases. The mean value of the lidar constant is $C_L^* = 16.96 \pm 2.94\,\mathrm{km}^3\,\mathrm{sr}$.

calibrated to $\Delta = 140$ (cf. sec. 3.3.2) which is henceforth used as reference value Δ^* for the lidar constant C_L. In Fig. 3.13, all determined lidar constants are shown. The gap between April 2011 and February 2012 results from a failure of the detector temperature stabilization. Since the efficiency of the APD depends on the temperature, only cases are considered when the detector temperature was at normal operation temperature of 25 °C, leading to only a few $C_L(t_i)$ during this time span. The larger number of successful derivations of $C_L(t_i)$ since August 2012 can be explained by the extension of the range of possible high voltage values supplied to the APD, resulting in a better SNR. The lidar constant C_L^* of our Jenoptik ceilometer CHM15kx can be determined to $C_L^* = 16.96 \pm 2.94\,\mathrm{km}^3\,\mathrm{sr}$ at $\Delta = 140$. A long-term drift of the lidar constant during the 5 years of operation can not be observed. But, if considering only one year, seasonal fluctuations of $C_L(t_i)$ become apparent with lower values during autumn and winter and higher values during spring and summer, however, with smooth transitions. Possible reasons for this seasonal variation can be changes of the ambient temperature although the system is operating in a housing with regulated temperature. By comparing temperatures saved in the housekeeping data with corre-

sponding lidar constants, no significant dependency could be found. To account for this seasonal variation, a sinus fit could be applied to minimize the resulting error in C_L. However, as long as no technical reasons for the C_L-changes are communicated by the manufacturer, they must remain speculation. As a consequence, a linear regression is used in order to obtain an overall C_L^* from all C_L, valid for the whole year.

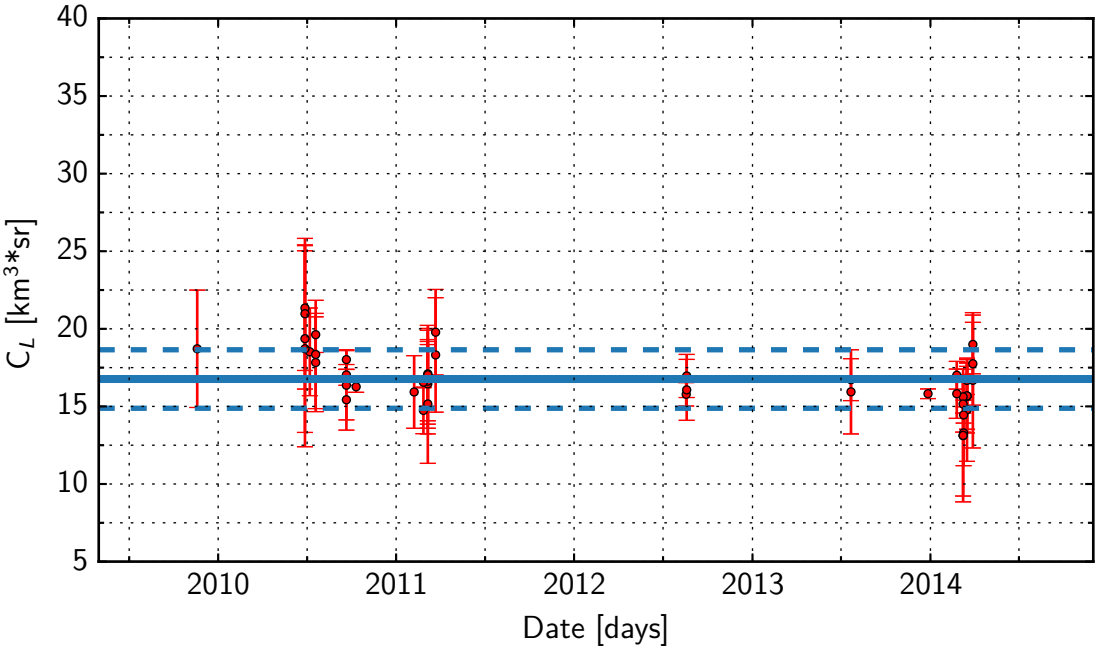

Figure 3.14: Single lidar constants C_L^* of the ceilometer CHM15kx as derived from the absolute calibration at $\Delta^* = 140$ with additional co-located sun photometer measurements—in total 47 cases. The mean value of the lidar constant is $C_L = 16.77 \pm 1.88\,\mathrm{km^3\,sr}$.

In order to reduce the error in the determined lidar constant $C_L(t_i)$ co-located sun photometer measurements of τ_p can be used to constrain S_p (Wiegner and Geiß, 2012). However, this approach requires the fulfillment of additional conditions, consequently reducing the number of days usable for determining C_L. Sun photometer measurements are only possible during day, when the SNR of the ceilometer is low compared to nighttime measurements. The main problem is that coincident measurements can hardly be combined. To overcome this problem only time periods close to sunrise or sunset are chosen to minimize the difference, i. e. ceilometer measurements before sunrise or after sunset and corresponding sun photometer measurements vice versa.

We only accept differences between both measurements smaller than 3 h, necessitating a low variability of the aerosol distribution of at least 4–5 h in sum—conditions rarely occurring. A further constraint is the use of time periods which are cloud-free in the whole atmospheric column, since sun photometer measurements of τ_p can be affected by clouds and are thus not reliable. If all conditions are met, the Rayleigh calibration is applied as described above. However, instead of using a minimum and maximum lidar ratio of S_p, respectively, the lidar ratio is iterated until τ_p, calculated from ceilometer measurements by Eq. (3.6), equals τ_p measured by the sun photometer. As already mentioned in Sect. 3.2.1 an error of ± 0.01 must be taken into account for every single measurement of τ_p of the sun photometer. However, in this application an average over 1 h with stable meteorological conditions is used, thus minimizing this systematic error. The standard deviation s_τ of the 1 h-average of τ_p is used as error estimate instead, yielding $\tau_p \pm s_\tau$. This additional error source is included in the determination of C_L by calculating a minimum lidar constant $C_{L,min}$ using β_{resi} and $\tau_p - s_\tau$. A maximum value $C_{L,max}$ is obtained by using $\beta_p(z_{max}) = 0$ and $\tau_p + s_\tau$.

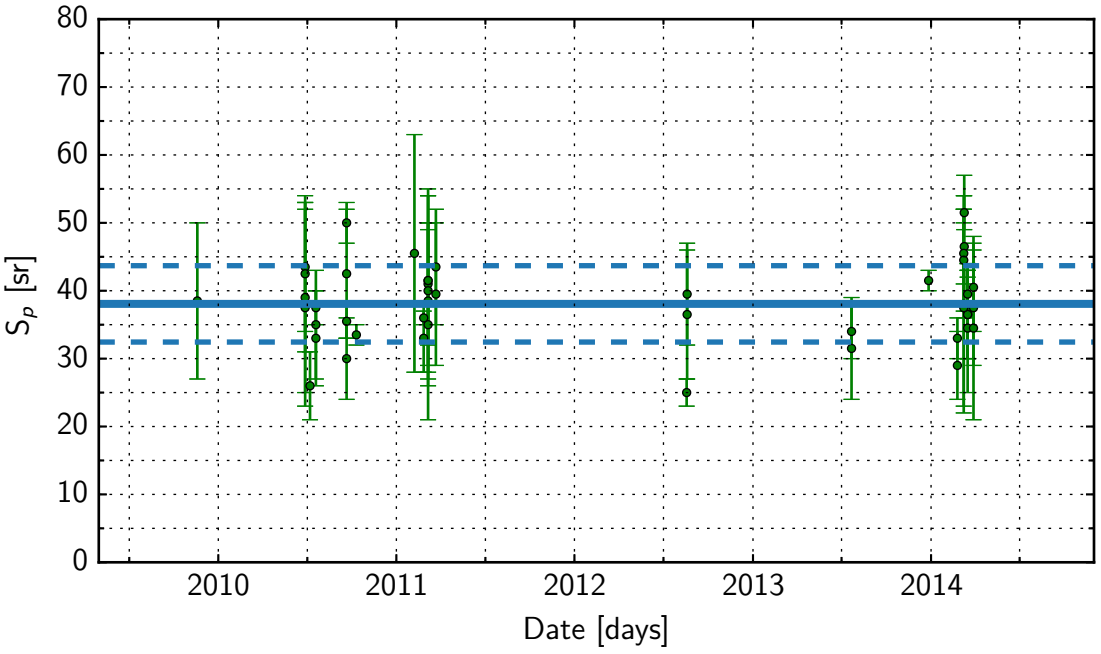

Figure 3.15: Lidar ratios S_p at 1064 nm derived from the absolute calibration with colocated sun photometer measurements in 47 cases.

In Fig. 3.14 the lidar constants $C_L(t_i)$ are displayed which are determined by the absolute calibration with co-located sun photometer measurements applied to YALIS. A

total of only 47 cases on 19 days could be found fulfilling the strict requirements. The final lidar constant C_L^* can be determined by linear regression to $C_L^* = 16.77 \pm 1.88\,\mathrm{km^3\,sr}$ at $\Delta = 140$. This results in a relative error of 11.2% which is significantly lower than the relative error of 17.3% derived by the first method. However, possible seasonal variations can not be detected since the temporal coverage is sparse, a reason for treating the higher accuracy with caution. The corresponding lidar ratios S_p that are found in the absolute calibration are shown in Fig. 3.15. The error bars are corresponding to the lidar constants $C_{L,min}$ and $C_{L,max}$, respectively, with the mean value in the center. By ranging between 25 sr and 52 sr with a mean value of 38 sr, they are in good agreement with values presented in Sect. 2.2.1. It should be stated that Fig. 3.15 is not a representative climatology of the lidar ratio over Munich but a demonstration that no unrealistic values are found in the absolute calibration procedure.

Since co-located sun photometer measurements are not always available and the advantage of higher accuracy is limited due to the concomitant lower temporal coverage of determined lidar constants, the overall lidar constant C_L^* derived by only using ceilometer measurements is used in the following for retrieving particle backscatter coefficient profiles $\beta_p(z)$.

3.4 Automated derivation of meteorological products

The continuous operation and the corresponding large data sets make it necessary to automatize data evaluation. This is in particular true if networks of instruments are available. Whereas mixing layer height, aerosol distribution in the atmosphere as well as cloud base heights with high temporal and spatial resolution can be derived from uncalibrated signals, calibration is required for quantitative products, i. e. β_p-profiles. By knowing C_L^* and application of the forward Klett/Fernald-algorithm, β_p-profiles can be derived during any weather conditions at day and night without the need of an aerosol-free region with high SNR.

3.4.1 Optical properties — β_p-profiles

Profiles of the particle backscatter coefficient $\beta_p(z)$ can be calculated with Eqs. (2.19), (2.20) and (2.21) by inserting C_L^* for C_L. In consideration of the incomplete overlap region, β_p-profiles can only be retrieved down to height $z_{ml,c}$. For heights $z < z_{ml,c}$ the β_p-profile is extrapolated down to the ground, i. e. $\beta_p(z) = \beta_p(z_{ml,c})$ for $z < z_{ml,c}$. The

uncertainty of the retrieved profiles $\beta_p(z)$ comprises the uncertainty in the lidar ratio S_p, the error of C_L^* and the error of the conversion factors $\delta\eta$, $\delta\eta_s$ and $\delta\eta_d$. The lidar ratio is estimated with $S_p = 50 \pm 10\,\mathrm{sr}$. The relative error δC_L of C_L is calculated as follows:

$$\delta C_L = \sqrt{\left(\frac{\Delta C_L^*}{C_L^*}\right)^2 + (\delta\eta)^2 + (\delta\eta_d)^2} \tag{3.38}$$

It should be noted, that $\delta\eta = \delta\eta_s$ in Eq. (3.38) if the operation mode has changed and $\delta\eta_d = 0$ if no change of operation took place. As an example, assuming a measurement with $\Delta = 110$ without a change of operation mode before, the resulting relative error of C_L would be 17.3%. However, in case a change of operation occurred, an additional uncertainty due to $\delta\eta_d$ must be considered which is approx. 3%, yielding an overall relative error δC_L of 17.6%. Hence, mainly the uncertainty of C_L^* contributes to the uncertainty δC_L.

To demonstrate the potential of the automated retrieval of particle backscatter profiles under varying and complex atmospheric conditions, the β_p-profiles from 27 March until 5 April 2014 are plotted as a time height cross section in Fig. 3.16. The fourth day of this series (30 March 2014) with a distinctive elevated aerosol layer has already been shown in Fig. 3.4. Considering the full 10 day period gives a good illustration of the importance of continuous quantitative aerosol monitoring to understand the complex evolution of the aerosol distribution. At the beginning of the episode a clear troposphere with a pronounced diurnal cycle of the mixing layer height is observed. From the fourth day, elevated aerosol layers are dominating, showing significant aerosol backscatter in the height range between 4 km and 6 km, likely caused by long range transport. In the last days from 1st until 3rd April 2016, mixing with boundary layer particles occurs.

All days are showing the inherent problem of a ceilometer having a low laser power for eye safety reasons: although averaging each profile over 10 min, the SNR is decreasing during daytime, obvious from increasing noise, and hence limiting the range where $\beta_p(z)$ can be determined. This is in particular visible on 1 April 2014 at noon when the background radiation is high due to bright cirrus clouds at a height between 6 km and 11 km. Thus, $\beta_p(z)$ cannot be determined below the clouds, although a high aerosol concentration can be expected there.

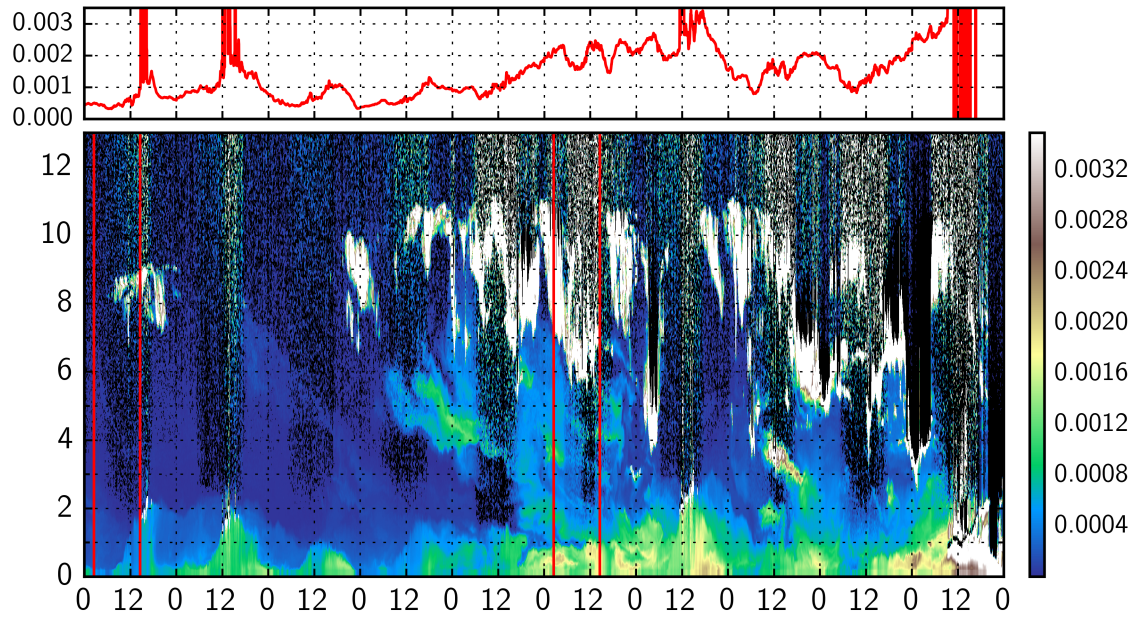

Figure 3.16: First panel: Particle backscatter coefficient at 1064 nm integrated from 0–2 km from 27 March until 5 April 2014 in [sr^{-1}]. Second panel: Corresponding time height cross section of the particle backscatter coefficient at 1064 nm (x-axis: time in UTC; y-axis: height in km; colors: β_p in $km^{-1}sr^{-1}$). Each profile is averaged over 10 min.

Starting at 27 March 2014 high cirrus clouds (white) and the well mixed boundary layer, growing from around 06:00 UTC until 17:00 UTC are visible. Profiles of β_p and their uncertainties from 02:30 UTC and 14:30 UTC (marked by red lines in Fig. 3.16, upper panel) are shown in the first and second panel of Fig 3.17, respectively. Values of $0.0002\,km^{-1}sr^{-1} < \beta_p < 0.0005\,km^{-1}sr^{-1}$ are observed in the nocturnal boundary layer at 02:30 UTC. At 14:30 UTC, homogeneous values of $\beta_p \approx 0.0006\,km^{-1}sr^{-1}$ are observed in the mixing layer. Both profiles show, that there was no elevated aerosol. On the next day, the ML-evolution can again be clearly tracked. After sunset of the third day, with increasing SNR an elevated aerosol layer can be observed at around 6–8 km decreasing to 3–4 km the next day, however, with relatively low values of β_p. On 30 March 2014 a distinct aerosol layer between 4 km and 6 km ($\beta_p \leq 0.0012\,km^{-1}sr^{-1}$ in peak) is observed. The elevated aerosol layer subsides the following five days and is mixed into the boundary layer, leading to $\beta_p \approx 0.002\,km^{-1}sr^{-1}$ in maximum—unusually high. Profiles of β_p from 1 April at 02:30 UTC and 14:30 UTC are again shown in Fig: 3.17. Up to 7 km, $0.0005\,km^{-1}sr^{-1} < \beta_p < 0.0015\,km^{-1}sr^{-1}$ is

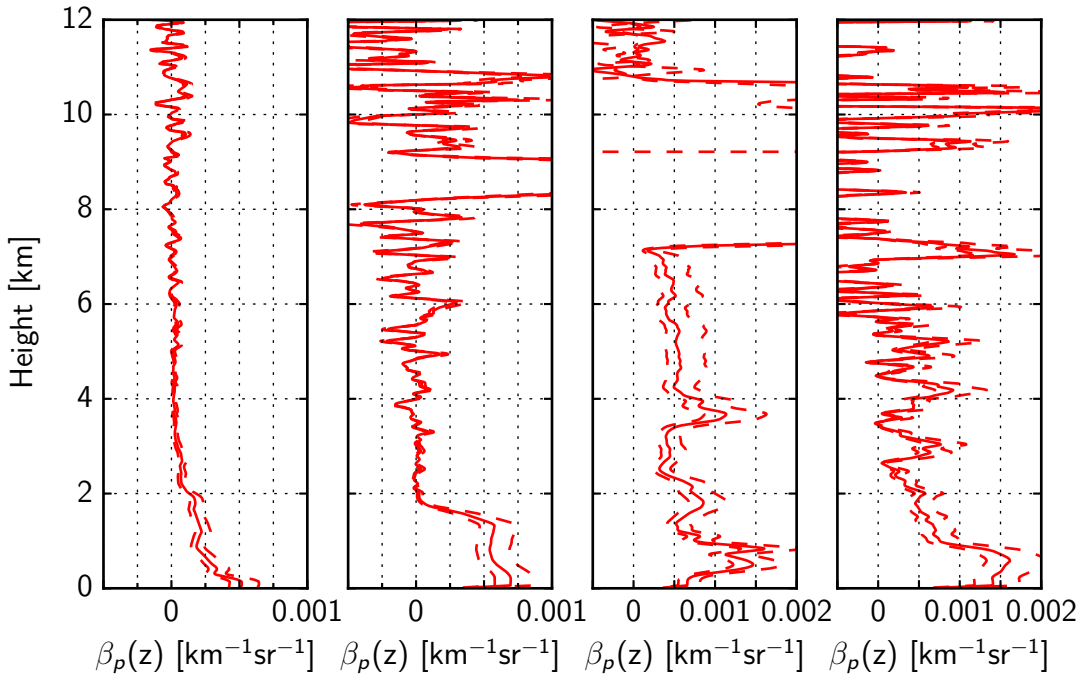

Figure 3.17: Profiles of the particle backscatter coefficient at 1064 nm derived from YALIS and averaged over 10 min. Shown are the profiles with uncertainties corresponding to red bars in Fig. 3.16. First panel: 27 March 2014 at 02:30 UTC; second panel: 27 March 2014 at 14:30 UTC; third panel: 1 April 2014 at 02:30 UTC; fourth panel: 1 April 2014 at 14:30 UTC.

observed. The strong increase of β_p within the boundary layer during the whole episode is illustrated in the first panel of Fig. 3.16 where the integrated particle backscatter coefficient $\int_0^z \beta_p(z')dz' = \beta_{int}$ is shown. Since the aerosol optical depth τ calculated according to Eq. (3.6) is affected by the large uncertainty of the lidar ratio S_p, the integrated particle backscatter coefficient is better suited and provides a measure of the turbidity with less uncertainty. Even if S_p is not constant, β_{int} can be assumed to be proportional to the aerosol optical depth τ_p as a first approximation. Here, β_p is integrated from 0–2 km, including the maximum heights of the grown mixing layer around noon each day. On the first two days, β_{int} shows a pronounced diurnal cycle with low values during night and increasing values during day. When the elevated aerosol is mixed into the boundary layer, β_{int} is strongly increasing up to $\beta_{int} \approx 0.003\,\mathrm{sr}^{-1}$. Backward trajectories calculated with Hysplit (Draxler and Rolph, 2012) for a duration of 120 hours with ending on 30 March 2014 at 4 km, 5 km and 6 km above Munich (48.15° N, 11.57° E) are shown in Fig. 3.18. They show that a possible source

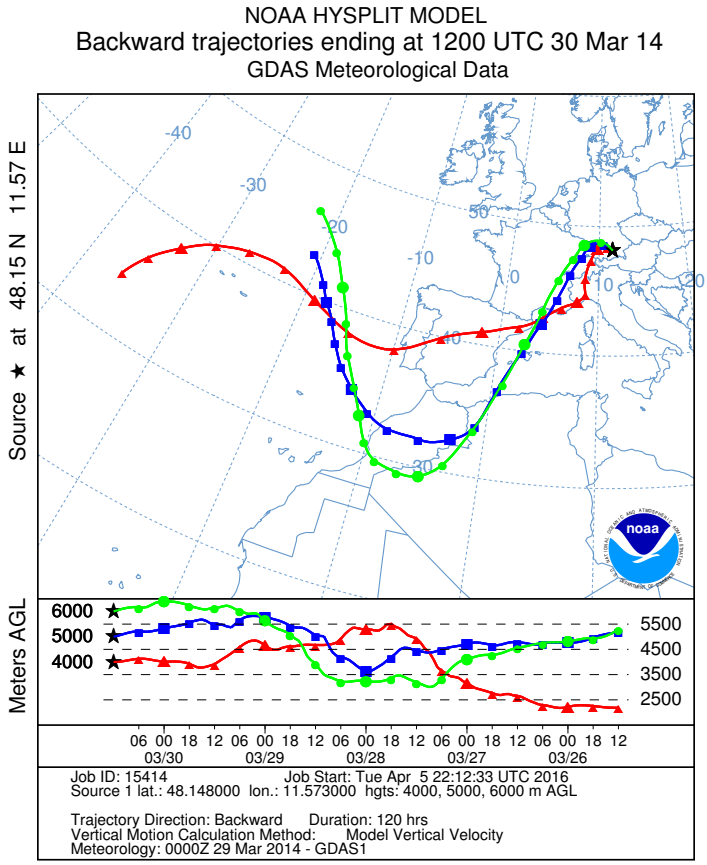

Figure 3.18: Backward trajectories calculated with Hysplit for a time period of 120 hours, ending on 30 March 2014 at 12:00 UTC over Munich (48.15° N, 11.57° E) at a height of 4 km, 5, km and 6 km, respectively.

region of this elevated aerosol can be the Sahara. Saharan dust reaching latitudes north of the Alps is not uncommon (Flentje et al., 2015).

Visual inspection of Fig. 3.16 suggests that the retrieval of the mixing layer height should be easy. In the next section, we will show that this can be done, even on the basis of uncalibrated signals.

3.4.2 Mixing layer height

Review of ML-height retrieval algorithms

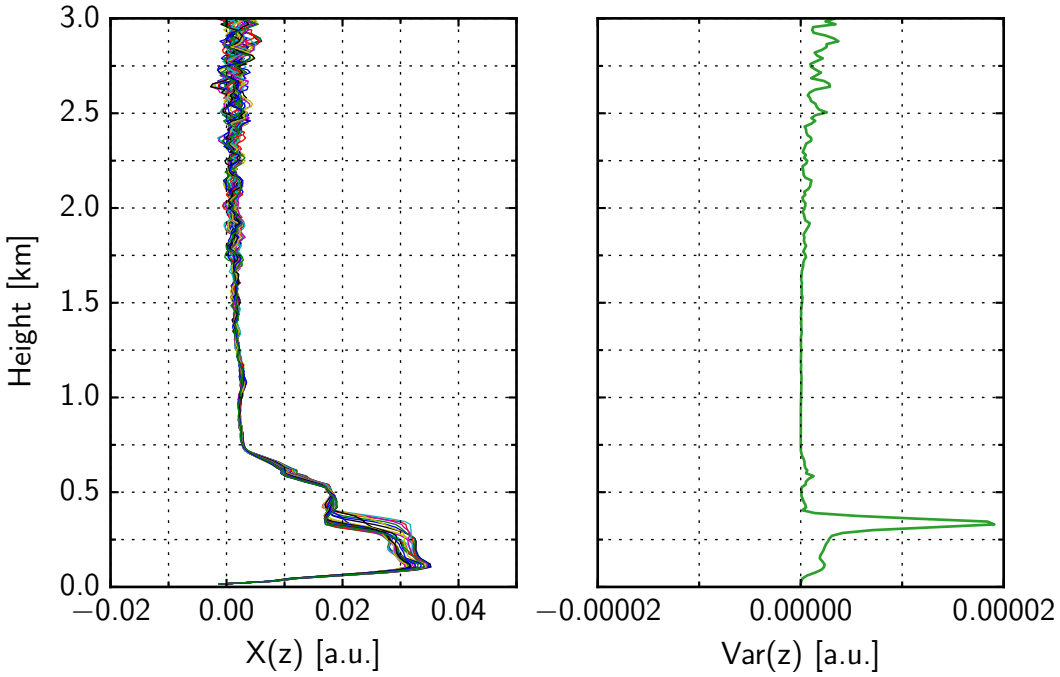

Figure 3.19: 15 minute time series of range corrected ceilometer signals of 8 April 2010 with 30 s resolution at 08:00 UTC (left) and corresponding temporal variance (right).

As described in Sect. 1, entrainment processes take place at the mixing layer top when rising turbulent thermals force a mixing of less turbulent air from the free troposphere or the residual layer into the growing mixing layer. This feature of the developing mixing layer can be used to determine the ML-top especially in case of convective boundary layers. The variance as a measure for the turbulence at height z can be calculated from a time series of $X(z)$-profiles:

$$Var(z) = \frac{1}{2N+1} \sum_{l=-N}^{N} \left(X(t_{i-l}, z) - \overline{X(t_i, z)} \right)^2 \tag{3.39}$$

Figure 3.19 shows an example of a variance calculation on 8 April 2010 by using a 15 min time series of 30 s-profiles of the range-corrected signal around 08:00 UTC. The temporal variability of the aerosol structure in the ML can be clearly seen in the left panel. Strong fluctuation is evident in the region between 125 m and 400 m

which also shows up as a peak in the variance (right panel). The maximum of the variance at 350 m can be related to the ML-top. The increasing variance beyond 1.75 km, however, results from the decreasing SNR with height and has to be taken into account to avoid false detections when applying the variance method. Use of this method under nighttime conditions, i. e. statically stable, is difficult since during nighttime, turbulence and mixing can only be induced by strong winds.

Another frequently used method for detecting ML-heights from ceilometer signals is the application of first derivatives (Endlich et al., 1979; Flamant et al., 1997; Menut et al., 1999). In general, aerosols are primarily emitted at the surface and trapped in the ML. The strong decrease of aerosol backscatter at the ML-top yields a strong negative gradient in the first derivative of the range-corrected signal $X(z)$. This can be used to determine the ML-top. However, vertical smoothing of the signal is important because this method suffers from noise.

Since ceilometer measurements provide profiles of aerosol backscatter in high temporal and spatial resolution, a 2-D method for gradient detection can be applied for ML-height determination. Haeffelin et al. (2012) used a Canny edge detector (Canny, 1986) utilizing the so-called Sobel derivation operators (Duda and Hart, 1973) for the determination of gradients in two, e. g. horizontal ($\mathbf{G}_x$) and vertical ($\mathbf{G}_y$) direction or time ($\mathbf{G}_t$) and height ($\mathbf{G}_z$). If applying the Sobel operators $\mathbf{S}_t$ and $\mathbf{S}_z$ to ceilometer data, i. e. the time-dependent range-corrected signal $X(t, z)$, the temporal and vertical gradients are obtained by a convolution as follows:

$$\mathbf{G}_t(t, z) = \mathbf{S}_t * X(t, z) \quad \text{with} \quad \mathbf{S}_t = \begin{bmatrix} 1 & 0 & -1 \\ 2 & 0 & -2 \\ 1 & 0 & -1 \end{bmatrix} \tag{3.40}$$

and

$$\mathbf{G}_z(t, z) = \mathbf{S}_z * X(t, z) \quad \text{with} \quad \mathbf{S}_z = \begin{bmatrix} 1 & 2 & 1 \\ 0 & 0 & 0 \\ -1 & -2 & -1 \end{bmatrix} \tag{3.41}$$

where the subscript t and z denote the temporal and vertical gradient, respectively. The absolute value of the gradient can be calculated with

$$\mathbf{G}(t, z) = \sqrt{(\mathbf{G}_z(t, z))^2 + (\mathbf{G}_t(t, z))^2} \tag{3.42}$$

and the direction of the gradient is derived by

$$\mathbf{\Theta}(t,z) = \text{atan2}\left(\mathbf{G}_t(t,z), \mathbf{G}_z(t,z)\right) \tag{3.43}$$

The resulting angles are in a range of $]-\pi,\pi]$ and can be mapped to $[0,2\pi]$ by adding 2π to the negative values. In Fig. 3.20 the different gradient directions are shown. The plus and minus sign are representing high and low aerosol content, respectively. If changing the edge direction by turning the arrow and the signs, the pointing direction yields the angle calculated with Eq. (3.43). An advantage of this method is the consideration of adjacent backscatter profiles and the option of deciding which gradient orientations are used for a ML-height detection.

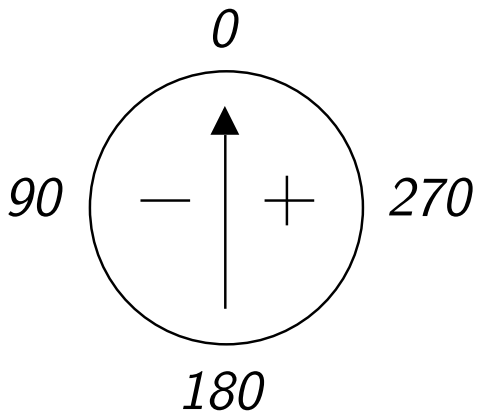

Figure 3.20: Gradient directions calculated with Sobel operators.

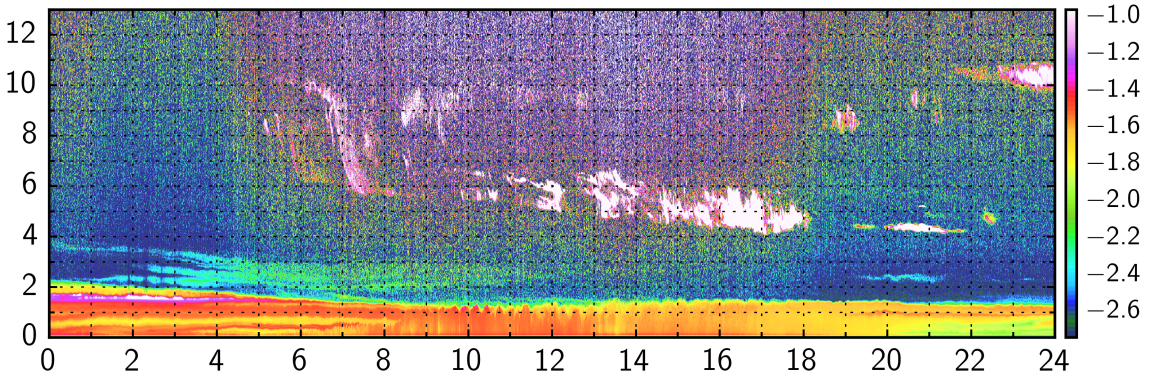

Figure 3.21: Time height cross section of the range-corrected signal (in logarithmic scale, a.u.) at 1064 nm from YALIS, 22 April 2010.

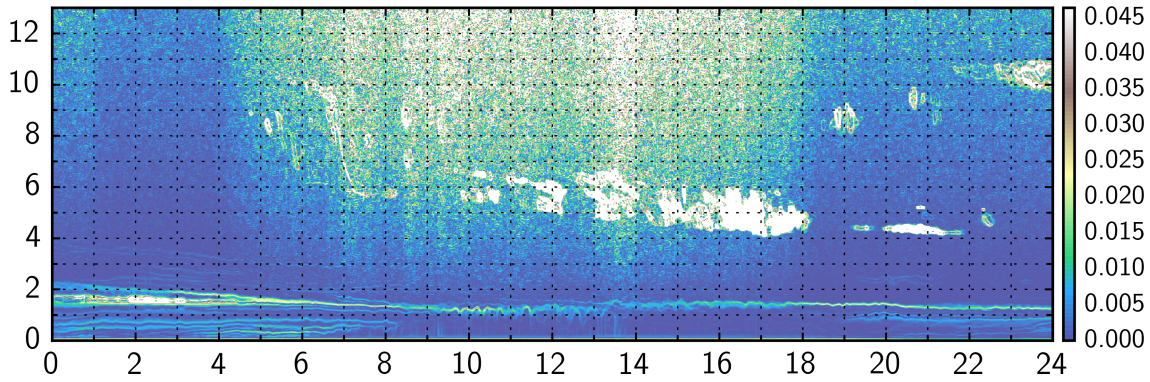

Figure 3.22: Time height cross section of the gradient magnitude **G** for 22 April 2010.

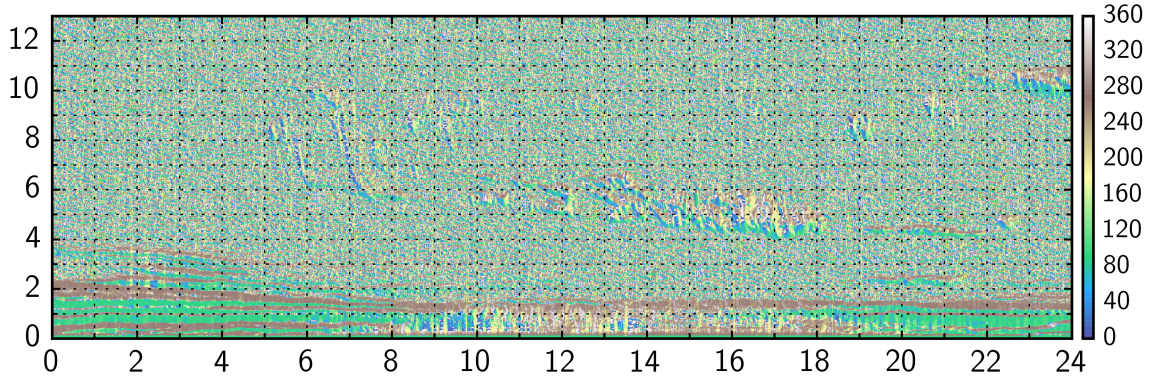

Figure 3.23: Time height cross section of the gradient directions **Θ** in degree for 22 April 2010.

An example of the 2-D method is shown in Figs. 3.22 and 3.23. The Sobel operators are applied to the range-corrected signal of the 22 April 2010 (cf. Fig. 3.21) and the magnitude **G** (Fig. 3.22) as well as the gradient direction **Θ** (Fig. 3.23) are obtained. Different aerosol layers can be located near the surface in both plots with different vertical directions before 08:00 UTC, i. e. angles of around 270° and 90°, respectively. From 08:00 UTC until 19:00 UTC only one distinct gradient with an orientation of $\approx 270°$ can be observed at around 1.3 km with weak gradients of changing directions beneath—often an indication of a turbulently mixed layer. However, signal smoothing is mandatory as this procedure is sensitive to noise as being a sort of first derivative method. An alternative approach which solves the noise problem, is the wavelet covariance transform.

The wavelet covariance transform method (WCT) gained popularity in recent years as gradient locator for signal processing purposes. First used in lidar applications by Davis et al. (1997), Cohn and Angevine (2000) and Brooks (2003), the WCT method showed the best performance compared to other retrieval techniques. In the WCT method the ceilometer profile is convolved with a wavelet. A form frequently used for the detection of mixing layer height from ceilometer backscatter profiles is the Haar wavelet:

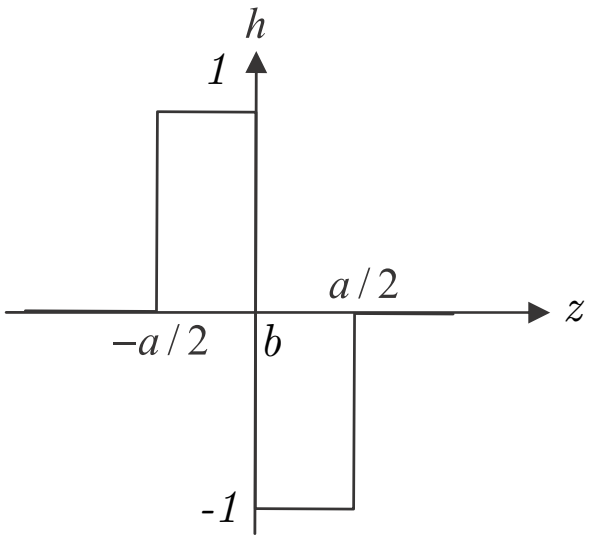

Figure 3.24: Definition of the Haar wavelet $h\left(\frac{z-b}{a}\right)$.

$$h\left(\frac{z-b}{a}\right) = \begin{cases} +1 & \text{if} \quad b - \dfrac{a}{2} \leq z \leq b \\ -1 & \text{if} \quad b \leq z \leq b + \dfrac{a}{2} \\ 0 & \text{elsewhere.} \end{cases} \tag{3.44}$$

Here z denotes the distance from the ceilometer and the wavelet is centered at the translation b. By translating the Haar wavelet with a scalable dilation a over a range of heights of a signal $f(z)$, the covariance transform $W_f(a,b)$ is obtained. In principle, it can be described by a convolution of the Haar wavelet and a function $f(z)$ which is in case of a ceilometer the range-corrected backscatter signal $X(z)$:

$$W_f(a,b) = \frac{1}{a}\int_{z_0}^{z_{max}} f(z)\, h\left(\frac{z-b}{a}\right)\, dz \tag{3.45}$$

The integration limits z_0 and z_{max} are specified by the dilation a which causes a cut-off in a distance of $a/2$ from the upper and lower end of the signal. The result of this convolution is normalized by the dilation expressed by the factor $1/a$. Because the wavelet has equal size on both sides of the translation b, a constant backscatter profile with height would result in a WCT of zero. Differences in the aerosol distribution and thus in the signal yield positive or negative values in the WCT if the signal decreases or increases with height, respectively—a characteristic, suitable for ML detection. Since the values of $X(z)$ of both sides of the translation are summed up over a height range depending on a, the WCT method also acts as a low-pass filter which is a benefit of this procedure. This must be taken into account when choosing the dilation a: small dilations allow the detection of small-scale fluctuations in $X(z)$ but are susceptible to noise whereas large dilations are better for detecting large-scale differences with a better noise suppression.

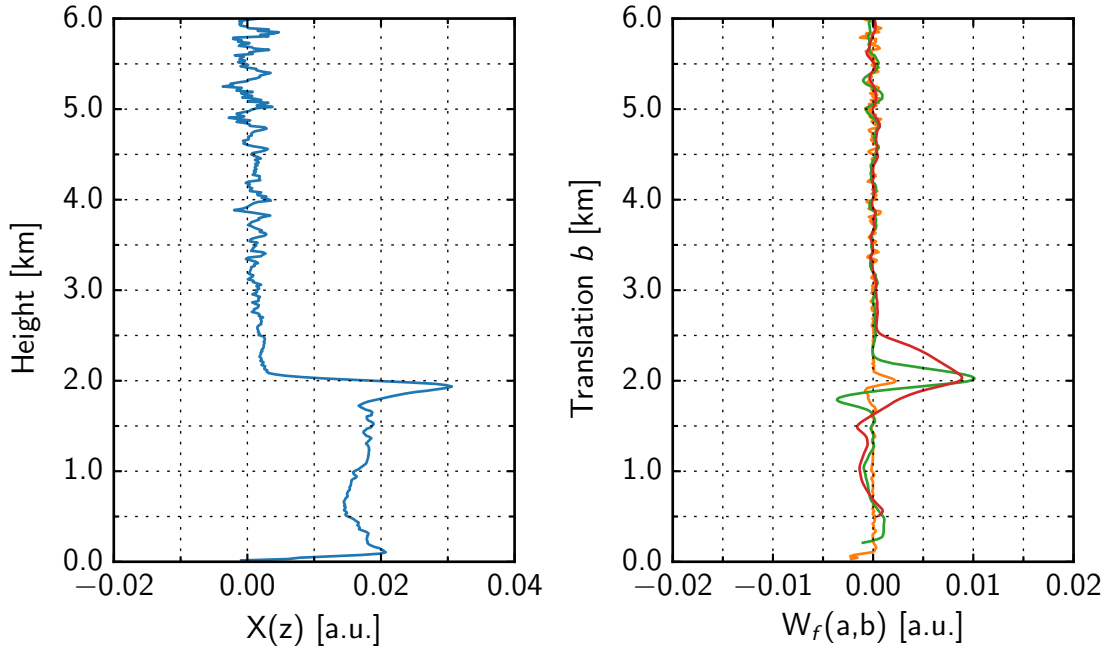

Figure 3.25: Range corrected ceilometer signal $X(z)$ of 28 April 2010 (left) with corresponding covariance transform W_f for dilations of 30 m (orange), 390 m (green) and 990 m (red).

An example of the WCT method is shown in Fig. 3.25. In the range-corrected signal (left) the ML is apparent up to 2 km where a strong decrease in the signal indicates the ML-top. Above 2 km, the low signal is an evidence for the aerosol-free troposphere,

however, dominated by noise. The steep decrease in the first 200 m is caused by the incomplete overlap. The corresponding covariance transform W_f is shown in the right panel with a dilation a of 30 m (orange), 390 m (green) and 990 m (red), respectively. It is obvious that depending on the dilation only results are obtained for a height starting at $a/2$—important when considering low boundary layers. In practice, the lower integration limit should be calculated from $z_{ovl,min} + a/2$ upwards to avoid artificial layers induced by the incomplete overlap. The noise reduction of the signal by the low-pass filter characteristic of the WCT becomes apparent by means of a smoother W_f with increasing dilation at higher altitudes. In all three cases the ML top can be related to the maximum in W_f at around 2 km, however, less pronounced when using a small dilation of 30 m.

The WCT method cannot be applied to 2-D-fields as it is implicitly done when using Sobel operators. A different approach of the WCT method with equivalent result is shown by Comerón et al. (2013). It can be demonstrated that using a Haar wavelet is equivalent to the gradient method applied to a spatially low-pass filtered range-corrected ceilometer signal. Equation (3.44) can be expressed by

$$h\left(\frac{z-b}{a}\right) = -\frac{d}{dz}\,\Lambda\left(\frac{z-b}{a}\right) \tag{3.46}$$

with a low-pass filter $\Lambda\left(\frac{z-b}{a}\right)$ defined as

$$\Lambda\left(\frac{z-b}{a}\right) = \begin{cases} \dfrac{a}{2} - z + b & \text{if} \quad b - \dfrac{a}{2} \le z \le b \\ \dfrac{a}{2} + z - b & \text{if} \quad b \le z \le b + \dfrac{a}{2} \\ 0 & \text{elsewhere.} \end{cases} \tag{3.47}$$

.

In practice, the WCT method can be considered as a particular form of the first derivative method and $W_f(a,b)$ is calculated as follows:

$$W_f(a,b) = -\frac{d}{dz}\,\frac{1}{a}\int_{z_0}^{z_{max}} f(z)\,\Lambda\left(\frac{z-b}{a}\right)\,dz, \tag{3.48}$$

with $f(z) = X(z)$ in case of the ceilometer.

An illustration of the equivalence of both calculation methods of $W_f(a,b)$, i. e. of Eq. (3.45) and Eq. (3.48), is presented in Fig. 3.26. A range-corrected signal of 28 April 2010 (green) is low-pass-filtered with a triangle filter of $a = 330$ m width (orange). The

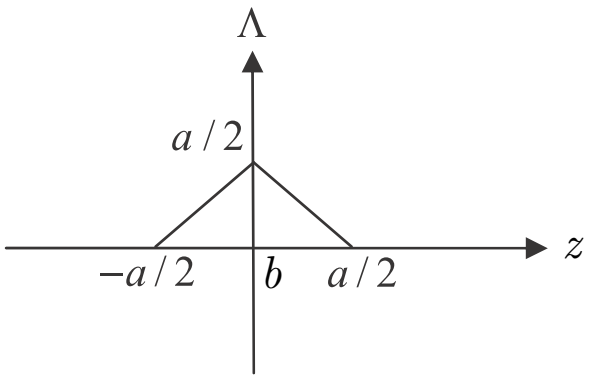

Figure 3.26: Definiton of the low-pass filter $\Lambda\left(\frac{z-b}{a}\right)$.

reverse sign first derivative of the filtered range-corrected signal and thus $W_f(a,b)$ is shown in red. The corresponding WCT is depicted in the right panel. Peaks in both results are coinciding which confirms the identity of both methods.

COBOLT - Algorithm description

Since the planetary boundary layer evolution is assumed to be a continuous process, no jumps in the temporal development of the ML top height should occur, except in cases of strong precipitation. This behavior is the basic concept of the algorithm developed in this thesis, which is the combination of ceilometer profiles of adjacent time steps by applying a time-height tracking method. That means, not only single profiles are considered as it is done by previously mentioned methods (cf. Sect. 1). Here, the range-corrected signal or particle backscatter coefficient profiles of a whole day are considered as one two-dimensional function of time and height and different image processing procedures as well as meteorological principles are incorporated.

The COBOLT (Continuous Boundary Layer Tracing) algorithm is based on a two-stage process:

1. Data preprocessing including averaging, noise filtering and edge detection by a combination of different ML detection methods weighted with the solar zenith angle and definition of a parameter H.

2. Application of a sun position-dependent time-height tracking technique to the traceable parameter H derived in step one.

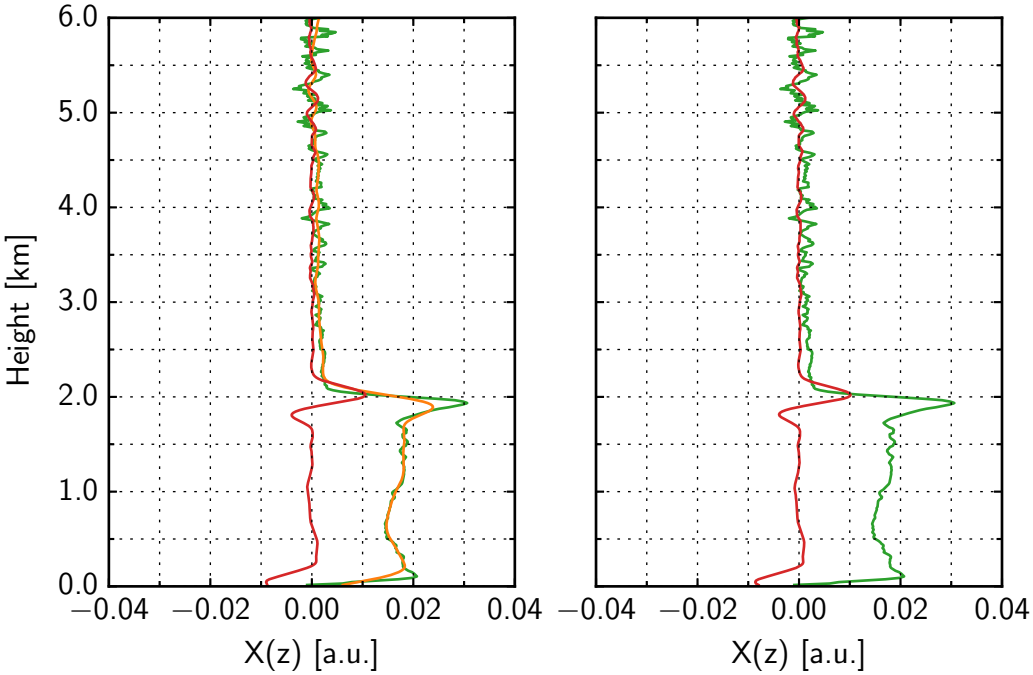

Figure 3.27: Left: Range-corrected signal $X(z)$ of 28 April 2010 (green), after application of a low-pass filter with $a = 330\,\mathrm{m}$ (orange) and differentiated with respect to z (red). Right: green, same as left and corresponding WCT with $a = 330\,\mathrm{m}$ (red).

Data processing—COBOLT hybrid parameter

The data preprocessing is done to retrieve a quantity which provides traceable edges—suitable to apply a tracking algorithm. It is a hybrid process combining different methods, e. g. first derivatives, second derivatives, temporal variance of the ceilometer signal and wavelet covariance transform. Each method alone works quite well for appropriate weather or aerosol conditions but can fail or yield unrealistic results (e. g. sudden jumps in MLH) if these conditions are not met.

A combination of these methods in the COBOLT algorithm as a "best of all methods"-approach to define the traceable hybrid parameter $H(t, z)$ is illustrated in Fig. 3.28. A mathematical formulation of $H(t, z)$ is as follows:

$$H(t,z) = \frac{\epsilon_g\, M_g(t,z)}{99^{\mathrm{th}}(\epsilon_g\, M_g(t,z))} + \frac{\epsilon_v\, M_v(t,z)}{99^{\mathrm{th}}(\epsilon_v\, M_v(t,z))} \tag{3.49}$$

The determination of $M_g(t,z)$ and $M_v(t,z)$ and its meaning are shown in the following. The weighting factors ϵ_g and ϵ_v are determined empirically and the summation of both quantities is done after normalization with their 99th-percentile.

To implement the advantageous low-pass characteristic of the WCT method, a triangle filter of height-dependent width is used. To account for the decreasing SNR with height, the filter-width a is defined for three regions: $a = 120\,\mathrm{m}$ for $0\,\mathrm{m} \leq z < 1500\,\mathrm{m}$, $a = 330\,\mathrm{m}$ for $1500\,\mathrm{m} \leq z \leq 3000\,\mathrm{m}$ and $a = 570\,\mathrm{m}$ for $z > 3000\,\mathrm{m}$. Heights with $SNR < 1$ are excluded. The low-pass filter is applied to 6 min averages of $X(t,z)$-profiles; the result is defined as $X_\Lambda(t,z)$. On this basis, according to Eqs. (3.42),(3.43),(3.40) and (3.41) the Sobel operators yield the magnitude $M_g(t,z)$ and the direction $\mathbf{\Theta}(t,z)$ of the gradients. For a proper weighting of ML-tops, gradients with angles $\mathbf{\Theta}(t,z)$ that are unlikely for ML-tops in a meteorological sense are reduced in magnitude by a factor ϵ_g:

$$\epsilon_g(t,z) = \begin{cases} 0.1 & \text{if} \quad 0° \leq \mathbf{\Theta} \leq 5° \\ 0.1 & \text{if} \quad 175° \leq \mathbf{\Theta} \leq 360° \\ 1 & \text{elsewhere} \end{cases} \tag{3.50}$$

.

In the majority of cases, this procedure emphasizes the gradients with the highest probability of being a ML-top. However, a remaining residual layer with strong aerosol content can inverse the gradient of the ML-top and leads to wrong ML detections.

For this reason, the variance method is included since a ML-top with an inverse gradient has a high temporal variability as well. Furthermore, this holds for a developing turbulent ML in the morning—a way do distinguish between ML-top and stratified nocturnal aerosol layers in the RL. The variance is therefore calculated from 10 min averaged profiles of $X_\Lambda(t,z)$ at time t_i and height z_j on basis of 21 time steps and 3 range bins as follows:

$$M_v(t,z) = Var(t,z) = \frac{1}{(2N+1)(2M+1)} \sum_{k=-N}^{N} \sum_{l=-M}^{M} \left(X_\Lambda(t_{i-k}, z_{j-l}) - \overline{X_\Lambda(t_i, z_j)} \right)^2 \tag{3.51}$$

For a compensation of the decreasing SNR with height, a weighting factor ϵ_v is used to increase $M_v(t,z)$ at low-levels by an amount proportional to their distance below 3000 m. Heights with $SNR < 5$ are excluded for $M_v(t,z)$. In addition, variances in

regions with gradient directions of $-5° \leq \mathbf{\Theta} \leq 5°$ and $175° \leq \mathbf{\Theta} \leq 185°$ are neglected for emphasizing only potential ML-tops.

$$\epsilon_v(t,z) = \begin{cases} 0 & \text{if} \quad -5° \leq \mathbf{\Theta} \leq 5° \\ 0 & \text{if} \quad 175° \leq \mathbf{\Theta} \leq 185° \\ 1 - \dfrac{z}{3000\,\mathrm{m}} & \text{elsewhere} \end{cases} \tag{3.52}$$

.

The hybrid parameter $H(t,z)$ is the sum of $\epsilon_g\, M_g(t,z)$ and $\epsilon_v\, M_v(t,z)$ after normalizing each with its 99th percentile (see Eq. (3.49)).

For an application of a time-height tracking procedure, conducted in the second step of this algorithm, a traceable parameter is needed. After testing and empirical adjustment of different combinations of filters, the application of a maximum filter to H yields the best results. The direction of the maximum filter is chosen in such a way that different steps in the ML evolution, i. e. growing and decaying phases, are highlighted. Since the ML development is strongly dependent on the solar zenith angle, the maximum filter is defined for three parts of the day according to Stull (1988 // 1997):

Until two hours after local noon, a growing ML is expected, thus:

$$\begin{aligned} H(t_{-3},z_{-3}) = H(t_{-2},z_{-2}) = H(t_{-1},z_{-1}) = H(t_0,z_0) = \\ = H(t_{+1},z_{+1}) = H(t_{+2},z_{+2}) = H(t_{+3},z_{+3}) = \\ max(H(t_{-3},z_{-3}), H(t_{-2},z_{-2}), H(t_{-1},z_{-1}), H(t_0,z_0), H(t_{+1},z_{+1}), H(t_{+2},z_{+2}), H(t_{+3},z_{+3})) \end{aligned} \tag{3.53}$$

Afterwards, until 1 h before sunset, the ML height usually remains constant:

$$\begin{aligned} H(t_{-3},z_0) = H(t_{-2},z_0) = H(t_{-1},z_0) = H(t_0,z_0) = \\ = H(t_{+1},z_0) = H(t_{+2},z_0) = H(t_{+3},z_0) = \\ max(H(t_{-3},z_0), H(t_{-2},z_0), H(t_{-1},z_0), H(t_0,z_0), H(t_{+1},z_0), H(t_{+2},z_0), H(t_{+3},z_0)) \end{aligned} \tag{3.54}$$

For the rest of the day, the ML decays:

$$H(t_{-3}, z_{+1}) = H(t_{-2}, z_{+1}) = H(t_{-1}, z_{+1}) = H(t_0, z_0) =$$
$$= H(t_{+1}, z_{-1}) = H(t_{+2}, z_{-1}) = H(t_{+3}, z_{-1}) =$$
$$max(H(t_{-3}, z_{+1}), H(t_{-2}, z_{+1}), H(t_{-1}, z_{+1}), H(t_0, z_0), H(t_{+1}, z_{-1}), H(t_{+2}, z_{-1}), X(t_{+3}, z_{-1})) \tag{3.55}$$

The maximum filter is only applied to gradient directions of $5° \leq \mathbf{\Theta} \leq 175°$. Now, by closing gaps in the hybrid parameter H, it can be used to trace the ML-top for any time step in the time-height tracking part of the COBOLT algorithm.

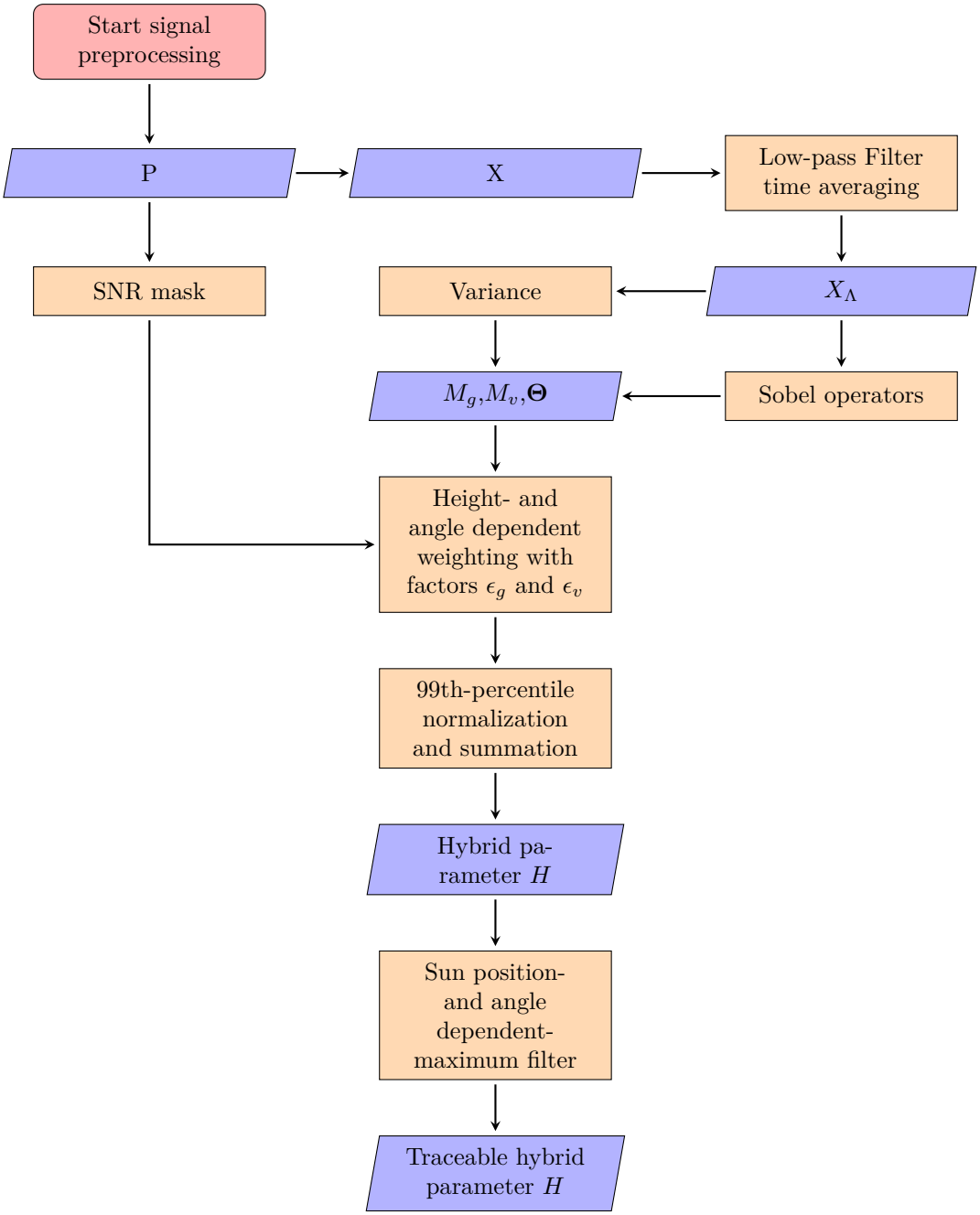

Figure 3.28: COBOLT algorithm—signal preparation (see text for details).

Time-height tracking

The second step of COBOLT is based on a time-height tracking procedure, i. e. the ML-height z_{ml} at time t_i is determined using z_{ml} of the previous time step t_{i-1} as first guess. A window with variable width in height is moved from one time step to another. The maximum value of H in this window is used as z_{ml} for this time step. It defines the new center of the search window for the next time step—a way to obtain continuous ML-heights without large steps.

For the initialization of the time-height tracking procedure a starting time t_{ini} and starting height z_{ini} is necessary. For this purpose, a time is selected when the growing ML can be reliably distinguished from stratified aerosol layers in the RL. The strong turbulence of the ML, especially in the morning hours in the absence of low clouds, provides this distinction. Thus, to determine a time with an already growing but still shallow ML, the duration of sunshine is estimated. Starting from sunrise, every time step where no clouds are existent up to 1700 m and thus not preventing direct radiation to heat the surface, are counted as sunshine. After 2.5 h–3.5 h from sunrise, the ML is assumed to be existent as shown by Boers et al. (1984), Beyrich (1995), Angevine et al. (2001) and Wildmann et al. (2015). In consideration of the minimum measurement range $z_{ovl,min}$ as defined in Sect. 3.3.1, a sum of 3 h of sunrise is chosen for YALIS. The time when this threshold is reached yields the initialization time t_{ini}. In case that this sum is not reached until 10:00 UTC due to clouds or rain, t_{ini} is set to 3.5 hours after sunrise. At time t_{ini}, the lowest local maximum of the variance M_v is determined at each time step within a time span of 10 min around t_{ini}—the variance is best representing the strong turbulence in the ML. The mean of all local maxima yields the starting height z_{ini}.

Beginning at t_{ini}, the search window is moved forward and backward in time limited to a maximum height dependent on the solar zenith angle, i. e. until 30 min after sunrise up to 500 m and afterwards up to 3800 m. The search window length is dependent on time t, i. e. its width in z-direction is largest between t_{ini} and 2 h after noon, then decreases until 2 h before sunset.

Since clouds are typically not forming in but at the top of a ML, it is first checked if a cloud is located between the upper boundary of the search window and the surface, i. e. if in any height $\frac{X_\Lambda(z_i)}{X_\Lambda(z_{i+1})} > 10$. Thus, z_{ml} is set to the strongest signal decrease above the strongest signal inside the cloud, induced by the saturation of the detector due to strong backscattering from water droplets. This assumption for the ML-height

in case of low boundary layer clouds yields good results when comparing with z_{ml} in time steps before the cloud appears. If no cloud is found in this region, the maximum of H inside the search window is chosen as z_{ml}.

Subsequent to the determination of z_{ml} for each time step, one to three validity checks are performed in one or optional three parts. First of all, it is verified that no significant aerosol layer is present below z_{ml}. "Significant" means, if in any height $\frac{X_\Lambda(z_i)}{X_\Lambda(z_{i+1})} > 1.5$, which is found to be a value usually not appearing in a well mixed boundary layer. In this case, the lowest height where this is true yields z_{ml} for this time step. If no significant layer is found, the previously determined ML-height is considered as correct and remains unchanged. In cases when threshold values for the range-corrected ceilometer signal were determined to define a low (few aerosol) and high (rain) signal, respectively, or a quantitative parameter (e. g. β_p) is used, two additional quality checks can be applied. If the mean value $\overline{X}$ below z_{ml} is smaller than a threshold, representing a reasonably aerosol-free regime, it can be assumed that the detected z_{ml} is incorrect and a very shallow ML is existent which is below $z_{ovl,min}$, i. e. $z_{ml} < z_{ovl,min}$. In this case, $z_{ml} = z_{ovl,min}$. In contrast, if $\overline{X}$ is larger than a threshold assumed for rain, z_{ml} is kept constant in the following time steps until this condition no longer holds. This is done in order to avoid steps in z_{ml} if only short precipitation occurs but usually no significant changes in the ML-height are expected.

This time-height tracking procedure yields continuous ML-heights for clearly defined gradients but is sensible to the *a priori* defined search window length as well as to sunshine duration for the determination of t_{ini} if no distinct gradients are existent. Hence, a multi-member approach is introduced. The time-height tracking is performed by combining variable parameters in different configurations, resulting in a total number of 40 members. That means, sunshine durations for determining t_{ini} are chosen between 100 min and 190 min in steps of equal distance, search window lengths are ranging from 180 m to 360 m between t_{ini} and 2 h after noon, from 75 m to 270 m until 2 h before sunset and from 45 m to 180 m for the rest of the day. However, for all members a window length of 120 m is set for times before 3 h after sunrise to account for the lower growth rates when the sun is still low. With computing all 40 members, a set of possible diurnal cycles of z_{ml} is obtained. To select the most likely ML-height from all members, a function C is calculated as follows:

$$C(z_{ml}) = \frac{\sum_{i=0}^{N} H(t_i, z_{ml})}{\sum_{i=0}^{N-1} \sqrt{(t_{i+1} - t_i)^2 + (z_{ml}(t_{i+1}) - z_{ml}(t_i))^2}} \tag{3.56}$$

The reason for this definition of $C(z_{ml})$ is that large steps in the ML would increase the denominator and a wrong ML, most likely having weaker gradients, would decrease the numerator—both leading to a small value in $C(z_{ml})$. Thus, the member with maximum $C(z_{ml})$ yields the correct ML-height.

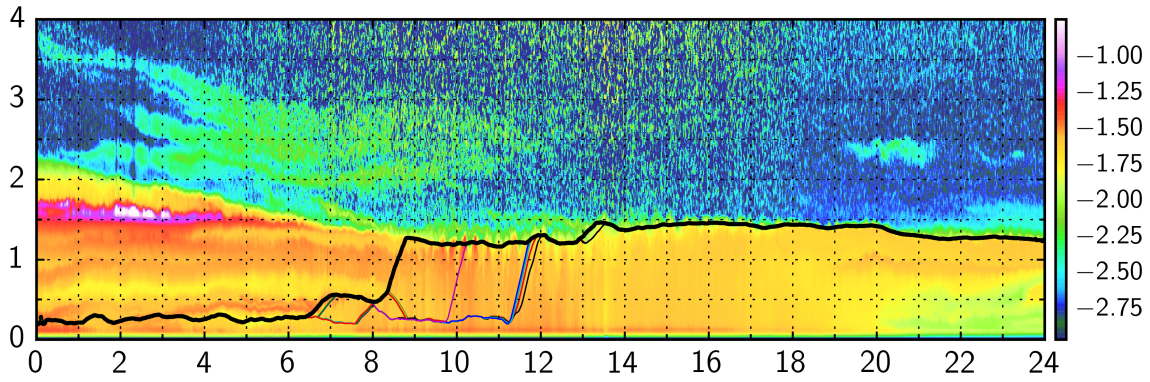

Figure 3.29: Time height cross section of the range-corrected signal (in logarithmic scale, a.u.) measured by YALIS, 22 April 2010. The color lines are representing the different members detected by the COBOLT algorithm. The thick black line marks the ML-height with maximum $C(z_{ml})$. Its start point is in 465 m at 07:50 UTC.

An example of the time-height tracking method is shown in Fig. 3.29. The measurements of the range-corrected signal from YALIS on 22 April 2010 are selected. Sunrise is at 04:12 UTC and sunset at 18:12 UTC. The green to red colors mark regions with high aerosol load, whereas light to dark blue colors are representing low aerosol concentration. The different ML-height members computed by COBOLT are shown as color lines. The thick black line marks the member with $C(z_{ml})$. Until 07:00 UTC a strong RL with a stratified aerosol structure is present at 1.5 km (reddish to violet). The nocturnal SBL is detected in approximately 250 m height and gets erased by the growing ML at around 06:00 UTC, however, not clearly visible. At this time some members detected a wrong layer near the surface, hence not tracing the real ascent of the ML-height at around 08:30 UTC. The ML-height selected as correct, however, can follow this steep increase and thus reliably detects the most likely ML-height in the following—a benefit of choosing different start points and search window lengths.

This time-height tracking method with a multi-member approach provides reliable results for the ML-height but tends to follow the residual layer top when turbulent mixing has already stopped. When considering the PBL evolution described in Sect. 1

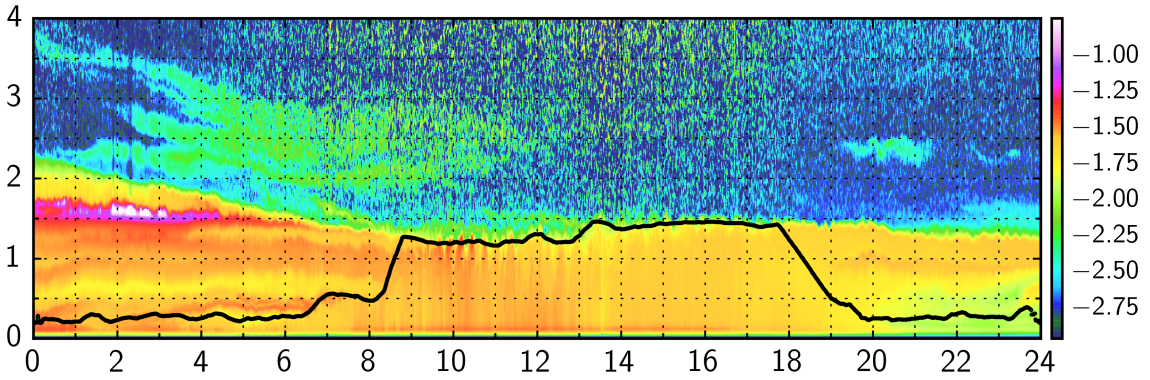

Figure 3.30: Same as Fig. 3.29, but with final ML-height.

the nocturnal stable boundary layer starts to grow when radiative cooling establishes at the surface—usually right after sunset (Kolev et al., 2000). To avoid a tracing of the RL when both, the RL and the SBL are existent, the time-height tracking procedure is applied a second time. In this case the initial time is set to 3 h after sunset when already expecting an established SBL. At this time, the maximum variance is determined as done in the first application but now only within the first 350 m. The search window is limited to a height of 500 m, however, its length is only between 45 m and 150 m in order to account for small growth rates of the SBL. The time steps examined in this run are between sunset, the start of the SBL development, and 24:00 UTC, the last profile of the day.

To account for the process of decaying thermals between a well developed mixing layer and the beginning of the SBL-establishment (Grant, 1997; Grimsdell and Angevine, 2002) a transition zone from 30 min before sunset until 60 min after sunset is introduced. In this time span the detected ML-height and the SBL-height is merged by weighting the ML-height with a factor decreasing from 0 to 1, and the SBL-height vice versa.

In Fig. 3.30 the resulting ML-height is shown on base of Fig. 3.29. The transition from the ML to the SBL is clearly visible between 18:00 UTC and 19:00 UTC. The SBL becomes visible at around 20:00 UTC. When comparing with Fig. 3.29, a misleading detection of the RL is avoided. At the end, one single ML-height is obtained by COBOLT. An overview of the operation of this time-height tracking procedure is shown in Fig. 3.31.

The presented algorithm COBOLT with a novel time-height tracking and multi-member approach yields ML-heights at any weather condition. The user has the option of tuning initialization parameters which enables different degrees of freedom in the retrieval. In addition, the algorithm provides the user with cloud flags and rain flags. The problem of coexistent residual layer and stable boundary layer, a problem of many available MLH-retrieval algorithms, is overcome. To show the reliability of COBOLT under any weather conditions, different meteorological cases are investigated in the following section.

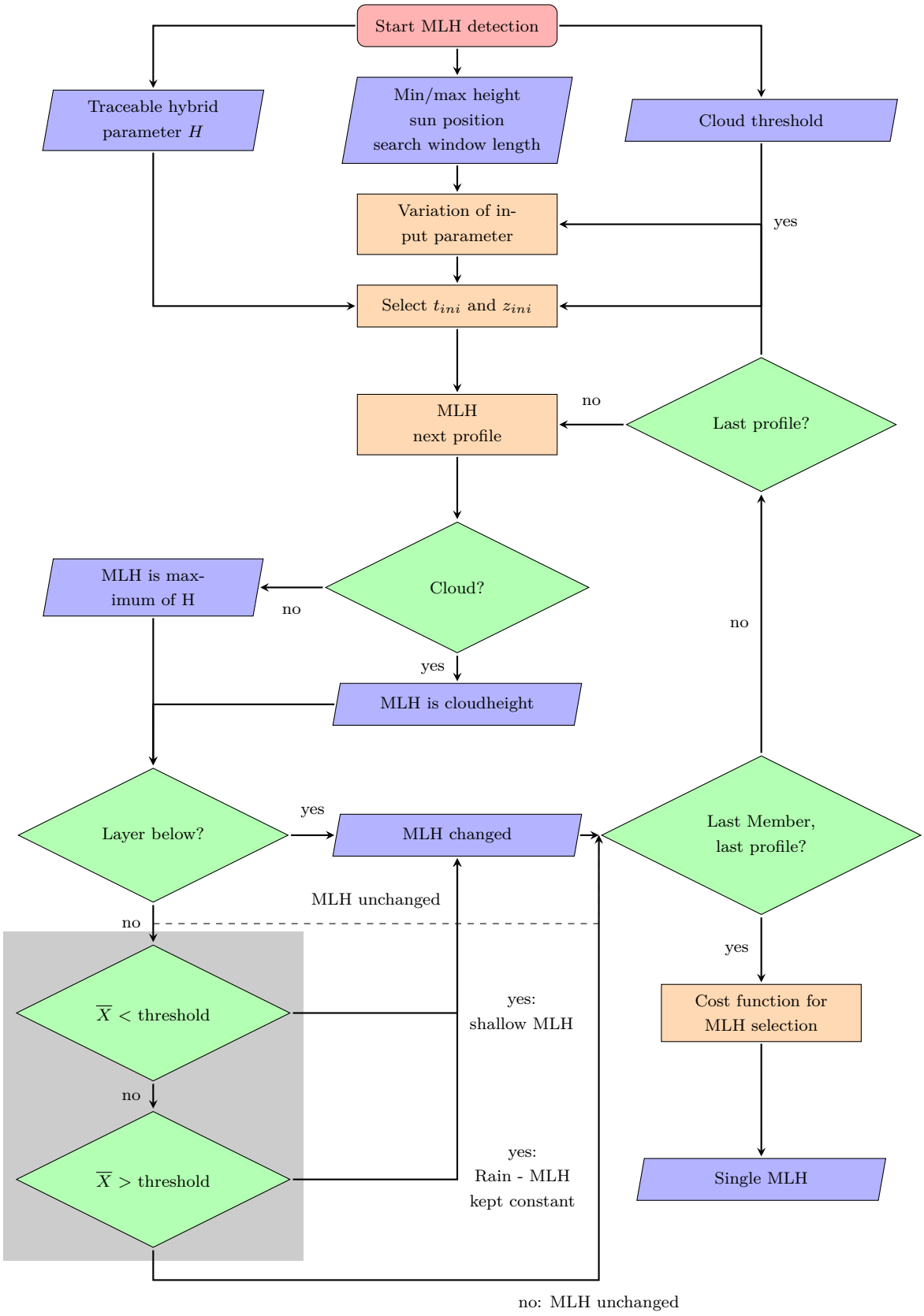

Figure 3.31: COBOLT algorithm—time-height tracking; grey shaded region shows optional validity checks.

Examples and Discussion

In this section, the performance of the COBOLT-algorithm is demonstrated for several days with quite different but typical atmospheric conditions occurring over the measurement site in Munich. Range-corrected signals $X(z)$ from YALIS are used as input parameter. An overlap correction is applied (cf. Sect. 3.3.1) which yields $z_{ovl,min} = 135\,\text{m}$, hence signals can be evaluated for $z > 135\,\text{m}$. The two optional check routines are applied by using a threshold of $X(z) = 0.0035$ for a weak signal, and $X(z) = 0.14$ for a strong signal.

Fast growing convective ML with clear sky

Clear sky conditions were prevailing on 5 May 2011 (cf. Fig. 3.32). A high RL is existent up to 2.5 km at 00:00 UTC, gradually decreasing until 08:00 UTC to 1.8 km. Near the surface a well developed nocturnal SBL with a height of approximately 200 m is detected by COBOLT. Two hours after sunrise, a convective mixing layer starts to grow (≈06:00 UTC). After reaching the SBL-top at around 07:00 UTC the growth rate drastically increases and the RL-top is reached at 1.6 km height within only 1.5 h. This is typical for a neutrally stable RL. At 18:00 UTC the transition from the ML to the SBL starts when the ML collapses. At 20:00 UTC the SBL can be located near the surface between 250 m and 500 m but is not well pronounced.

This example demonstrates that COBOLT could reliably determine the steep increase of the convective ML as well as the nocturnal SBL. The ML-height of COBOLT at 12:00 UTC is 1.61 km and has only an offset of 0.17 km from the ML-height of 1.78 km retrieved with radiosonde data from ascents at Oberschleißheim.

Convective ML with broken clouds

A convective mixing layer capped by clouds and with short precipitation events was observed on 7 June 2010 (cf. Fig. 3.33). Starting to develop at around 06:00 UTC, 3 hours and 15 min after sunrise, first clouds are already forming at the top of the ML at 07:00 UTC. However, COBOLT can reliably detect and track the ongoing development, not affected by short precipitation at 09:45 UTC and 11:15 UTC. The maximum ML-height can be determined with 1500 m at 16:00 UTC. In contrast to the first case, no distinct RL can be measured in the morning hours due to precipitation but an SBL is located by COBOLT between 250 m and 500 m during rain. Before mixing starts,

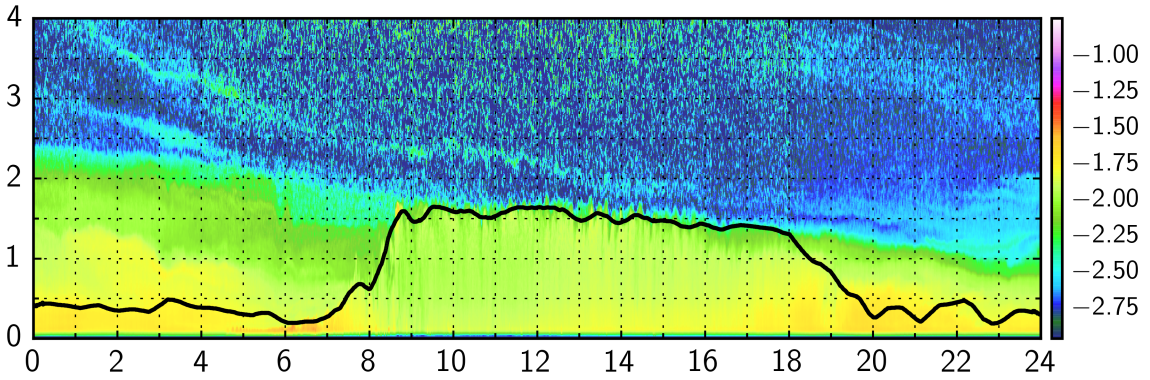

Figure 3.32: Time height cross section of the range-corrected signal (in logarithmic scale, a.u.) from ceilometer CHM15kx in Munich, 5 May 2011. The thick black line marks the ML-height determined by COBOLT. The start point is in 225 m at 06:30 UTC. Sunrise is at 03:50 UTC and sunset at 18:30 UTC. ML-height at 12:00 UTC derived from radiosonde data is 1.78 km (not shown in plot).

a very shallow SBL of 180 m is detected—almost the lower detection limit of YALIS. An SBL can again be tracked at 21:00 UTC below 250 m.

This case shows that a PBL-height determination with COBOLT is possible even under very cloudy conditions with complex aerosol structures. The ML-height at 12:00 UTC determined by COBOLT is 960 m and agrees well with a ML-height of 850 m derived from radiosonde data.

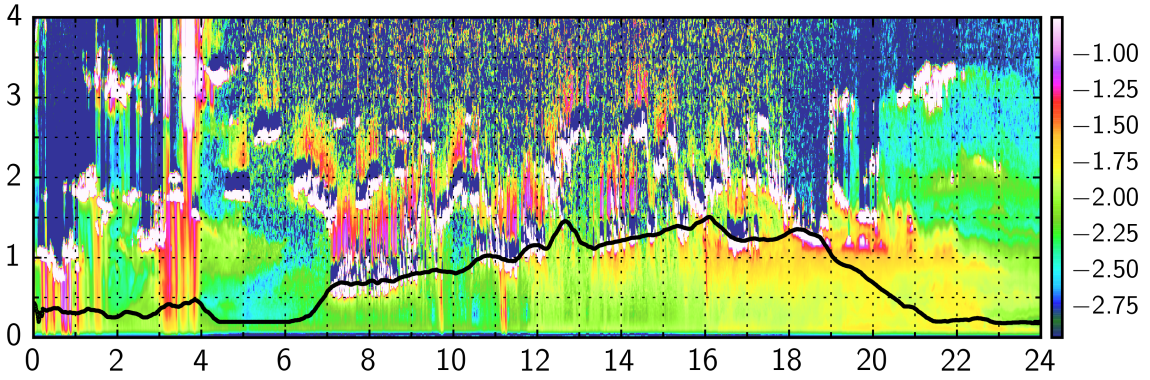

Figure 3.33: Same as Fig. 3.32, but on 7 June 2010. The start point is in 300 m at 06:46 UTC. Sunrise is at 03:15 UTC and sunset at 19:09 UTC. ML-height at 12:00 UTC determined from radiosonde data is 850 m (not shown in plot).

Convective ML with turbid RL

On 11 June 2010 strong aerosol backscatter was measured up to 3.5 km during the whole day (cf. Fig. 3.34). COBOLT detects the SBL at around 450 m to 500 m in the morning with a very high aerosol backscatter, indicating a high aerosol concentration. Decreasing in height until 06:00 UTC, the SBL is dissolved by the growing ML. However, due to the high aerosol backscatter above the ML, the gradient of the $X(z)$-profile is inverted there. Normal gradient techniques would fail in this case but due to the combination of the variance method in COBOLT, the ML development can be reasonably tracked. Only between 08:00–09:00 UTC the ML-height seems to be underestimated. The ML-height maximum is detected in an altitude of 1500 m at 15:15 UTC. After sunset when the SBL is expected to be established, only a weak structure is found between 200 m and 400 m.

Although only an inverted gradient is existent during the strongest ML-growth, a ML-height is provided by COBOLT—a benefit of the hybrid parameter. However, since the contours of the ML are less pronounced, the results must be treated with caution. The comparison with the ML-height of 1135 m derived from radiosonde data shows the good result of COBOLT which yields 1210 m at 12:00 UTC.

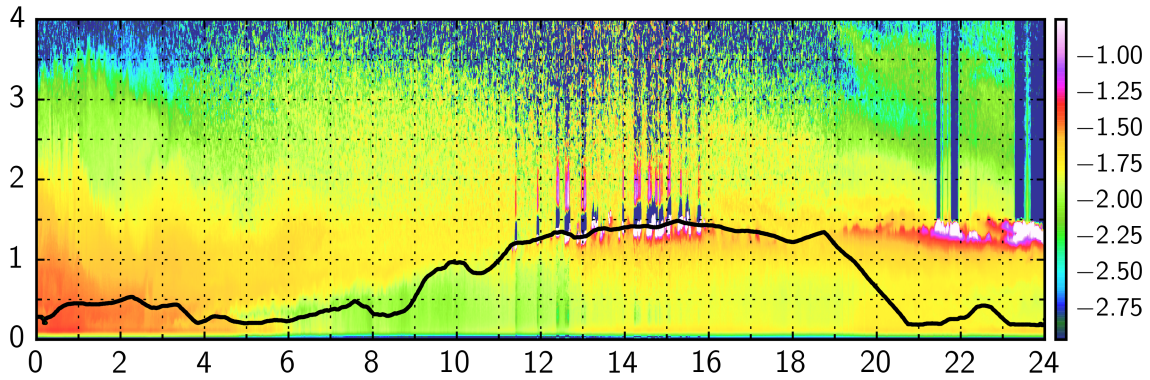

Figure 3.34: Same as Fig. 3.32, but on 11 June 2010. The start point is in 255 m at 06:24 UTC. Sunrise is at 03:13 UTC and sunset at 19:12 UTC. ML-height at 12:00 UTC determined from radiosonde data is 1135 m (not shown in plot).

Convective ML with rain

The ability of COBOLT to provide the full diurnal cycle even under unfavourable conditions is demonstrated on the 12 May 2011 (cf. Fig. 3.35). An SBL is detected between 00:00 UTC and 06:00 UTC. Its height is ranging from 230 m to 550 m. At

around 05:30 UTC the ML is growing until 10:00 UTC when a maximum height of 1175 m is reached. At 11:20 UTC, there was a small shower followed by a strong rain event from 12:00 UTC until 13:30 UTC. Even during this period, a ML-height was retrieved. It is set to a constant value found from analyzing the ceilometer signal right before the event.Afterwards, a new ML-height is found at the base of the remaining clouds—obviously a correct estimate. This procedure is repeated several times until it finally stops to rain at 21:10 UTC when a well-pronounced SBL is located at 200 m.

Even if rain is present, ML-heights can be derived from COBOLT. However, a proof of the reliability of values derived during rain is not possible. At this day, the ML-height derived from radiosonde data at 12:00 UTC is 1060 m. With COBOLT determining 835 m at the same time, this is a very good agreement even in this case. If the ML-height during precipitation is used for aerosol related studies or climatologies can easily be decided by the user through the use of the rain flags.

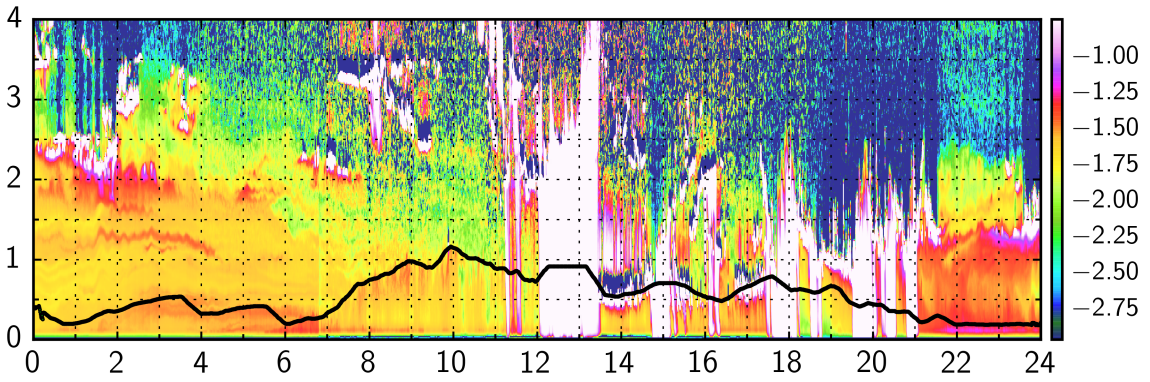

Figure 3.35: Same as Fig. 3.32, but on 12 May 2011. The start point is in 225 m at 06:51 UTC. Sunrise is at 03:40 UTC and sunset at 18:40 UTC. ML-height at 12:00 UTC determined from radiosonde data is 1060 m (not shown in plot).

Shallow boundary layer

For investigating the capability of detecting shallow boundary layers, data from 29 October 2011 are discussed as an example (cf. Fig. 3.36). On this date, a very shallow boundary layer was existent during the whole day. An SBL could be located in 140 m height between 00:00 UTC and 01:00 UTC. An increase in height was tracked up to 360 m until 04:00 UTC. However, since no information for heights $z < z_{ovl,min}$ is available, this determined increase cannot be regarded as reliable in case of an even lower SBL. At 05:00 UTC a significant structure is again visible at 140 m and can be traced

by COBOLT. At 05:51 UTC the sun rises and its radiation triggers the development of the ML at around 08:30 UTC. The ML-height reaches a maximum altitude of 310 m at around 13:00 UTC and is then decreasing until 17:30 UTC where low-level clouds are forming. In this case, the ML-top is set to the height where the strongest decrease in signal in the cloud is detected. A comparison of the ML-height at 12:00 UTC derived from COBOLT and from radiosonde data yields 280 m and 160 m, respectively.

The detection of shallow boundary layers requires instruments with a very low overlap or a very good overlap correction function. From our experience shallow boundary layers of less than 300 m vertical extent occur quite often. A boundary layer height below 300 m was existent in 30% of the 5 years of measurement of YALIS. The frequency of occurrence of even narrower MLs is not known, since the lower limit for the assessment of ML-heights with YALIS is $z_{ovl,min} = 135$ m. However, this case demonstrates that by means of measurements of YALIS, very low ML-heights of down to 135 m can reliably be determined.

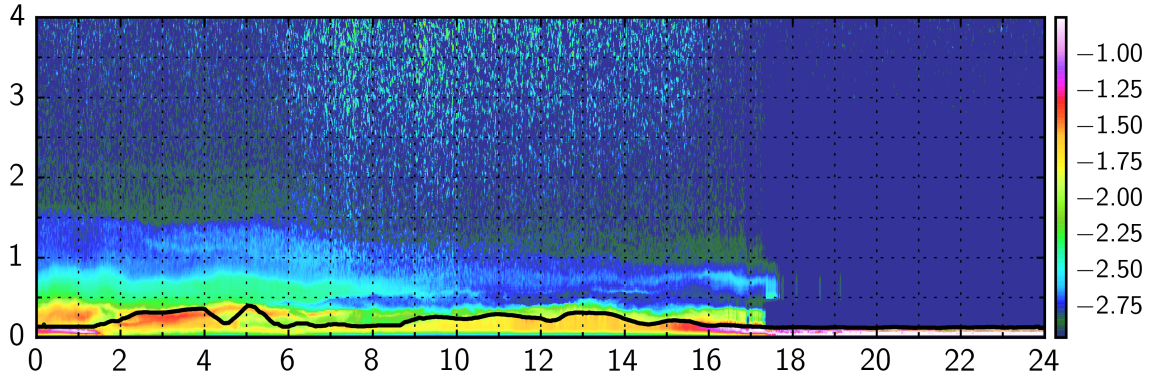

Figure 3.36: Same as Fig. 3.32, but on 29 October 2011. The start point is in 285 m at 08:03 UTC. Sunrise is at 05:51 UTC and sunset at 16:02 UTC.

Verification and crosschecks

To show the applicability of COBOLT to ceilometers of different manufacturers, and to demonstrate the potential of a time-height-tracking approach, comparisons with independently derived ML-heights from radiosonde data and two other ML-height detection algorithms are discussed in this section. First, ML-heights derived from COBOLT applied to YALIS-measurements are compared with independently derived

ML-heights from radiosonde ascents at Oberschleißheim. Second, COBOLT is applied to measurements of different ceilometers, i. e. a CL51 from Vaisala and two CHM15k from Jenoptik. Finally, COBOLT is compared to the algorithm BL-VIEW from Vaisala and STRAT (Structure of the Atmosphere) (Morille et al., 2007; Haeffelin et al., 2012).

Radiosondes

If radiosonde derived ML-heights are compared with ceilometer derived ML-heights, it must be considered that both retrievals are based on different physical measures. The ceilometer approach uses aerosol and its distribution in the ML as tracer whereas the radiosonde approach relies on the thermodynamic of the atmosphere. A reasonable agreement can be expected as the aerosol distribution is largely governed by the vertical exchange of air masses, primarily turbulence, but the agreement does not have to be perfect. Moreover, perfect temporal and spatial coincidence between ceilometer derived and radiosonde derived ML-heights can not be guaranteed. In particular at times shortly before noon, where strong ML growth is expected.

Radiosonde data is used from ascents in Oberschleißheim where observations are nominally performed at 00:00 UTC and 12:00 UTC. In fact, the launch is approximately one hour earlier. The measured profiles of pressure, temperature and humidity are used to determine the ML-height on the basis of the thermodynamics of the atmosphere. A well established method to detect the ML-height is the so-called parcel method (Holzworth, 1964; Holzworth, 1967). The profile of the virtual temperature Θ_v is calculated by

$$\Theta_v(z) = \Theta(z)(1 + 0.61w), \tag{3.57}$$

where Θ is the potential temperature and w the water vapor mixing ratio. Assuming an air parcel ascending from the surface with a virtual potential temperature $\Theta_v(0)$, the height z where $\Theta_v(z) = \Theta_v(0)$ is the mixing layer height z_{ml}. Ceilometer derived ML-heights are averaged from 11:00 UTC–11:20 UTC. The comparison is done on basis of the measurement series of YALIS from June 2009 until October 2014. Days where the parcel method could not be applied (e. g. stable stratified atmosphere) or a comparison makes no sense (e. g. continuous rain) are excluded. In total 1621 out of 1812 radiosonde ascents at 12:00 UTC were found where ML-heights $z_{ml,c}$ could be derived from COBOLT and ML-heights $z_{ml,r}$ from radiosonde data.

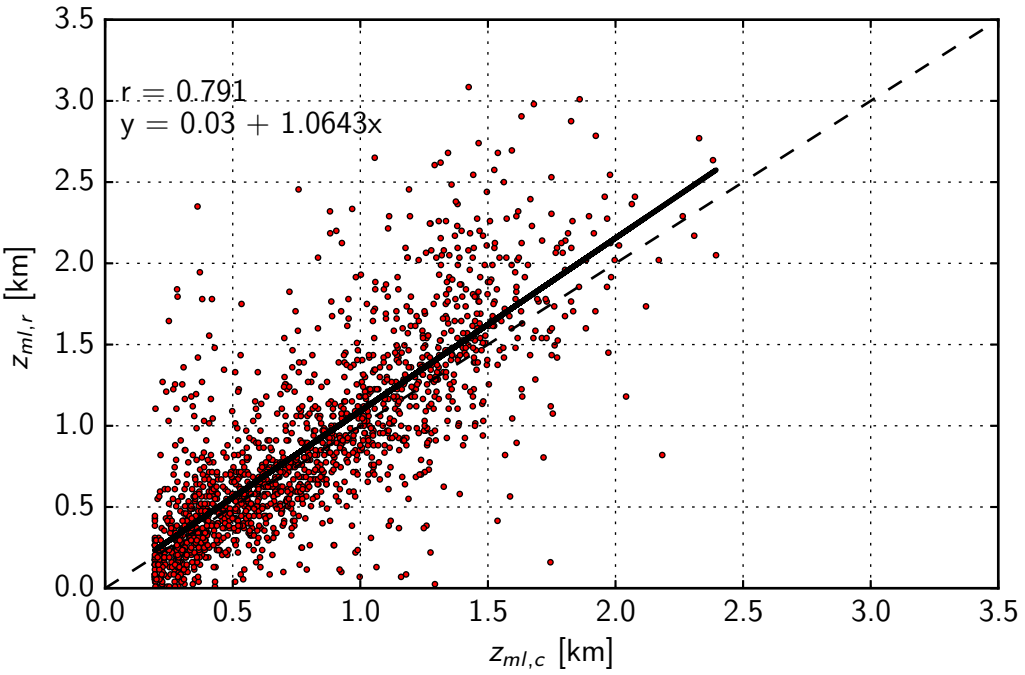

Figure 3.37: Comparison of MLH derived from ceilometer measurements with COBOLT ($z_{ml,c}$) and radiosonde observations with the parcel method ($z_{ml,r}$). Each point represents the ML-height at 12:00 UTC of days during the period June 2009–October 2014. The regression line is shown in black.

The comparison of $z_{ml,c}$ and $z_{ml,r}$ for all 1621 days is shown in Fig. 3.37 and the distribution of the corresponding differences $z_{ml,c} - z_{ml,r}$ is shown in Fig. 3.38. ML-heights of $10\,\text{m} \leq z_{ml,r} \leq 3135\,\text{m}$ are found from radiosondes and ML-heights of $135\,\text{m} \leq z_{ml,c} \leq 2395\,\text{m}$ are determined by COBOLT. The majority of cases show in general good agreement (correlation coefficient $r = 0.791$). Especially for heights with $z_{ml,r} < 1000\,\text{m}$ a bias of only 67 m with an RMSE of 248 m is found which is noticeable better than the bias of -79 m and an RMSE of 383 m found for all days (Fig. 3.38). But even when considering all days, only 226 cases are found with a difference $z_{ml,c} - z_{ml,r} > 500\,\text{m}$. 130 of these days can be related to ML-heights $z_{ml,c} > 1000\,\text{m}$, where $z_{ml,r}$ derived from radiosondes tend to be higher than $z_{ml,c}$ from COBOLT. This feature, in particular, can be observed in Fig. 3.39, where monthly mean ML-heights are shown. ML-heights from COBOLT are shown in blue and ML-heights derived from radiosondes in orange. The box edges are indicating the 25th and 75th percentile, respectively, with the median in between. The dashed lines are representing 1.5 times the interquartile range and outliers are marked as black crosses. A well pronounced annual cycle of the

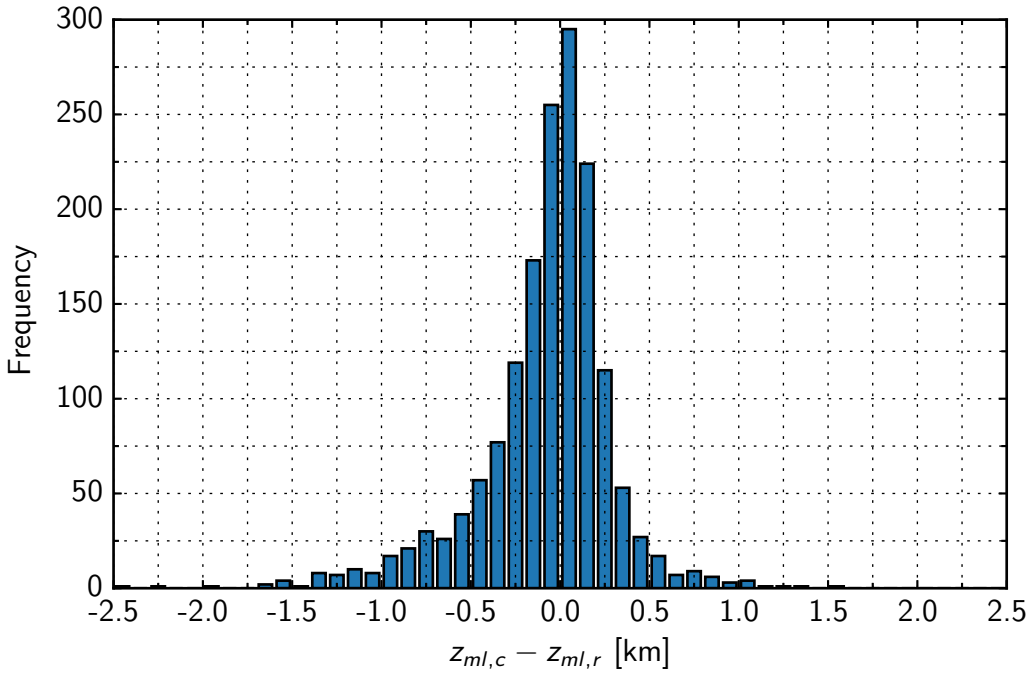

Figure 3.38: Distribution of the difference of ML-height derived from COBOLT and radiosonde data ($z_{ml,c} - z_{ml,r}$).

monthly mean ML-height is observed for Munich with higher MLs during summer and lower MLs during winter. The median of the ML-heights for the months January–March and September–December from both methods is within a difference of only 10 m. For the months April–August the difference is slightly larger with up to 260 m for June. The larger differences for higher ML can also be seen in Fig. 3.37. One reason can be the lower SNR of the ceilometer with increasing height. Especially during summer with small sun zenith angles the background radiation is higher, resulting in a lower SNR. This influences a reliable determination of very high ML ($z_{ml} > 1.5$ km and leads to lower ML-heights derived from COBOLT. Another reason can be elevated aerosol layers (cf. Fig. 3.16), which are reducing gradients in magnitude at the ML-top and thus hindering the detection of the ML-height. These events more often occur during summer (see Sect. 4.1.1).

BL-VIEW

During summer 2014 a dedicated field campaign, BAERLIN2014 (Berlin Air quality and Ecosystem Research: Local and long-range Impact of anthropogenic and Natural

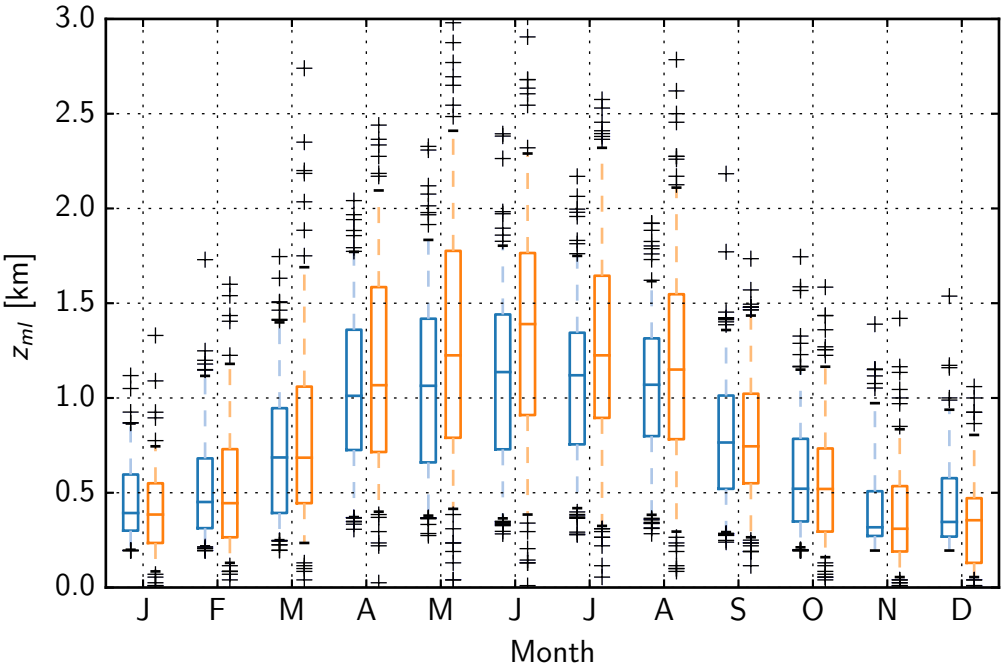

Figure 3.39: Comparison of ML-heights derived from ceilometer measurements with COBOLT (blue) and radiosonde observations with the parcel method (orange). Shown is a 5-year time series of monthly ML-heights. Box edges are indicating the 25th and 75th percentile, respectively, with median value in between. The dashed lines represent 1.5 times the interquartile range and outliers are marked as black cross.

hydrocarbons) was set up for three months. Several additional constituents were measured including mobile and airborne platforms. In this framework a Vaisala CL51 ceilometer was installed at one station (Berlin-Neukölln, Nansenstraße, 52.4894° N, 13.4309° E). Measurements of this instrument are used for the comparison of the BL-VIEW algorithm with COBOLT in the following. Data is available from 27 June until 2 September 2014. Because of its coaxial optical configuration, the minimum measurement range of the CL51 is quite low. According to Vaisala it is in the order of 50 m for the detection of aerosol layers. The spatial and temporal resolution is 10 m and 16 s, respectively. ML-heights $z_{ml,v}$ from this instrument are provided by the BL-VIEW algorithm for up to three altitudes, referred to as candidate levels in the following. They are determined from local minimums of the gradient of the backscatter profile considering data of a 14 minutes-time period prior to the actual measurement; in case of low signal-to-noise ratios this time span is extended to 20 minutes. To account

for the noise sensitivity of the gradient method, signals are smoothed along the line of sight. Cloud cases are excluded in the retrieval by using thresholds. Unrealistic outliers are deleted. During precipitation no $z_{ml,v}$ is provided. Each candidate level is given with a quality flag based on the absolute value of the gradient and the "width" of the local minimum (Münkel et al., 2011). Quality flags are 1,2 or 3, with 3 meaning the highest reliability. All candidate levels are provided to the user and he can decide which $z_{ml,v}$ he trusts and chose as the right ML-height. Henceforward, candidates of the lowest level having a quality flag of at least one are denoted by "L1", L2 and L3 accordingly.

To facilitate a comparison of both algorithms, time is assigned to the center of the interval of the BL-VIEW retrieval, i. e. we use times 7 minutes earlier than that given by BL-VIEW. However, due to different averaging lengths and properties of both algorithms, a perfect temporal co-incidence is not possible.

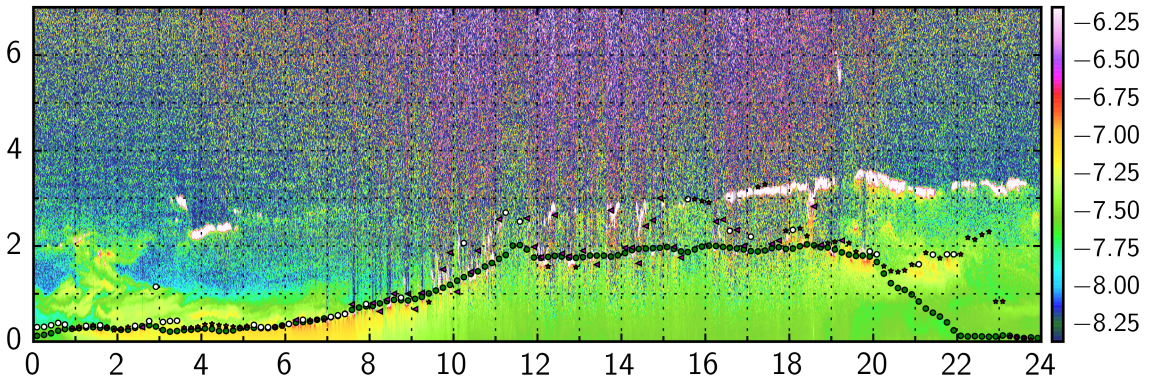

Figure 3.40: Time height cross section of range-corrected signal (in logarithmic scale, a.u.) from Vaisala ceilometer CL51 in Berlin, 1 July 2014. Green dots: ML-height $z_{ml,c}$ from COBOLT; ML-height $z_{ml,v}$ from BL-VIEW with L3-criterion (white circles), L2-criterion (red stars) and L1-criterion (magenta triangles).

In Fig. 3.40 a typical example of the ML-height from CL51 measurements is shown. The range-corrected signal $X(z)$ of 1 July 2014 is color coded up to 7 km and time is in CET. Sunrise is at 03:46 CET and sunset is at 20:32 CET. Broken cloud fields are present from 09:00 CET to 16:00 CET at different altitudes and inhomogeneous aerosol layers up to 2 km before sunrise and up to 3 km after sunset. The ML-height detected by COBOLT is marked by green dots. The ML-height from BL-VIEW is shown for different criterion; L1 is visualised by white circles, L2 by red stars and L3 by magenta triangles. The temporal resolution is 10 minutes. It can be seen that

the ML heights of COBOLT and the L3 values from BL-VIEW are coinciding very well until 09:00 CET. Even L2 and L1 heights are in good agreement in this time. After 09:00 CET, first clouds are forming at the ML-top, resulting in larger deviations between both algorithms. Disagreements are more frequent around noon when L1 or L2 is applied instead of L3. The BL-VIEW retrievals tend to select the top of elevated aerosol layers and sometimes clouds. This in particular has effect when the residual layer is already developing at 21:00 CET and its top is misinterpreted as ML-height instead of the SBL-top below. It is obvious that an application only of L1 and L2 values would lead to large temporal gaps in the diurnal ML-height. However, the reliability is increased if only L3 heights are chosen although L1 and L2 heights must not be wrong.

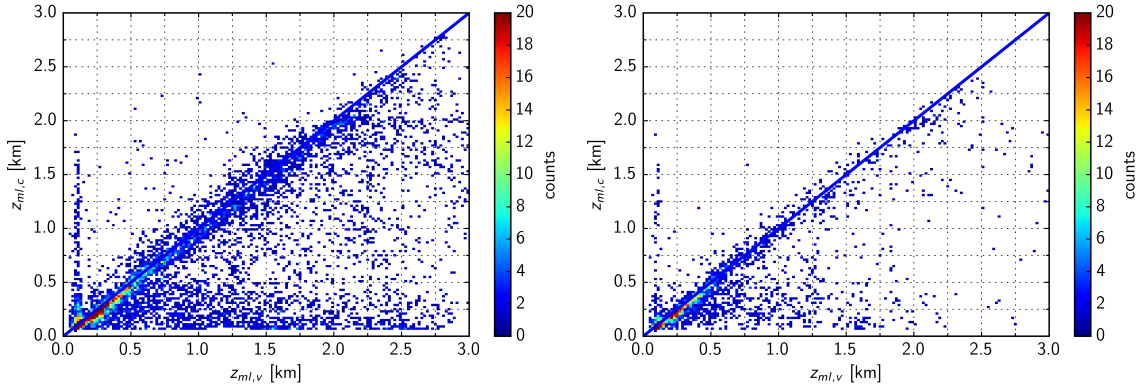

Figure 3.41: Comparison of $z_{ml,v}$ retrieved by COBOLT and BL-VIEW for 67 day. Left: L1, L2 and L3 are applied; The total number of points is 8346. Right: Only L3 is applied; The total number of points is 2998.

When analyzing the whole period of 67 days, these impressions also hold what can be seen in Fig. 3.41. The ML-heights $z_{ml,v}$ and $z_{ml,c}$ are shown on the x-axis and y-axis, respectively. In the left plot the weak condition L1 is applied for BL-VIEW. As expected from the example shown in Fig. 3.40, the agreement is good with a correlation coefficient of $r = 0.652$, but many cases with $z_{ml,v} < z_{ml,c}$ exist. The false detection of ML-heights in case of elevated aerosol layers or clouds, as well as the different behavior of both algorithms in the presence of a residual layer is reflected in the whole time series. If only L3 values are used, the correlation coefficient can be increased to $r = 0.754$. The cases with $z_{ml,v} < z_{ml,c}$ are still more frequent, but less frequent than before. As already mentioned, if using only L3 values, the amount

of co-incident z_{ml}-retrievals is drastically reduced. With a weak criterion (L1), 8346 values can be compared, whereas in the case of L3 only 2998 value are available.

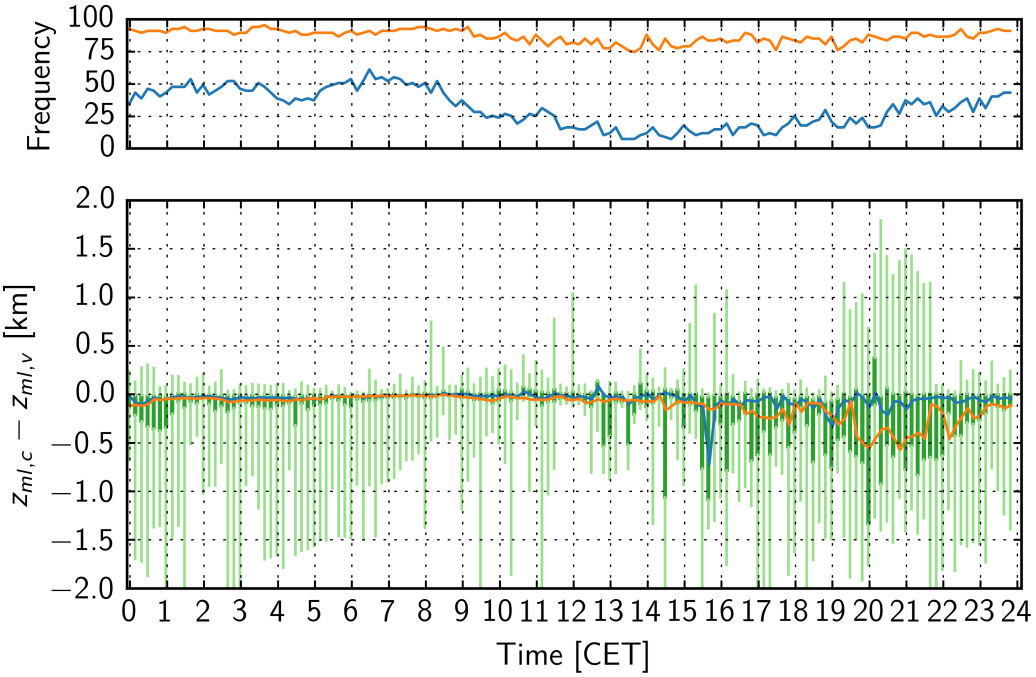

Figure 3.42: Upper panel: relative number of $z_{ml.v}$-retrievals (L3 in blue and L1 in orange). Lower pandel: Difference Δz of the retrieved MLH from COBOLT and BL-VIEW L3 for all days: bold lines indicate the interval from the 25th to the 75th percentile, thin lines the total range of the values. The blue line is the median of the distribution. For comparison the corresponding median from the L1-criterion is shown (orange line).

To find the reason for these discrepancies, the difference Δz of both algorithms, i. e. $\Delta z = z_{ml,c} - z_{ml,v}$ is discussed in Fig. 3.42. The bottom panel shows the 25th and 75th percentiles (bold lines) as well as the minimum and maximum of the difference (L3-criterion) for all 10 minute intervals. The blue line illustrates the median vlaue. For comparison the corresponding median of the L1-approach (orange line) is shown. It is obvious that the median is very small for both BL-VIEW apporaches and stays between +0.03 and -0.11 km before noon. Between 15:00 CET and 23:00 CET Δz is clearly shifted to negative values and the median becomes negative (up to -0.39 km and -0.57 km for L3 and L1, respectively). This is a clear indication that with the establishment of the residual layer in the late afternoon and after sunset, the BL-VIEW algorithm often selects the top of the residual layer as $z_{ml,v}$, especially if the user

applies the L1-criterion. L3 gives a much better agreement with COBOLT, however, as already briefly mentioned, the stricter L3-criterion leads to considerable temporal gaps in the z_{ml}-retrieval: in the upper panel of Fig. 3.42 it can be seen that the relative number of 10 minutes time intervals that allow to determine $z_{ml,v}$ is never larger than 61%. Between 10:00 CET and 20:00 CET the availability is typically only in the 15–25%-range because in the majority of cases the lowest candidate level does not have the highest quality flag as has already been discussed above. If the weaker criterion (L1) is applied, the availability of $z_{ml,v}$ is significantly increased (see the orange line in the upper panel) and reaches values of more than 75% throughout the day, however, at the expense of the good agreement between $z_{ml,v}$ and $z_{ml,c}$.

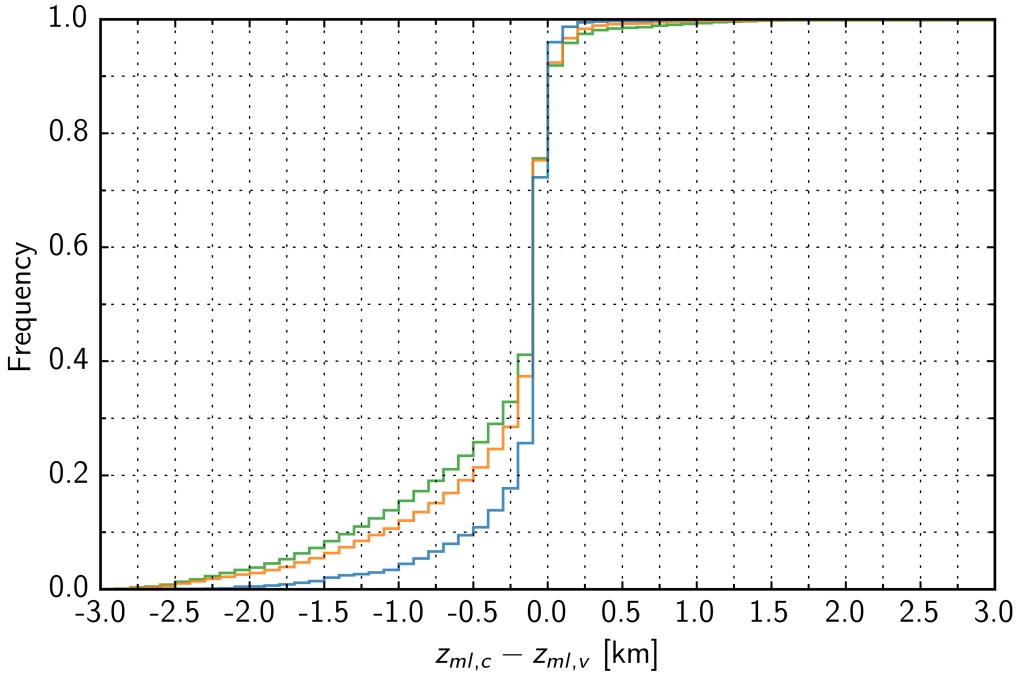

Figure 3.43: Cumulative distribution of the difference Δz of all 67 days: complete diurnal cycle, L1 vs. COBOLT (green line), only measurements before sunset, L1 vs. COBOLT (orange line) and only measurements before sunset, L3 vs. COBOLT (blue line).

If we compare only MLH-retrievals before sunset the agreement between both approaches is indeed improved. The differences Δz are shown in Fig. 3.43 as cumulative distributions. The blue line corresponds to the BL-VIEW L3 retrieval (2445 cases), and the orange line to the L1 approach (6855 cases). It can be seen that the differences are smaller for the L3-approach with only 9.5% of Δz being smaller than -0.5 km

(i. e. large absolute values), whereas the corresponding number for the L1-approach is 19.1%. To demonstrate that the removal of measurements after sunset improves the agreement, the original comparison, considering the complete diurnal cycle and the L1-criterion, is added (green line, 8346 cases). In this case 23.4% of the inter-comparisons show large negative differences (Δz < -0.5 km). Figure 3.43 also clearly shows that the cases when COBOLT retrieves larger z_{ml} than BL-VIEW are quite rare. A difference of more than 0.5 km occurs in less than 2% of the cases for all three approaches.

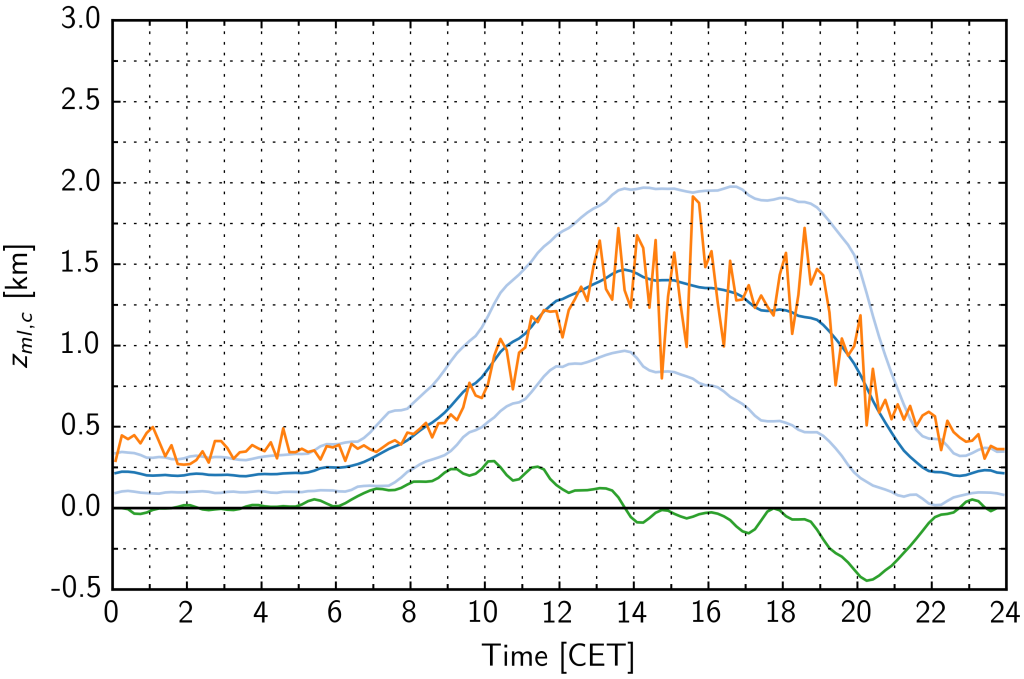

Figure 3.44: Mean diurnal cycle of $z_{ml,c}$ (blue line) and $z_{ml,v}$ (orange line), averaged over 67 days.

Figure 3.44 shows the mean diurnal cycle of z_{ml} as retrieved by BL-VIEW and COBOLT, respectively, averaged over all 67 days. The dark blue line corresponds to $z_{ml,c}$ whereas the orange line is for $z_{ml,v}$ (L3-criterion). The light blue lines indicate the range of the temporal variability as calculated from the standard deviation (s_c from COBOLT).

The green line shows the first derivative of $z_{ml,g}$. This quantity is relevant in view of temporal averaging, e. g. when z_{ml} is correlated with concentration measurements with a lower temporal resolution. It can be seen that the mean z_{ml} rises with up

to 0.29 km/h before noon, and that after sunset rates of -0.45 km/h can occur. For individual days these rates can be even larger. Thus, one shall be careful to calculate temporal averages of z_{ml} during these time periods. The mean $z_{ml,c}$ at night is in the range of 0.2 km underlining the need of ceilometers with a very low overlap (or a reliable overlap correction function) for studies on the boundary layer. The maximum vertical extent is on average below 1.5 km but the temporal variability is high. As this finding is based on COBOLT that provides complete temporal coverage it might be considered as representative for summer months in Berlin. The most prominent differences between BL-VIEW and COBOLT are the larger $z_{ml,v}$ during night and the rapid changes of $z_{ml,v}$ around noon. The main reason for these "fluctuations" is the low number of retrievals when L3 is applied, e. g. for some of the 10 minutes intervals only in 5 out of 67 days $z_{ml,v}$ could be found. Thus, on the one hand the statistical significance is limited, on the other hand $z_{ml,v}$ is within the range of $z_{ml,c} \pm s_c$.

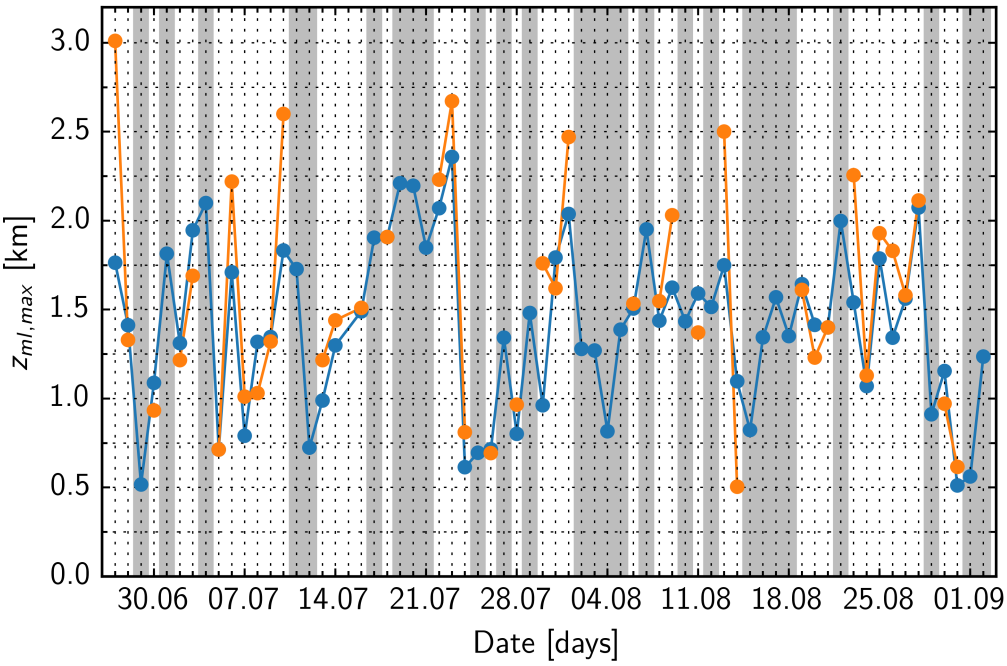

Figure 3.45: Daily maximum of z_{ml} as derived from COBOLT (blue dots) and BL-VIEW L3 (orange dots) between 27 June and 2 September 2014. The shaded areas highlight days when $z_{ml,v}$ could not be retrieved.

For air quality studies it might be worthwhile to also determine the daily maximum of z_{ml}. Based on the mean diurnal cycle (Fig. 3.44) we define the maximum as the average over the 2-hour time period starting 30 minutes after noon. Figure 3.44 shows

the results from COBOLT (blue dots) and L3 (orange dots). Note, that BL-VIEW with the strict L3-criterion fails to determine $z_{ml,v}$ in 26 days (shaded areas) for the reasons mentioned above. If simultaneous values are available, the general agreement is however good. Only few cases exist when $z_{ml,v}$ is much larger than the respective COBOLT-results (e. g. 27 June, 10 July and 13 August). It is concluded that the main discrepancies between COBOLT and BL-VIEW originate from the presence of the residual layer whereas problems from broken cloud fields and elevated aerosol layers during daytime are less important. The main drawback of the present version of BL-VIEW is the limited temporal coverage in comparison with COBOLT.

STRAT

STRAT (Morille et al., 2007; Haeffelin et al., 2012) is an accepted and frequently used algorithm which aims to identify different parts of the atmosphere, i. e. cloud layers, aerosol layers, particle-free regions and boundary layer. The focus is on single wavelength instruments operating in networks and thus require automated evaluation methods. STRAT is coded in the commercial software MATLAB, a version using open source software is, to our knowledge, not yet available. That is the reason we have to restrict ourselves to only three qualitative comparisons in the following and no extended time series can be analyzed. The evaluations were performed with STRAT version "01.04". As a first step, the raw data of the ceilometer must be converted to a file readable by STRAT, which is done by a conversion tool named "Raw2L1". To define which output parameters shall be provided and to control the determination process, a configuration file defining detection methods and threshold values (e. g. maximum and minimum possible ML-height) has to be written. The STRAT boundary layer detection algorithm is based on a combination of a wavelet covariance transform using the first derivative of a Gaussian function as wavelet, and the application of the Canny edge detection technique (Canny, 1986) with temporal and spatial gradients. In contrast to COBOLT, which provides one diurnal cycle of the ML-height, STRAT provides three candidates of possible boundary layer tops. The user can choose between the "lowest altitude gradient", the "maximum global gradient" and the "second maximum global gradient" as the ML-height. According to Morille et al. (2007), the best performance of STRAT is provided during day with a convective mixing layer. During night when aerosol layers are predominantly stratified, a distinction between the boundary layer top and residual layer is not possible.

The comparison of COBOLT and STRAT is done by means of relative calibrated measurement data ($\Delta = 140$) of YALIS on 22 April 2010, 16 March 2011 and 12 July 2013. The MLH derived with COBOLT (black line) and with STRAT (blue dots: lowest altitude gradient; red dots: maximum global gradient; green dots: second maximum global gradient) is shown as a time height cross section of the color coded range corrected signal (Figs. 3.46, 3.47 and 3.48)

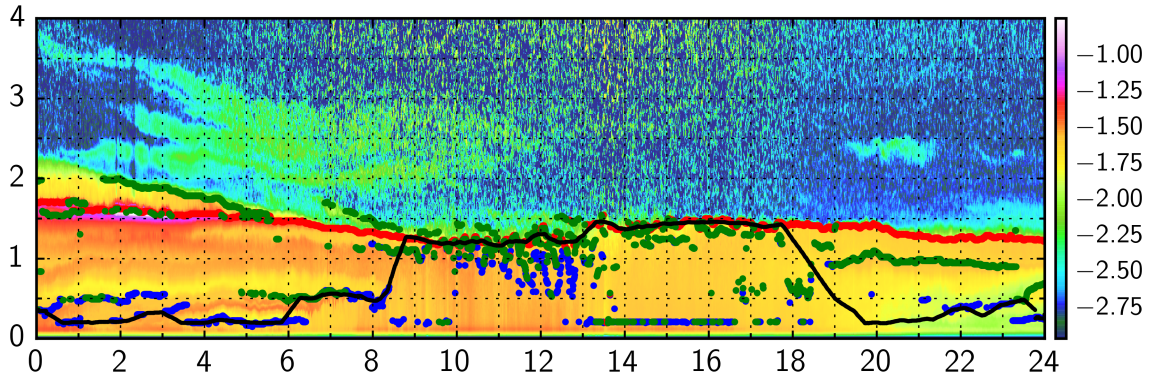

Figure 3.46: Time height cross section of the range-corrected signal (in logarithmic scale, a.u.) from YALIS, 22 April 2010. The thick black line depicts the ML-height determined by COBOLT. The ML-height from STRAT is marked as blue dots (lowest altitude gradient), red dots (maximum global gradient) and green dots (second maximum global gradient), respectively. Radiosonde derived ML-heights at 12:00 UTC is 1300 m (not shown). Sunrise is at 04:12 UTC and sunset at 18:14 UTC.

Fig. 3.46 shows the diurnal cycle of 22 April 2010 which was already presented in Fig. 3.30 as a first example. A strong RL with a stratified aerosol distribution is present between 1.5 km and 2 km until 07:00 UTC. STRAT detects the first global maximum gradient (red dots) in this region. The green dots indicating the second maximum global gradient at the RL-top. The ML-height derived by COBOLT could detect the nocturnal SBL at approximately 250 m height, i. e. the same height identified by STRAT when the lowest altitude gradient (blue dots) method is applied. The ML-growth from $\approx$ 250 m to $\approx$ 500 m between 06:00 UTC and 08:00 UTC is tracked by COBOLT, and STRAT detects the lowest altitude- and second maximum global gradient at this height. The following steep increase after 08:00 UTC is not detected by STRAT. Between 09:00 UTC and 18:00 UTC when COBOLT locates the ML-top between 1.3 km and 1.5 km, STRAT determines the global maximum gradient and also the second global maximum gradient in the same region, the latter, however, with

strong fluctuations. Lowest gradients are detected far below the actual ML-height. When comparing the ML-height of COBOLT and STRAT with the ML-height of 1.3 km derived from the radiosonde ascent at 12:00 UTC, a good agreement can be found. After sunset at 18:14 UTC, when the ML-height is expected to decrease, both algorithms are showing large differences. STRAT is locating the maximum global gradient at the RL-top and detects another layer with second maximum global gradients beneath. From around 21:30 UTC, STRAT is again able to detect the lowest altitude gradient between 0.3 km and 0.5 km.

This day is a representative example of the advantageous boundary layer tracing of COBOLT. With respect to an automated operation it is a benefit that COBOLT does not require user input to choose the right ML-height from several candidates as it is necessary for STRAT. However, being able to detect the right boundary layer height with one of its three candidates the user has to decide carefully which one represents the correct ML-height. If following the recommendation of the STRAT developers to choose the lowest altitude gradient during nighttime and the maximum global gradient during daytime for the determination of the ML-height, the agreement between ML-heights derived by COBOLT is quite good.

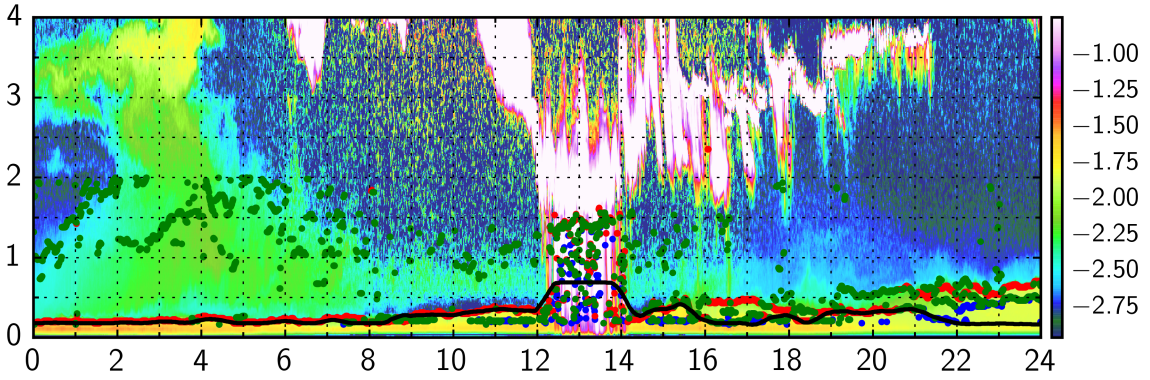

Figure 3.47: Same as Fig. 3.46 but for 16 March 2011. Radiosonde derived MLH at 12:00 UTC is 350 m (not shown). Sunrise is at 05:28 UTC and sunset at 17:19 UTC.

A completely different situation is given in Fig. 3.47. On 16 March 2011 a shallow distinct ML was present the whole day with precipitation between 12:30 UTC and 14:00 UTC. Aerosols are visible up to a height of 4 km from 00:00 UTC until 08:00 UTC. Between 06:00 UTC and 22:00 UTC clouds and precipitation can be detected above 1.5 km (white colors). From 00:00 UTC until 08:00 UTC, STRAT and COBOLT have

no problems in detecting the sharp edges of the boundary layer at a height nearly constant around 0.2 km. STRAT is locating the maximum global gradients in this region. At 08:00 UTC the ML is slightly growing up to 0.36 km which is reasonably tracked by both algorithms. The ML-height calculated from radiosonde data yields 0.35 km at 12:00 UTC which is in very good agreement. When it starts to rain at 12:30 UTC the distinct ML-top disappears and strong varying signals during the precipitation process are measured. COBOLT is also providing a ML-height during this event, however, determined at 1.1 km—presumably too high. The feature of keeping the ML-height constant in case of a rain (validity check for rain) is clearly visible and facilitates a further boundary layer tracing after the precipitation process. The derived ML-height in this period, however, must be treated with caution. With a detected ML-height spread between 0.2 km and 1.5 km, STRAT is having problems with a correct determination under such conditions. After 14:00 UTC the ML-height is detected between 185 m and 410 m by both algorithms with COBOLT agreeing better with the lowest altitude- and second maximum global gradient of STRAT. After 22:00 UTC a shallow SBL can be detected by COBOLT at 185 m whereas STRAT determines the SBL-height varying between 0.38 km and 0.75 km. To conclude, the results of both algorithms on this day are similar until 12:30 UTC, when rain occurs and the strong boundary between the ML and the free troposphere disappears. Weaker and shallower gradients after 14:00 UTC are spreading STRAT-derived ML-heights, however, when choosing lowest altitude gradients instead of first maximum global gradients a better agreement of COBOLT and STRAT is found in this case.

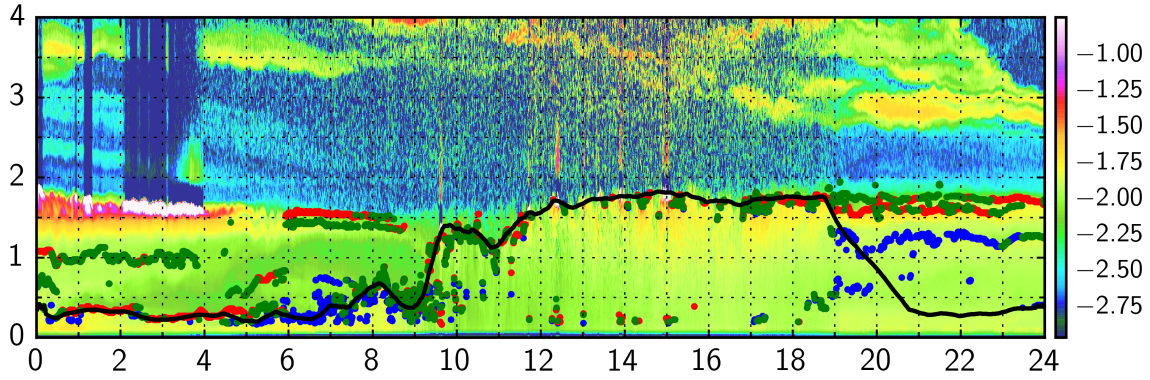

Figure 3.48: Same as Fig. 3.46 but for 12 July 2013. No radiosonde is available on this day. Sunrise is at 03:23 UTC and sunset at 19:16 UTC.

In the last example shown in Fig. 3.48, both algorithms are compared on 12 July 2013—a day with a relatively thick ML and elevated aerosol layers above. Clouds are visible at the RL-top from 00:00 UTC until 04:00 UTC and occasional at the ML-top between 11:30 UTC and 15:00 UTC. A strong RL exists at 1.5–1.8 km and is slowly decreasing in height from 00:00 UTC until 10:00 UTC. A distinct SBL becomes apparent near the surface between 0.25 km and 0.35 km from 00:00 UTC until sunrise at 05:28 UTC. It can be reliably detected by COBOLT. STRAT determines mostly first global maximum gradients at the SBL-top. Shortly after sunrise the developing ML starts to raise up to 0.68 km until 08:10 UTC when a short interruption of the growth process takes place, hence leading to a decrease of the ML down to 0.39 km at 09:00 UTC. A strong increase of the ML-height can be tracked afterwards, when a height of 1.4 km is reached at 09:45 UTC. Followed by a second decrease thereafter until 10:50 UTC, the ML subsequently raises from 1.13 km up to 1.82 km where it has its maximum. This complex growing process is reasonably and continuously traced by COBOLT which is an advantage if studying mixing layer growth rates. Since STRAT only provides different candidates, a continuous boundary layer monitoring is difficult, especially when they are spread as is the case here. When the growth process starts, the first maximum global gradients are shifted to the RL-top at 1.5 km at around 06:00 UTC, after having been detected at the SBL-top before. During the further increase/decrease, the ML-height can hardly be located as the second maximum global gradient. Between 12:00 UTC and 16:45 UTC only a few candidates are located at the ML-top. From 16:45 UTC the first and second maximum global gradients are detected at the ML-top and the RL-top, respectively. The starting development of the SBL shortly after sunset at 19:16 UTC is reliably tracked by COBOLT, although the gradients are weak. In contrast, STRAT is able to determine the SBL only from 23:25 UTC—a feature already mentioned by the developer.

Summary

The performed comparisons with different ML-height determination algorithms as well as crosschecks with ML-heights independently derived from radiosonde data show that COBOLT can be reliably used to determine ML-heights under even complex meteorological conditions, e. g. weak gradients, shallow ML, presence of clouds. The agreement with radisonde-derived ML-heights is slightly better in winter months than in summer months but ML-heights from COBOLT still provide sufficient reliability to study

ML-evolutions. Due to its continuous time height tracking technique, the developed algorithm has great advantages over algorithms which only provide candidates for single profiles, often having large steps in the determined ML-height from subsequent retrievals when choosing the wrong candidates. Furthermore, the continuous boundary layer tracing method gives a high temporal resolution of the determined ML-height which can be used to calculate growth rates of the developing ML.

4 Applications

Ceilometers offer great potential for aerosol remote sensing, especially due to their automated and continuous operation and their high temporal and spatial resolution. If calibrated, the evaluation is not restricted to a qualitative interpretation of the aerosol distribution, even optical properties (β_p) can be provided in a quantitative way. In this chapter, the absolute calibrated ceilometer YALIS (Sect. 3.3) is used to study profiles of particle backscatter coefficients β_p above Munich by taking advantage of a 5 years measurement series (Sect. 4.1). A selection of the wide field of applications of the retrieved ML-heights is presented in the following. To investigate annual and diurnal cycles of mixing layer heights, the mixing layer height retrieval algorithm COBOLT (Sect. 3.4.2) is applied to YALIS (Sect. 4.2.1). By including two other ceilometer types, operating at different measurement sites (Sect. 4.2.1), ML-heights can be evaluated on a regional scale. To demonstrate the performance of COBOLT compared with numerical simulations of the ML-height, calculations from the model MCCM (Mesoscale Climate-Chemistry Model) are used (Sect. 4.2.1). Finally a comparison of ML-heights with measurements of PM1, PM2.5 and PM10 in Berlin demonstrates the potential of ceilometers for air quality assessments (Sect. 4.2.2).

4.1 β_p-profiles above Munich

4.1.1 Monthly mean profiles

To show the typical annual and diurnal aerosol distribution above Munich, profiles of the particle backscatter coefficient β_p are derived as described in Sect. 3.4.1 from the 5 years measurement series of YALIS by using a constant lidar ratio $S_p = 50\,\mathrm{sr}$. Note that the influence of S_p on the accuracy of β_p is small. To show the diurnal variability of the atmospheric aerosol distribution, measurements at 12:00 UTC and 14:00 UTC are chosen, which are best representing a well developed mixing layer (Fig. 4.1). Nighttime conditions are presented in Fig. 4.2 with profiles derived at 23:00 UTC and 02:00 UTC.

For the derivation of β_p only profiles which are cloud-free up to 6 km for at least 150 min were considered. This is the average length for the profiles and is necessary to guarantee an SNR sufficient to obtain information also about elevated aerosol layers. Individual profiles for January (top left) until December (bottom right) are shown up to 6 km in gray; monthly averaged profiles are shown in red.

When considering daytime profiles in Fig. 4.1, the ML-height can be clearly located in the lowest 1.5 km where β_p is often almost constant with height—a feature of a well mixed boundary layer. A pronounced difference of the ML-height between different months is obvious. Higher MLs of around 1.5 km occur during summer and lower MLs with mean heights of around 400 m during winter. Monthly mean values of β_p inside the ML are varying between $0.0007\,\mathrm{km^{-1}sr^{-1}} < \beta_p < 0.0012\,\mathrm{km^{-1}sr^{-1}}$. However, no distinct annual cycle of monthly mean values of β_p inside the ML is found. Considering single profiles, days with maximum values of $\beta_p \approx 0.0027\,\mathrm{km^{-1}sr^{-1}}$ and minimum values of $\beta_p \approx 0.0002\,\mathrm{km^{-1}sr^{-1}}$ can be found. Profiles of β_p at nighttime are not showing this well mixed region near the ground. Instead, β_p is increasing towards the surface. Here again, no clear annual cycle of β_p inside the ML is found.

Another main difference in the annual cycle of β_p-profiles can be observed in the free troposphere between December–February and March–November. A frequent presence of elevated aerosol layers above the mixing layer, indicated by β_p-values larger than 0, is observed from March until November. The highest values are observed in July and August with a mean value of $\beta_p \approx 0.0003\,\mathrm{km^{-1}sr^{-1}}$ above 2 km. For single profiles even values of $\beta_p \approx 0.0015\,\mathrm{km^{-1}sr^{-1}}$ appear. These elevated aerosol layers typically result from long-range aerosol transport, primarily Saharan dust (cf. Sect. 3.4.1) but also forest fire plumes. A reason for the higher occurrence in summer months is the higher probability for meridional circulation patterns, inducing advection of air masses from the Saharan region with southerly flows. But also biomass burning aerosol transported from, e. g. Canada or eastern Europe is measured. These events more often occur during the biomass burning and forest fire season in summer. The potential of ceilometers for determining aerosol optical properties, i. e. β_p and—provided a reliable estimate of the lidar ratio is available—α_p, in elevated aerosol layers as well as determining their geometrical extent, can contribute to validation and improvements of chemistry transport models. In case of volcanic eruptions, a localization of the ash plume is possible.

Inspection of Figs. 4.1 and 4.2 reveals a very strong variability of the vertical profile of β_p, not only with respect to their absolute values, but also in the shape of the profiles. As a conclusion one should be aware that an individual profile can significantly deviate from the corresponding monthly mean, and thus monthly averages must be interpreted very carefully.

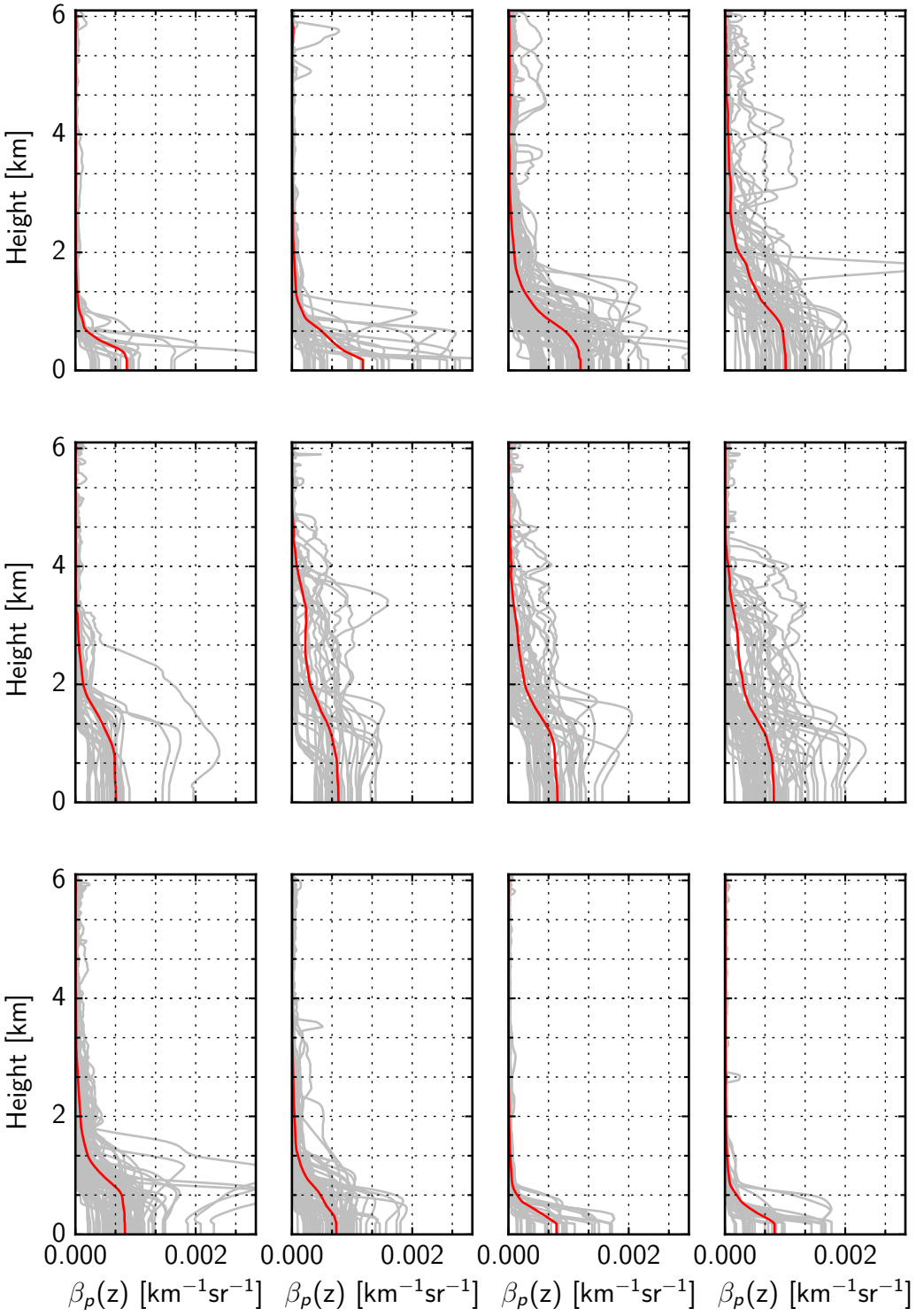

Figure 4.1: Monthly mean β_p-profiles at 1064 nm derived from YALIS measurements at 12:00 UTC and 14:00 UTC at cloud-free conditions up to 6 km.

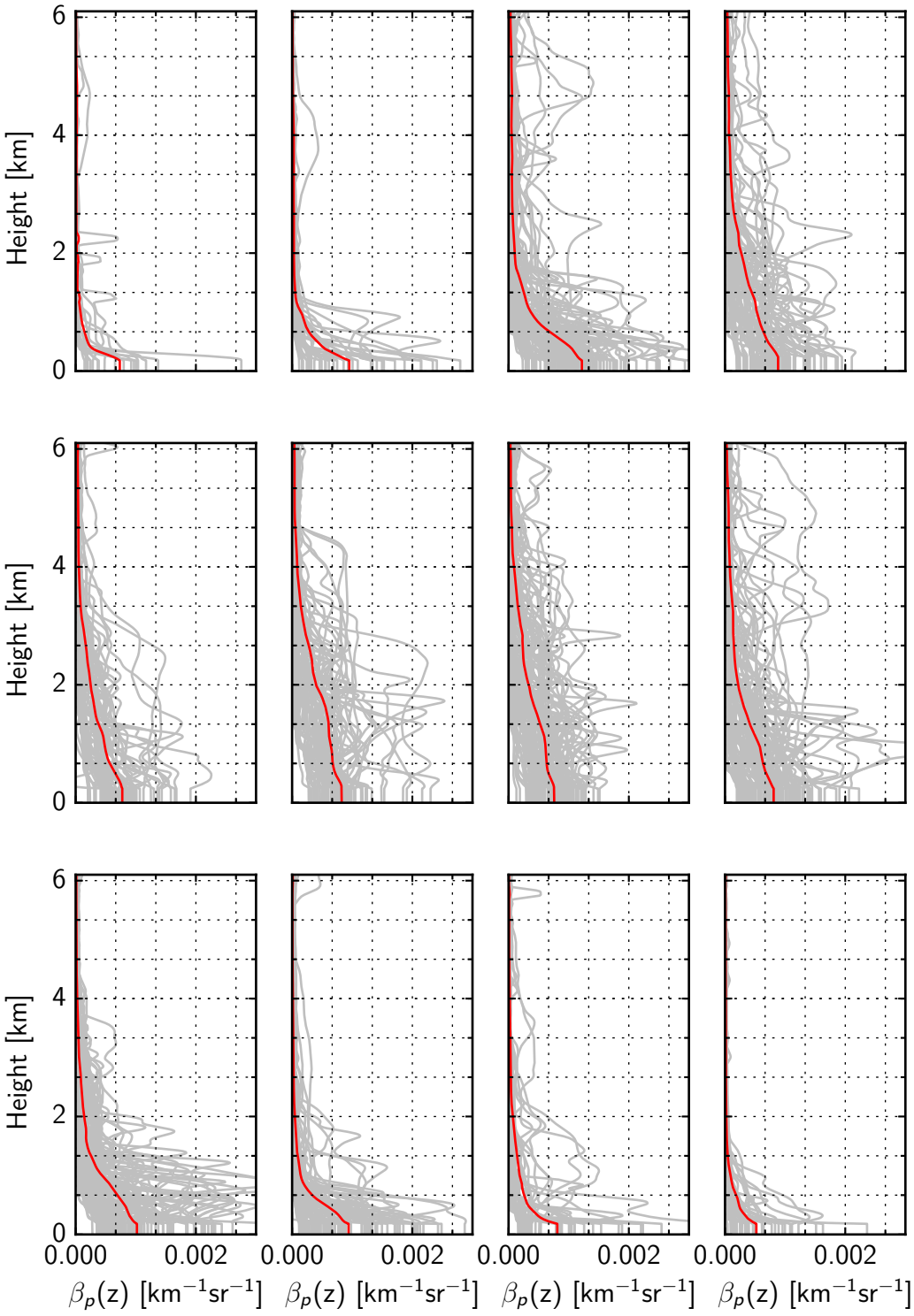

Figure 4.2: Monthly mean β_p-profiles at 1064 nm derived from YALIS measurements at 23:00 UTC and 02:00 UTC at cloud-free conditions up to 6 km.

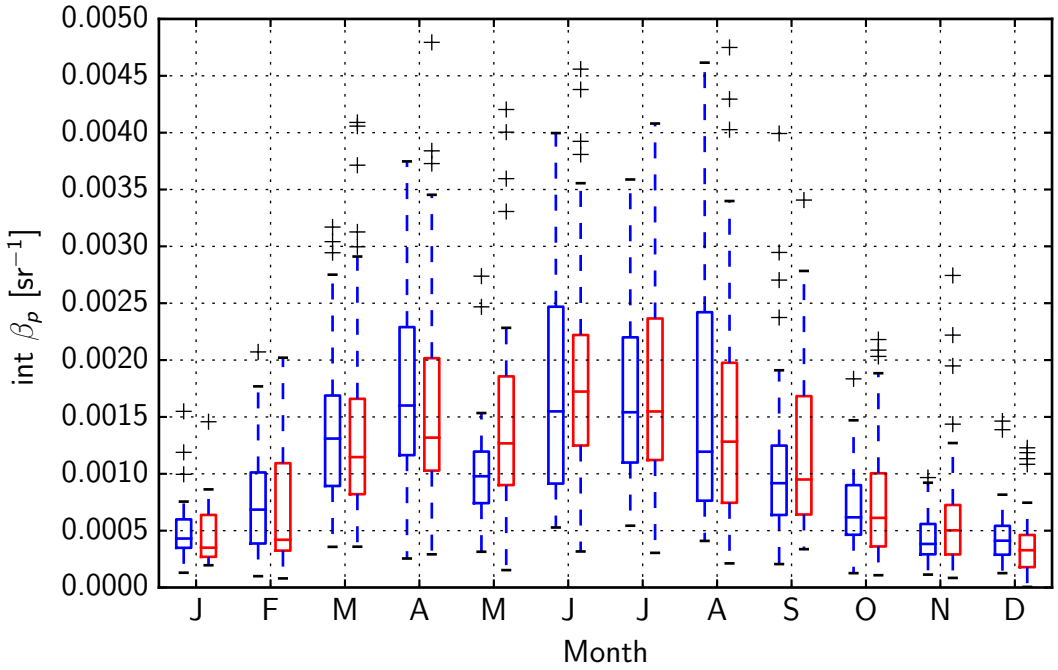

Figure 4.3: Integrated β_p-profiles β_{int} at 1064 nm of the total atmospheric column at nighttime (red) and daytime (blue). Box edges are indicating the 25th and 75th percentile, respectively, with median value in between. The dashed lines represent 1.5 times the interquartile range and outliers are marked as black crosses.

To illustrate the turbidity of the atmosphere and its annual variation, the integrated particle backscatter coefficient β_{int} is used. Even if S_p is not constant, β_{int} can be assumed to be proportional to the aerosol optical depth τ_p as a first approximation. β_{int} corresponding to the monthly mean values shown in Figs. 4.1 and 4.2, are discussed on the basis of the box plot in Fig. 4.3. Box edges are indicating the 25th and 75th percentile, respectively, with the median value in between. The dashed lines represent 1.5 times the interquartile range and outliers are marked as black crosses. With $\beta_{int} < 0.0005\,\mathrm{sr}^{-1}$ for the winter months, a steady increase until April is observed when a median value of $\beta_{int} = 0.0016\,\mathrm{sr}^{-1}$ is reached during day and $\beta_{int} = 0.0013\,\mathrm{sr}^{-1}$ during night. For May, slightly lower β_{int} are shown, which can be also due to the low number of available profiles for this month. The integrated particle backscatter coefficient remains high in June and July and is decreasing until the end of the year with a median value of β_{int} below $0.001\,\mathrm{sr}^{-1}$ in September. When considering single values of β_{int}, days exceeding a value of $\beta_{int} > 0.003\,\mathrm{sr}^{-1}$ are only observed from March until September.

In order to quantify the relative contribution of the ML to the total β_{int}, i. e. $\epsilon = \frac{\beta_{int,ml}}{\beta_{int}}$, the ML is determined by COBOLT from YALIS measurements in the next section.

4.1.2 Contribution of the mixing layer to total β_{int}

COBOLT is used to detect the ML-height, thus it is possible to determine the contribution of $\beta_{int,ml}$ in the mixing layer to $\beta_{int,c}$ of the total atmospheric column during the year. COBOLT is applied to the same data from Sect. 4.1.1. For the comparison of column and mixing layer values of β_{int}, however, only daytime values at 12:00 UTC and 14:00 UTC are used in Fig. 4.1, when a well developed ML can be expected. The integrated particle backscatter coefficient $\beta_{int,c}$ of the total atmospheric column is shown in red and $\beta_{int,ml}$ for the mixing layer in blue. The data is again visualized with a box plot.

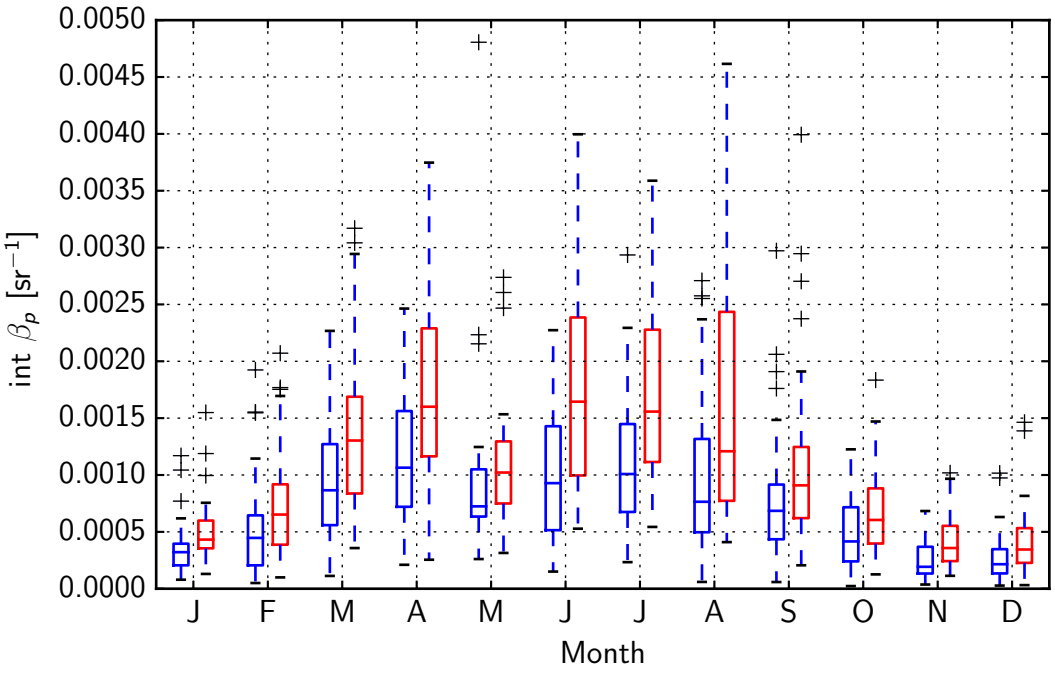

Figure 4.4: Integrated β_p-profiles at 1064 nm derived at 12:00 UTC and 14:00 UTC for the total atmospheric column (red) and the ML (blue).

The integrated particle backscatter coefficient $\beta_{int,ml}$ shows a clear annual cycle with median values of $\beta_{int,ml} < 0.0005\,\mathrm{sr}^{-1}$ from October until February. From March until September, median values are between $0.00075\,\mathrm{sr}^{-1} < \beta_{int,ml} < 0.001\,\mathrm{sr}^{-1}$. The

75th percentile of March, April, June, July and August reaches $\beta_{int,ml} = 0.0015\,\mathrm{sr}^{-1}$. Hence, March–August are the months having the highest aerosol load in the ML. When considering the column value $\beta_{int,c}$, median values of $\beta_{int,c} < 0.0005\,\mathrm{sr}^{-1}$ are observed for November until January and are increasing with median values of approximately $0.0013\,\mathrm{sr}^{-1} < \beta_{int,c} < 0.0017\,\mathrm{sr}^{-1}$ from March until August. 75th percentiles of up to $\beta_{int,c} = 0.0025\,\mathrm{sr}^{-1}$ are derived for April, June, July and August. When putting them into relation with $\beta_{int,ml}$, the large fraction of β_{int} in the free troposphere clearly shows the strong contribution of elevated aerosol layers to the turbidity of the atmosphere from April until August.

4.1.3 Sun photometer comparison

To investigate the potential of extinction coefficients estimated from particle backscatter coefficients derived from ceilometer measurements, we calculate the aerosol optical depth $\tau_{p,y}$ obtained from YALIS measurements and compared it with the aerosol optical depth $\tau_{p,s}$ determined from sun photometer measurements (cf. Sect. 3.2.1). Observations at 12:00 UTC, 14:00 UTC and 16:00 UTC are used for the comparison—times typically providing a well developed mixing layer. For the comparison, cloud-free conditions for at least 150 min are required. This duration is necessary for the derivation of particle backscatter coefficient profiles from YALIS measurements. Sun photometer measurements are averaged over the same time period of 150 min. $\tau_{p,y}$ is calculated according to Eq. (3.6) with a lidar ratio estimated with $S_p = 50 \pm 10\,\mathrm{sr}$. Due to the linear conversion of β_p to α_p a large uncertainty of 20% of S_p in addition to the uncertainty of typically 18% of β_p must be taken into account when calculating α_p. This results in an uncertainty for $\tau_{p,y}$ of up to 40%. However, this uncertainty is an inherent problem of every backscatter lidar as described in Sect. 2.2.1 and is not only related to ceilometers. The accuracy of $\tau_{p,s}$ is in the order of ± 0.01 (see Sect. 3.2.1), and thus considerable better. Note, that from the geometry of the measurements, $\tau_{p,y}$ concerns the range $z_{ovl,c}$ up to the height where $SNR < 1$, whereas $\tau_{p,s}$ concerns the total atmospheric column and thus, in principle $\tau_{p,y} < \tau_{p,s}$ is expected.

Both independently derived AODs $\tau_{p,y}$ and $\tau_{p,s}$ are shown as monthly mean values in Fig. 4.5 in red and green, respectively. The bars are indicating the uncertainties. The large uncertainty of $\tau_{p,y}$ derived from ceilometer measurements is obvious. An annual cycle of the AOD can be observed with YALIS and the sun photometer. Low values of $\tau_p < 0.03$ are derived for November, December and January and are in very good

agreement between both instruments. From February until June an increase of τ_p up to 0.092 is found from YALIS measurements, whereas sun photometer measurements are only showing an increase up to 0.072 in May. However, the uncertainty of $\tau_{p,y}$ is very large for high τ_p and hence $\tau_{p,y}$ and $\tau_{p,s}$ are still agreeing within their accuracy. From June until December a decrease in τ_p from 0.092 and 0.064 to 0.025 is observed with YALIS and the sun photometer, respectively. The best agreement in between the period of decreasing AOD is found from September–December.

The good overall agreement of $\tau_{p,y}$ from YALIS measurements and $\tau_{p,s}$ from sun photometer measurements demonstrates that it is possible to estimate monthly mean values of AOD. However, that $\tau_{p,y} > \tau_{p,s}$ suggests that the assumed lidar ratio was overestimated for the corresponding month. It must be mentioned that this application is useful for monthly mean values, since diurnal differences are averaged. The advantage of ceilometers over sun photometers which are frequently used for climatologies and statistics is the nighttime capability, which is not provided by sun photometers.

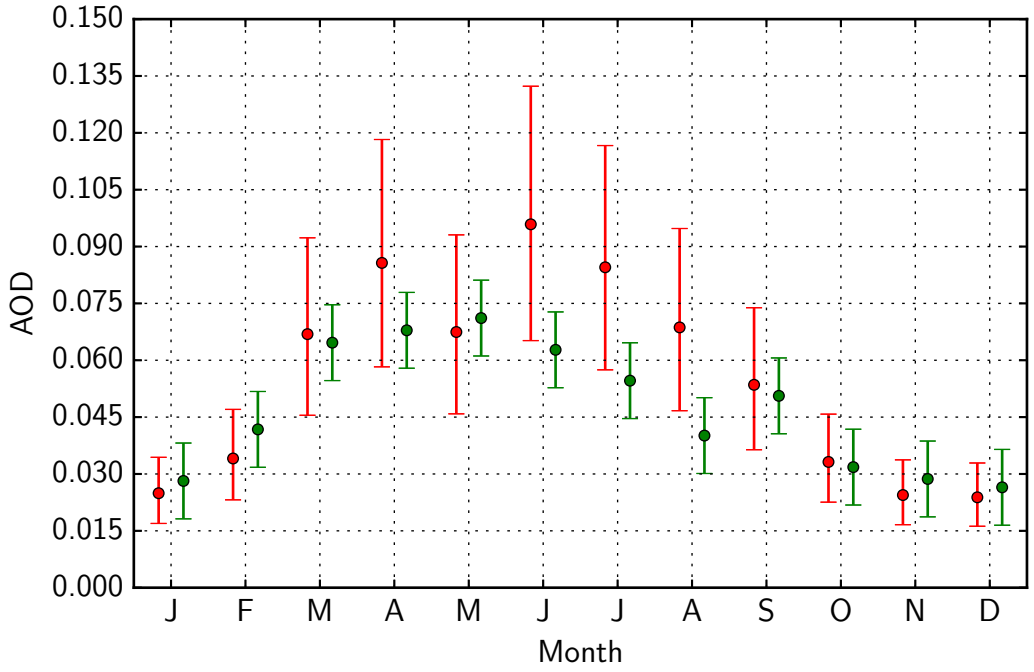

Figure 4.5: Comparison of monthly AOD τ_p at 1064 nm derived from ceilometer (red) and sun photometer (green).

With a comparison of the integrated particle backscatter coefficient β_{int} of the total atmospheric column derived from YALIS measurements and τ_p determined from sun

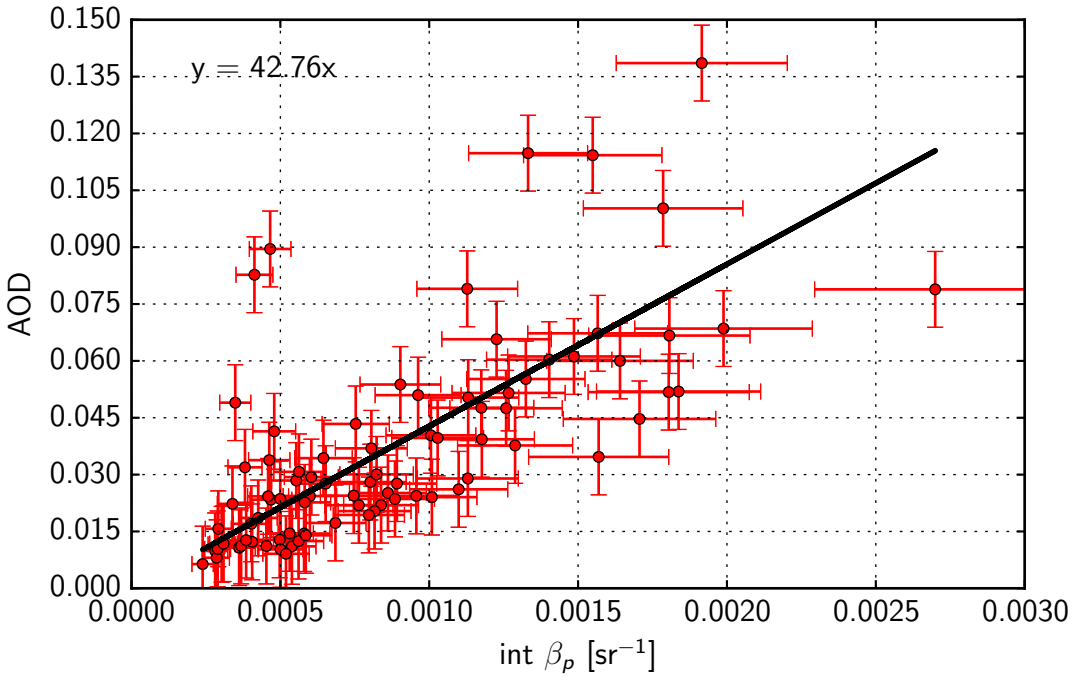

Figure 4.6: AOD at 1064 nm derived from ceilometer (red) vs. sun photometer (green). The slope gives the mean lidar ratio S_p.

photometer measurements, the columnar lidar ratio S_p of aerosol mixtures can be estimated. Again, only cloud-free time periods of 150 min length around 12:00 UTC, 14:00 UTC and 16:00 UTC are used. Data pairs of β_{int} derived from 150 min-averages of YALIS measurements and τ_p determined from sun photometer measurements during the comparison periods are compared in Fig. 4.6. Horizontal and vertical error bars are depicting the uncertainties of β_{int} and τ_p. The three pairs of values in the left, are presumably outliers, influenced from overseen cirrus clouds. The lidar ratio S_p is obtained from relation $\tau_p/\beta_{int} = S_p$ (cf. Eq. 3.6) and is illustrated for a mean $S_p \approx 43$ sr of all measurements as the slope of a regression line shown in black. Deviating from the mean value of $S_p = 43$ sr also smaller and larger values are observed, however, the large uncertainties of β_{int}, illustrated in Fig. 4.6, are hindering a reliable determination of S_p.

4.2 Mixing layer height

4.2.1 Mixing layer characteristics above Munich

5 years of atmospheric observations obtained from YALIS are available for studying ML-characteristics above the measurement site in Munich. The Munich area surrounded by flat terrain might be considered as representative for many regions in Germany. The mixing layer height retrieval algorithm COBOLT (cf. Sect. 3.4.2) provides a reliable (cf. Sect. 3.4.2) continuous derivation of ML-heights at almost any weather conditions. This advantage is used for the following statistical analysis of the ML.

Statistics of ML-heights and growth rates

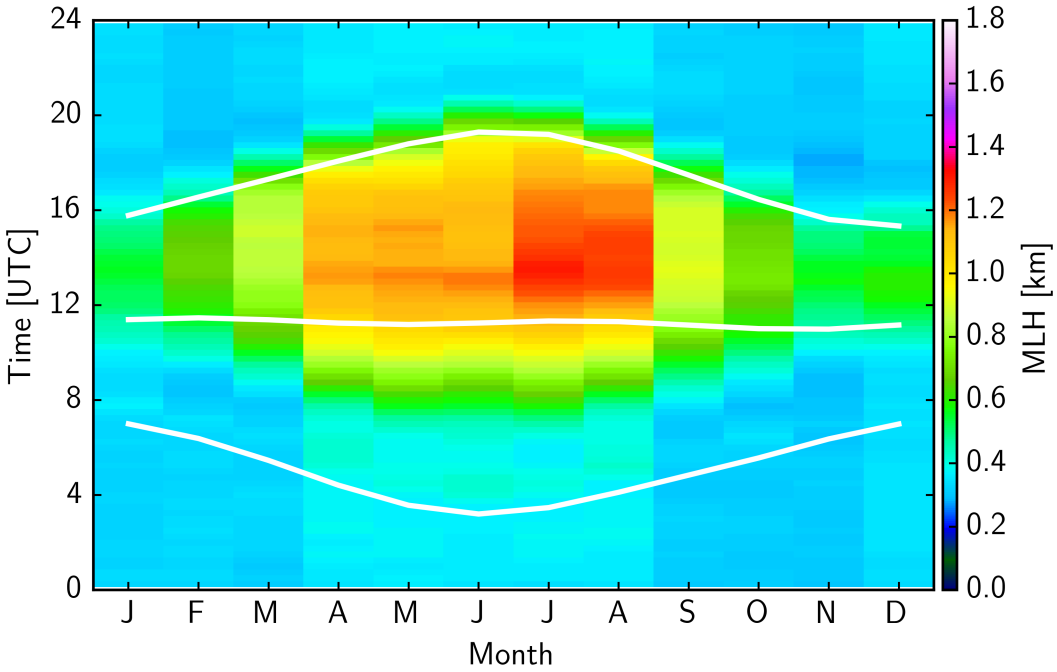

Figure 4.7: Annual cycle of the diurnal cycle of the ML-height derived at any weather condition. x-axis: month; y-axis: time in UTC; colors: ML-height in kilometer. White lines are representing sunrise, noon and sunset, respectively.

To investigate the annual and diurnal cycle of the ML-height above Munich, COBOLT is applied to YALIS-measurements from June 2009 until October 2014 without any restrictions of special weather conditions. That means, also days with clouds and rain

are included. The resulting diurnal cycles of the ML-height are averaged for each month and are illustrated in Fig. 4.7 color coded in kilometer as a function of month (x-axis) and time in UTC (y-axis). The white lines indicate sunrise, noon and sunset, respectively, showing the characteristic annual cycle of northern mid-latitude regions. Sunrise is varying between 03:14 UTC in December–January and 07:04 UTC in June; sunset is varying between 16:19 UTC in December and 21:16 UTC in June. The dependence of the ML-height on the length of daylight period and the solar zenith angle is clearly visible. 3–4 hours after sunrise the ML starts to grow and is reaching its maximum height at around 2 hours after noon. For November–January, mean ML-heights of up to 600 m maximum height are found. Increasing in height from February, MLs with maximum mean heights of around 900 m are already found in March. April–June are showing maximum mean ML-heights of up to 1.1 km. Highest mean MLs are observed in the summer months July and August, when ML-tops at around 1.3 km are observed. Beginning at autumn, mean ML-heights are decreasing again until December. In general, highest MLs are found for summer, whereas winter has the lowest MLs. Comparing spring and autumn, higher MLs are found for spring. A possible reason for this are cold air masses, still prevailing during spring and the strong heating rates already provided by the sun, which induces strong convection and hence mixing layer growth. During autumn, in contrast, high pressure systems are dominant over Europe. In addition, with less frequent strong temperature contrasts with cold air at higher altitudes, the atmospheric layering is more stable, reducing days with strong convection.

To emphasize only days with large solar insolation where mixing layer growth processes are forced, diurnal cycles of ML-heights, which are not dominated by clouds are shown in Fig. 4.8. The selection criterion is no occurrence of clouds up to 3000 m for more than 2 hours during the strongest expected growth of the ML which is between 2 hours after sunrise and noon. As in Fig. 4.7 a diurnal cycle of the annual cycle of the ML is visible, however, more pronounced. Where during winter only slight changes of the ML-height compared to Fig. 4.7 are observed, clear differences are found for spring, summer and autumn in Fig. 4.8. In all three seasons higher MLs are observed. March shows ML-heights up to 1.1 km. From April until June the mixing layer reaches mean heights between 1.2 km and 1.4 km. July is found to be the month with highest mean mixing layers up to 1.5 km.

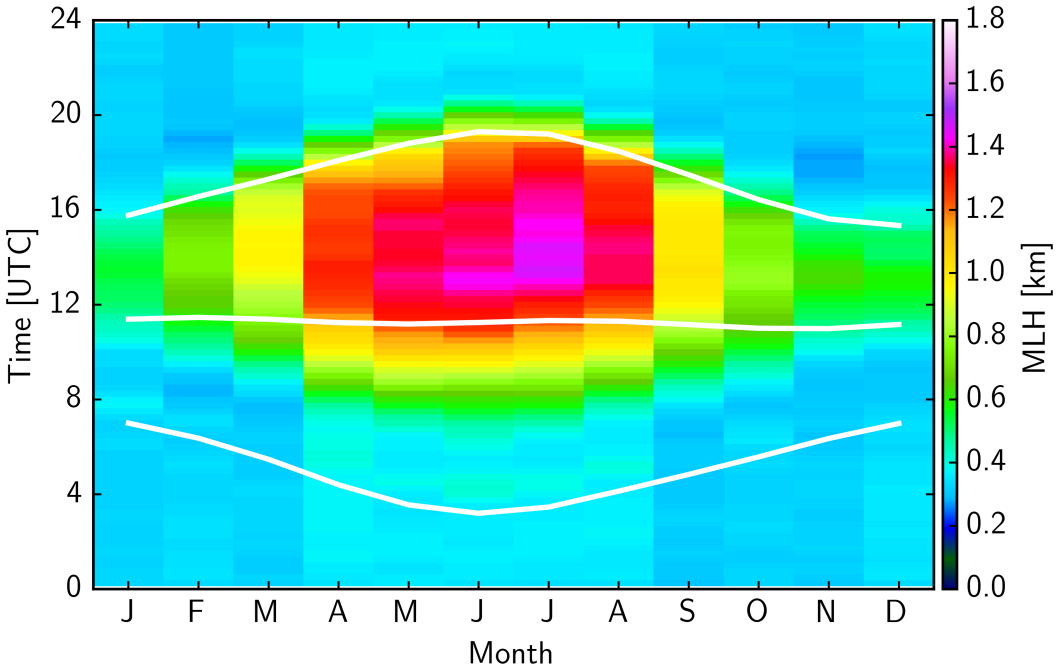

Figure 4.8: Annual cycle of the diurnal cycle of the ML-height derived on days with only fair weather clouds and a maximum of short rain. x-axis: month; y-axis: time in UTC; colors: ML-height in kilometer. White lines are representing sunrise, noon and sunset, respectively.

The continuous monitoring of diurnal mixing layer developments allow to derive another important property of MLs—their growth rate. The speed of the development of the ML is driven by e. g. atmospheric stability and the surface heat balance. With COBOLT providing a continuous ML-height retrieval, mean growth rates and maximum growth rates are calculated in the following, corresponding to the monthly mean diurnal cycles of ML-heights shown in Figs. 4.7 and 4.8.

For the growth rate calculations, a 1-hour sliding average is applied to the determined ML-height. The maximum of the second derivative of z_{ml} from 1 hour until 3 hours after sunrise is chosen as the beginning of the ML development. The minimum of the second derivative found between 60 minutes before and 180 minutes after noon is chosen as the end of the growth process. The height difference of z_{ml} at both reference times yields the mean growth rate. The maximum of the first derivative in between is set as the maximum growth rate. Monthly mean values of mean (blue) and maximum (red) growth rates are shown as box plots in Figs. 4.9 and 4.10.

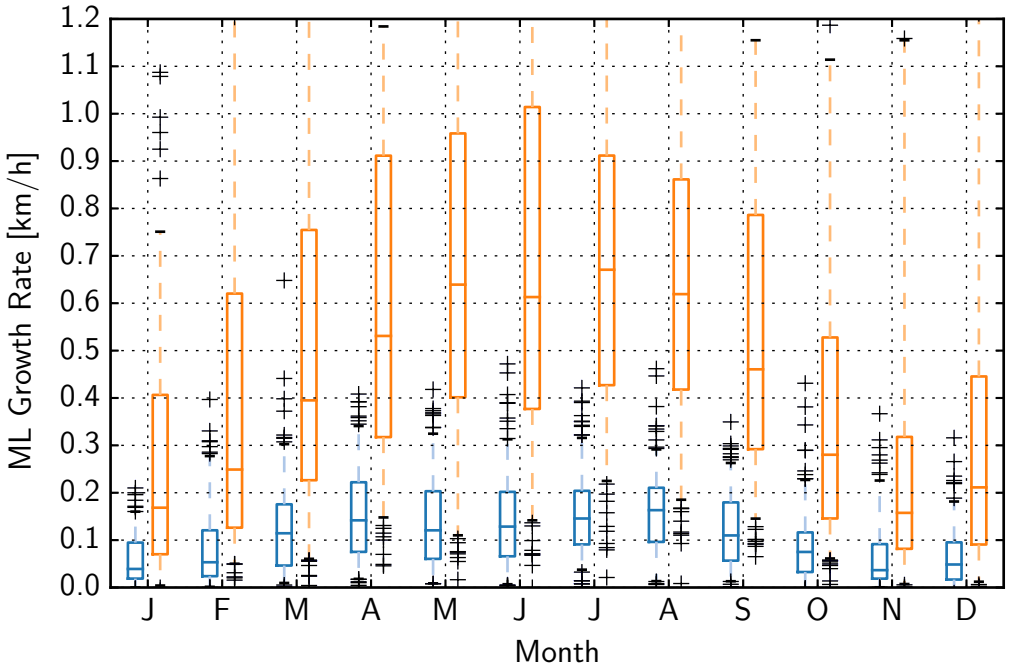

Figure 4.9: Growth rate of the ML at any weather condition. Mean growth rates are shown in blue, maximum growth rates in red.

Fig. 4.9 comprises all available diurnal cycles of MLs. An annual cycle of mean and maximum growth rates with larger values during summer can be observed. The annual cycle of mean growth rates, however, is less pronounced. From October–February, mean growth rates mainly below $0.1\,\mathrm{km\,h^{-1}}$ with a median around $0.05\,\mathrm{km\,h^{-1}}$ are observed. For March and September slightly larger growth rates with a median of $0.1\,\mathrm{km\,h^{-1}}$ are found. Mean growth rates with median values between $0.1\,\mathrm{km\,h^{-1}}$ and $0.2\,\mathrm{km\,h^{-1}}$ are obtained from April until August. These small differences of mean growth rates between winter and summer are not explaining the large differences of ML-heights obtained for both seasons. However, when taking the different daytime length into account with potentially more time for the sun in summer to heat the surface, a longer duration of the growth process is the fundamental reason for the pronounced annual cycle of the ML-height. The stronger incoming shortwave radiation due to smaller solar zenith angles, however, are particularly noticeable in the maximum growth rates. In January a median value of only $0.2\,\mathrm{km\,h^{-1}}$ is found. The maximum growth rate steadily increases up to $0.6\,\mathrm{km\,h^{-1}}$ until May and remains con-

stant between 0.6–0.7 km h^{-1} until August. If 75th percentiles are considered, the largest maximum growth rates up to 1.0 km h^{-1} can be found for June.

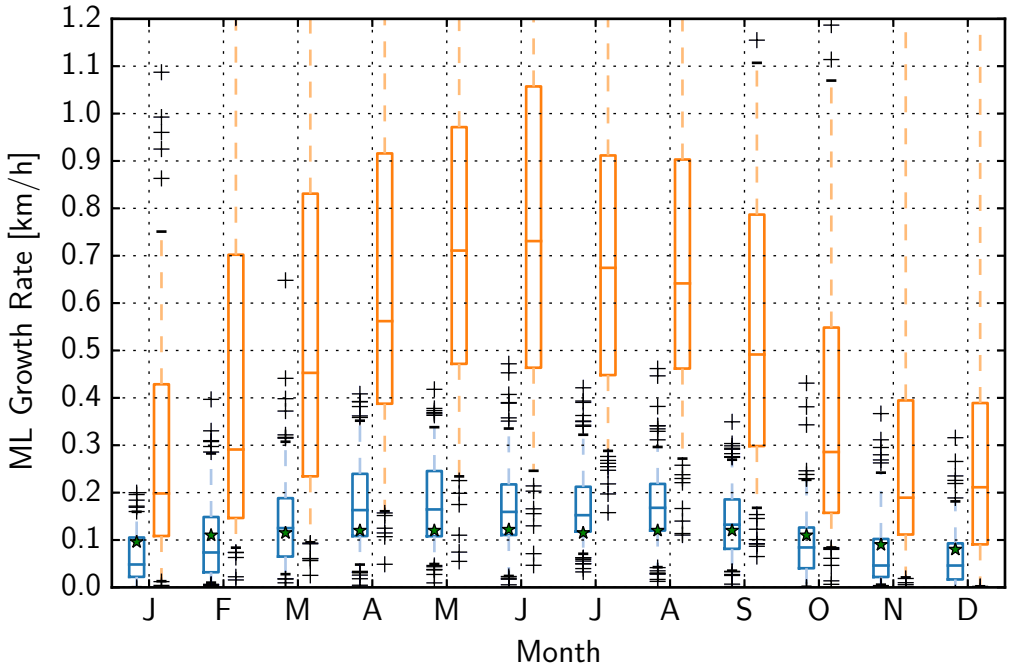

Figure 4.10: Growth rate of the ML during cloud-free and only partly cloudy conditions. Mean growth rates are shown in blue, maximum growth rates in red. Green stars are representing growth rates calculated by Gold (1933)

Corresponding to Fig. 4.8, the growth rates derived during only cloud-free and partly cloudy conditions are shown in Fig. 4.10. Compared with growth rates determined for all days, larger values are found for mean and maximum growth rates, but again the monthly changes of the mean growth rates remain small.

First attempts in predicting mixing layer growth rates and maximum ML-heights were made by Gold (1933). He used temperature and dew point data from atmospheric soundings in a tephigram to calculate monthly mean daily amounts of solar radiation and corresponding heights up to which they would change an isothermal state to an adiabatic state—the ML-height. His results are valid for latitudes at 52° N when almost cloud-free conditions are prevailing and a dry surface is present. His findings are shown in Fig. 4.10 as green stars. Within the 25th and 75th percentile, a very good agreement between both independently derived mean growth rates is found, although the measurement site is located at 48.148° N. This demonstrates the success of Gold's first attempts in predicting ML-heights and growth rates.

ML-height comparison of stations near Munich

Meteorological investigations of urban areas mainly focus on air quality issues. With the implementation of ceilometers a new option is available to also study effects of the structure and height of the ML. The increasing number of ceilometers operating in networks allows the observation of the ML at a significant number of locations and can show differences of the ML at regional scales, e. g. differences between rural areas and cities. The continuous determination of ML-heights allows to investigate variations of the diurnal ML development with a high temporal resolution. Differences of ML-heights can be caused by different terrain and land-use—e. g. the so called urban heat island effect (Rotach et al., 2005; Pal et al., 2012; Barlow, 2014). Since the ML is that part of the atmosphere, where pollutants can be mixed vertically and thus can influence human health, a study of ML-height-differences between urban and rural sites is especially interesting. To demonstrate the potential of providing such studies, one case study including the comparison of only 3 stations and a limited period is discussed as an example in the following. It should be emphasized that such investigations must be extended to come to general conclusions.

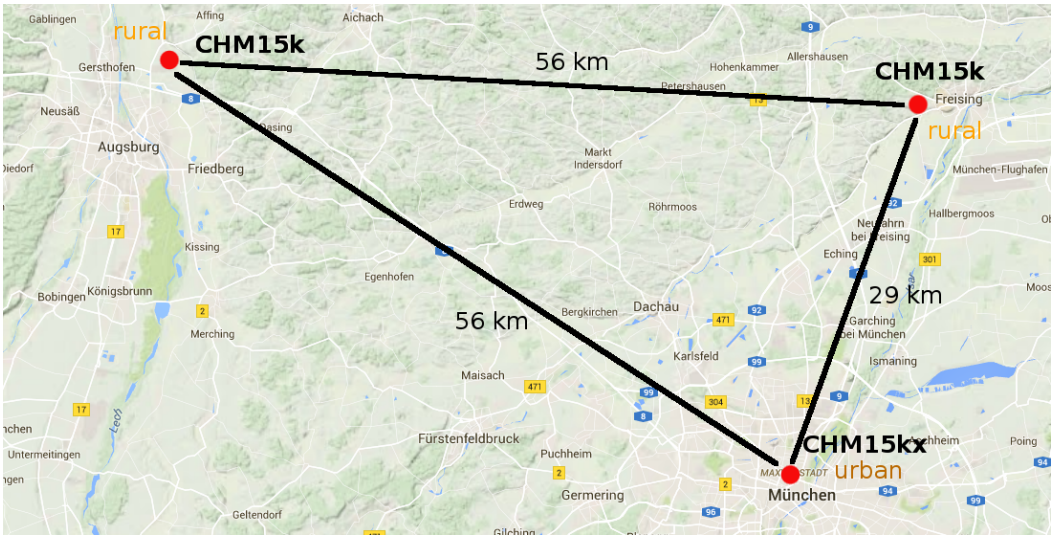

Figure 4.11: Overview of the measurement area including the rural measurement sites Augsburg (red dot, top left) and Weihenstephan (red dot, top right), and the urban measurement site in Munich (red dot, bottom).

Within the ceilometer network of the German weather service DWD, two ceilometers near Munich are available and suitable for a comparison with YALIS. Fig. 4.11 shows the three measurement sites as red dots: rural measurement sites near Augsburg

(top left) and Weihenstephan (top right), and the urban site in the center of Munich (bottom). Augsburg (48.43° N, 10.94° E) with a distance of 56 km from Munich is located in the Lech valley at 461 m altitude. Weihenstephan (48.40° N, 11.70° E) is located at the boarder of the Isar valley 29 km northeast of Munich at an altitude of 477 m. The orography between Weihenstephan and Augsburg can be characterized as hilly. Between Weihenstephan and Munich, flat terrain is predominant. The instruments operating at Augsburg and Weihenstephan are Jenoptik CHM15k, having a higher z_{ovl} than YALIS. An overlap correction is applied according to Sect. 3.3.1 which yields a $z_{ovl,min} = 300$ m for both instruments. Their data has undergone a relative calibration as described in Sect. 3.3.2.

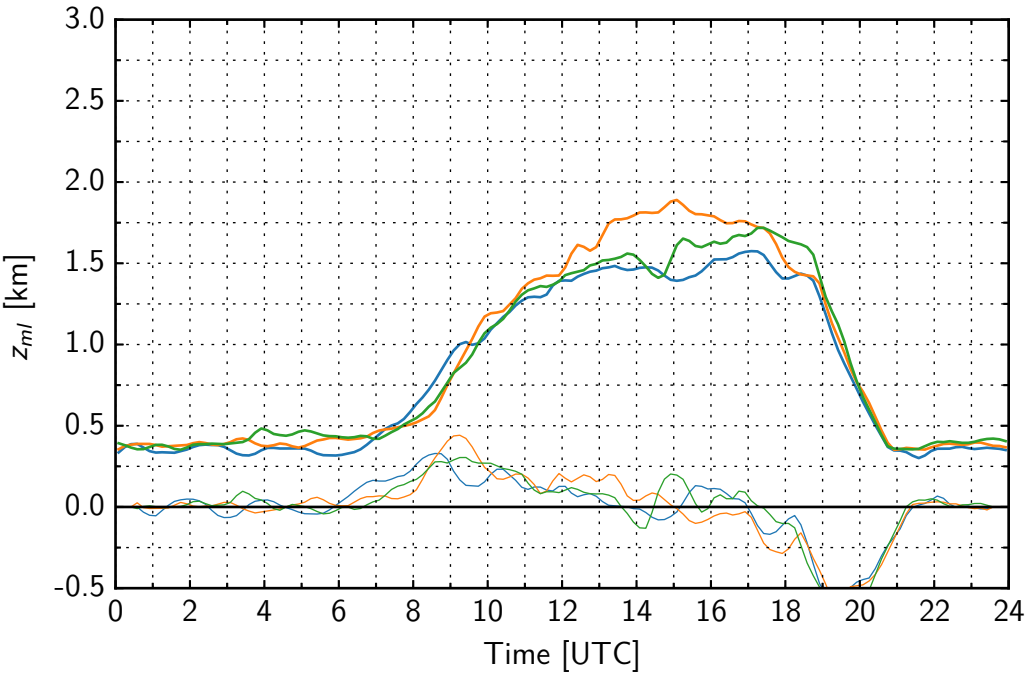

Figure 4.12: Mean diurnal cycle of the ML-height (thick lines) and growth rates in km/h (thin lines) between 30 June 2010–13 July 2010 for Augsburg in orange, Munich in blue and Weihenstephan in green.

For the comparison, a time period with pronounced diurnal ML-height cycles is chosen, i. e. with less precipitation and low cloudiness. A suitable time period could be found from 30 June 2010–13 July 2010. During this time span a low pressure system was located between Iceland and the British Isles. An extensive high pressure system reached from the Azores over the Iberian Peninsula to the Baltic Sea. Over the southeastern part of Germany, a predominantly easterly flow was prevailing near

the surface. The 1st, 4th–6th, 8th and 12th July are excluded due to precipitation events or continuous cloud cover at one of the stations. Hence, 8 days are used for the comparison.

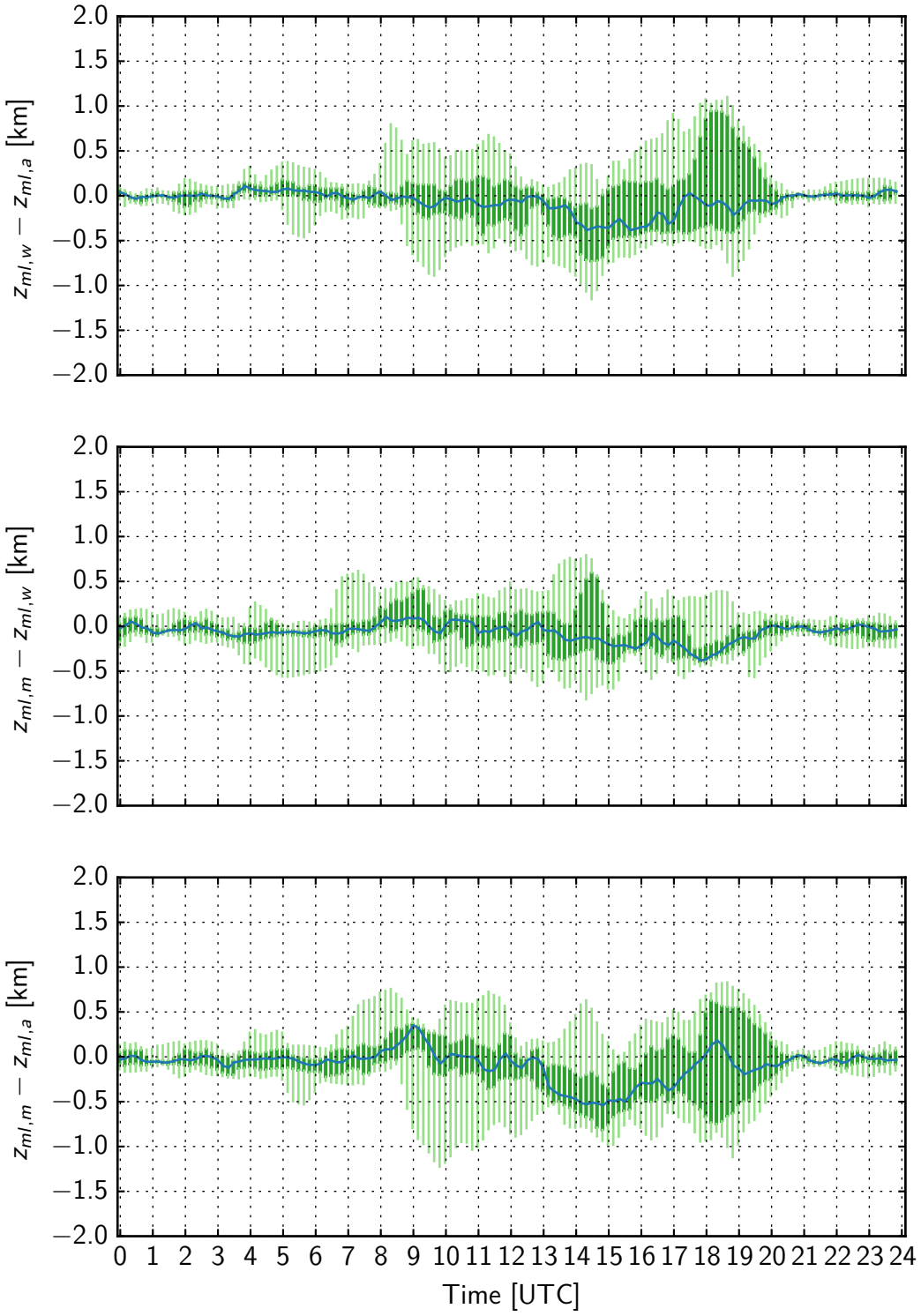

Figure 4.13: Differences of ML-heights derived for Augsburg ($z_{ml,a}$), Weihenstephan ($z_{ml,w}$) and Munich ($z_{ml,m}$) between 30 June 2010–13 July 2010. First panel: $z_{ml,w} - z_{ml,a}$; Second panel: $z_{ml,m} - z_{ml,w}$; Third panel: $z_{ml,m} - z_{ml,a}$. Thick green lines are indicating 25th and 75th percentiles. Thin green lines are representing minimum and maximum values.

A mean diurnal cycle of the ML-height of all days is shown in Fig. 4.12 for Augsburg (thick orange line), Weihenstephan (thick green line) and Munich (thick blue line). The thin lines at the bottom represent the growth rate in km/h, determined as described in the previous section. Sunrise for the comparison period is at around 03:22 UTC, sunset is at around 19:14 UTC. A well pronounced diurnal cycle is visible for all stations with an increase of the ML-height at around 3–4 hours after sunrise, reaching the maximum ML-height 2–3 hours after noon. The ML-height growth for Augsburg remains strong until 14:00 UTC whereas the growth rates for the stations Weihenstephan and Munich already decrease after 11:00 UTC, resulting in lower ML-heights of $1.4\,\text{km} < z_{ml} < 1.6\,\text{km}$ between 12:00-17:00 UTC. For Augsburg a mean maximum ML-height of $z_{ml} = 1.8\,\text{km}$ is reached between 14:00–16:00 UTC. However, the ML in Munich and Weihenstephan is growing until 17:00 UTC, whereas the ML in Augsburg stops to grow at 15:00 UTC. The ML-heights found for Munich and Weihenstephan are in very good agreement for the whole diurnal cycle, but lowest ML-heights are found for the urban site in Munich. This is somewhat surprising as larger ML-heights are expected for urban areas because of the urban heat island effect. However, when considering times after sunrise, a difference between the rural sites and the urban site is found for growth rates and ML-heights during the early development process. The growth rate for Munich is already increasing at 06:00 UTC, while the other stations show increasing growth rates beginning at 07:00 UTC. This results in a higher ML for Munich between 07:00 UTC and 09:00 UTC.

To further investigate the development of the ML, differences of the diurnal cycles between each station are shown for each hour in Fig. 4.13. Box plots indicate the 25th and 75th percentiles (thick green line), and minimum and maximum values (thin green line). The blue line represents the median. The first panel shows the differences of the ML-height at Augsburg ($z_{ml,a}$) and Weihenstephan ($z_{ml,w}$). The second panel shows the differences between Munich ($z_{ml,m}$) and Weihenstephan and the third panel shows the differences between Munich and Augsburg. In particular, between 08:00–09:30 UTC a distinct difference between the rural and urban sites with a median value up to 0.25 km and 25th percentile larger than 0 is found and can be caused by faster heating of the urban area. This feature is not found in the first panel for the differences of both rural sites. The clear difference between 13:00 UTC and 17:00 UTC between Augsburg and the other stations illustrates the fast growth of the ML up to its larger maximum height.

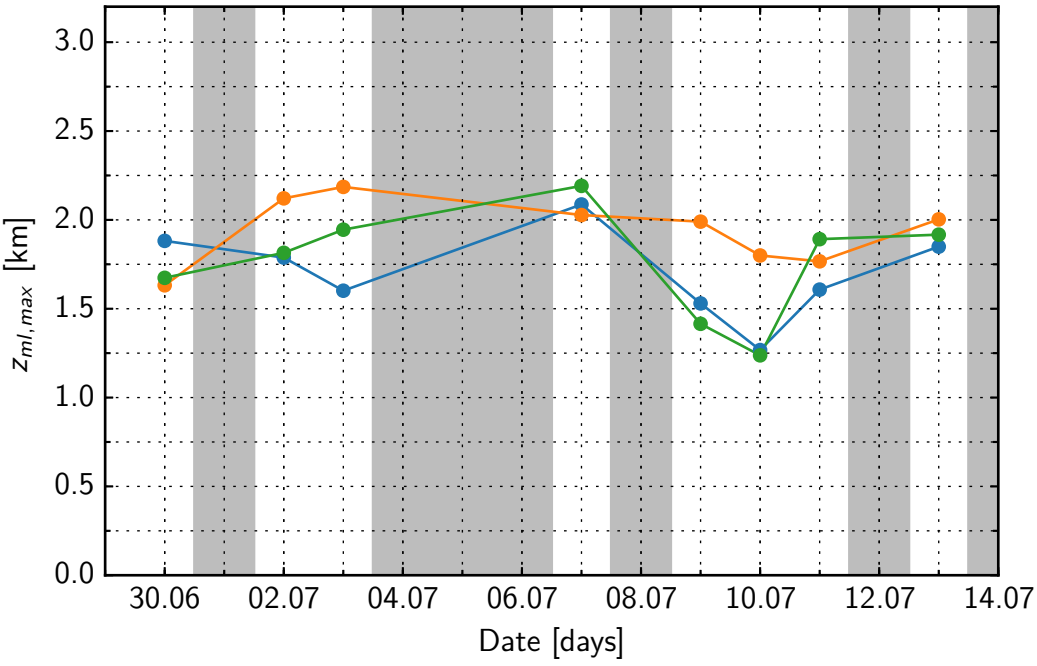

Figure 4.14: Maximum ML-heights for the comparison period above Augsburg in orange, Munich in blue and Weihenstephan in green.

The daily maximum ML-heights of Augsburg (orange), Weihenstephan (green) and Munich (blue) are compared in Fig. 4.14. Maximum ML-heights reached at Augsburg are the highest for most of the days with 1.75 km $< z_{ml,a} <$ 2.25 km. The MLs for Weihenstephan and Munich stay below 2 km for the whole comparison period except for 7 July. The strong decrease in maximum ML-heights between 9–11 July can be caused by a strong elevated aerosol layer which was observed up to 5 km from 9–12 July (not shown here). The maximum ML-heights at Munich and Weihenstephan have a better overall agreement with slightly lower values for Munich. An urban heat island effect is not evident from the maximum ML-heights.

Comparison with model MCCM

As already stated, there is a strong demand to estimate ML-heights as an indicator for air quality and its influence on human health. For this reason, several numerical chemistry transport models provide ML-heights (e. g. WRF-Chem, COSMO-ART). In principle, ML-heights from weather prediction models can be used for air quality forecasts provided that the parameterization of the ML-height has been validated by

measurements. Comparisons between modeled and observation-derived ML-heights can be found in literature (Balzarini et al., 2014; Bachtiar et al., 2014; Korhonen et al., 2014). However, a thorough validation of calculated ML-heights needs continuous diurnal ML-height cycles. These can be provided using ceilometer measurements. In the following, mixing layer heights derived with COBOLT are compared with ML-heights predicted by the Mesoscale Climate-Chemistry Model (MCCM) (Grell et al., 2000).

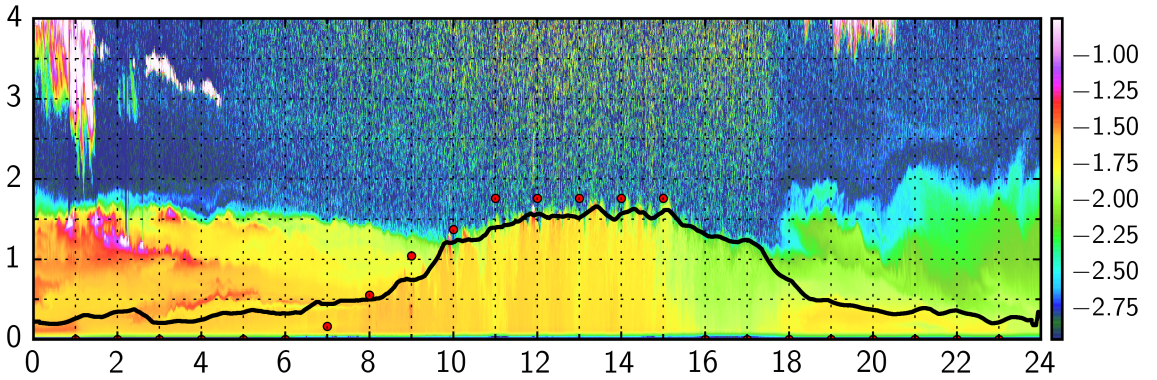

Figure 4.15: Time height cross section of the range-corrected signal (in logarithmic scale, a.u.) from YALIS, 7 April 2014. The thick black line marks the ML-height determined by COBOLT. Red dots are representing ML-heights calculated by the model MCCM.

The online coupled meteorology atmospheric chemistry model MCCM is used for investigations of air quality during episodes of particular interest such as summer smog situations or wintertime episodes with high particulate matter concentrations, real time weather and air quality forecasts, as well as for the investigation of climate impact on regional air quality (Forkel and Knoche, 2006). Aerosol processes are described with the modal aerosol module MADE/SORGAM (Schell et al., 2001) which distinguishes three modal particle size distributions. The turbulence parameterization is based on the second-order, level 3 scheme developed by Burk and Thompson as described by Grell et al. (2000). The ML-height is determined from the calculated turbulence subsequently. For unstable conditions: ML-height is the height z where the virtual potential temperature at height z is the same as at the surface, i. e. $\Theta_v(z) = \Theta_v(0)$. For stable conditions: ML-height is the height where the Bulk-Richardson number $Ri(z) > 0.2$ (Hansen, 1966). The simulations used here, are from routine forecasts published by IMK-IFU, Garmisch-Partenkirchen (www.imk-ifu.kit.edu), covering a

time period from 1 January 2014 until 27 October 2014. The horizontal resolution is set to 2 km and the vertical resolution is several meters near the ground and increases with height. The ML-height is only provided for daytime, where turbulent mixing forced by thermal heating of the ground is present.

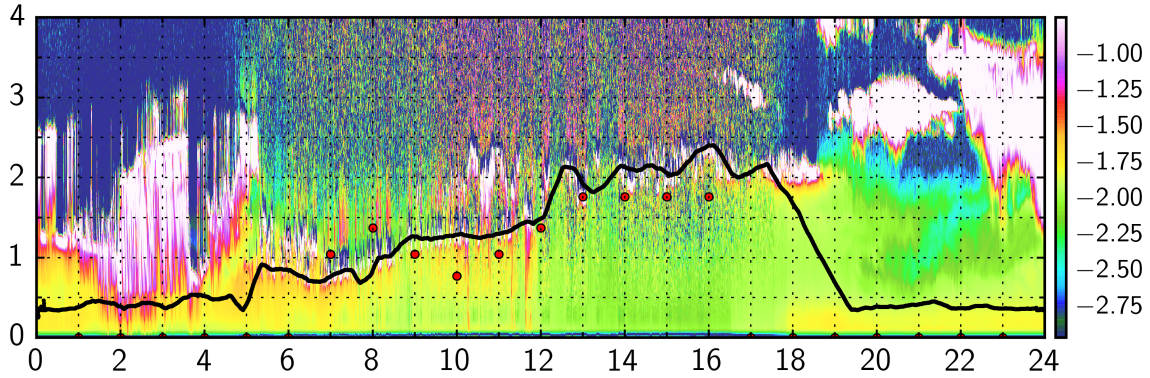

Figure 4.16: Same as Fig. 4.15 but on 9 April 2014.

To demonstrate the applicability of MCCM for ML-height forecasts, three example days with ML-heights derived from YALIS measurements (black line) and MCCM (red dots) are shown in Figs. 4.15, 4.16 and 4.17.

Fig. 4.15 shows the time height cross section of the range corrected signal from YALIS measured on 7 April 2014. A well pronounced diurnal ML-cycle can be observed with the growth starting at around 08:00 UTC and a maximum ML-height of $z_{ml} =$ 1.7 km reached at 13:30 UTC. The ML starts to decrease at 15:00 UTC. COBOLT traces the ML-height during its whole development process continuously. The ML-height predicted by the model is in very good agreement with the ML-height derived by COBOLT. The start of the growth process, the subsequent increase and the almost constant height of the ML between 12:00–15:00 UTC is mapped.

Fig. 4.16 shows a second example (9 April 2014) with a convective ML with broken clouds and short light precipitation events between 12:00–14:00 UTC. A steady increase of the ML-height from 07:00 UTC until 16:00 UTC is found by COBOLT. This complex case is also resolved by the model, however, not in detail. Larger deviations of the model from COBOLT occur between 07:00 UTC and 10:00 UTC when broken cloud fields are observed. These meteorological conditions make a reliable forecast of ML-heights difficult. Small mismatches in time and place of clouds are likely to occur and influence the calculated ML-height.

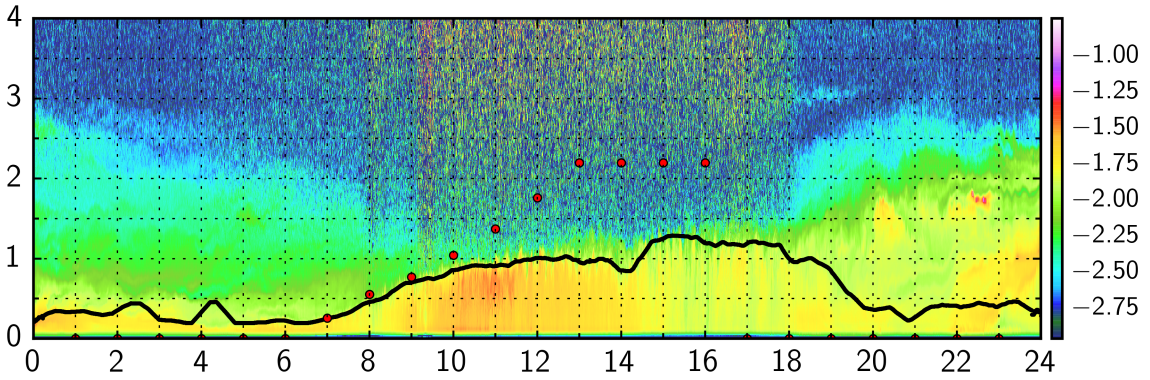

Figure 4.17: Same as Fig. 4.15 but on 25 April 2014.

In Fig. 4.17 the time height cross section of the range corrected signal from 25 April 2014 is shown. A convective well pronounced mixing layer is observed on this day. At 07:00 UTC the ML starts to grow until it reaches its maximum height at 15:00 UTC. It is constant at 1.2 km until 18:00 UTC. The model MCCM can predict the beginning of the growth process, however overestimates the ML-height after 10:00 UTC, reaching a maximum ML-height of 2.2 km, which is 1 km above the maximum ML-height found by COBOLT. This overestimation can be found on several days.

All available ML-heights are compared in Fig. 4.18. No days are excluded due to special weather conditions. The x-axis shows ML-heights $z_{ml,m}$ predicted by the model, the y-axis shows ML-heights $z_{ml,c}$ determined by COBOLT. The decreasing vertical resolution of the model with height is clearly visible and must be taken into account when comparing with high resolution data of the ceilometer. A correlation coefficient $r = 0.86$ is obtained. Up to $z_{ml,m} = 1050\,\mathrm{m}$ both ML-heights show a good agreement within the 75th percentile. For ML-heights $z_{ml,m} > 1050\,\mathrm{m}$ the model tends to an overestimation of the ML-height—the same feature already observed in Fig. 4.17. This overestimation cannot be explained solely by the coarse vertical model resolution. Another discrepancy of the ML-height is observed for ML-heights $z_{ml,m} < 1050\,\mathrm{m}$ when ML-heights $z_{ml,c}$ are often much too large. One reason for this is the minimum measurement range of $z_{ovl,min} = 135\,\mathrm{m}$, which doesn't allow a detection of even lower $z_{ml,c}$. To investigate if meteorological conditions have influence, only days with cloud-free conditions up to 3000 m are compared in Fig. 4.19. Then, the outliers for ML-heights $z_{ml,m} < 1050\,\mathrm{m}$ disappear. This reveals the difficulties of the model in predicting ML-heights when precipitation or small-scale clouds occur. COBOLT

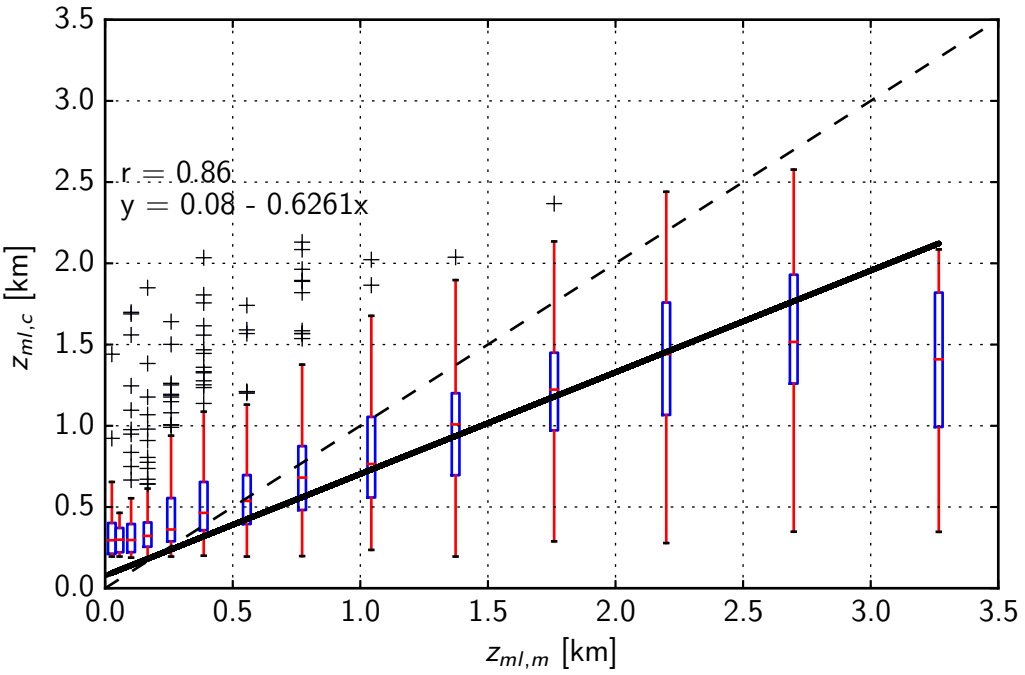

Figure 4.18: Comparison of ML-heights derived from YALIS measurements with COBOLT ($z_{ml,c}$) and calculated by the model MCCM ($z_{ml,m}$). The regression line is shown in black.

can trace the ML-top even under such conditions, whereas even small displacements in time and space of the modelled cloud distribution might prevent the model to calculate right ML-heights. But even when applying the cloud filter, the trend to larger $z_{ml,m}$ for ML-heights $_{ml,m} > 1050\,\mathrm{m}$ remains.

To obtain reliable ML-heights from weather forecast models, further investigations with respect to the application and validation of different ML-height pramaterizations are necessary.

4.2.2 Impact of ML-height on air pollution

To describe the relation between air pollution, expressed in terms of concentration of particles or trace gases, and the meteorological condition, often the concept of the mixing layer is introduced. The underlying assumption is that high concentrations close to the surface coincide with narrow mixing layers, in other words, the mixing layer height can be used as a proxy for the air quality (e g. Svensson

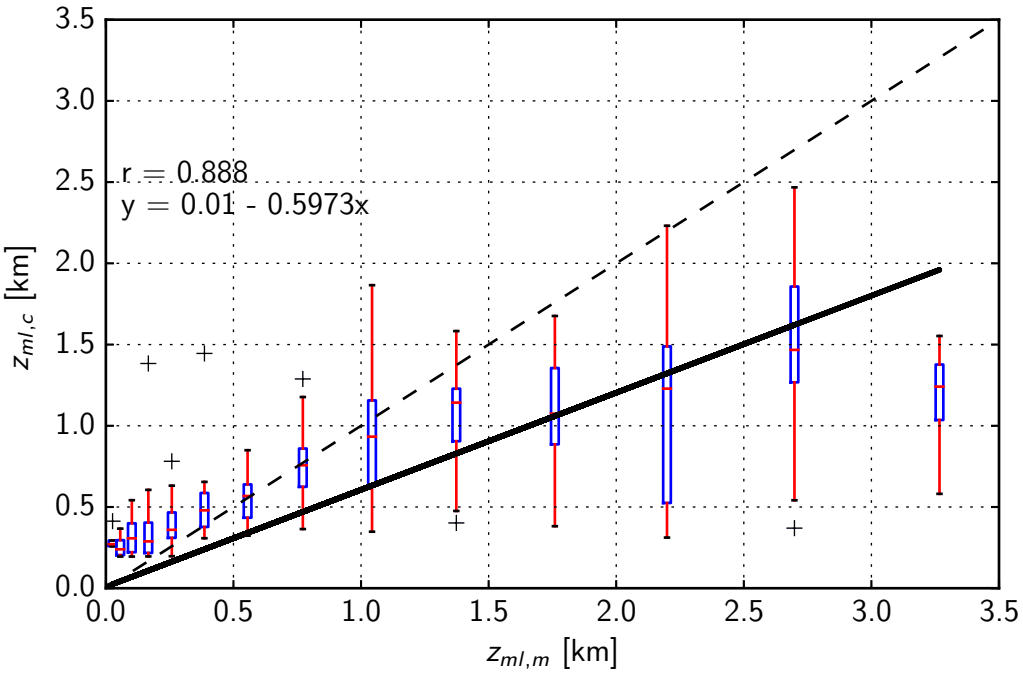

Figure 4.19: Same as Fig. 4.18 but only cases without clouds below 3000 m.

et al. (2011)). This assumption is investigated in the following by means of measurement data obtained during the BAERLIN2014 campaign (see Sect. 3.4.2, BLVIEW), however, only briefly outlined to demonstrate the potential of this application in general. Co-located to the measurements of the Vaisala ceilometer CL51 (Berlin-Neukölln, Nansenstraße, 52.4894° N, 13.4309° E), observations of PM1, PM2.5 and PM10 were performed by the Federal Environment Agency (UBA) of Germany with an optical particle counter (GRIMM 1.108). The measurement station can be considered as "urban background site" with only four years since 2000 when the PM10-threshold (daily average of 50 µg/m^3) was exceeded in more than 35 days (http://ec.europa.eu/environment/air/quality/standards.htm). The annual average of 2013 was 23 µg/m^3 and 16.8 µg/m^3 of PM10 and PM2.5, respectively.

Particle mass concentrations are available as half hour averages of PM10, PM2.5, and PM1. Note, that all times are given in CET, which is one hour different to UTC ("UTC + 1 hour = CET"). Fig. 4.20 shows the mean diurnal cycles of the ML $z_{ml,c}$ derived with COBOLT from CL51 measurements (first panel) and mean diurnal cycles of particle mass concentrations for several size ranges (second panel). It can be seen, that the temporal variability of PM1 and PM2.5 is small, i. e. less than 5 µg/m^3 over

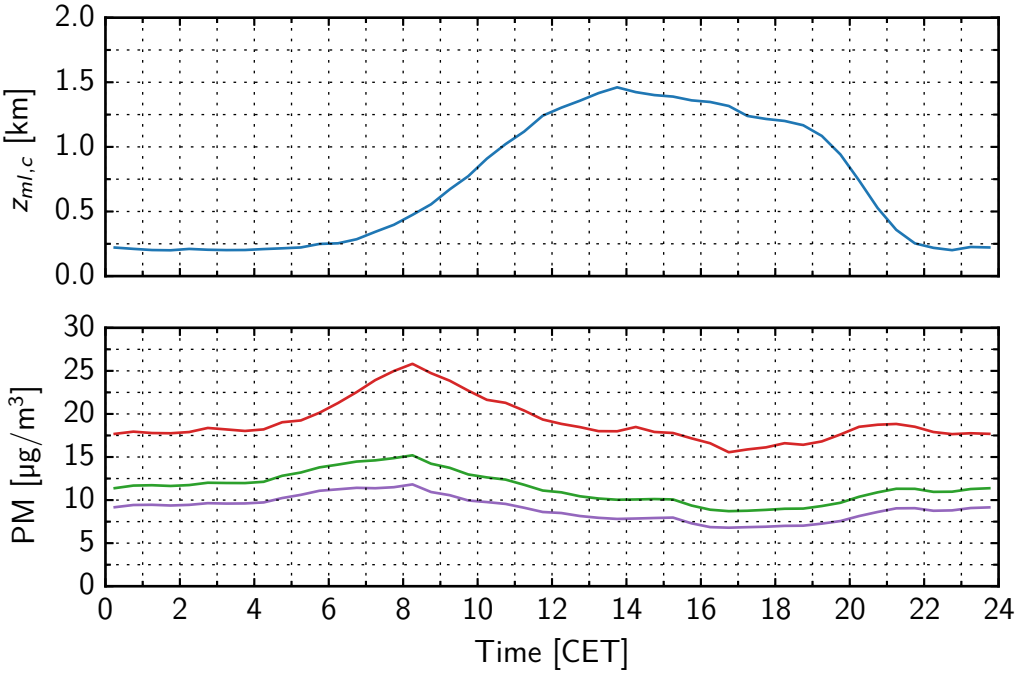

Figure 4.20: Mean diurnal cycles of particulate matter, averaged over 67 days. PM1 (violet), PM2.5 (green), and PM10 (red) as derived by UBA-measurements, PM10 (brown) as measured by the BLUME-network.

the day with a "shallow" minimum in the afternoon. The temporal dependence of the PM10-concentration, however, is much more pronounced, showing a distinct maximum at around 08:00 CET. A gradual increase in the late evening (approximately 20:00–22:00 CET) is similar at all size ranges.

Comparing the mean diurnal cycles of the ML-height (first panel) and particle mass concentrations (second panel) reveals that the temporal development of ML-height better fits the PM1 and PM2.5 curves. For the PM10-curve one would rather expect a decrease during the $z_{ml,c}$ increase between 06:00 and 08:00 CET.

Fig. 4.21 shows the correlation between the mean ML-heights and particle mass concentrations on the basis of 30-minute averages. As expected from the previous figure, the absolute values of the correlation coefficients are quite high, $r = -0.70$ and $r = -0.63$ for PM1 and PM2.5, respectively, but significantly lower for PM10 ($r = -0.27$). This is related to the fact, that the PM10-curve shows this increase between 06:00 and 08:00 CET.

A possible explanation for this increase of the PM10-curve can be the stable stratified nocturnal boundary layer. During night it prevents trace gases which are emitted or

already present in the residual layer (e. g. pollutant emission from chimneys) to reach the ground, where particulate matter observations are performed. The growing mixing layer after sunrise, however, forces a down-mixing of these trace elements when the ML reaches the residual layer. Thus, there should be the highest values in particulate matter (Neu et al., 1994).

Temporal fluctuations in PM due to varying meteorological conditions or pollutant emissions disappear when averages over the whole campaign period are investigated. Lower correlation is found when individual pairs of ML-height and PM from the BAERLIN campaign period are considered. In Fig. 4.22, the large variation of ML-heights and corresponding particulate matter is visible. A negative correlation is found for all size ranges, however less clear than for averaged values in Fig. 4.21. Low correlation coefficients of $r = -0.22$, $r = -0.22$ and $r = -0.12$ are obtained for PM1, PM2.5 and PM10, respectively. However, if considering the maximum values of PM for all ML-heights, a clear dependence is found. That means, maximum values of particulate matter are influenced by the ML-height. This feature is also found by Wagner and Schäfer (2015) who investigated correlations of ML-heights and PM10, amongst others, during winter 2011/2012 at an urban station in Essen.

These results suggest that there in fact is a link between air quality and the ML-height. For a final conclusion on the potential of ML-height to estimate air quality and for the assessment of the strength of the correlations, more studies are however required. Cities with local air quality networks and ceilometers can provide a promising testbed for this kind of studies.

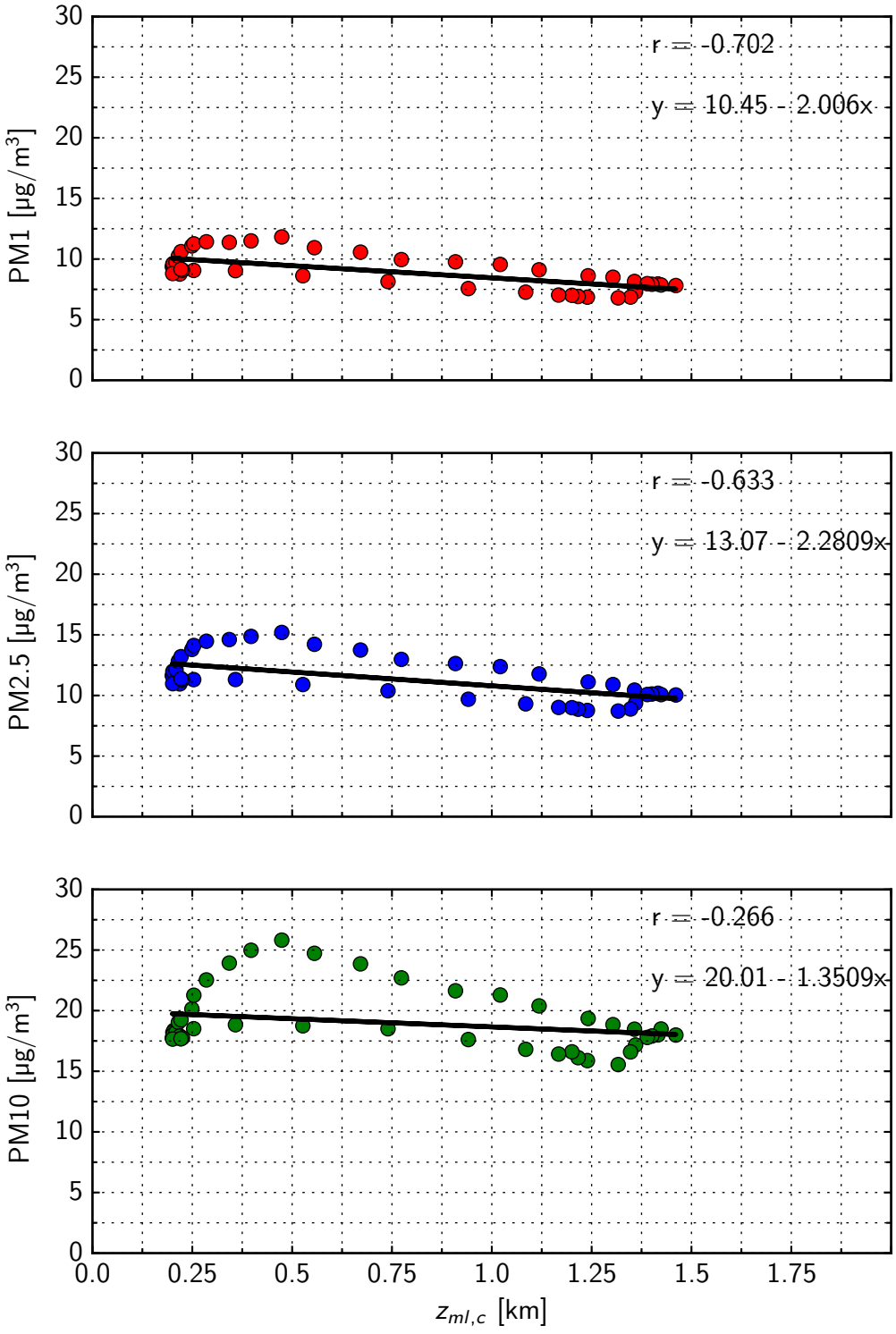

Figure 4.21: Correlation between 30-minute averages of $z_{ml,c}$ and particulate matter, averaged over the full BAERLIN campaign period. From top to bottom panel: PM1, PM2.5, and PM10 from the UBA-network.

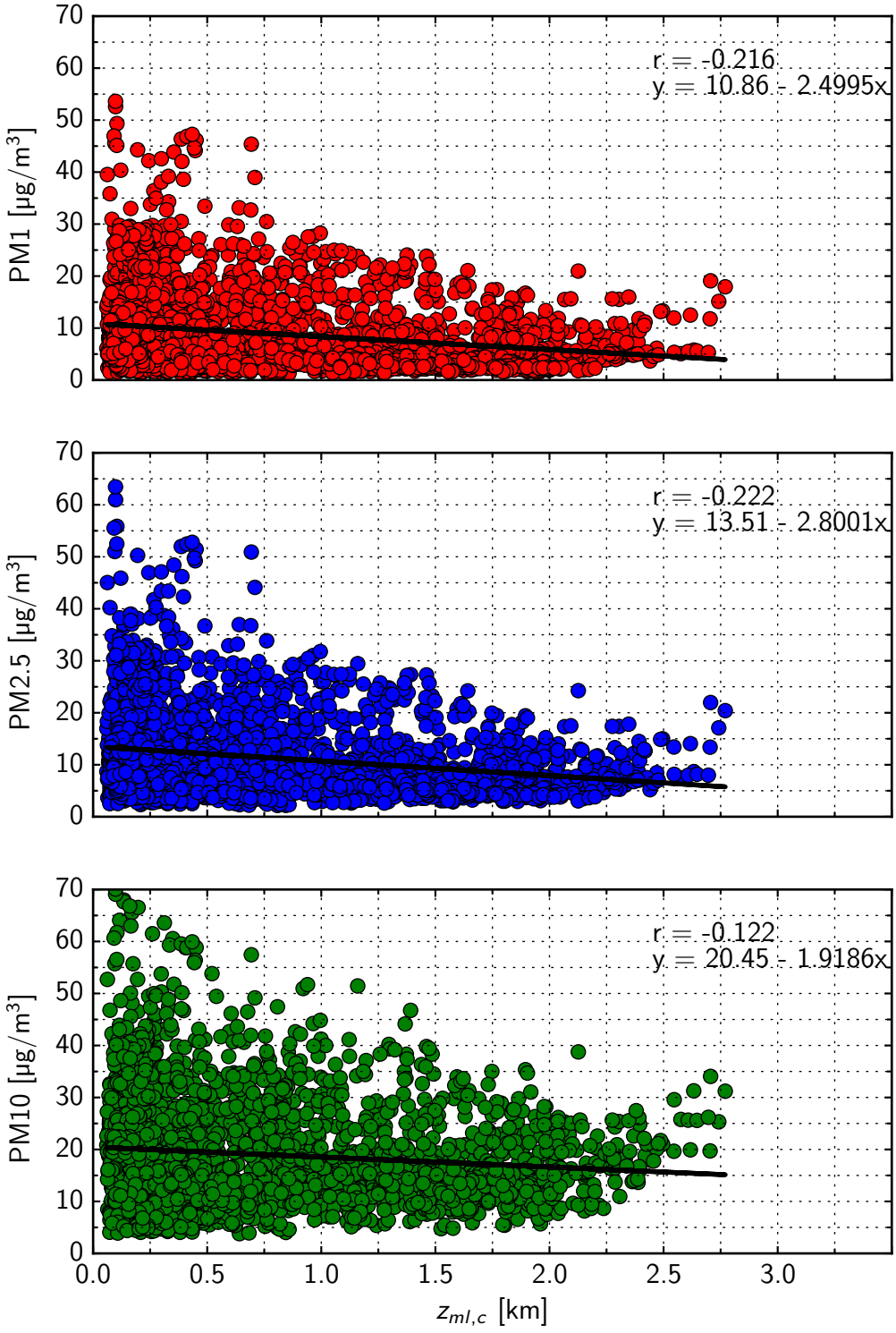

Figure 4.22: Correlation between 30-minute averages of $z_{ml,c}$ and particulate matter. From top to bottom panel: PM1, PM2.5, and PM10 from the UBA-network

5 Conclusion

Recently, networks of automated single-wavelength backscatter lidars ("ceilometers") were implemented, primarily by weather services. Because of their low cost and low maintenance, the amount of operating ceilometers is still increasing. As a consequence, the potential of ceilometers for aerosol remote sensing must be investigated. To process the large amount of data, fully automated algorithms are required which must take account of the large diversity of instruments available from different manufacturers.

In this work, the determination of the lidar constant and thus of the particle backscatter coefficient β_p from ceilometer data was fully automated and demonstrated. A novel boundary layer tracing approach for the determination of the mixing layer height was developed.

Automated Calibration

In order to derive particle backscatter coefficient profiles $\beta_p(z)$ in near real-time from ceilometer measurements, the absolute calibration approach was fully automated and applied to a Jenoptik ceilometer CHM15kx. This approach is based on the determination of the lidar constant C_L and allows the derivation of β_p from ceilometer measurements at virtually any weather condition during day and night with high temporal and spatial resolution. The main issue of ceilometers—the limited signal-to-noise ratio—has been overcome in this approach. That means, a Rayleigh calibration which requires a sufficiently large SNR in the free troposphere is only necessary for the determination of C_L, but no longer necessary when β_p-profiles are subsequently derived by means of C_L.

The automation of the procedure is based on three steps: In the first step, a correction of the incomplete overlap, which is limiting the near range of every ceilometer, is applied. It is necessary in order to extend the measurement range to the surface and thus to minimize the uncertainty of the determined C_L. Furthermore, it allows a better detection of shallow boundary layers. With regard to ceilometer networks where mainly vertically pointing ceilometers are operated, an approach is applied

where overlap functions are determined by using a homogeneous aerosol distribution in the mixing layer. Two new measurement ranges are defined: one further extended $z_{ovl,min}$ for qualitative retrievals and $z_{ovl,c}$ with higher accuracy for quantitative retrievals. Applied to the Jenoptik ceilometer CHM15kx, a high voltage dependence of the overlap function from this instrument has been found.

In the second step, an automated relative calibration of the ceilometer signal is performed. As the sensitivity of some ceilometers changes with the solar background but also regularly during a system reset at night, the lidar constant must be treated as a function of time. A correction of these temporal changes is required for a lidar constant determination. Conversion factors for different operation modes were found, showing a high-voltage dependence. The changes of the sensitivity can be tracked with a system specific parameter which is stored in the housekeeping data. After applying the relative calibration, a normalized signal without steps is obtained.

In the third step a lidar constant is determined. By applying a time- and height selection process, an aerosol-free reference height, required for applying a Rayleigh calibration, is searched and a lidar constant C_L is determined. With regard to the low SNR of the ceilometer this Rayleigh calibration is modified to account for overseen aerosol in the reference range. To constrain the lidar ratio in order to reduce the uncertainty of C_L, the third step can be combined with measurements of the aerosol optical depth from a sun photometer.

Because of the automated applicability of the algorithm, lidar constants from ceilometers can be determined with high temporal coverage. In case of the Jenoptik CHM15kx, a determination of C_L was possible on 391 days out of 1900 available days. The dense coverage revealed an annual cycle of the lidar constant. The differences between instruments from different manufacturers but even between instruments of the same type make an individual lidar constant determination inevitable. In addition, housekeeping data must be tracked, to avoid the use of corrupted data in case of e. g. detector temperature failure. The accuracy of β_p-profiles derived from ceilometers is compromised of uncertainties in the relative calibration and in the absolute calibration. With our CHM15kx, β_p-profiles can be derived within an accuracy of approximately 17%. Large errors are introduced when an estimate of the lidar ratio is required, e.g., for the retrieval of particle extinction coefficients α_p.

Several applications are possible with a calibrated ceilometer. The potential for deriving β_p-profiles even in elevated aerosol layers was demonstrated for Munich. A

climatology of monthly mean β_p-profiles was presented and an annual cycle, with more frequent elevated aerosol layers during summer was observed. The integrated particle backscatter coefficient can be used as a proxy for the atmospheric turbidity and shows an annual cycle for the station in Munich with higher values during summer. The feasibility of a comparison with sun photometer-derived aerosol optical depth was shown and yielded very good agreements during winter. However, the large uncertainty in ceilometer-derived aerosol optical depth due to the unknown lidar ratio must be considered.

ML-height retrieval algorithm COBOLT

Being an important parameter for air quality assessments, the ML-height must be tracked in high temporal and vertical resolution in order to be of benefit for weather forecast models (e. g. initial parameter, validation) but also for ML-height studies. The ceilometer provides a great potential for this purpose. However, most of the state-of-the-art algorithms do not provide ML-heights without large jumps or temporal gaps. An algorithm is needed which is applicable to the large variety of ceilometers and must work fully automatic. Therefore, COBOLT, an algorithm for detecting the whole diurnal ML-height cycle was developed. Based on an best-of-all-methods approach it uses wavelet covariance transform technique, Sobel operators and the temporal variance of the signal to define a hybrid parameter in the first stage of data preprocessing. By applying empirically derived weighting filters with regard to physical and meteorological aspects, a traceable parameter H is obtained which is used in the second stage. With including several validity checks, the continuous boundary layer tracing procedure accounts for the circumstance that usually no large jumps in the diurnal ML-cycle can occur. A multi-member approach allows the variation of input parameters, e. g. search window length, and a set of diurnal ML-cycles is obtained. A function is used to choose the best and realistic ML-cycle. Validations and crosschecks with radiosonde-derived ML-heights as well as comparisons with two other frequently used ML-height retrieval algorithms demonstrated the reliability of COBOLT.

This algorithm opens a wide field of applications—a few examples were shown. Besides studying the ML-height at only certain stations, ceilometer networks allow the investigation of ML-height features at several stations. Important characteristics of the ML-height are growth rate and maximum ML-height, amongst others, and can be reliably determined by COBOLT. This was shown for a 5 years measurement series

in Munich and for a comparison of rural stations with an urban station. Since also flags for precipitation and rain are provided by COBOLT, the user can decide which cases to use. For Munich, the 5 years statistic of the ML-height revealed a maximum of monthly mean ML-heights in July with a height of around 1500 m. Minimum ML-heights are observed during winter (approximately 500 m). Mean growth rates were found between $0.04\,\mathrm{km\,h^{-1}}$ and $0.17\,\mathrm{km\,h^{-1}}$ with a distinct annual cycle. Maximum growth rates of up to $0.7\,\mathrm{km\,h^{-1}}$ were observed during summer.

In order to validate the performance of chemistry transport models and its parameterization scheme for ML-height calculations, ML-heights derived by COBOLT were the basis of a comparison of the model MCCM. With a correct parameterization of the ML-height, weather prediction models can be used for air quality forecasts, provided that correlations between particulate matter and ML-heights occur. This was tested by means of data from a measurement campaign in Berlin. Therefore, COBOLT was applied to a Vaisala CL51 ceilometer and ML-heights were compared to PM1, PM2.5 and PM10. Correlations especially between the maximum values of PM and the ML-height were found.

Outlook

To benefit from calibrated ceilometer data and from the potential the algorithm COBOLT provides, further investigations are interesting. Regarding whole ceilometer networks, the calibration of operating ceilometers would be a large step towards an harmonized data set. For example the GAW Aerosol Lidar Observation Network (GALION, GAW (2007)) focusses on the harmonization of existing ceilometer and lidar networks. In addition, and especially with respect to a harmonization of ceilometer networks, the individual absolute calibration provides information about each instrument for the manufacturer. They can use this information in order to characterize their systems and take this into account for future developments. By today, all ceilometers show large differences in e. g. overlap region, SNR and long term stability. If already well characterized or even if calibrated instruments would be supplied by factory, a harmonization could be easier or even not required. As long as this is not the case, comparisons of all instruments are essential for a characterization. The Ceilinex2015 ceilometer comparison campaign in Lindenberg 2015 was a first step.

The absolute calibration, however, cannot only be useful for future operation, but also for data already measured. Older Jenoptik ceilometers for example, which were

operating first in the ceilometer network of the DWD, showed the feature of relative changes in the signal intensity with changing solar background. The application of the automated calibration would provide an interesting data set from, e. g. the Eyjafjallajokull eruption which is not yet quantitatively evaluated in an automatic way by today. Regarding future volcanic eruptions, a calibrated network provides the basis to track and locate but also to quantify the amount of ash on basis of several assumptions. This information can decrease the airspace closure time and cost for interrupted flight operation significantly in case of a next eruption.

Because of the continuous operation and the fully automated evaluation a huge amount of data can be processed. This allows to study seasonal aerosol climatologies, which can be used for example for projects like AeroCom (Aerosol Comparisons between Observations and Models, Textor et al. (2006), Schulz et al. (2006) and Kinne et al. (2006)). Its aim is to compare available aerosol measurements (ground based and spaceborne) with state-of-the-art aerosol models to gain deeper knowledge of the global impact of aerosols on climate.

Furthermore, calibrated ceilometer networks can be used to validate airborne lidars, e. g. Aladin Airborne Demonstrator (A2D) (Reitebuch et al., 2009; Chouza et al., 2015) or spaceborne lidars, e. g. Airborne Cloud-Aerosol Transport System (CATS) (Yorks et al., 2014), EarthCARE and ADM-Aeolus.

The ML-height as a qualitative parameter does not necessarily rely on absolutely calibrated data. For Vaisala instruments which are operating at a wavelength of around 905 nm the absolute calibration is only possible after a water vapor correction was applied (Wiegner and Gasteiger, 2015). The ML-height retrieval can be done by using raw data. This provides an even larger data set since most of the ceilometers currently worldwide operating are Vaisala instruments.

Studies of the ML-height, for example at different latitudes, near the sea or near deserts, are possible and can provide important knowledge about ML processes. Moreover, reliably determined ML-cycles can be used to improve dispersion models (White et al., 2009). When using modeled ML-heights for quality assessments, further comparisons of different models and parameterizations are necessary. Knowledge about ML-processes is important for analyzing the air quality. Not only the amount of local pollutant emissions is influencing air quality, but also ML-heights. This is in particular interesting in urban areas with regard to emission limit values.

A An analytical solution of the lidar equation

The derivation of the particle backscatter coefficient $\beta_p(z)$ with the lidar equation (2.11) is presented by Fernald et al. (1972). Therefore the transmission term can be divided into an aerosol and a molecular part $T_p^2(z)$ and $T_m^2(z)$, respectively:

$$T_m^2(z) = \exp\left\{-2\int_0^z \alpha_m(z')\,dz'\right\} = \exp\left\{-2\,S_m\int_0^z \beta_m(z')\,dz'\right\} \tag{A.1}$$

$$T_p^2(z) = \exp\left\{-2\int_0^z \alpha_p(z')\,dz'\right\} = \exp\left\{-2\int_0^z S_p(z')\,\beta_p(z')\,dz'\right\} \tag{A.2}$$

This yields the lidar equation in the following form:

$$P(z) = C_L\,\frac{1}{z^2}\,[\beta_p(z) + \beta_m(z)]\,T_m^2(z)\,T_p^2(z) \tag{A.3}$$

After differentiating (A.2) with respect to the distance z and solving for $\beta_p(z)$, one obtains

$$\beta_p(z) = \frac{-1}{2\,S_p(z)\,T_p^2(z)}\frac{dT_p^2(z)}{dz}. \tag{A.4}$$

Substituting this expression into (A.3) yields:

$$P(z) = C_L\,\frac{1}{z^2}\,\left[\beta_m(z) - \frac{1}{2\,S_p(z)\,T_p^2(z)}\frac{dT_p^2(z)}{dz}\right]\,T_m^2(z)\,T_p^2(z) \tag{A.5}$$

This equation can be expressed as a first order differential equation according to $\frac{dy}{dx} + y\,P(x) = Q(x)$:

$$\frac{dT_p^2(z)}{dz} - 2\,\beta_m(z)\,T_p^2(z) = -\frac{2\,S_p(z)\,P(z)\,z^2}{C_L\,T_m^2(z)} \tag{A.6}$$

Where $-2\,\beta_m(z)$ can be regarded as $P(x)$ and $-\frac{2\,S_p(z)\,P(z)\,z^2}{C_L\,T_m^2(z)}$ as $Q(x)$. Solving this equation for $T_p^2(z)$ yields

$$T_p^2(z) = \exp\left[2\int_0^z S_p(z')\,\beta_m(z')dz'\right] \cdot\left\{1 - \frac{2}{C_L}\int_0^z \frac{S_p(z')\,P(z')\,z'^2}{T_m^2(z')}\exp\left[-2\int_0^{z'} S_p(z'')\,\beta_m(z'')dz''\right]dz'\right\} \quad \text{(A.7)}$$

With equation (A.3) solved for $\beta_p(z)$,

$$\beta_p(z) = \frac{P(z)\,z^2}{C_L}\,T_m^{-2}(z)\,T_p^{-2}(z) - \beta_m(z) \quad \text{(A.8)}$$

and substitution of equation (A.7) and the relation from equation (A.1) into (A.8), the solution for the aerosol backscatter coefficient is obtained.

$$\beta_p(z) = \frac{Z_\alpha(z)}{S_p(z)\;N_\alpha(z)} - \beta_m(z) \quad \text{(A.9)}$$

with

$$Z_\alpha(z) = S_p(z)\,z^2\,P(z)\,\exp\left\{-2\int_0^z [S_p(z)\,\beta_m(z) - \alpha_m(z)]\,dz'\right\} \quad \text{(A.10)}$$

and

$$N_\alpha(z) = C_L - 2\int_0^z Z_\alpha(z')\,dz' \quad \text{(A.11)}$$

B List of abbreviations

Abbreviation	Definition
ACE	Aerosol Characterization Experiment
AERONET	Aerosol Robotic Network
AMMA	African Monsoon Multidisciplinary Analysis
AOD	Aerosol optical depth
APD	avalanche photodiode
BAERLIN	Berlin Air quality and Ecosystem Research: Local and long-range Impact of anthropogenic and Natural hydrocarbons
CALIOP	Cloud Aerosol Lidar with Orthogonal Polarization
CEILINEX	Ceilometer Performance Experiment
CHM	Cloud Height Meter
COBOLT	Continuous Boundary Layer Tracing
DWD	German Weather Service
EARLINET	European Aerosol Research Lidar Network
EZ	Entrainment Zone
GALION	GAW Aerosol Lidar Observation Network
GAW	Global Atmosphere Watch
HSRL	High Spectral Resolution Lidar
HB	High Background
HV	High Voltage
HYSPLIT	Hybrid Single Particle Lagrangian Integrated Trajectory Model
INDOEX	Indian Ocean Experiment
IPCC	International Panel on Climate Change
Laser	Light Amplification by Stimulated Emission of Radiation
LCL	Lifting condensation level
Lidar	Light Detection and Ranging
LMU	Ludwig-Maximilians-Universität
MCCM	Mesoscale Climate-Chemistry Model

MINOS	Mediterranean Intensive Oxidant Study
ML	Mixing Layer
MLH	Mixing Layer Height
MPLNET	Micro Pulse Lidar Network
Nd:YAG	Neodym-doped Yttrium Aluminium Granat
NEAQS	New England Air Quality Study
NetCDF	Network Common Data Format
OPAC	Optical properties of Aerosols and Clouds
PBL	Planetary Boundary Layer
Radar	Radio Detection and Ranging
RASS	Radio Acoustic Sounding System
RL	Residual Layer
RS485	Serial communication methods for computers and devices
SAFARI	Southern African Regional Science Initiative
SAMUM	Saharan Mineral Dust Experiment
SBL	Stable Boundary Layer
SNR	Signal/Noise Ratio
SODAR	Sound Detection and Ranging
STRAT	Structure of the Atmosphere
WCT	Wavelet Covariance Transform
YALIS	Yet Another Lidar System - LMU ceilometer

Bibliography

Ackermann, Jörg (1998). "The Extinction-to-Backscatter Ratio of Tropospheric Aerosol: A Numerical Study". In: *J. Atmos. Oceanic Technol.* 15.4, pp. 1043–1050. DOI: 10.1175/1520-0426(1998)015<1043:TETBRO>2.0.CO;2.

Ancellet, Gerard M., Michael J. Kavaya, Robert T. Menzies, and Alan M. Brothers (1986). "Lidar telescope overlap function and effects of misalignment for unstable resonator transmitter and coherent receiver". In: *Appl. Opt.* 25.17, pp. 2886–2890. DOI: 10.1364/AO.25.002886.

Aneja, Viney P., William H. Schlesinger, and Jan Willem Erisman (2008). "Farming pollution". In: *Nature Geoscience* 1.7, pp. 409–411. DOI: 10.1038/ngeo236.

Angevine, WayneM., HenkKlein Baltink, and FredC. Bosveld (2001). "Observations Of The Morning Transition Of The Convective Boundary Layer". In: *Boundary-Layer Meteorology* 101.2, pp. 209–227. DOI: 10.1023/A:1019264716195.

Ångström, Anders (1964). "The parameters of atmospheric turbidity". In: *Tellus* 16.1, pp. 64–75. DOI: 10.1111/j.2153-3490.1964.tb00144.x.

Ansmann, Albert, Frank Wagner, Dietrich Althausen, Detlef Müller, Andreas Herber, and Ulla Wandinger (2001). "European pollution outbreaks during ACE 2: Lofted aerosol plumes observed with Raman lidar at the Portuguese coast". In: *J. Geophys. Res* 106.D18, pp. 20725–20733. DOI: 10.1029/2000JD000091.

Ansmann, Albert, Andreas Petzold, Konrad Kandler, Ina Tegen, Manfred Wendisch, Detlef Müller, Bernadett Weinzierl, Thomas Müller, and Jost Heintzenberg (2011). "Saharan Mineral Dust Experiments SAMUM–1 and SAMUM–2: what have we learned?" In: *Tellus B* 63.4, pp. 403–429. DOI: 10.1111/j.1600-0889.2011.00555.x.

Baars, H., A. Ansmann, R. Engelmann, and D. Althausen (2008). "Continuous monitoring of the boundary-layer top with lidar". In: *Atmospheric Chemistry and Physics* 8.23, pp. 7281–7296. DOI: 10.5194/acp-8-7281-2008.

Bachtiar, V. S., F. Davies, and F. M. Danson (2014). "A combined model for improving estimation of atmospheric boundary layer height". In: *Atmospheric Environment* 98, pp. 461–473. DOI: 10.1016/j.atmosenv.2014.09.028.

Balzarini, A. et al. (2014). "Sensitivity analysis of PBL schemes by comparing WRF model and experimental data". In: *Geoscientific Model Development Discussions* 7.5, pp. 6133–6171. DOI: 10.5194/gmdd-7-6133-2014.

Barlow, Janet F. (2014). "Progress in observing and modelling the urban boundary layer". In: *ICUC8: The 8th International Conference on Urban Climate and the 10th Symposium on the Urban Environment* 10, Part 2, pp. 216–240. DOI: 10.1016/j.uclim.2014.03.011.

Beer, A. (1852). "Bestimmung der Absorption des rothen Lichts in farbigen Flüssigkeiten". In: *Annalen der Physik und Chemie* 86, pp. 78–88.

Beyrich, Frank (1995). "Mixing-height estimation in the convective boundary layer using sodar data". In: *Boundary-Layer Meteorology* 74.1, pp. 1–18. DOI: 10.1007/BF00715708.

Bissonnette, Luc R. (1986). "Sensitivity analysis of lidar inversion algorithms". In: *Appl. Opt* 25.13, pp. 2122–2125. DOI: 10.1364/AO.25.002122.

Boers, R., Eloranta, E. W., and Coulter, R. L. (1984). "Lidar Observations of Mixed Layer Dynamics: Tests of Parameterized Entrainment Models of Mixed Layer Growth Rate". In: *J. Climate Appl. Meteor.* 23.2, pp. 247–266. DOI: 10.1175/1520-0450(1984)023<0247:LOOMLD>2.0.CO;2.

Bouguer, P. (1729). *Essai d'optique sur la gradation de la lumière*. Claude Jombert, Paris.

Bright, David R. and Steven L. Mullen (2002). "The Sensitivity of the Numerical Simulation of the Southwest Monsoon Boundary Layer to the Choice of PBL Turbulence Parameterization in MM5". In: *Wea. Forecasting* 17.1, pp. 99–114. DOI: 10.1175/1520-0434(2002)017<0099:TSOTNS>2.0.CO;2.

Brooks, Ian M. (2003). "Finding Boundary Layer Top: Application of a Wavelet Covariance Transform to Lidar Backscatter Profiles". In: *J. Atmos. Oceanic Technol.* 20.8, pp. 1092–1105. DOI: 10.1175/1520-0426(2003)020<1092:FBLTAO>2.0.CO;2.

Canny, John (1986). "A Computational Approach to Edge Detection". In: *Pattern Analysis and Machine Intelligence, IEEE Transactions on* PAMI-8.6, pp. 679–698. DOI: 10.1109/TPAMI.1986.4767851.

Chouza, F., O. Reitebuch, S. Groß, S. Rahm, V. Freudenthaler, C. Toledano, and B. Weinzierl (2015). "Retrieval of aerosol backscatter and extinction from airborne coherent Doppler wind lidar measurements". In: *Atmospheric Measurement Techniques* 8.7, pp. 2909–2926. DOI: 10.5194/amt-8-2909-2015.

CIMEL Electronique (2000-10-09). *Automatic sun tracking Photometer Cimel CE-318*. Ed. by CIMEL Electronique.

Coakley, James A. and Robert D. Cess (1985). "Response of the NCAR Community Climate Model to the Radiative Forcing by the Naturally Occurring Tropospheric Aerosol: Journal of the Atmospheric Sciences". In: *J. Atmos. Sci* 42.16, pp. 1677–1692. DOI: 10.1175/1520-0469(1985)042<1677:ROTNCC>2.0.CO;2.

Cohen, Ariel E., Steven M. Cavallo, Michael C. Coniglio, and Harold E. Brooks (2015). "A Review of Planetary Boundary Layer Parameterization Schemes and Their Sensitivity in Simulating Southeastern U.S. Cold Season Severe Weather Environments". In: *Wea. Forecasting* 30.3, pp. 591–612. DOI: 10.1175/WAF-D-14-00105.1.

Cohn, Stephen A. and Wayne M. Angevine (2000). "Boundary Layer Height and Entrainment Zone Thickness Measured by Lidars and Wind-Profiling Radars". In: *J. Appl. Meteor.* 39.8, pp. 1233–1247. DOI: 10.1175/1520-0450(2000)039<1233:BLHAEZ>2.0.CO;2.

Collis, R. T. H. (1966). "Lidar: A new atmospheric probe". In: *Quarterly Journal of the Royal Meteorological Society* 92.392, pp. 220–230. DOI: 10.1002/qj.49709239205.

Comerón, Adolfo, Michaël Sicard, and Francesc Rocadenbosch (2013). "Wavelet Correlation Transform Method and Gradient Method to Determine Aerosol Layering from Lidar Returns: Some Comments". In: *J. Atmos. Oceanic Technol.* 30.6, pp. 1189–1193. DOI: 10.1175/JTECH-D-12-00233.1.

Coulter, Richard L. (1979). "A Comparison of Three Methods for Measuring Mixing-Layer Height". In: *J. Appl. Meteor.* 18.11, pp. 1495–1499. DOI: 10.1175/1520-0450(1979)018<1495:ACOTMF>2.0.CO;2.

Davidson, Cliff I., Robert F. Phalen, and Paul A. Solomon (2005). "Airborne Particulate Matter and Human Health: A Review". In: *Aerosol Science and Technology* 39.8, pp. 737–749. DOI: 10.1080/02786820500191348.

Davis, K., N. Gamage, C. Hagelberg, C. Kiemle, D. Lenschow, and P. Sullivan (2000). "An Objective Method for Deriving Atmospheric Structure from Airborne Lidar Observations". In: *J. Atmos. Oceanic Technol.* 17.11, pp. 1455–1468. DOI: 10.1175/1520-0426(2000)017<1455:AOMFDA>2.0.CO;2.

Davis, Kenneth J., Donald H. Lenschow, Steven P. Oncley, Christoph Kiemle, Gerhard Ehret, Andreas Giez, and Jakob Mann (1997). "Role of entrainment in surface-atmosphere interactions over the boreal forest". In: *Journal of Geophysical Research: Atmospheres* 102.D24, pp. 29219–29230. DOI: 10.1029/97JD02236.

Dho, Sang Whoe, Young Je Park, and Hong Jin Kong (1997a). "Application of Geometrical Form Factor in Differential Absorption Lidar Measurement". In: *Optical Review* 4.4, pp. 521–526. DOI: 10.1007/s10043-997-0521-3.

– (1997b). "Experimental determination of a geometric form factor in a lidar equation for an inhomogeneous atmosphere". In: *Appl. Opt.* 36.24, pp. 6009–6010. DOI: 10.1364/AO.36.006009.

Draxler, R.R and G.D Rolph (2012). *HYSPLIT (HYbrid Single-Particle Lagrangian Integrated Trajectory) Model*. Ed. by NOAA ARL READY NOAA Air Resources Laboratory. Silver Spring MD.

Duda, Richard and Peter Hart (1973). *Pattern Classification and Scene Analysis*. John Wiley & Sons Inc.

Durieux, Eric and Luca Fiorani (1998). "Measurement of the lidar signal fluctuation with a shot-per-shot instrument". In: *Appl. Opt.* 37.30, pp. 7128–7131. DOI: 10.1364/AO.37.007128.

Elbaum, Marek and Paul Diament (1976). "SNR in photocounting images of rough objects in partially coherent light". In: *Appl. Opt* 15.9, pp. 2268–2275. DOI: 10.1364/AO.15.002268.

Emeis, S., C. Münkel, Siegfried Vogt, Wolfgang J. Müller, and Klaus Schäfer (2004). "Atmospheric boundary-layer structure from simultaneous SODAR, RASS, and ceilometer measurements". In: *Atmospheric Environment* 38.2, pp. 273–286. DOI: 10.1016/j.atmosenv.2003.09.054.

Emeis, S., Klaus Schäfer, and C. Münkel (2008). "Surface-based remote sensing of the mixing-layer height – a review". In: *Meteorologische Zeitschrift* 17.5, pp. 621–630. DOI: 10.1127/0941-2948/2008/0312.

Endlich, R. M., F. L. Ludwig, and E. E. Uthe (1979). "An automatic method for determining the mixing depth from lidar observations". In: *Atmospheric Environment (1967)* 13.7, pp. 1051–1056. DOI: 10.1016/0004-6981(79)90015-5.

Eresmaa, N., A. Karppinen, Joffre, S. M., J. Räsänen, and H. Talvitie (2006). "Mixing height determination by ceilometer". In: *Atmos. Chem. Phys.* 6.6, pp. 1485–1493. DOI: 10.5194/acp-6-1485-2006.

Eresmaa, Noora, Jari Härkönen, Sylvain M. Joffre, David M. Schultz, Ari Karppinen, and Jaakko Kukkonen (2012). "A Three-Step Method for Estimating the Mixing Height Using Ceilometer Data from the Helsinki Testbed". In: *J. Appl. Meteor. Climatol.* 51.12, pp. 2172–2187. DOI: 10.1175/JAMC-D-12-058.1.

Evans, B. T. N. (1988). "Sensitivity of the backscatter/extinction ratio to changes in aerosol properties: implications for lidar". In: *Appl. Opt* 27.15, pp. 3299–3305. DOI: 10.1364/AO.27.003299.

Fernald, Frederick G. (1984). "Analysis of atmospheric lidar observations: some comments". In: *Appl. Opt* 23.5, pp. 652–653. DOI: 10.1364/AO.23.000652.

Fernald, Frederick G., Benjamin M. Herman, and John A. Reagan (1972). "Determination of Aerosol Height Distributions by Lidar: Journal of Applied Meteorology". In: *J. Appl. Meteor* 11.3, pp. 482–489. DOI: 10.1175/1520-0450(1972)011<0482:DOAHDB>2.0.CO;2.

Fiocco, G. and L. Smullin (1963). "Detection of Scattering Layers in the Upper Atmosphere (60-140 km) by Optical Radar". In: *Nature* 199.4900, pp. 1275–1276. DOI: 10.1038/1991275a0.

Fischer, B.E.A., J.J. Erbrink, S. Finardi, P. Jeannet, S. Joffre, M.G. Morselli, U. Pechinger, P. Seibert, and D.J. Thomson (1998). *COST Action 710-Final Report. Harmonisation of the pre-processing of meteorological data for atmospheric dispersion models*. EUR 18195 EN. Luxemburg.

Flamant, Cyrille, Jacques Pelon, Pierre H. Flamant, and Pierre Durand (1997). "Lidar determination of the entrainment zone thickness at the top of the unstable marine

atmospheric boundary layer". In: *Boundary-Layer Meteorology* 83.2, pp. 247–284. DOI: 10.1023/A:1000258318944.

Flamant, Cyrille et al. (2000). "Airborne lidar measurements of aerosol spatial distribution and optical properties over the Atlantic Ocean during a European pollution outbreak of ACE-2". In: *Tellus B* 52.2.

Flentje, H., B. Briel, C. Beck, M. Collaud Coen, M. Fricke, J. Cyrys, J. Gu, M. Pitz, and W. Thomas (2015). "Identification and monitoring of Saharan dust: An inventory representative for south Germany since 1997". In: *Atmospheric Environment* 109.0, pp. 87–96. DOI: 10.1016/j.atmosenv.2015.02.023.

Forkel, R. and R. Knoche (2006). "Regional climate change and its impact on photooxidant concentrations in southern Germany: Simulations with a coupled regional climate-chemistry model". In: *Journal of Geophysical Research Atmospheres* 111.12. cited By 54. DOI: 10.1029/2005JD006748.

Frey, S. (2012). *JenOptik Sensor Systems Business Unit, ESW GmbH, Oderstrasse 59, 14513 Teltow, Germany, personal communication.*

Gasteiger, J., S. Groß, V. Freudenthaler, and M. Wiegner (2011). "Volcanic ash from Iceland over Munich: mass concentration retrieved from ground-based remote sensing measurements". In: *Atmospheric Chemistry and Physics* 11.5, pp. 2209–2223. DOI: 10.5194/acp-11-2209-2011.

GAW (2007). *Plan for the implementation of the GAW Aerosol Lidar Observation Network GALION.* Ed. by GAW Report 178.

Gold, Ernest (1933). "Maximum day temperature and the tephigram". In: *London, H.M. Stationery Off.*

Granados-Muñoz, M. J., F. Navas-Guzmán, J. A. Bravo-Aranda, J. L. Guerrero-Rascado, H. Lyamani, J. Fernández-Gálvez, and L. Alados-Arboledas (2012). "Automatic determination of the planetary boundary layer height using lidar: One-year analysis over southeastern Spain". In: *Journal of Geophysical Research: Atmospheres* 117.D18, n/a–n/a. DOI: 10.1029/2012JD017524.

Grant, A. L. M. (1997). "An observational study of the evening transition boundary-layer". In: *Quarterly Journal of the Royal Meteorological Society* 123.539, pp. 657–677. DOI: 10.1002/qj.49712353907.

Grell, Georg A., Stefan Emeis, William R. Stockwell, Thomas Schoenemeyer, Renate Forkel, John Michalakes, Richard Knoche, and Winfried Seidl (2000). "Application of a multiscale, coupled MM5/chemistry model to the complex terrain of the {VOTALP} valley campaign". In: *Atmospheric Environment* 34.9, pp. 1435–1453. DOI: 10.1016/S1352-2310(99)00402-1.

Grimsdell, Alison W. and Wayne M. Angevine (2002). "Observations of the Afternoon Transition of the Convective Boundary Layer". In: *J. Appl. Meteor.* 41.1, pp. 3–11. DOI: 10.1175/1520-0450(2002)041<0003:OOTATO>2.0.CO;2.

Groß, Silke, Volker Freudenthaler, Matthias Wiegner, Josef Gasteiger, Alexander Geiß, and Franziska Schnell (2012). "Dual-wavelength linear depolarization ratio of volcanic aerosols: Lidar measurements of the Eyjafjallajökull plume over Maisach, Germany". In: *Atmospheric Environment* 48. Volcanic ash over Europe during the eruption of Eyjafjallajöekull on Iceland, April-May 2010, pp. 85 –96. DOI: 10.1016/j.atmosenv.2011.06.017.

Groß, S., V. Freudenthaler, K. Schepanski, C. Toledano, A. Schäfler, A. Ansmann, and B. Weinzierl (2015). "Optical properties of long-range transported Saharan dust over Barbados as measured by dual-wavelength depolarization Raman lidar measurements". In: *Atmospheric Chemistry and Physics* 15.19, pp. 11067–11080. DOI: 10.5194/acp-15-11067-2015.

Groß, S., J. Gasteiger, V. Freudenthaler, T. Müller, D. Sauer, C. Toledano, and A. Ansmann (2016). "Saharan dust contribution to the Caribbean summertime boundary layer - A lidar study during SALTRACE". In: *Atmospheric Chemistry and Physics Discussions* 2016, pp. 1–14. DOI: 10.5194/acp-2016-246.

Groß, Silke, Matthias Tesche, Volker Freudenthaler, Carlos Toledano, Matthias Wiegner, Albert Ansmann, Dietrich Althausen, and Meinhard Seefeldner (2011). "Characterization of Saharan dust, marine aerosols and mixtures of biomass-burning aerosols and dust by means of multi-wavelength depolarization and Raman lidar measurements during SAMUM 2". In: *Tellus B* 63.4.

Haeffelin, M. et al. (2012). "Evaluation of Mixing-Height Retrievals from Automatic Profiling Lidars and Ceilometers in View of Future Integrated Networks in Europe". In: *Boundary-Layer Meteorology* 143, pp. 49–75. DOI: 10.1007/s10546-011-9643-z.

Halldórsson, T. and J. Langerholc (1978). "Geometrical form factors for the lidar function". In: *Appl. Opt.* 17.2, pp. 240–244. DOI: 10.1364/AO.17.000240.

Hansen, Frank (1966). *The Richardson number in the planetary boundary layer*. ECOM 5053. White Sands Missile Range, New Mexico.

Hansen, J., M. Sato, and R. Ruedy (1997). "Radiative forcing and climate response". In: *J. Geophys. Res* 102.D6, pp. 6831–6864. DOI: 10.1029/96JD03436.

Hansen, James E., Andrew A. Lacis, Pauthon Lee, and Wei-Chyung Wang (1980). "Climatic effects of atmospheric aerosols". In: *Annals of the New York Academy of Sciences* 338.1, pp. 575–587. DOI: 10.1111/j.1749-6632.1980.tb17151.x.

Harms, J. (1979). "Lidar return signals for coaxial and noncoaxial systems with central obstruction". In: *Appl. Opt.* 18.10, pp. 1559–1566. DOI: 10.1364/AO.18.001559.

Heese, B., H. Flentje, D. Althausen, A. Ansmann, and S. Frey (2010). "Ceilometer lidar comparison: backscatter coefficient retrieval and signal-to-noise ratio determination". In: *Atmospheric Measurement Techniques* 3.6, pp. 1763–1770. DOI: 10.5194/amt-3-1763-2010.

Heese, Birgit and Matthias Wiegner (2008). "Vertical aerosol profiles from Raman polarization lidar observations during the dry season AMMA field campaign". In: *J. Geophys. Res* 113.D23, p. D00C11. DOI: 10.1029/2007JD009487.

Hennemuth, Barbara and Andrea Lammert (2006). "Determination of the Atmospheric Boundary Layer Height from Radiosonde and Lidar Backscatter". In: *Boundary-Layer Meteorology* 120.1, pp. 181–200. DOI: 10.1007/s10546-005-9035-3.

Hervo, M., Y. Poltera, and A. Haefele (2016). "An empirical method to correct for temperature dependent variations in the overlap function of CHM15k ceilometers". In: *Atmos. Meas. Tech. Discuss.* 2016, pp. 1–27. DOI: 10.5194/amt-2016-30.

Hess, M., P. Koepke, and I. Schult (1998). "Optical Properties of Aerosols and Clouds: The Software Package OPAC: Bulletin of the American Meteorological Society". In: *Bull. Amer. Meteor. Soc* 79.5, pp. 831–844. DOI: 10.1175/1520-0477(1998)079<0831:OPOAAC>2.0.CO;2.

Holben, B. N. et al. (1998). "AERONET—A Federated Instrument Network and Data Archive for Aerosol Characterization". In: *Remote Sensing of Environment* 66.1, pp. 1–16. DOI: 10.1016/S0034-4257(98)00031-5.

Holzworth, George C. (1964). "Estimates of mean maximum mixing depths in the contiguous United States". In: *Mon. Wea. Rev.* 92.5, pp. 235–242. DOI: 10.1175/1520-0493(1964)092<0235:EOMMMD>2.3.CO;2.

– (1967). "Mixing Depths, Wind Speeds and Air Pollution Potential for Selected Locations in the United States". In: *J. Appl. Meteor.* 6.6, pp. 1039–1044. DOI: 10.1175/1520-0450(1967)006<1039:MDWSAA>2.0.CO;2.

Hooper, William P. and Edwin W. Eloranta (1986). "Lidar Measurements of Wind in the Planetary Boundary Layer: The Method, Accuracy and Results from Joint Measurements with Radiosonde and Kytoon". In: *J. Climate Appl. Meteor.* 25.7, pp. 990–1001. DOI: 10.1175/1520-0450(1986)025<0990:LMOWIT>2.0.CO;2.

Huebert, Barry J., Timothy Bates, Philip B. Russell, Guangyu Shi, Young Joon Kim, Kimitaka Kawamura, Greg Carmichael, and Teruyuki Nakajima (2003). "An overview of ACE-Asia: Strategies for quantifying the relationships between Asian aerosols and their climatic impacts". In: *J. Geophys. Res* 108.D23, p. 8633. DOI: 10.1029/2003JD003550.

IPCC (2013). *Climate change 2013: The physical science basis*. Cambridge Univeristy Press.

Kaimal, J. C., Abshire, N. L., Chadwick, R. B., Decker, M. T., Hooke, W. H., Kropfli, R. A., Neff, W. D., F. Pasqualucci, and Hildebrand, P. H. (1982). "Estimating the Depth of the Daytime Convective Boundary Layer". In: *J. Appl. Meteor.* 21.8, pp. 1123–1129. DOI: 10.1175/1520-0450(1982)021<1123:ETDOTD>2.0.CO;2.

King, Michael D., Steven Platnick, Christopher C. Moeller, Henry E. Revercomb, and D. Allen Chu (2003). "Remote sensing of smoke, land, and clouds from the NASA ER-2 during SAFARI 2000". In: *J. Geophys. Res* 108.D13, p. 8502. DOI: 10.1029/2002JD003207.

Kinne, S. et al. (2006). "An AeroCom initial assessment – optical properties in aerosol component modules of global models". In: *Atmospheric Chemistry and Physics* 6.7, pp. 1815–1834. DOI: 10.5194/acp-6-1815-2006.

Klett, James D. (1981). "Stable analytical inversion solution for processing lidar returns". In: *Appl. Opt* 20.2, pp. 211–220. DOI: 10.1364/AO.20.000211.

– (1983). "Lidar calibration and extinction coefficients". In: *Appl. Opt* 22.4, pp. 514–515. DOI: 10.1364/AO.22.000514.

Klett, James D. (1985). "Lidar inversion with variable backscatter/extinction ratios". In: *Appl. Opt* 24.11, pp. 1638–1643. DOI: 10.1364/AO.24.001638.

Koepke, P., J. Gasteiger, and M. Hess (2015). "Technical Note: Optical properties of desert aerosol with non-spherical mineral particles: data incorporated to OPAC". In: *Atmospheric Chemistry and Physics* 15.10, pp. 5947–5956. DOI: 10.5194/acp-15-5947-2015.

Kolev, I., P. Savov, B. Kaprielov, O. Parvanov, and V. Simeonov (2000). "Lidar observation of the nocturnal boundary layer formation over Sofia, Bulgaria". In: *Atmospheric Environment* 34.19, pp. 3223–3235. DOI: 10.1016/S1352-2310(99)00490-2.

Korhonen, K. et al. (2014). "Atmospheric boundary layer top height in South Africa: measurements with lidar and radiosonde compared to three atmospheric models". In: *Atmospheric Chemistry and Physics* 14.8, pp. 4263–4278. DOI: 10.5194/acp-14-4263-2014.

Kovalev, Vladimir A. and William E. Eichinger (2004). *Elastic lidar: Theory, practice, and analysis methods.* Hoboken, NJ: Wiley-Interscience.

Kunkel, K., E. Eloranta, and S. Shipley (1977). "Lidar Observations of the Convective Boundary Layer". In: *J. Appl. Meteor.* 16.12, pp. 1306–1311. DOI: 10.1175/1520-0450(1977)016<1306:LOOTCB>2.0.CO;2.

Kunz, Gerard J. and Gerrit de Leeuw (1993). "Inversion of lidar signals with the slope method". In: *Appl. Opt.* 32.18, pp. 3249–3256. DOI: 10.1364/AO.32.003249.

Kuze, Hiroaki, Hideki Kinjo, Yasushi Sakurada, and Nobuo Takeuchi (1998). "Field-of-view dependence of lidar signals by use of Newtonian and Cassegrainian telescopes". In: *Appl. Opt.* 37.15, pp. 3128–3132. DOI: 10.1364/AO.37.003128.

Lambert, J. H. (1760). *Photometria sive de mensura et gradibus luminis, colorum et umbrae.* Eberhardt Klett, Augsburg, Germany.

Lelieveld, J. et al. (2002). "Global Air Pollution Crossroads over the Mediterranean". In: *Science* 298.5594, pp. 794–799. DOI: 10.1126/science.1075457.

Maiman, T. (1960). "Stimulated Optical Radiation in Ruby". In: *Nature* 187.4736, pp. 493–494. DOI: 10.1038/187493a0.

Marsik, Frank J., Kenneth W. Fischer, Tracey D. McDonald, and Perry J. Samson (1995). "Comparison of Methods for Estimating Mixing Height Used during the 1992 Atlanta Field Intensive". In: *J. Appl. Meteor.* 34.8, pp. 1802–1814. DOI: 10.1175/1520-0450(1995)034<1802:COMFEM>2.0.CO;2.

McClung, F. J. and R. W. Hellwarth (1962). "Giant Optical Pulsations from Ruby". In: *Journal of Applied Physics* 33.3, pp. 828–829. DOI: 10.1063/1.1777174.

McIntyre, R.J (1966). "Multiplication noise in uniform avalanche diodes". In: *IEEE Transactions on Electron Devices* 13.1, pp. 164–168. DOI: 10.1109/T-ED.1966.15651.

Melfi, S., J. Spinhirne, S-H. Chou, and S. Palm (1985). "Lidar Observations of Vertically Organized Convection in the Planetary Boundary Layer over the Ocean". In: *J. Climate Appl. Meteor.* 24.8, pp. 806–821. DOI: 10.1175/1520-0450(1985)024<0806:LOOVOC>2.0.CO;2.

Menut, Laurent, Cyrille Flamant, Jacques Pelon, and Pierre H. Flamant (1999). "Urban Boundary-Layer Height Determination from Lidar Measurements Over the Paris Area". In: *Appl. Opt.* 38.6, pp. 945–954. DOI: 10.1364/AO.38.000945.

Middleton, W.E.K. and A. F. Spilhaus (1953). *Meteorological Instruments*. University of Toronto Press.

Mie, G. (1908). "Beiträge zur Optik trüber Medien, speziell kolloidaler Metallösungen". In: *Annalen der Physik* 330, pp. 377–445. DOI: 10.1002/andp.19083300302.

Morille, Y., M. Haeffelin, P. Drobinski, and J. Pelon (2007). "STRAT: An Automated Algorithm to Retrieve the Vertical Structure of the Atmosphere from Single-Channel Lidar Data: Journal of Atmospheric and Oceanic Technology". In: *J. Atmos. Oceanic Technol* 24.5, pp. 761–775. DOI: 10.1175/JTECH2008.1.

Müller, Detlef, Frank Wagner, Dietrich Althausen, Ulla Wandinger, and Albert Ansmann (2000). "Physical properties of the Indian aerosol plume derived from six-wavelength lidar Observations on 25 March 1999 of the Indian Ocean Experiment". In: *Geophys. Res. Lett* 27.9, pp. 1403–1406. DOI: 10.1029/1999GL011217.

Münkel, Christoph, Klaus Schäfer, and Stefan Emeis, eds. (2011). *Adding confidence levels and error bars to mixing layer heights detected by ceilometer*. Vol. 8177. DOI: 10.1117/12.898122.

Neu, Urs, Thomas Künzle, and Heinz Wanner (1994). "On the relation between ozone storage in the residual layer and daily variation in near-surface ozone concentration — A case study". In: *Boundary-Layer Meteorology* 69.3, pp. 221–247. DOI: 10.1007/BF00708857.

Optik Systeme GmbH, JENOPTIK Laser (2006). *Wolkenhöhenmessgerät CHM15kx - Benutzerhandbuch*. Ed. by JENOPTIK Laser Optik Systeme GmbH.

Pal, S. et al. (2012). "Spatio-temporal variability of the atmospheric boundary layer depth over the Paris agglomeration: An assessment of the impact of the urban heat island intensity". In: *Atmospheric Environment* 63, pp. 261–275. DOI: 10.1016/j.atmosenv.2012.09.046.

Pappalardo, G. et al. (2014). "EARLINET: towards an advanced sustainable European aerosol lidar network". In: *Atmospheric Measurement Techniques* 7.8, pp. 2389–2409. DOI: 10.5194/amt-7-2389-2014.

Quinn, Patricia K. and Timothy S. Bates (2005). "Regional aerosol properties: Comparisons of boundary layer measurements from ACE 1, ACE 2, Aerosols99, INDOEX, ACE Asia, TARFOX, and NEAQS". In: *J. Geophys. Res* 110.D14, p. D14202. DOI: 10.1029/2004JD004755.

Raes, Frank, Timothy Bates, Frank McGovern, and Marc van Liedekerke (2000). "The 2nd Aerosol Characterization Experiment (ACE-2): general overview and main results". In: *Tellus B* 52.2, pp. 111–125. DOI: 10.1034/j.1600-0889.2000.00124.x.

Ramanathan, V. et al. (2001). "Indian Ocean Experiment: An integrated analysis of the climate forcing and effects of the great Indo-Asian haze". In: *J. Geophys. Res* 106.D22, pp. 28371–28398. DOI: 10.1029/2001JD900133.

Rayleigh (1899). "XXXIV. On the transmission of light through an atmosphere containing small particles in suspension, and on the origin of the blue of the sky". In: *Philosophical Magazine Series 5* 47.287, pp. 375–384. DOI: 10.1080/14786449908621276.

Reitebuch, Oliver, Christian Lemmerz, Engelbert Nagel, Ulrike Paffrath, Yannig Durand, Martin Endemann, Frederic Fabre, and Marc Chaloupy (2009). "The Airborne Demonstrator for the Direct-Detection Doppler Wind Lidar ALADIN on ADM-Aeolus. Part I: Instrument Design and Comparison to Satellite Instrument". In: *J. Atmos. Oceanic Technol.* 26.12, pp. 2501–2515. DOI: 10.1175/2009JTECHA1309.1.

Rotach, W. et al. (2005). "BUBBLE – an Urban Boundary Layer Meteorology Project". In: *Theoretical and Applied Climatology* 81.3, pp. 231–261. DOI: 10.1007/s00704-004-0117-9.

Russell, Philip B., Edward E. Uthe, Francis L. Ludwig, and Neil A. Shaw (1974). "A comparison of atmospheric structure as observed with monostatic acoustic sounder and lidar techniques". In: *Journal of Geophysical Research* 79.36, pp. 5555–5566. DOI: 10.1029/JC079i036p05555.

Sasano, Y., H. Shimizu, N. Takeuchi, and M. Okuda (1979). "Geometrical form factor in the laser radar equation: an experimental determination". In: *Appl. Opt.* 18.23, pp. 3908–3910. DOI: 10.1364/AO.18.003908.

Sasano, Yasuhiro and Hideaki Nakane (1984). "Significance of the extinction/backscatter ratio and the boundary value term in the solution for the two-component lidar equation". In: *Appl. Opt* 23.1, 11_1–13. DOI: 10.1364/AO.23.0011\textunderscore.

Sasano, Yasuhiro, Edward V. Browell, and Syed Ismail (1985). "Error caused by using a constant extinction/backscattering ratio in the lidar solution". In: *Appl. Opt* 24.22, pp. 3929–3932. DOI: 10.1364/AO.24.003929.

Sassen, Kenneth and Gregory C. Dodd (1982). "Lidar crossover function and misalignment effects". In: *Appl. Opt.* 21.17, pp. 3162–3165. DOI: 10.1364/AO.21.003162.

Satheesh, S. K. and K. Krishna Moorthy (2005). "Radiative effects of natural aerosols: A review". In: *Atmospheric Environment* 39.11, pp. 2089–2110. DOI: 10.1016/j.atmosenv.2004.12.029.

Schell, B., I.J. Ackermann, H. Hass, F.S. Binkowski, and A. Ebel (2001). "Modeling the formation of secondary organic aerosol within a comprehensive air quality model system". In: *Journal of Geophysical Research Atmospheres* 106.D22, pp. 28275–28293.

Schmid, Beat and Christoph Wehrli (1995). "Comparison of Sun photometer calibration by use of the Langley technique and the standard lamp". In: *Appl. Opt.* 34.21, pp. 4500–4512. DOI: 10.1364/AO.34.004500.

Schroeder, Daniel J., ed. (2000). *Astronomical Optics (Second Edition)*. San Diego: Academic Press.

Schulz, M. et al. (2006). "Radiative forcing by aerosols as derived from the AeroCom present-day and pre-industrial simulations". In: *Atmospheric Chemistry and Physics* 6.12, pp. 5225–5246. DOI: 10.5194/acp-6-5225-2006.

Schween, J. H., A. Hirsikko, U. Löhnert, and S. Crewell (2014). "Mixing-layer height retrieval with ceilometer and Doppler lidar: from case studies to long-term assessment". In: *Atmospheric Measurement Techniques* 7.11, pp. 3685–3704. DOI: 10.5194/amt-7-3685-2014.

Seibert, Petra, Frank Beyrich, Sven-Erik Gryning, Sylvain Joffre, Alix Rasmussen, and Philippe Tercier (2000). "Review and intercomparison of operational methods for the determination of the mixing height". In: *Atmospheric Environment* 34.7, pp. 1001–1027. DOI: 10.1016/S1352-2310(99)00349-0.

Seidel, D.J, C.O Ao, and K. Li (2010). "Estimating climatological planetary boundary layer heights from radiosonde observations: Comparison of methods and uncertainty analysis". In: *J. Geophys. Res.* 115.D16, p. D16113.

Shaw, Glenn E. (1976). "Error analysis of multi-wavelength sun photometry". In: *pure and applied geophysics* 114.1, pp. 1–14. DOI: 10.1007/BF00875487.

Shimizu, Atsushi et al. (2004). "Continuous observations of Asian dust and other aerosols by polarization lidars in China and Japan during ACE-Asia". In: *J. Geophys. Res* 109.D19, D19S17. DOI: 10.1029/2002JD003253.

Smirnov, A., B. N. Holben, T. F. Eck, O. Dubovik, and I. Slutsker (2000). "Cloud-Screening and Quality Control Algorithms for the AERONET Database". In: *Remote Sensing of Environment* 73.3, pp. 337–349. DOI: 10.1016/S0034-4257(00)00109-7.

Stelmaszczyk, Kamil, Marcella Dell'Aglio, Stanislaw Chudzyński, Tadeusz Stacewicz, and Ludger Wöste (2005). "Analytical function for lidar geometrical compression form-factor calculations". In: *Appl. Opt.* 44.7, pp. 1323–1331. DOI: 10.1364/AO.44.001323.

Steyn, D., M. Baldi, and R. Hoff (1999). "The Detection of Mixed Layer Depth and Entrainment Zone Thickness from Lidar Backscatter Profiles". In: *J. Atmos. Oceanic Technol.* 16.7, pp. 953–959. DOI: 10.1175/1520-0426(1999)016<0953:TDOMLD>2.0.CO;2.

Stull, Roland B. (1988 // 1997). *An Introduction to Boundary Layer Meteorology // An introduction to boundary layer meteorology.* Reprinted with errata. Vol. 13. Dordrecht [u.a.]: Kluwer Acad. Publ.

Svensson, G. et al. (2011). "Evaluation of the Diurnal Cycle in the Atmospheric Boundary Layer Over Land as Represented by a Variety of Single-Column Models: The Second GABLS Experiment". In: *Boundary-Layer Meteorology* 140.2, pp. 177–206. DOI: 10.1007/s10546-011-9611-7.

Takamura, Tamio, Yasuhiro Sasano, and Tadahiro Hayasaka (1994). "Tropospheric aerosol optical properties derived from lidar, sun photometer, and optical particle counter measurements". In: *Appl. Opt* 33.30, pp. 7132–7140. DOI: 10.1364/AO.33.007132.

Tesche, Matthias, Silke Gross, Albert Ansmann, Detlef Müller, Dietrich Althausen, Volker Freudenthaler, and Michael Esselborn (2011). "Profiling of Saharan dust and biomass-burning smoke with multiwavelength polarization Raman lidar at Cape Verde". In: *Tellus B* 63.4.

Textor, C. et al. (2006). "Analysis and quantification of the diversities of aerosol life cycles within AeroCom". In: *Atmospheric Chemistry and Physics* 6.7, pp. 1777–1813. DOI: 10.5194/acp-6-1777-2006.

Toledano, C. et al. (2011). "Optical properties of aerosol mixtures derived from sun-sky radiometry during SAMUM-2". In: *Tellus B* 63.4, pp. 635–648. DOI: 10.1111/j.1600-0889.2011.00573.x.

Tomine, Kikuro, Chikara Hirayama, Kouichiro Michimoto, and Nobuo Takeuchi (1989). "Experimental determination of the crossover function in the laser radar equation for days with a light mist". In: *Appl. Opt.* 28.12, pp. 2194–2195. DOI: 10.1364/AO.28.002194.

Twomey, S. (1974). "Pollution and the planetary albedo". In: *Atmospheric Environment (1967)* 8.12, pp. 1251–1256. DOI: 10.1016/0004-6981(74)90004-3.

Velotta, Raffaele, Bruno Bartoli, Roberta Capobianco, Luca Fiorani, and Nicola Spinelli (1998). "Analysis of the Receiver Response in Lidar Measurements". In: *Appl. Opt* 37.30, pp. 6999–7007. DOI: 10.1364/AO.37.006999.

Wagner, Patrick and Klaus Schäfer (2015). "Influence of mixing layer height on air pollutant concentrations in an urban street canyon". In: *Urban Climate*. DOI: 10.1016/j.uclim.2015.11.001.

Wallace, John M. and Peter V. Hobbs, eds. (2006). *Atmospheric Science (Second Edition)*. San Diego: Academic Press.

Weinzierl, Bernadett et al. (2012). "On the visibility of airborne volcanic ash and mineral dust from the pilot's perspective in flight". In: *Physics and Chemistry of the Earth, Parts A/B/C* 45–46. Volcanic ash: an agent in Earth systems, pp. 87 –102. DOI: 10.1016/j.pce.2012.04.003.

Weitkamp, Claus, ed. (2005). *Lidar: Range-resolved optical remote sensing of the atmosphere*. Vol. 102. New York [u.a.]: Springer.

Welton, E. J., J.R Campbell, J.D Spinhirne, and V.S Scott (2001). "Global monitoring of clouds and aerosols using a network of micro-pulse lidar systems". In: *Lidar remote sensing for industry and environment monitoring*. Ed. by Kevin G. Harding. Vol. 4153. Bellingham and Wash: SPIE, pp. 151–158.

Wex, H. et al. (2016). "Aerosol arriving on the Caribbean island of Barbados: Physical properties and origin". In: *Atmospheric Chemistry and Physics Discussions* 2016, pp. 1–34. DOI: 10.5194/acp-2016-244.

White, J., J. Bowers, S. Hanna, and J. Lundquist (2009). "Importance of Using Observations of Mixing Depths in order to Avoid Large Prediction Errors by a Transport and Dispersion Model". In: *Journal of Atmospheric and Oceanic Technology* 26.1, pp. 22–32. DOI: 10.1175/2008JTECHA1134.1.

Wiegner, M. and J. Gasteiger (2015). "Correction of water vapor absorption for aerosol remote sensing with ceilometers". In: *Atmospheric Measurement Techniques* 8.9, pp. 3971–3984. DOI: 10.5194/amt-8-3971-2015.

Wiegner, M. and A. Geiß (2012). "Aerosol profiling with the Jenoptik ceilometer CHM15kx". In: *Atmos. Meas. Tech.* 5.8, pp. 1953–1964. DOI: 10.5194/amt-5-1953-2012.

Wiegner, Matthias, S. Emeis, Volker Freudenthaler, Birgit Heese, Wolfgang Junkermann, C. Münkel, Klaus Schäfer, Meinhard Seefeldner, and Siegfried Vogt (2006).

"Mixing layer height over Munich, Germany: Variability and comparisons of different methodologies". In: *Journal of Geophysical Research: Atmospheres* 111.D13. DOI: 10.1029/2005JD006593.

Wiegner, Matthias, Josef Gasteiger, Silke Groß, Franziska Schnell, Volker Freudenthaler, and Renate Forkel (2012). "Characterization of the Eyjafjallajökull ashplume: Potential of lidar remote sensing". In: *Physics and Chemistry of the Earth, Parts A/B/C* 45–46. Volcanic ash: an agent in Earth systems, pp. 79 –86. DOI: 10.1016/j.pce.2011.01.006.

Wildmann, Norman, GerritAnke Rau, and Jens Bange (2015). "Observations of the Early Morning Boundary-Layer Transition with Small Remotely-Piloted Aircraft". In: *Boundary-Layer Meteorology* 157.3, pp. 345–373. DOI: 10.1007/s10546-015-0059-z.

Yorks, John E., Matthew J. McGill, V. Stanley Scott, Shane W. Wake, Andrew Kupchock, Dennis L. Hlavka, William D. Hart, and Patrick A. Selmer (2014). "The Airborne Cloud–Aerosol Transport System: Overview and Description of the Instrument and Retrieval Algorithms". In: *Journal of Atmospheric and Oceanic Technology* 31.11, pp. 2482–2497. DOI: 10.1175/JTECH-D-14-00044.1.

Young, Andrew T. (1981). "Rayleigh scattering". In: *Appl. Opt.* 20.4, pp. 533–535. DOI: 10.1364/AO.20.000533.

Acknowledgments

This thesis was developed at the Meteorological Institute of the Ludwig-Maximilians-Universität, Munich. During the years of research, development and finally putting the results on paper, many people supported me. The most important subject-specific person in this time has been my supervisor Dr. Matthias Wiegner, head of the lidar group. He has contributed with his expertise in this field of research in many ways to my work, especially by constructive discussions, suggestions and guidance. Furthermore, I thank Prof. Dr. Bernhard Mayer for helpful discussions and also his motivation. Besides Prof. Mayer I want to thank Dr. Martin Weissmann for reviewing this thesis as co-examiner.

Rich data are the foundation of testing automated calibration. Important data from the chemistry transport model MCCM were provided by Dr. Renate Forkel (IMK-IFU, Garmisch). Prof. Dr. Klaus Schäfer (IMK-IFU, Garmisch) provided the data of the Berlin measurement campaign. Besides them I want to thank Dr. Frank Wagner and Dr. Ina Mattis (DWD) for supplying me with data of the DWD ceilometer network and for vital information exchange about any ceilometer related issues. In addition, I thank Holger Wille and Kornelia Pönitz from the ceilometer manufacturer Lufft for the fruitful intercommunication about any technical aspects. Special thanks goes to the AERONET-Team for providing data and maintenance of the station in Munich.

I want to thank also Dr. Silke Gross (DLR) and Dr. Volker Freudenthaler (LMU) who accompanied my first steps in the field of lidar and gave me a first review of the possibilities. Special thanks go to Meinhard Seefeldner and Anton Lex for their overall hands-on help and for sending YALIS on journeys to see the sky above more regions than Munich.

Finally, I thank my family, especially my parents Christiane and Dietmar, for the constant moral support.

Thank you Veronika, for all your love and support.

The research leading to these results has received funding from the European Union Seventh Framework Programm (FP7/2007-2013) under grant agreement n° 262254